OKLAHOMA STATE UNIVERSITY

NIBLACK RESEARCH SCHOLARS

2022-23

FINAL REPORTS

NIBLACK RESEARCH SCHOLARS

PREFACE

Oklahoma State University is pleased to present the enclosed reports of the 2022-23 Niblack Research Scholars.

Thanks to the continued support of OSU alumnus and retired Pfizer executive Dr. John Niblack, the Niblack Research Scholars program affords OSU students the unique opportunity to conduct real scientific research as undergraduates. Dr. Niblack himself participated in research at OSU during his undergraduate experience and believes it impacted his decision to pursue science as a career. His vision and passion to inspire a new generation of scientists lives on in this program.

Dr. John and Heidi Niblack with the 2022-23 Niblack Research Scholars.

(front row, L to R)
Sam Glenn, Natalee Richardson, Heidi Niblack,
Dr. John Niblack, Samantha Stobbe, Rabeca Richardson

(back row, L to R)
OSU V.P. for Research Dr. Kenneth Sewell, Sarah Teeman, Kaitlyn Cotton,
Rebecca Wilson, Charlie Vermeire, Mary Erdmann, Brinkli Abbitt, Dr. Stephen McKeever

SESSION ONE:

Rabeca Richardson

"Effects of Drought and Clipping Timing on Mycorrhizal Symbiosis and Growth of Johnsongrass, an Invasive Grass in Oklahoma"
Research Area: Integrative Biology
Faculty Sponsor: Dr. Bo Zhang
Graduate Student Mentor: Allasandra Valdez

Kaitlyn Cotton

"Effects of Organoantimony Compounds on the Fungal Pathogen *Cryptococcus neoformans*"
Research Area: Microbiology and Molecular Genetics
Faculty Sponsor: Dr. Karen Wozniak
Graduate Student Mentor: Brittney Conn

Mary Erdmann

"Regulation of the Type III Secretion System by PtsN in *Pseudomonas aeruginosa*"
Research Area: Microbiology and Molecular Genetics
Faculty Sponsor: Dr. Matthew Cabeen
Graduate Student Mentor: Somalisa Pan

Effects of drought and clipping timing on mycorrhizal symbiosis and growth of Johnsongrass, an invasive grass in Oklahoma

Rabeca Richardson

Integrative Biology
Faculty Sponsor: Bo Zhang
Graduate Student Mentor: Allasandra Valdez

ABSTRACT

Invasive species threaten ecosystem stability and biodiversity, particularly in rangelands, where drought-resistant grasses cause biodiversity loss. Understanding the role of the soil microbiome, specifically mycorrhizal fungi, in controlling invasions under climate change is crucial. We conducted a greenhouse experiment on Johnsongrass, *Sorghum halepense*, to examine the effects of drought and clipping treatment intervals on mycorrhizal colonization. We examined various physiological parameters driving plant growth such as biomass, leaf nutrient content, and fungal abundance. No significant differences were observed in biomass measurements across the different clipping and drought treatments. Similarly, there were no significant findings in arbuscular mycorrhizal associations. This might suggest that Johnsongrass does not heavily rely on arbuscular mycorrhizal fungi for nutrient acquisition or growth. Additionally, clipping treatments were ineffective in managing the grass itself. The lack of significant findings in this study only suggests that further exploration into factors influencing the success of invasive C4 grasses like Johnsongrass is needed to develop more effective control strategies against invasive species during drought.

1. Introduction:

The competitive success of invasive species threatens the overall stability of the environment by decreasing biodiversity and potentially altering the functionality within ecosystems (Vetter et al, 2020). Rangelands are one of the best areas for carbon sequestrations and consist primarily of native plant communities managed, typically, for livestock production; unfortunately, rangelands are being plagued by invasive grasses, especially drought resistant C4 grasses, resulting in a cascading effect of biodiversity loss (Flanders et al.,2006). Notably, species invasion is expected to be promoted by impacts of climate change, e.g., increasing drought favors invasion of the above C4 grasses (Bradley, et al., 2012).

Previous studies have considered multiple mechanisms of species invasion and related control strategies under changing climate conditions (Bradley, et al., 2010; Bajwa et al., 2016). However, little is known about roles of soil microbiome in affecting invasive species and native species relations, let alone if they play a major role as an invasion mechanism. Although mycorrhizal symbiosis has been shown to improve plant growth and competitive ability by increasing nutrient and water uptake for the host (Rashidi et al., 2021), the effects of the symbiotic association on invasive species under drought remain elusive, and the existence of variation in association with specific invasion-control treatments (e.g., clipping) is largely unknown. In the absence of such knowledge, the capability to project species invasion under future drought is restricted, and there would be a critical uncertainty to apply invasion-control treatments effectively.

The preservation of native biodiversity and ecosystem stability necessitates the effective control of invasive grasses (Beaury et al., 2020; DiTomaso et al., 2010). Among the most employed strategies is physical removal management (PRM), which encompasses techniques such as clipping, grazing, and mowing to control species invasion (Weidlich et al., 2020). Nevertheless, considerable uncertainty persists regarding the true efficacy of this approach, particularly in the face of escalating drought conditions. Given the substantial costs and labor-intensive nature associated with managing invasive grasses, enhancing the efficiency of management strategies assumes great importance (Eiswerth and Johnson, 2002). Prior research has established the significant influence of management timing and intensity on efficacy (Gao et al., 2009; Tang et al., 2009). However, it remains unclear how increased drought may impact the established benchmarks for enhanced efficiency. To bridge this knowledge gap, we conducted a greenhouse experiment investigating the interactive effects of various drought and clipping treatment timings on the colonization of arbuscular mycorrhizal (AM) fungi in an urgent invasive species prevalent in Oklahoma, Johnsongrass (*Sorghum halepense*).

2. Experimental Details

We conducted a factorial-designed greenhouse experiment with two levels of drought, presence and absence, and three clipping treatment intervals, early-season applied, late-season applied, and a control with no clip. The study took place over the course of 14 weeks using an open-air-rain-out shelter at the Rigdon-Afansiev Memorial Arboretum in Stillwater, OK. We used Johnsongrass, *Sorghum halepense*, as our model species due to its ability to outcompete native species and ability to thrive in warm conditions (Schwinning et al., 2017). Johnsongrass is a highly invasive C4 grass plaguing grasslands all over the United States and costing farmers tens of millions of dollars to cover management and yield losses (Sezen et al., 2016).

2.1 Experimental Design

We used a randomized block design with two types of treatment: (1) Drought: there were two levels for drought—presence and absence. (2) Clipping interval: there were three levels of clipping intervals—early applied (every two weeks), late applied (every 4 weeks), and a control no clipping (14 weeks final harvest). There were three repeats for each treatment combination, totaling 18 beds (2 drought X 3 clipping X 3 repeats). The planting beds were built with three layers of landscaping material lining the bottoms of the beds to prevent rhizomes and roots from breaking through. Additionally, the beds were organized into 3 blocks of 6 beds, with 1 of each treatment combination organized in a random placement within each block. This was to account for the potential difference in light availability and other external factors. The soil used for each bed was collected from the Cross Timbers Experimental Range, Stillwater, OK to mimic the natural soil conditions of Oklahoma and including native AM fungi composition. The soil was then mixed in a 3:1 ration with sand. We transplanted Johnsongrass rhizomes that were collected from the surrounding area from naturally occurring Johnsongrass colonies. The rhizomes were planted in 5 rows across the width of each bed (See **Fig. 1**).

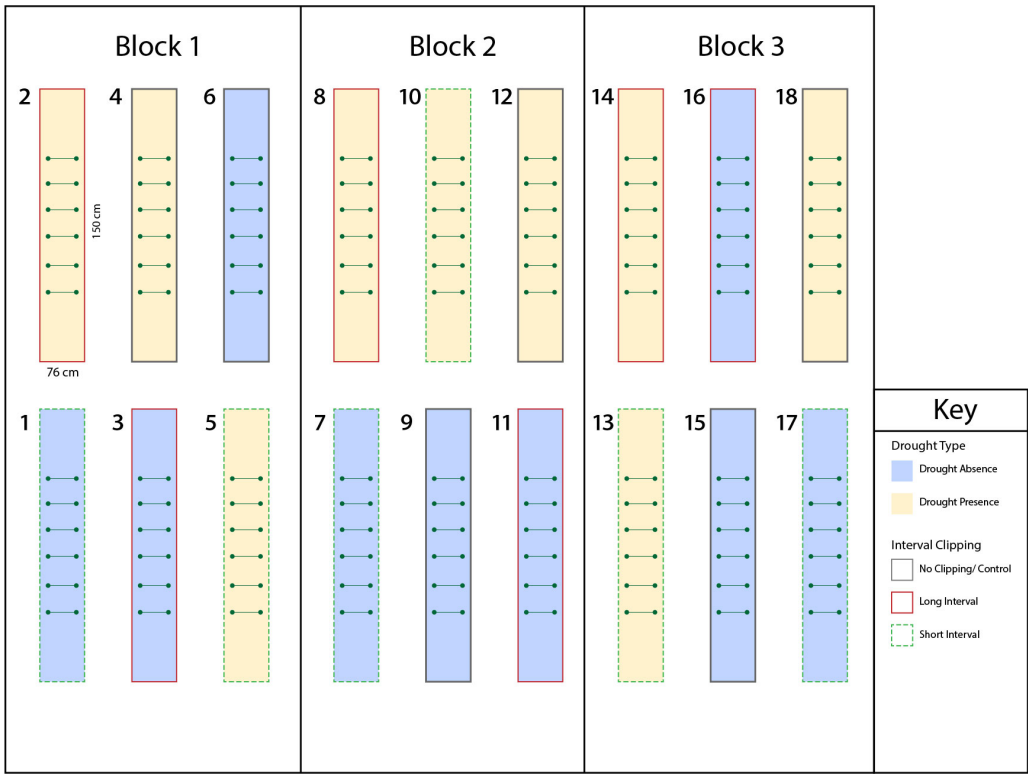

Figure 1: Schematic layout of the greenhouse design. Blue beds indicate drought absence, and yellow beds indicated drought presence. The gray border indicates the control, the red

border indicates the long clipping (late applied), and the green boarder indicates the short clipping (early applied).

2.2 Treatments

The drought intensity was determined using soil water content (SWC) and leaf water potential (LWP). The SWC was taken daily using the HydroSense II Soil Moisture Sensor. The LWP was monitored once the SWC reached 5% using a pressure chamber. The non-droughted beds were watered once the SWC dropped below 10%, while the droughted beds were only watered once the SWC dropped below 3% and the pre-dawn LWP reached -1.7MPa~ -2.2 MPa. This range of negative pressure indicates drought stress on Johnsongrass, as it leads to a 50% loss in rate of photosynthetic assimilation (Nunez, 1983). The beds were watered to saturation (42 L) on watering days.

There were three clipping intervals: short, long, and a control no clipping. The clipped beds were cut down to 7.62 cm (3 inches) aboveground, which is the standard clipping height for most larger mowers in this study region. All clipped materials were dried at 60ºC and immediately weighed for biomass measurements and included in the final biomass readings.

2.3 Sample Testing Procedures

The belowground biomass was collected at the final harvest. Three leaf samples were randomly selected from each bed to analyze P and K contents through the Soil, Water, and Forage Analytical Lab at Oklahoma State University.

A subsample of live roots was collected and washed for determination of AM fungal abundance intra-radically. The roots were first bleached with 10% KOH and stained blue for visibility using trypan blue in lacto-glycerol (Phillips & Hayman, 1970). Mycorrhizae were counted under a digital microscope (Hirox KH 7700, Hirox, Japan), using the magnified gridline intersect presence-absence method (McGonigle et al., 1990) to determine percent colonization. Extra-radical AM fungi abundance (hyphae and spores) was measured using the surrounding rhizosphere soil, which was collected as a composite sample for each bed. We determined the relative abundance extra-radically using phospholipid fatty acid (PLFA) and neutral lipid fatty acid (NLFA) analyses. Since PLFAs are major components of cell walls strongly related to biovolume, they are often used in determining fungal biomass (Tunlid & White, 2021). NLFAs were used in assessing the AM fungal spore biomass, as NLFAs act as a major storage product and energy reserve for many fungi (Larsen & Bødker, 2001). The lipids were extracted and separated for analysis.

2.4 Statistical Analysis

We employed a combination of generalized least squares and mixed models to measure the extent of variation in drought, clipping, and their interactions. To determine random variables and potential variations in light availability, we utilized a block design approach. Additionally, the bed factor was treated as a random variable. The statistical analysis described above was performed using the 'nlme' package (Pinheiro et al., 2022) within the R environment Field.

3. Results

3.1 Biomass

There were no statistically significant differences in biomass observed between the treatments with no clipping and late-season management. This lack of variation was evident in both absence of drought conditions ($p = 0.36$, total biomass, Fig. 2A; $p = 0.68$, aboveground biomass, Fig. 2B; $p = 0.26$, belowground biomass, Fig. 2D) and the presence of drought conditions ($p = 0.99$, total biomass, Fig. 2A; $p = 0.99$, aboveground biomass, Fig. 2B; $p = 0.99$, belowground biomass, Fig. 2D).

Similarly, there were no significant differences observed between the no clipping and early-season management treatments in the absence of drought conditions ($p = 0.24$, total biomass, Fig. 2A; $p = 0.71$, aboveground biomass, Fig. 2B; $p = 0.13$, belowground biomass, Fig. 2D) and in the presence of drought conditions ($p = 1.0$, total biomass, Fig. 2A; $p = 0.99$, aboveground biomass, Fig. 2B; $p = 0.99$, belowground biomass, Fig. 2D). Additionally, there were no significant differences observed between the two management strategies of early-season and late-season interval clippings for drought absence ($p = 0.99$, total biomass, Fig. 2A; $p = 0.99$, aboveground biomass, Fig. 2B; $p = 0.99$, belowground biomass, Fig. 2D) or drought presence ($p = 0.99$, total biomass, Fig. 2A; $p = 0.92$, aboveground biomass, Fig. 2B; $p = 0.99$, belowground biomass, Fig. 2D). However, there was a significant decrease in aboveground biomass at harvest under drought between no clipping and early-season interval ($p = 0.03$, Fig. 2C) as well as the late season interval ($p = 0.02$, Fig. 2C). There was no significant difference between the two interval clipping treatments ($p = 0.99$, Fig. 2C). This reduction was not observed under drought presence between the no clipping and early-season strategy ($p = 0.70$, Fig. 2C), between the no clipping and late-clipping treatment ($p = 0.57$, Fig. 2C), or between the interval-based treatments ($p = 0.99$, Fig. 2C).

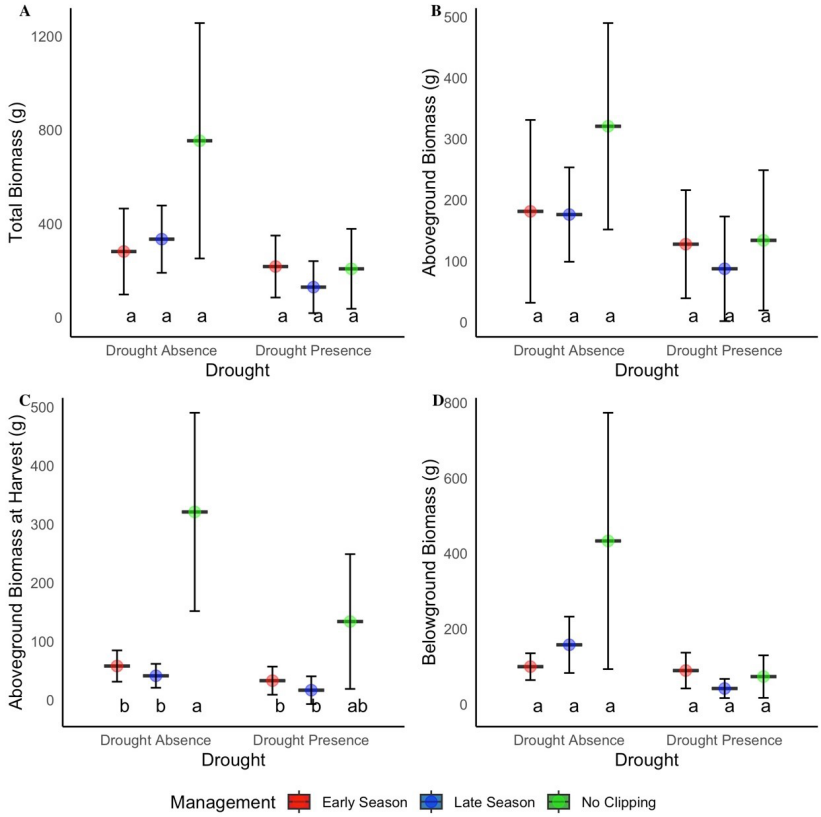

Figure 2: The total biomass (A), total aboveground biomass (B), aboveground biomass at harvest (C), and belowground biomass (D). The total biomass consisted of both above- and belowground biomass. The box plot components include the mean and whiskers, one standard deviation above and below the mean of the data. Significance was determined by $p<0.05$.

3.2 Extraradical AMF, intraradical AMF, and leaf phosphorous content

No significant differences were observed in NLFA extraradical AMF (Fig. 3A), PLFA extraradical AMF (Fig. 3B), or intraradical AMF (Fig. 3C). However, in the absence of drought conditions, a significant increase in leaf phosphorous content was detected for late-season clipping compared to no clipping ($p < 0.01$, Fig. 5D). Additionally, there was a marginal increase, though not statistically significant, in leaf phosphorous content for early-season clipping compared to no clipping in the absence of drought ($p = 0.09$, Fig. 5D).

However, under droughted conditions, there were no significant differences in leaf phosphorous content between no clipping and late-season clipping ($p = 0.90$, Fig. 5D) or early-season clipping ($p = 0.30$, Fig. 5D). Similarly, there were no significant differences between early-season clippings and late-season clippings in terms of leaf phosphorous

content, both in drought absence (p = 0.12, Fig. 5D) and drought presence (p = 0.84, Fig. 5D).

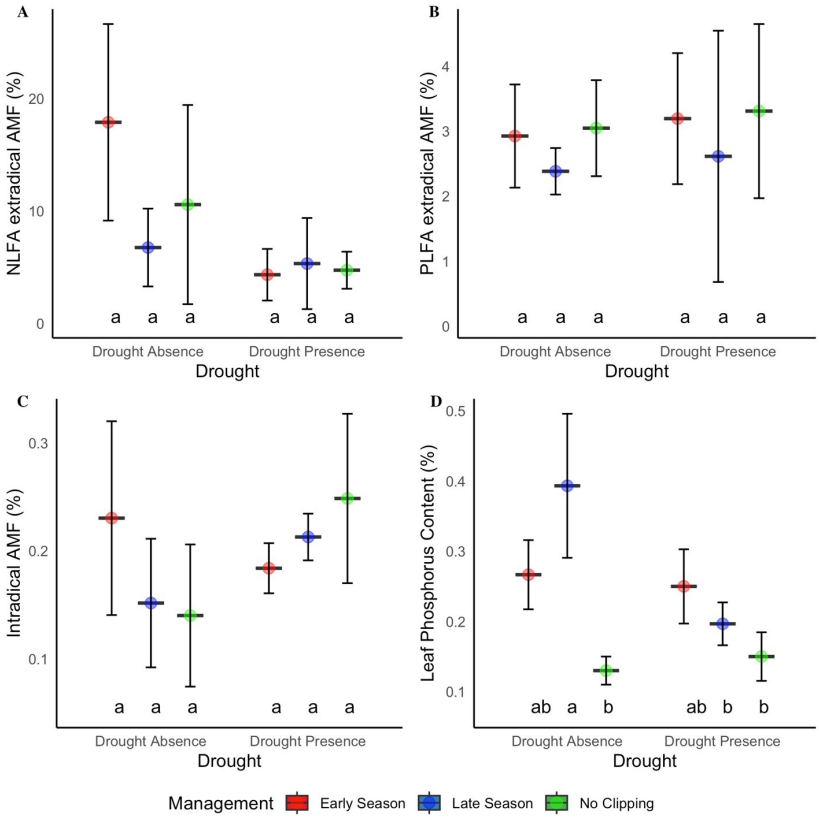

Figure 3: NLFA extraradical AM fungi (A), PLFA extraradical AM fungi (B), intraradical AM fungi within roots (C), and leaf phosphorous (D). The figure components are the same as those defined in Fig. 2.

4. Discussion and Conclusions

4.1 Growth of invasive grass was not inhibited by clipping treatments or their timing.

Based on the findings of this study, it can be deduced that the efficiency of PRM is limited, particularly when drought conditions are present. While a significant decrease in aboveground biomass at harvest was observed during drought absence, we did not observe comparable patterns in above-, below-, or total biomass (Fig. 2). Furthermore, we did not detect any variance between late- and early-season management strategies over all the biomass measures (Fig. 2). The findings of this study contradict previous research, which has indicated that altering the timing and intensity of clipping during various stages of the

growing season can effectively reduce biomass of invasive grasses (Jacobs and Sheley, 1999; Tang et al., 2010).

In future studies, it may be advantageous to explore the potential benefits of increasing the interval between clipping treatments as well as increasing the total number of clippings performed. This approach could help enhance the effectiveness of the PRM performed. Prior research has demonstrated that augmenting the frequency of clippings to four or more treatments can potentially enhance the efficiency of PRM (Milbrath et al., 2016). Combining increased frequency with longer intervals between treatments may prove to be a more effective management strategy compared to our current study design. Additionally, the limited sample size used in our study may have influenced the results. Increasing the sample size would be an important consideration for future studies aiming to comprehensively understand the impacts of PRM and species management under changing climate conditions.

4.2 AM fungi did not play a role in the decreased efficiency of clipping treatments.

Plant-associated microbes play a crucial role in enhancing nutrient acquisition and improving tolerance to various stresses, including drought or defoliation (PRM) (Smith et al., 2011; Pieterse et al., 2014). Mycorrhizae can enhance the tolerance of grassland plants by influencing the availability of phosphorus (P) and nitrogen (N) and modifying biomass allocation patterns. This promotes resilience after defoliation or facilitates compensatory regrowth (Coughenour et al., 1985; Kula et al., 2005; McNaughton et al., 1983). Our study did not find significant differences in intraradical or extraradical AM fungi associations (Fig. 3A-C). These findings are not consistent with previous studies, which found demonstrated that AM fungi possess the capacity to withstand a reduction in carbohydrate input from the host plant, enabling them to sustain or potentially increase their growth and abundance (Barto & Rillig, 2010; Eom et al., 2001; Su & Guo, 2007). For example, subsequent to the clipping of a solitary host plant species, there were disparities observed in the relative abundance of intraradical structures among various AM fungal species (Klironomos et al., 2004). The absence of significant findings might imply that S. *halpense* does not heavily depend on AM fungi for growth or nutrient update. This conclusion is supported by the fact that neither drought conditions nor clipping treatments had any discernible impact on the associations between intraradical or extraradical AM fungi.

Nevertheless, it remains important to study the factors contributing to the success of Johnsongrass and other invasive C4 grasses to develop effective strategies against them. Future studies can focus on identifying the most effective treatments or combinations thereof to combat these invasive grasses plaguing our grasslands.

5. Summary

Johnsongrass is a highly invasive C4 grass plaguing grasslands all over the U.S.. We conducted a study focusing on how Johnsongrass responds to drought and physical removal management, specifically focusing on how the interval of the applied mechanical treatment impacted its efficiency. Overall, Johnsongrass showed no significant response in biomass or mycorrhizal associations under drought or varying interval clipping treatments, leaving us only to continue to hypothesize how we can manage it more effectively.

6. Appendices

6a. Acknowledgements

I would like to thank Dr. and Mrs. Niblack as well as Oklahoma EPSCoR for their financial support. I would also like to thank my mentors, Bo Zhang, Lu Zhai, and Ally Valdez, as well as the Departments of Integrative Biology and Natural Recourse Ecology Management for their support on this project.

6b. Papers Published

Co-authorship on Papers:

- Valdez, **R. Richardson**, E.B. Duell, R. Will, G. Wilson, B. Zhang, L. Zhai. Drought Decreases Efficacy of Physical Removal Management in Limiting Growth of Invasive Plant Species. (To be submitted).
- Valdez, **R. Richardson**, R. Will, G. Wilson, B. Zhang, L. Zhai. The Efficacy of Physical Removal Management in Controlling an Invasive Plant Growth during Early-season and Late-season Interval Clippings. (To be submitted).

Poster Symposiums:

- Apr 2023 – **R. Richardson**, A. Valdez, L. Zhai, B. Zhang. Projecting mechanical treatment outcomes on invasive grass to improve control efficiency. 2023 Karen L. Smith Symposium, Stillwater, OK, US. (Poster)
- Apr 2023 – **R. Richardson**, A. Valdez, L. Zhai, B. Zhang. Projecting mechanical treatment outcomes on invasive grass to improve control efficiency. 2023 OSU Undergraduate Research Symposium, Stillwater, OK, US. (Poster)
- Apr 2023 – **R. Richardson**, A. Valdez, L. Zhai, B. Zhang. Projecting mechanical treatment outcomes on invasive grass to improve control efficiency. 2023 Research Day at the Capitol, Oklahoma City, OK, US. (Poster)

Awarded:

- First place in the research-intensive institution category in the 2023 Research Day at the Capitol event, **$500**
- First place in the Karen Smith Symposium, OSU, **$250**

6c. Literature Cited

Bajwa, A.A., Chauhan, B.S., Farooq, M., Shabbir, A., Adkins, S.W., 2016, What do we really know about alien plant invasion? A review of the invasion mechanism of one of the world's worst weeds. *Planta*, 244: 39-57.

Barto, E. K., Rillig, M. C., 2010. Does herbivory really suppress mycorrhiza? A meta-analysis. *Journal of Ecology*, *98*(4): 745-753.

Beaury, E. M., Fusco, E. J., Jackson, M. R., Laginhas, B. B., Morelli, T. L., Allen, J. M., Pasquarella, V. J., & Bradley, B. A., 2020. Incorporating climate change into invasive species management: insights from managers. *Biological invasions*, *22*(2): 233-252.

Bradley, B.A., Blumental, D.M., Early, R., Grosholz, E.D., Lawler, J.J., Miller, L.P., Sorte, C.J., D'Antonio, D.M., Diez, J.M., Dukes, J.S., Ibanez, I., Olden, J.D., 2011, Global change, global trade, and the next wave of plant invasions. *Frontiers in Ecology and the Environment*, 10(1): 20-28.

Bradley, B.A., Blumenthal, D.M., Wilcove, D.S., Ziska, L.H., 2010, Predicting plant invasion in an era of global change. *Trends Ecol Evol*., 35(5): 310-8.

Coughenour, M., McNaughton, S., & Wallace, L., 1985, Responses of an African graminoid (Themeda triandra Forsk.) to frequent defoliation, nitrogen, and water: a limit of adaptation to herbivory. *Oecologia*, 105-110.

DiTomaso, J. M., Masters, R. A., & Peterson, V. F., 2010. Rangeland invasive plant management. *Rangelands*, *32*(1): 43-47.

Eiswerth, M.E., Johnson, W.S., 2002, Managing nonindigenous invasive species: insights from dynamic analysis. *Environmental and Resource Economics* 23**:** 319–342.

Eom, A.-H., Wilson, G. W., Hartnett, D. C., 2001. Effects of ungulate grazers on arbuscular mycorrhizal symbiosis and fungal community structure in tallgrass prairie. *Mycologia*, *93*(2): 233-242.

Flanders, A.A., Kuvlesky, W.P., Ruthven, D.C., Zaiglin, R.E., Bingham, R.L., Fulbright, T.E., Hernandez, F., Brennan, L.A., 2006, Effects of invasive exotic grasses on South Texas rangeland breeding birds. *The Auk,* 123(1): 171-182.

Gao, Y., Tang, L., Wang, J., Wang, C., Liang, Z., Li, B., Chen, J., Zhao, B., 2009, Clipping at early florescence is more efficient for controlling the invasive plant *Spartina alterniflora*. *Ecological Research*, 24: 1033-1041.

Hartnett, D. C., & Wilson, G. W., 2002, The role of mycorrhizas in plant community structure and dynamics: lessons from grasslands. *Plant and Soil*, *244*, 319-331.

Jacobs, J. S., & Sheley, R. L., 1999. Grass defoliation intensity, frequency, and season effects on spotted knapweed invasion. *Rangeland Ecology & Management/Journal of Range Management Archives*, *52*(6): 626-632.

Klironomos, J. N., McCune, J., Moutoglis, P., 2004. Species of arbuscular mycorrhizal fungi affect mycorrhizal responses to simulated herbivory. *Applied Soil Ecology*, *26*(2): 133-141.

Kula, A., Hartnett, D., & Wilson, G., 2005, Mycorrhizal symbiosis and insect herbivory in tallgrass prairie microcosms. *Ecology letters*, *81*, 61-69.

Larsen, J., & Bødker, L., 2001, Interactions between pea root-inhabiting fungi examined using signature fatty acids. *New Phytologist*, *149*(3), 487-493.

McGonigle, T. P., Miller, M. H., Evans, D., Fairchild, G., & Swan, J. A., 1990, A new method which gives an objective measure of colonization of roots by vesicular—arbuscular mycorrhizal fungi. *New Phytologist*, *115*(3), 495-501.

McNaughton, S., Wallace, L. L., & Coughenour, M. B., 1983, Plant adaptation in an ecosystem context: effects of defoliation, nitrogen, and water on growth of an African C4 sedge. *Ecology*, *64*(2), 307-318.

Milbrath, L.R., DiTommaso, A., Biazzo, J., Morris, S.H., 2016. Tolerance of swallowworts (Vincetoxicum spp.) to multiple years of artificial defoliation and clipping. *Invasive plant science and management*, 9(1): 1-11.

Nunez, J. R., 1983. *Diurnal fluctuation of leaf solutes and their role in the osmotic adjustment of a johnsongrass (Sorghum halepense (L.) Pers.) cultivar in response to low-water stress*. Texas A&M University.

Phillips, J. M., & Hayman, D. S., 1970, Improved procedures for clearing roots and staining parasitic and vesicular-arbuscular mycorrhizal fungi for rapid assessment of infection. *Transactions of the British Mycological Society*, *55*(1), 158,IN116-161,IN118.

Pieterse, C.M., Zamioudis, C., Berendsen, R.L., Weller, D.M., Van Wees, S.C., Bakker, P.A., 2014, Induced systemic resistance by beneficial microbes. *Annu Rev Phytopathol,* 52:347-75.

Pinheiro, J., Bates, D., DebRoy, S., & Sarkar, D., 2022, R Core Team. 2021. nlme: linear and nonlinear mixed effects models. R package version 3.1-153. *Availble at: https://cran. r-project. org/web/packages/nlme/index. html (Accessed March 31, 2022)*.

Rashidi, S., Yousefi, A.R., Pouryousef, M., Goicoechea, N., 2021, Mycorrhizal impact on competitive relationships and yield parameters in Phaseolus vulgaris L. – weed mixtures. *Mycorrhiza*, 31(5):599-612.

Schwinning, S., Meckel, H., Reichmann, L. G., Polley, H. W., & Fay, P. A., 2017, Accelerated development in Johnsongrass seedlings (Sorghum halepense) suppresses the growth of native grasses through size-asymmetric competition. *PLoS ONE*, *12*(5), e0176042.

Sezen, U. U., Barney, J. N., Atwater, D. Z., Pederson, G. A., Pederson, J. F., Chandler, J. M., Cox, T. S., Cox, S., Dotray, P., Kopec, D., Smith, S. E., Schroeder, J., Wright, S. D., Jiao, Y., Kong, W., Goff, V., Auckland, S., Rainville, L. K., Pierce, G. J., . . . Paterson, A. H., 2016, Multi-Phase US Spread and Habitat Switching of a Post-Columbian Invasive, Sorghum halepense. *PLoS ONE*, *11*(10)

Smith, S.E., Jakobsen, I., Gronlund, M., Smith, F.A., 2011, Roles of arbuscular mycorrhizas in plant phosphorous nutrition: interactions between pathways of phosphorous uptake in arbuscular mycorrhizal roots have important implications for understanding and manipulating plant phosphorous acquisition. *Plant Physiology*, 156: 1050-1057.

Su, Y.-Y., Guo, L.-D., 2007. Arbuscular mycorrhizal fungi in non-grazed, restored and over-grazed grassland in the Inner Mongolia steppe. *Mycorrhiza*, *17*: 689-693.

Tang, L., Gao, Y., Wang, J., Wang, C., Li, B., Chen, J., Zhao, B., 2009, Designing an effective clipping regime for controlling the invasive plant *Spartina alterniflora* in an estuarine salt marsh. *Ecological Engineering,* 35(5): 874-881.

Tang, L., Gao, Y., Wang, C., Wang, J., Li, B., Chen, J., & Zhao, B., 2010. How tidal regime and treatment timing influence the clipping frequency for controlling invasive Spartina alterniflora: implications for reducing management costs. *Biological invasions*, *12*(3): 593-601.

Tunlid, A., & White, D. C., 2021, Biochemical analysis of biomass, community structure, nutritional status, and metabolic activity of microbial communities in soil. In *Soil biochemistry* (pp. 229-262). CRC Press.

Vetter, V.M., Kreyling, J., Dengler, J., Apostolova, I., Arfin-Khan, M.A., Berauer, B.J., Berwaers, S., De Boeck, H.J., Nijs, I., Schuchardt, M.A., Sopotlieva, D., Gillhausen, P., Wilfahrt, P.A., Zimmermann, M., Jentsch, A., 2020, Invader presence disrupts the stabilizing effect of species richness in plant community recovery after drought. *Glob Change Biol.*, 26(6): 3539-3551.

Weidlich, E. W., Flórido, F. G., Sorrini, T. B., & Brancalion, P. H., 2020. Controlling invasive plant species in ecological restoration: A global review. *Journal of Applied Ecology*, *57*(9): 1806-1817.

Effects of drought and clipping timing on mycorrhizal symbiosis and growth of invasive Johnsongrass

By: Rabeca Richardson
Department of Integrative Biology
Faculty Sponsor: Bo Zhang
Graduate Student Mentor: Allasandra Valdez

BACKGROUND - JOHNSONGRASS

Sorghum halpense, also known as **Johnsongrass** – a drought-resistant C4 grass native to Asia and Northern Africa [5].

- C4 refers to the type of photosynthesis it undergoes.
- It reproduces sexually and asexually.
- Johnsongrass is an urgent invasive species here in Oklahoma and all throughout the United States [5], threatening the stability of many grassland ecosystems and the biodiversity within them.
    - **Johnsongrass** was selected as our model species due to its ability to outcompete native species and thrive in warm conditions [6].

Johnsongrass (Sorghum halpense)

JOHNSONGRASS CONTINUED

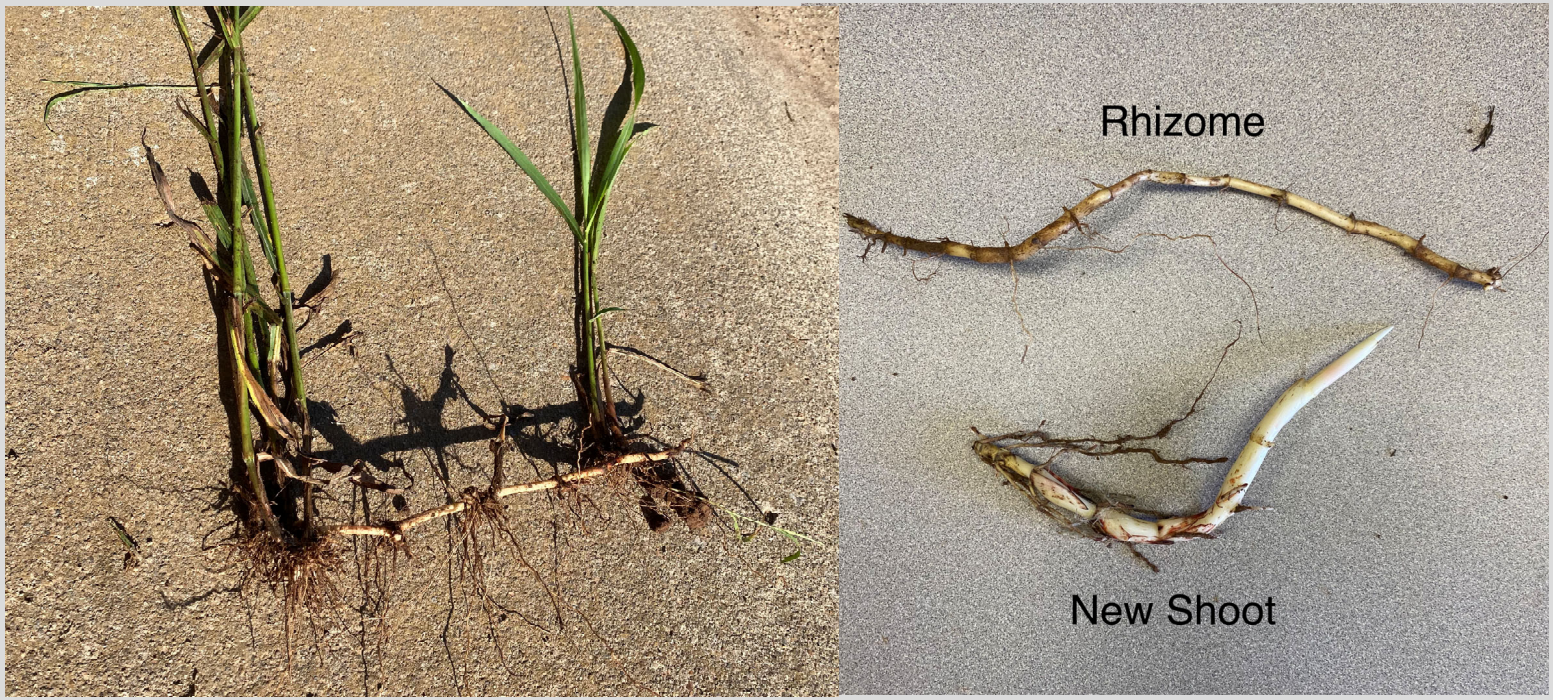

Pictured on the left is a rhizome connecting two Johnsongrass plants. The image to the right shows a rhizome and a rhizome with a new shoot sprouting up from it.

CURRENT JOHNSONGRASS DISTRIBUTION

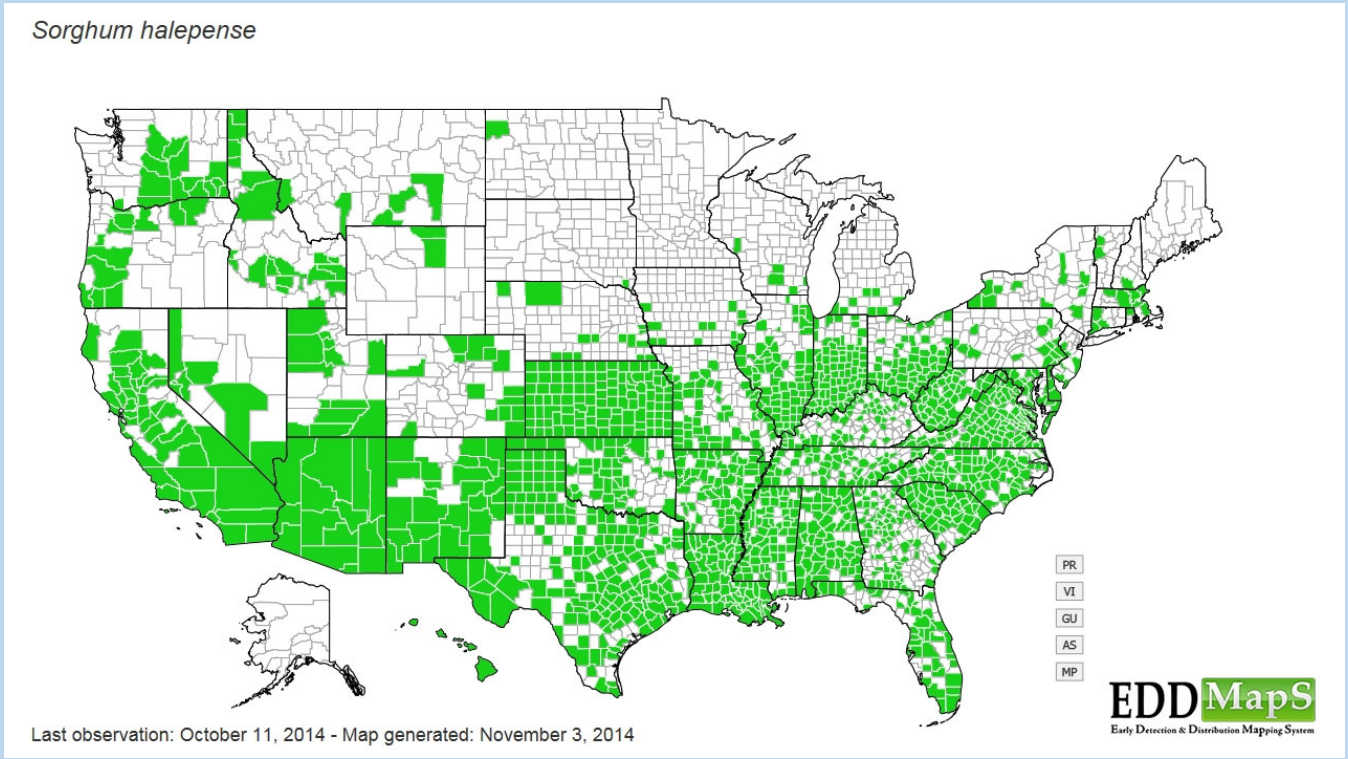

WHY IS THIS IMPORTANT?

Patch of Johnsongrass alongside a road.

- Increased drought due to climate change is projected to intensify the expansion of invasive plant species [2].
- These invasive species pose a great threat to the overall stability of the environment [3].
- Rangelands are being plagued by invasive grasses, especially drought-resistant C4 grasses [4].
- Very little research has focused on how clipping **timing** impacts:
  - The efficiency of PRM
  - Mycorrhizal Colonization
  - As well as if mycorrhizae even play a role as an invasion mechanism
- <u>Our goals:</u>
  - **Identify an optimal clipping treatment timing under drought and non-drought conditions**
  - **Determine whether mycorrhizae play a role in the invasive success of a model species** – Johnsongrass

EXPERIMENT OVERVIEW

- We conducted a greenhouse experiment focusing on the interactive effects of drought and clipping treatment timing on the growth of an invasive C4 grass.

- **Physical Removal Management (PRM),** such as clipping, mowing, and grazing, is one of the most commonly employed invasive control strategies.

    - However, the true effectiveness of this strategy, especially under various stress conditions (e.g., drought), remains uncertain.

Open-air rainout shelter used for the greenhouse experiment

EXPERIMENT OVERVIEW – CONT.

- **Arbuscular Mycorrhizal Fungi (AMF)** live symbiotically with almost 80% of plant species, providing increased nutrient uptake and stress resistance in plants in exchange for essential nutrients (e.g., carbohydrates) [1].
    - Little is known about the roles of the soil microbiome in affecting invasive species and native species relations, let alone if they play a major role as an invasion mechanism.
    - The effect of drought and PRM on this relationship is largely unknown.
- Factors to Consider:
    - Nutrient absorption and allocation
    - **Above and belowground biomass**
    - Carbon assimilation rate, transpiration rate, etc
    - My portion of the experiment focused on the **soil microbiome**

Clipping of the beds.

METHODS – EXPERIMENTAL DESIGN

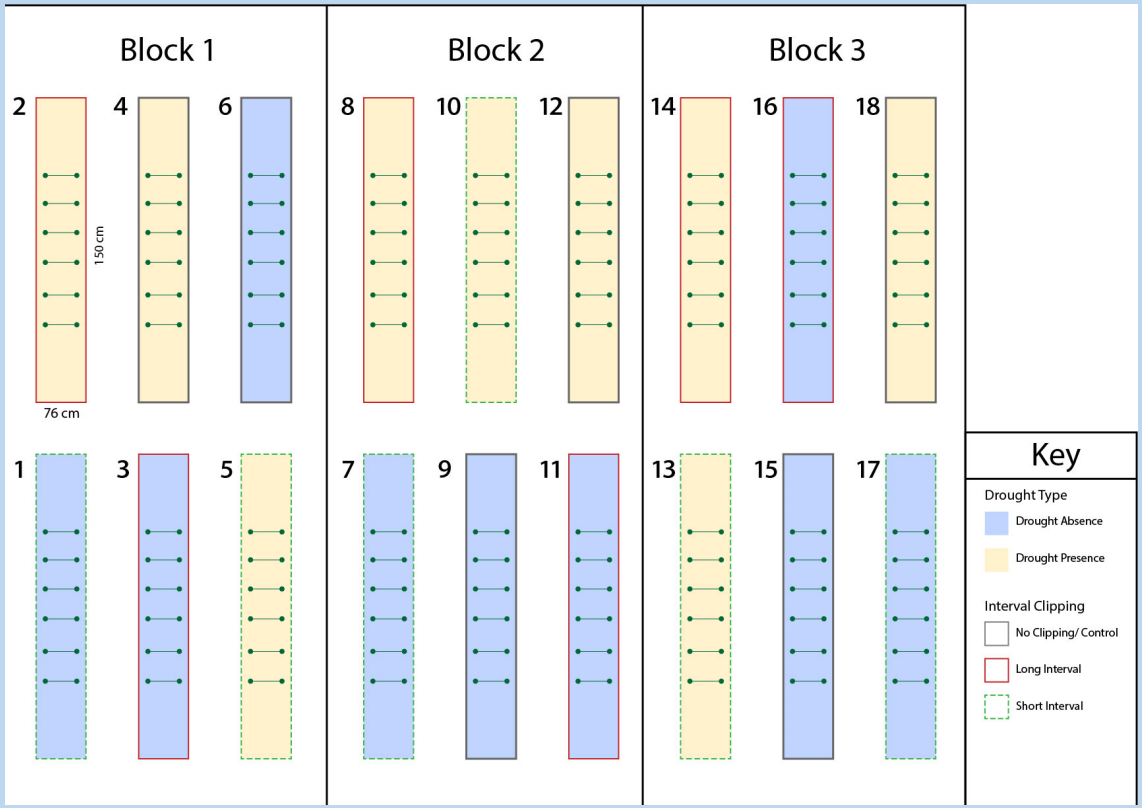

Randomized block design.

- **Factorial-designed Greenhouse experiment**
  - Two levels of drought
    - Presence
    - Absence
  - Three clipping treatments
    - Early-season (clipped every 2 weeks)
    - Late-season (clipped every 4 weeks)
    - No clipping (clipped at 14 weeks final harvest)
  - 6 treatment combinations x 3 repeats = 18 beds total
- The study took place over14 weeks using an open-air-rain-out shelter
- Beds were organized into 3 blocks of 6, one of each treatment combination organized in a random placement within each block

EXPERIMENTAL DESIGN CONT.

- We collected our soil from the Cross Timbers Experimental Range here in Stillwater in order to mimic Oklahoma soil conditions.
- We conducted a **transplant.**
  - Rhizomes were planted in 5 rows across the width of each bed.

Group of undergraduates in our lab (including myself) collecting soil from the field (left). Collection of Johnsongrass rhizomes from the field (middle). The growing beds all set up with the collected soil mixed with sand (right).

METHODS – TREATMENTS

- Drought intensity
  - Determined using the **soil water content (SWC)** and **leaf water potential (LWP).**
    - Nondrought beds were watered once the SWC reached below 10%.
    - Droughted beds were watered once the SWC reached below 3% and the LWP reached -1.7MPa ~ -2.2 Mpa.
- Clipping
  - Each time a clipping treatment was performed, the plants within the beds were cut down to about 7.62 cm (3 in).
  - The clippings were dried at 60C and weighed for biomass measurements.

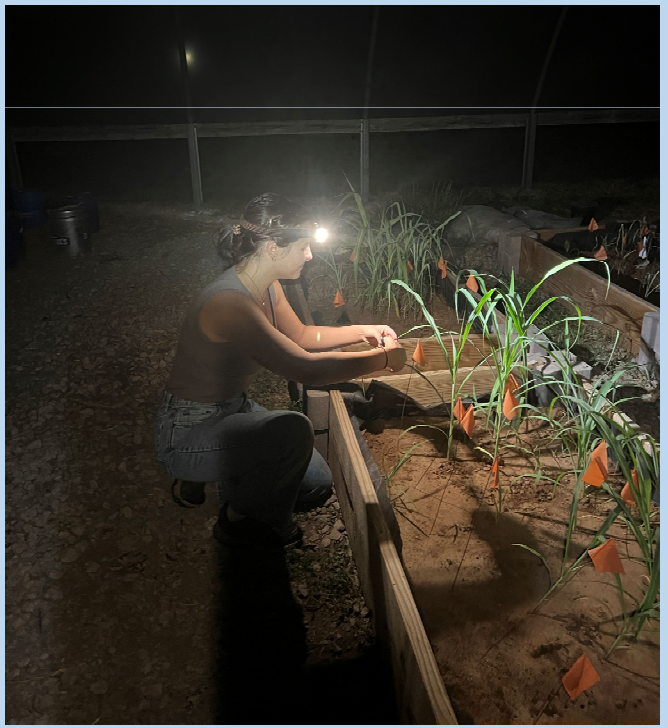

Clipping a leaf sample for pre-dawn LWP measurements.

METHODS – SAMPLE TESTING

- **Biomass** –
  - above- and belowground biomass, including biomass from previous clippings, was collected and dried at 60 degrees C to be weighed for analysis.

- **P and K contents –**
  - three leave samples from each bed were randomly selected for P and K analysis through the Soil, Water, and Forage Analytical Lab at OSU

Aboveground biomass collected at one of the clipping events.

SAMPLE TESTING CONT.

- **Mycorrhizae colonization and abundance –**
  - Intra-radical AM fungi percent colonization - three subsamples of **live roots** were collected, washed, bleached, and stained.
  - Extra-radical AM fungi abundance – using **surrounding rhizosphere soil**, collected compositely for each bed
    - Hyphae – phospholipid fatty acid (PLFA) analysis – measures fungal biomass using the PLFAs in cell walls [7].
    - Spores – neutral lipid fatty acids (NLFA) analysis – NLFAs are strongly associated with fungal spore biomass [8].

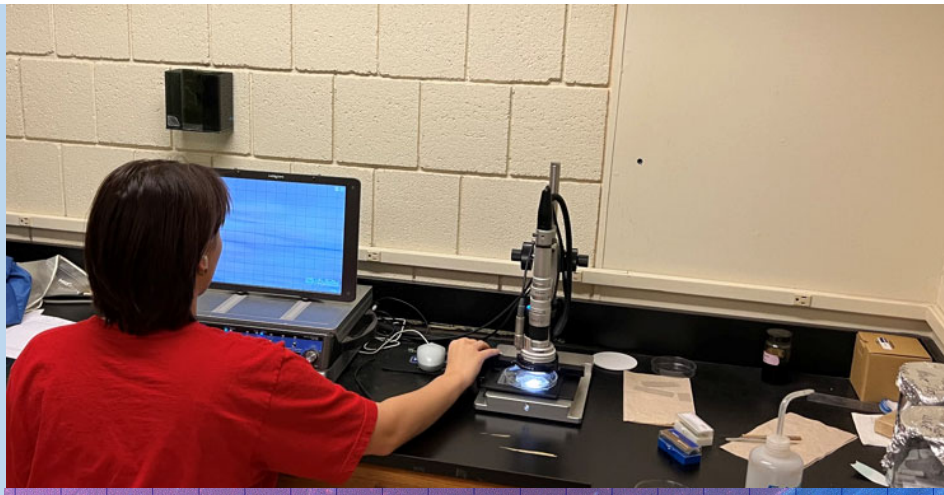

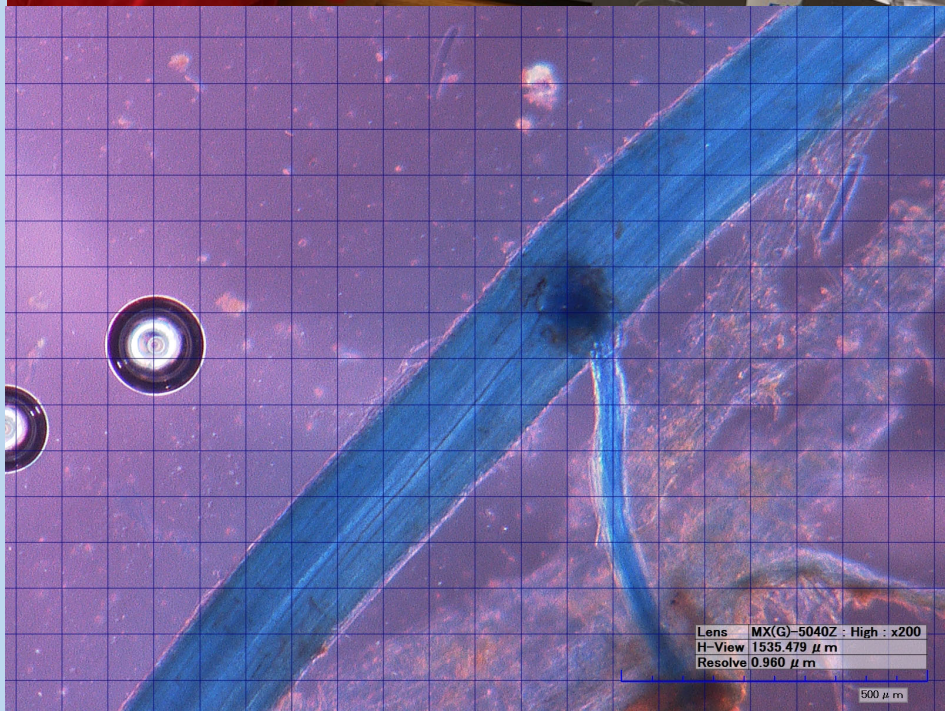

Root subsample magnified x200 (bottom); Microscope setup for presence-absence counting (top).

ANALYSIS AND RESULTS

For our analysis, we employed a combination of generalized least squares and mixed models created using the 'nlme' package in R.

Biomass Results:

- There were no significant differences between the treatments for Total biomass, Aboveground Biomass, and Belowground Biomass ($p>0.05$).

- In drought absence of final harvest aboveground biomass, a significant decrease in biomass was observed for both the early- ($p=0.03$) and late-season ($p=0.02$) clipping treatments.
  - There was no significant difference between the two interval clippings ($p>0.05$).

- There was no significant difference observed between the treatments for final harvest biomass under drought presence ($p>0.05$).

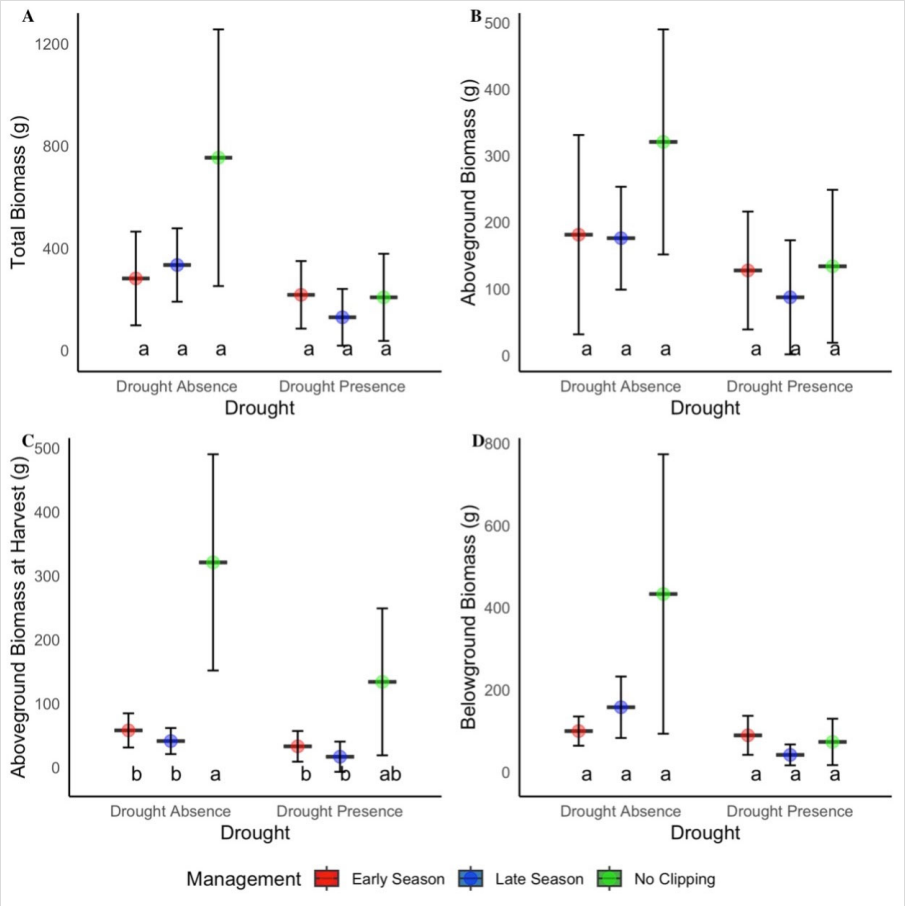

The total biomass (A), total aboveground biomass (B), aboveground biomass at harvest (C), and belowground biomass (D). The total biomass consisted of both above- and belowground biomass. The box plot components include the mean and whiskers, one standard deviation above and below the mean of the data. Significance was determined by $p<0.05$.

ANALYSIS AND RESULTS

Extraradical AMF, Intraradical AMF, and Leaf Phosphorous Content Results:

- There was no significant difference observed for ($p>0.05$). NLFA extraradical, PLFA extraradical, or intraradical AMF colonization

- In drought absence, there was a significant increase in leaf phosphorous for the late-season compared to no clipping ($p<0.01$) and a marginal increase for the early-season compared to no clipping ($p=0.09$).

    - In drought presence, there were no significant differences between the late- and early-season compared to no clipping ($p>0.05$).

    - Additionally, there were no significant differences between early- and late-season leaf phosphorous under drought absence and presence ($p>0.05$).

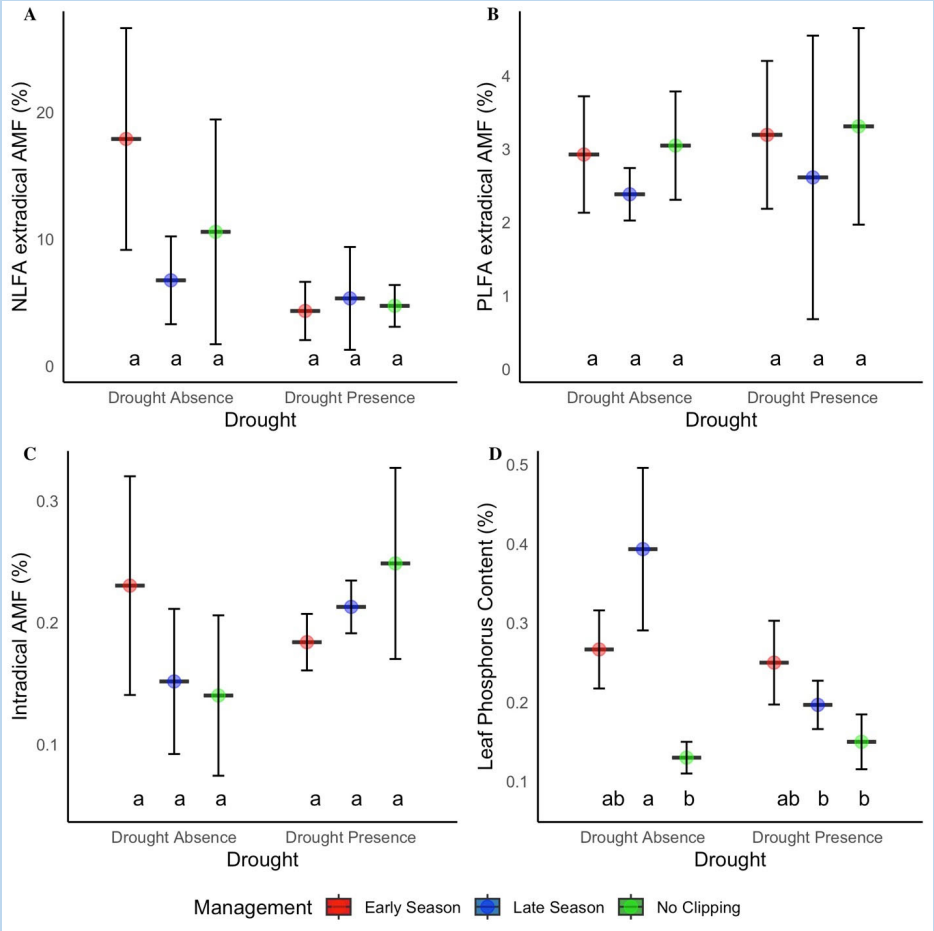

NLFA extraradical AM fungi (A), PLFA extraradical AM fungi (B), intraradical AM fungi within roots (C), and leaf phosphorous (D). The figure components are the same as those defined in the previous figure.

DISCUSSION

- **Growth of invasive grass was not inhibited by clipping treatments or their timing.**
  - The efficiency of physical removal management (PRM) is limited, especially under droughted conditions.
  - The decrease in final harvest biomass for the clipping treatments was not observed in the above-, below, or total biomass measures. Additionally, no variance was detected between the management strategies for any of the treatments.
  - This contradicts previous research showing that altering timing/intensity of clippings can effectively reduce biomass [9][10]
  - <u>Future studies:</u>
    - Increase time between clippings
    - Increase number of clippings
    - Increase sample size

Aboveground growth in the beds.

DISCUSSION

- **AM fungi did not play a role in the decreased efficiency of clipping treatments**
  - While plant-associated microbes play a crucial role in enhancing nutrient acquisition and improving tolerance to various stresses, our study did not find significant differences in intraradical or extraradical AM fungi associations.
  - This is inconsistent with previous research, which found disparities in host AMF colonization subsequent to clipping of those plants [10]
  - The absence of significant findings might imply that S. *halpense* does not heavily depend on AM fungi for growth or nutrient uptake, as there were no discernable differences in intraradical or extraradical AMF.

Nevertheless, it remains important to study the factors contributing to the invasive success of Johnsongrawss and other invasive C4 grasses to develop effective strategies against them.

Future studies can continue to focus on trying to identify the most effective treatments or combinations thereof to combat these invasive grasses plaguing our grasslands.

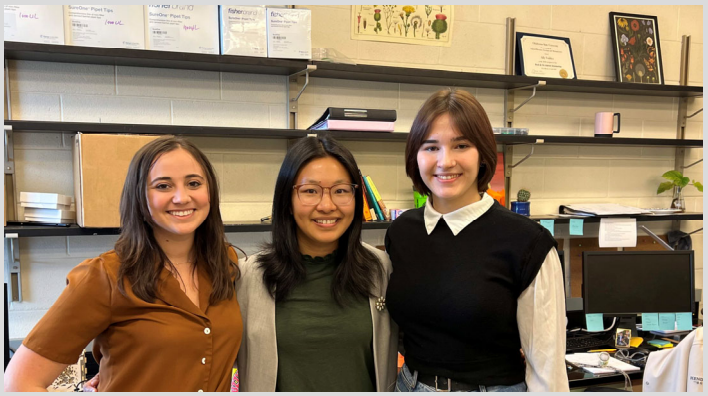

ACKNOWLEDGEMENTS

- Dr. and Mrs. Niblack
- Oklahoma EPSCoR
- Departments of Integrative Biology and Natural Resource Ecology
- Fellow Undergraduates in the lab
- Bo Zhang and Lu Zhai
- Ally Valdez

LITERATURE CITED

[1] Rashidi, S., Yousefi, A.R., Pouryousef, M., Goicoechea, N., 2021, Mycorrhizal impact on competitive relationships and yield parameters in Phaseolus vulgaris L. – weed mixtures. *Mycorrhiza*, 31(5):599-612.

[2] Yang, B., Cui, M., Du, Y., Ren, G., Li, J., Wang, C., Li, G., Dai, Z., Rutherford, S., & Wan, J. S. (2022). Influence of multiple global change drivers on plant invasion: Additive effects are uncommon. *Frontiers in Plant Science*, *13*.

[3] V. M. Vetter *et al. (2020).* Invader presence disrupts the stabilizing effect of species richness in plant community recovery after drought. *Global Change Biol* **26**, 3539-3551.

[4] A.A. Flanders et al., Effects of invasive exotic grasses on south Texas rangeland breeding birds. *Ornithology* **123**, 171-182 (2006).

[5] Sezen, U. U., Barney, J. N., Atwater, D. Z., Pederson, G. A., Pederson, J. F., Chandler, J. M., Cox, T. S., Cox, S., Dotray, P., Kopec, D., Smith, S. E., Schroeder, J., Wright, S. D., Jiao, Y., Kong, W., Goff, V., Auckland, S., Rainville, L. K., Pierce, G. J., . . . Paterson, A. H., 2016, Multi-Phase US Spread and Habitat Switching of a Post-Columbian Invasive, Sorghum halepense. *PLoS ONE*, *11*(10)

[6] Schwinning, S., Meckel, H., Reichmann, L. G., Polley, H. W., & Fay, P. A., 2017, Accelerated development in Johnsongrass seedlings (Sorghum halepense) suppresses the growth of native grasses through size-asymmetric competition. *PLoS ONE*, *12*(5), e0176042.

[7] Tunlid, A., & White, D. C., 2021, Biochemical analysis of biomass, community structure, nutritional status, and metabolic activity of microbial communities in soil. In *Soil biochemistry* (pp. 229-262). CRC Press.

[8] Larsen, J., & Bødker, L., 2001, Interactions between pea root-inhabiting fungi examined using signature fatty acids. *New Phytologist*, *149*(3), 487-493.

[9]Jacobs, J. S., & Sheley, R. L., 1999. Grass defoliation intensity, frequency, and season effects on spotted knapweed invasion. *Rangeland Ecology & Management/Journal of Range Management Archives*, *52*(6): 626-632.

[10] Tang, L., Gao, Y., Wang, C., Wang, J., Li, B., Chen, J., & Zhao, B., 2010. How tidal regime and treatment timing influence the clipping frequency for controlling invasive Spartina alterniflora: implications for reducing management costs. *Biological invasions*, *12*(3): 593-601.

[11] Klironomos, J. N., McCune, J., Moutoglis, P., 2004. Species of arbuscular mycorrhizal fungi affect mycorrhizal responses to simulated herbivory. *Applied Soil Ecology*, *26*(2): 133-141.

Effects of Organoantimony Compounds on the Fungal Pathogen *Cryptococcus neoformans*

Kaitlyn Cotton

Microbiology & Molecular Genetics
Faculty Sponsor: Dr. Karen Wozniak
Graduate Student Mentor: Brittney Conn

ABSTRACT

Cryptococcus neoformans is an opportunistic pathogen that causes pulmonary cryptococcosis and cryptococcal meningitis in immune-compromised individuals. Overall, fungal infections are responsible for approximately 1.5 million deaths each year. In contrast to antibacterial drugs, the quantity of antifungal drugs capable of combating fungal infections remains low. With the high toxicity and increased resistance to antifungals in recent years, the importance of finding new options for antifungal therapy is even more crucial. We hypothesized that a series of organoantimony compounds that previously exhibited antifungal activity could serve as effective antifungal drugs. Preliminary research identified several compounds that were antifungal against *C. neoformans* and non-toxic to mammalian cells. RNA sequencing identified several *C. neoformans* genes and pathways (including those associated with membrane transport and formation, ribosome biogenesis, and gene expression) that were up- or down-regulated following treatment with three of the compounds. EM studies show altered morphology and membrane/cell wall damage following the treatment of *C. neoformans* with five of the compounds. *Galleria mellonella* infection models with *C. neoformans* exhibited the effectiveness of compound $SbPh_4(ECO)$ at 120 ug/ml *in vivo*. These studies show that organoantimony compounds are promising antifungal therapies, and more studies are currently underway to narrow down their mechanism of anti-fungal activity.

1. Introduction:

Fungal infections are a large concern in the world today, with upwards of 1 billion cases and over 1.5 million deaths annually (Bongomin et al., 2017). Of those fungal infections, 220,00 cases and 181,000 deaths can be attributed to the fungal pathogen *Cryptococcus neoformans* (Rajasingham et al., 2017). *Cryptococcus neoformans* is an opportunistic fungal pathogen found around the world in soil and bird droppings, which can cause infections through the inhalation of spores (Levitz, 1991). Individuals who are immune-compromised, such as patients with HIV-AIDS, transplants, or chemotherapy, can develop pulmonary cryptococcosis, or an acute or chronic infection in the lungs, and cryptococcal meningitis, an infection of the brain and spinal column (Sabiiti and May, 2012, Williamson, 2017).

In contrast to antibiotics, the quantity of available antifungal drugs remains low. There are currently only four main classes of antifungal drugs approved for use in the US: polyenes, azoles, echinocandins, and pyrimidines (Houšť et al., 2020, Robbins et al., 2016). Such a limited drug arsenal exists largely due to the high cytotoxicity of antifungals. Fungal pathogens are eukaryotic, making them much more like their human hosts than bacterial pathogens. As a result, the number of molecular targets for antifungals that do not also induce high host cytotoxicity is greatly reduced compared to those of bacteria (Robbins et al., 2016).

Rising resistance to antifungals in recent years coupled with the toxicity of available antifungal drugs makes it crucial to develop new antifungal therapies (Perlin et al., 2017). A recent study by Gerasimchuk et al. developed novel organoantimony(V) cyanoximates (SbPh4(ACO), SbPh4(MCO), SbPh4(ECO), SbMe3(TCO)2, SbMe3(ECO)2, and SbMe3(MCO)2) that exhibited activity against several bacterial species and fungal pathogens C. neoformans and Candida albicans, while remaining non-toxic to mammalian cells (Gerasimchuk et al., 2022). In this article, we further examine the activity of those compounds on C. neoformans and examine their potential as future antifungal drugs.

2. Materials and Methods:

Strains and Media*:* *C. neoformans* strain H99 was grown in a Yeast Peptone Dextrose (YPD) broth at 30ºC in a shaking incubator for 18hrs. The cells were then washed with sterile phosphate-buffered saline (PBS) three times. The concentration of cells was counted using a hemacytometer, with trypan blue being used to exclude dead cells. The concentrations for the assay inoculums were determined using the hemacytometer counts.

Compounds: Novel organoantimony compounds $SbPh_4(ACO)$, $SbPh_4(MCO)$, $SbPh_4(ECO)$, $SbMe_3(TCO)_2$, $SbMe_3(ECO)_2$, and $SbMe_3(MCO)_2$ produced by Dr. Nikolay Gerasimchuck (Missouri State University, Springfield, MO) were tested to determine their fungistatic and fungicidal properties (Gerasimchuk et al., 2022).

RNA Extraction and Sequencing: *C. neoformans* at concentrations of $10x10^6$ cells/ml were incubated with different organoantimony compounds at the minimum inhibitory concentrations (MICs) for 24 hours. RNA was then extracted and purified according to the Qiagen AllPrep Fungal DNA/RNA/Protein Quick-Start Protocol. RNA purity was verified via 260/280 optical density measurements on a plate reader (BioTek). RNA was sent to Novogene (Novogene Corp, Sacramento, CA) for sequencing. Genes with significantly different expression values were grouped into signaling pathways using GO Enrichment Analysis (Gene Ontology Consortium).

Scanning Electron Microscopy: *C. neoformans* at a concentration of $10x10^6$ cells/ml were incubated with different organoantimony compounds at the MIC concentrations for 4, 8, and 12h. Following incubation, the samples were washed three times with a 0.2M

cacodylate buffered wash and fixed for a minimum of 2h in a 0.1M cacodylate and 2% glutaraldehyde fixative. The sample was washed again, rinsed three times with the buffered wash, and fixed in osmium tetroxide (OsO_4) for 1h. Following another set of three buffered wash rinses, the samples were dehydrated with a series of ethanol washes. Two hexamethyldisilane (HMDS) washes were performed before the samples were mounted on stubs and given an Au-Pd coat. Samples were then imaged at 20,000X magnification using an FEI Quanta 600 field emission gun ESEM with Bruker EDS and HKL EBSD.

Galleria mellonella* Infection Model*: *G. mellonella* larvae were separated into groups of ten and injected with H99 at a concentration of $1x10^4$ cells/ml. Control groups were also created with 10 µl injections of heat-killed H99 at the same concentration or PBS. Following a 2-hour incubation period, the larvae were injected with 10 µl of the selected compound at the desired concentration (treatment) or 10 µl PBS (control). The larvae were incubated at 37ºC and survival was measured for 10 days.

Data Analysis: GraphPad Prism version 5.00 for Windows was used to create graphs and conduct statistical analyses. One-way ANOVA with Tukey's multiple comparison test (to compare pairs of columns) was used to compare data between 3 groups, and an unpaired t-test was used to compare data between 2 groups. The log-rank test was used to compare the survival of groups in the infection model.

3. Results:

Treatment With Compounds Affects Gene Expression of *C. neoformans*. In an effort to reveal the underlying mechanism of action behind the experimental compounds' antifungal activity, RNA sequencing was performed to determine the difference in the gene expression between treated and untreated *C. neoformans* cells. *C. neoformans* cells were incubated in RPMI-MOPS alone, or along with each compound diluted to its respective MIC (at $10x10^6$ *C. neoformans* cells/ml) using RPMI-MOPS for 24h at 37° C in a humidified incubator. The RNA was then extracted and purified from the cryptococcal cells using the AllPrep Fungal DNA/RNA/Protein kit (Qiagen). Following confirmation of RNA purity via 260/280 optical density measurements, the RNA was sent to Novogene (Novogene Corp, Sacramento, CA) for sequencing and analysis. Using GO Enrichment Analysis, Novogene identified multiple signaling pathways that were significantly ($p < 0.05$) up- or down-regulated in the treated *C. neoformans* cells (Figure 1). Treatment with $SbPh_4$(ECO) resulted in the significant ($p < 0.05$) up-regulation of pathways associated with membrane transport and membrane formation, and the down-regulation of pathways associated with ribosome biogenesis and rRNA processing. Treatment with $SbPh_4$(MCO) resulted in the up-regulation of pathways associated with peptidase activity, organelle and ribosome formation, and DNA replication, and the down-regulation of an oxidoreductase pathway. Finally, treatment with $SbPh_4$(ACO) resulted in the down-regulation of pathways associated with gene expression, RNA processing, and ribosome biogenesis.

Treatment With Compounds Results in Morphological Changes in *C. neoformans* Cells. In an attempt to further narrow down the antifungal mechanism of action, scanning electron microscopy (SEM) was performed on treated and untreated *C. neoformans* cells. *C. neoformans* cells were incubated in RPMI-MOPS alone, or along with $SbPh_4$(ACO) or $SbPh_4$(ECO) diluted to their respective MIC (at $10x10^6$ *C. neoformans* cells/ml) using RPMI-

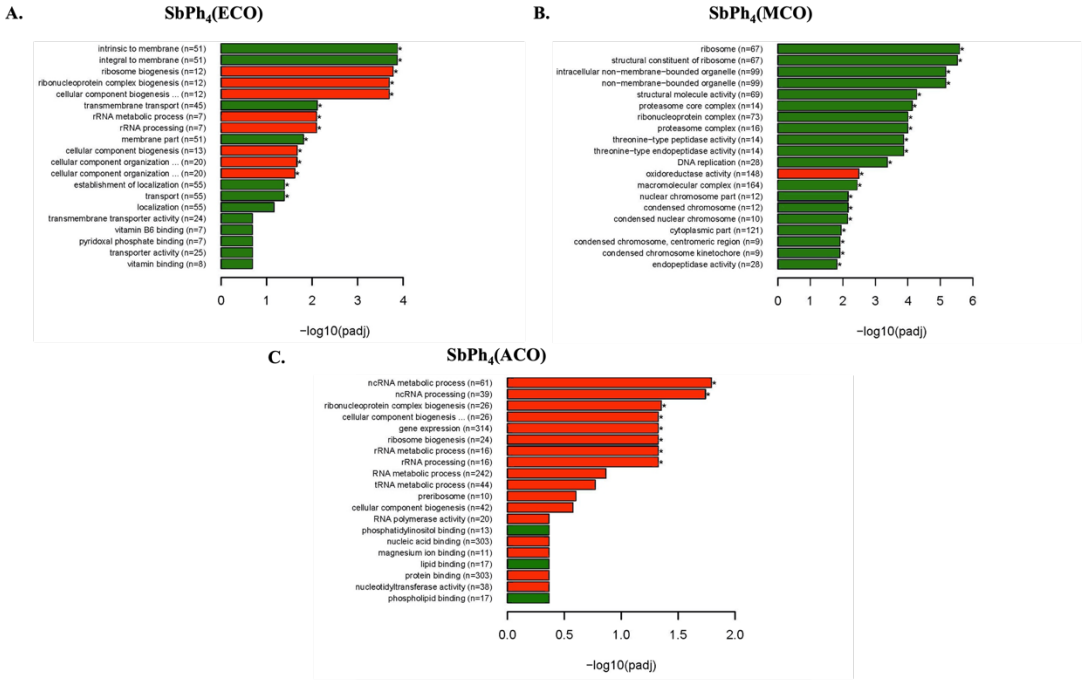

Figure 1. Pathways up- and down-regulated in *C. neoformans* treated with experimental compounds. RNA sequencing of untreated *C. neoformans* was compared with *C. neoformans* treated with compounds (A) $SbPh_4$(ECO), (B) $SbPh_4$(MCO), and (C) $SbPh_4$(ACO). Pathways that were mostly up-regulated are shown in green, while pathways that were mostly down-regulated are shown in red. (A) Treatment with $SbPh_4$(ECO) resulted in the up-regulation of pathways associated with membrane transport and membrane formation, and the down-regulation of pathways associated with ribosome biogenesis and rRNA processing. (B) Treatment with $SbPh_4$(MCO) resulted in the up-regulation of pathways associated with peptidase activity, organelle and ribosome formation, and DNA replication, and the down-regulation of an oxidoreductase pathway. (C) Treatment with $SbPh_4$(ACO) resulted in the down-regulation of pathways associated with gene expression, RNA processing, and ribosome biogenesis. $SbPh_4$(MCO) and $SbPh_4$(ACO) experiments were conducted three separate times and sent for sequencing together. The data shown are compiled data from the three independent experiments. The $SbPh_4$(ECO) experiment was conducted once and the data is representative of that single experiment. * indicates a significant difference between gene expression of treated and untreated *C. neoformans* cells ($p<0.05$).

MOPS for 4h, 8h, or 12h at 37° C in a humidified incubator. The 4h, 8h, and 12h timepoints were chosen to allow the compounds' effects on the fungal cells to be viewed at multiple time points throughout treatment while still ensuring the survival of some fungal cells. Following fixing, processing, and sectioning, the samples were imaged at 20,000X using an FEI Quanta 600 field emission gun ESEM with Bruker EDS and HKL EBSD. Images were arranged by treatment group and incubation time (Figure 2). The control samples (*C. neoformans* cells incubated alone) exhibit globose, budding cells with a fibril network radiating out from the cell capsule, all indicative of a healthy *C. neoformans* sample (Cleare and Casadevall, 1999). Treatment with $SbPh_4$(ACO) resulted in smooth capsular morphology that lacks the fibril network as well as multiple connected cells that did not separate

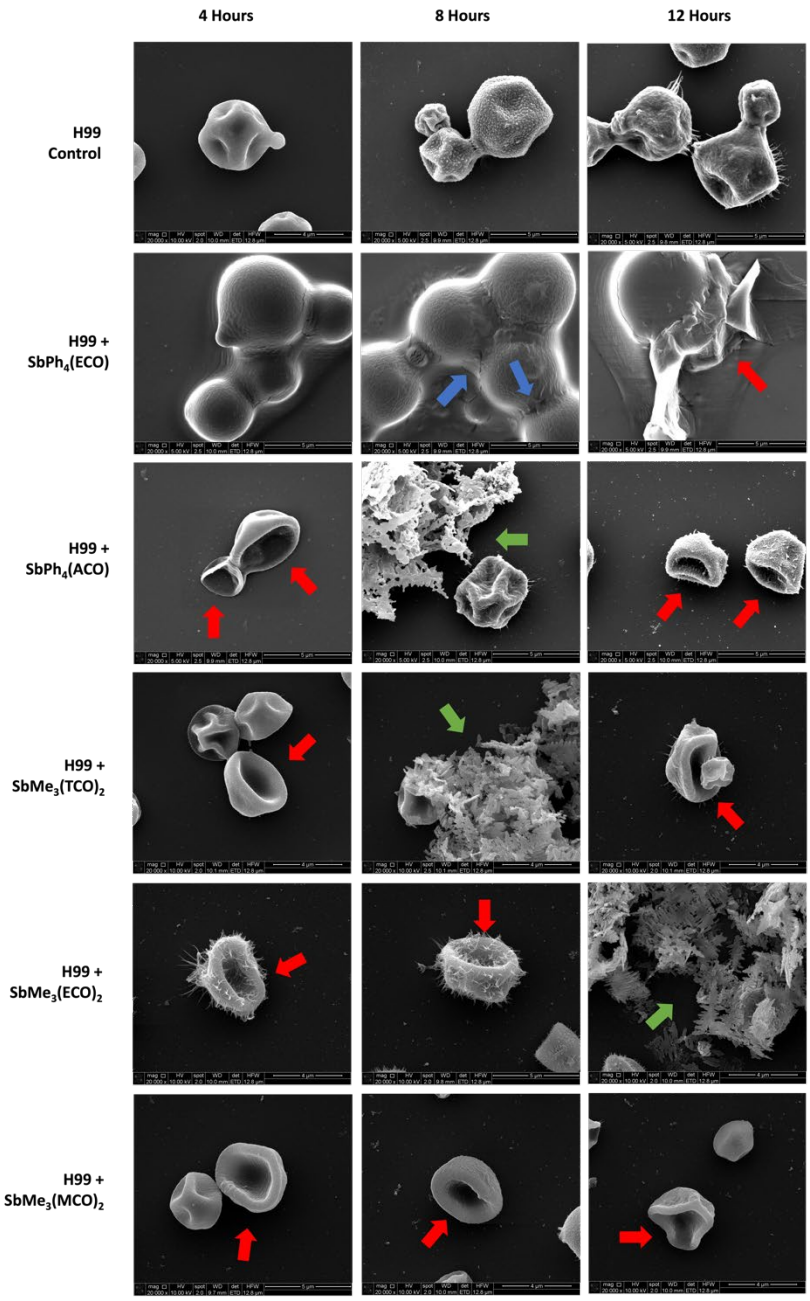

Figure 2. Treatment with experimental compounds results in distinct morphological changes in *C. neoformans* cells. Scanning electron microscopy (SEM) with *C. neoformans* (H99) alone, treated with $SbPh_4(ECO)$, $SbPh_4(ACO)$, $SbMe_3(TCO)_2$, $SbMe_3(ECO)_2$, or $SbMe_3(MCO)_2$ at 4, 8, or 12 hours of incubation. *C. neoformans* alone exhibits a round morphology with dividing cells and stringy capsular components. The treatment with $SbPh_4(ECO)$, results in a smoother capsular morphology and a lack of cell separation following budding. Cracks can be seen in the capsule between cells at the 8hr timepoint (blue arrow) and cell death is seen at the 12hr time point (red arrow). The treatments with $SbPh_4(ACO)$, $SbMe_3(TCO)_2$, and $SbMe_3(ECO)_2$ resulted in cellular death, as seen by the c-shaped cells at multiple time points (red arrows), and the formation/release of an unknown extracellular structure (green arrow). Treatment with $SbMe_3(MCO)_2$ also resulted in c-shaped cells indicative of cellular death (red arrows). Images were taken at 20,000X magnification and are representative of at least 10 fields per condition and time point.

following cell division events. By 8 hours cracks are forming in the capsule between the connected cells and by 12 hours cell death is seen through the leakage of intracellular components into the surrounding environment. In contrast, treatment with $SbPh_4(ECO)$, $SbMe_3(TCO)_2$, $SbMe_3(ECO)_2$, and $SbMe_3(MCO)_2$ resulted in cell death throughout all the time points, as shown by the presence of c-shaped cryptococcal cells (Hole et al., 2012). Also seen throughout all three timepoints of samples treated with $SbPh_4(ECO)$, $SbMe_3(TCO)_2$, and $SbMe_3(ECO)_2$ was the presence of an unknown extracellular structure.

SbPh4(ECO) is an Effective Antifungal Therapy in a *Galleria mellonell*a Infection Model. To examine the effectiveness of these experimental compounds *in vivo*, a *G. mellonella* infection model with *C. neoformans* was used. For this model, *G. mellonella* larvae were infected with *C. neoformans* and subsequently treated with the experimental

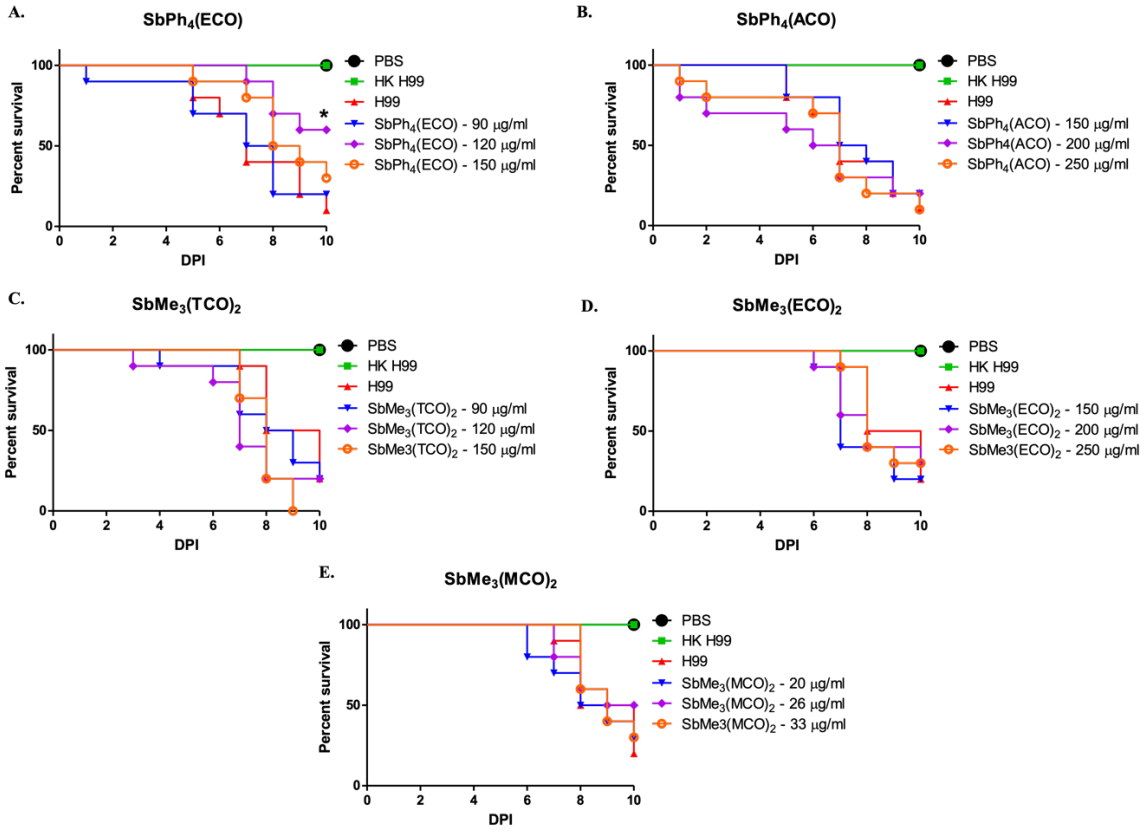

Figure 3. Infection model using *Galleria mellonella* shows *in vivo* effectiveness of only one compound against *Cryptococcus neoformans* infection. *G. mellonella* larvae were infected with $1x10^4$ cells/ml of *C. neoformans* strain H99, heat-killed H99, or injected with PBS. Larvae were treated with either PBS or antifungal compounds, (A) $SbPh_4(ECO)$, (B) $SbPh_4(ACO)$, (C) $SbMe_3(TCO)_2$, (D) $SbMe_3(ECO)_2$, or (E) $SbMe_3(MCO)_2$, diluted in PBS and monitored for survival for 10 days. For all groups, the heat-killed (non-infectious) *C. neoformans* and PBS controls resulted in 100% survival. (A) Treatment with $SbPh_4(ECO)$ at 120 µg/ml resulted in longer survival than the *C. neoformans* (H99) control (p-value < 0.05), while treatment with $SbPh_4(ECO)$ at 90 µg/ml and 150 µg/ml resulted in similar survival to the *C. neoformans* control. (B) Treatment with $SbPh_4(ACO)$ at 150 µg/ml, 200 µg/ml, and 250 µg/ml resulted in similar survival as the *C. neoformans* control. (C) Treatment with $SbMe_3(TCO)_2$ at 90 µg/ml, 120 µg/ml, and 150 µg/ml resulted in similar survival as the *C. neoformans* control. (D) Treatment with $SbMe_3(ECO)_2$ at 150 µg/ml, 200 µg/ml, and 250 µg/ml resulted in similar survival as the *C. neoformans* control. (E) Treatment with $SbMe_3(MCO)_2$ at 150 µg/ml, 200 µg/ml, and 250 µg/ml resulted in similar survival as the *C. neoformans* control. Each experiment was conducted with 10 *G. mellonella* larvae per group. * indicates a significant difference in survival between the treatment and the control groups ($p<0.05$).

compounds (at roughly 7.5X, 10X, and 12.5X the *in-vitro* MIC) with PBS-infected, heat-killed *C. neoformans*-infected, and *C. neoformans*-infected with PBS-treated larvae serving as the controls. Survival was monitored over 10 days to determine if any of the treatments resulted in increased survival of *G. mellonella* larvae relative to the *C. neoformans*-infected control. The negative controls (PBS-infected and heat-killed *C. neoformans*-infected larval

groups) exhibited 100% survival over the 10 days. Treatment with $SbPh_4(ECO)$ at 120 μg/ml resulted in significantly ($p < 0.05$) increased survival of *G. mellonella* larvae compared to *C. neoformans* alone (Figure 3A). The other concentrations of $SbPh_4(ECO)$ tested, as well as all the concentrations of $SbPh_4(ACO)$ (Figure 3B), $SbMe_3(TCO)_2$ (Figure 3C), $SbMe_3(ECO)_2$ (Figure 3D), and $SbMe_3(MCO)_2$ (Figure 3E) tested were not effective at extending the life of the infected *G. mellonella* larvae relative to the control.

4. Discussion:

Fungal infections are a rising concern in the world today. Thanks to medical advances in the treatment of HIV-AIDS and other immunocompromising diseases, we are seeing a jump in opportunistic fungal infections in recent decades (Badiee and Hashemizadeh, 2014). We are also seeing an increase in multi-drug resistant fungal strains, the rise of infections by dimorphic fungal pathogens, and the spread of fungal pathogens to new regions, likely due to climate change (Friedman and Schwartz, 2019). Due to the limited drug arsenal against these fungal pathogens (coupled with the high cytotoxicity of many of those existing anti-fungal drugs), it is important to discover new antifungal therapies (Perlin et al., 2017).

Novel organoantimony(V) cyanoximates produced by Gerasimchuk et al. showed promising antifungal activity in a disc assay against *C. neoformans* and *C. albicans* (Gerasimchuk et al., 2022). Based on those results, we hypothesized that these organoantimony(V) cyanoximates could prove to be effective antifungals.

The gene expression of untreated C. neoformans cells and the gene expression of C. neoformans cells treated with SbPh4(ACO), SbPh4(MCO), and SbPh4(ECO) were compared to understand the genes/pathways that were significantly up- or down-regulated following treatment. Looking at the overall pathways that were up- or down-regulated following treatment with the three compounds, treatment with SbPh4(ECO) and SbPh4(ACO) resulted in the down-regulation of pathways associated with ribosome biogenesis and rRNA processing, with SbPh4(ECO) also causing the up-regulation of pathways associated with membrane transport and membrane formation. This indicates that the cryptococcal cells are diverting energy away from growth and metabolism and instead focusing that energy towards strengthening the membrane and fighting off the anti-fungal compound. In contrast, treatment with SbPh4(MCO) resulted in the up-regulation of pathways associated with growth (organelle/ribosome formation and DNA replication). This is the opposite of what we saw with SbPh4(ECO) and SbPh4(ACO), and future studies will be performed to try to understand the reasoning behind this.

Overall, these RNA sequencing results indicate that these compounds may be inhibiting *C. neoformans* growth by interfering with cell metabolism, membrane production, or membrane transport, decreasing the uptake of nutritional requirements while increasing the export of materials from the cell. However, more studies will need to be performed using

mutant libraries to narrow down exactly what genes/pathways these compounds are targeting to produce their anti-fungal activity.

To look further into the possible mechanism of anti-fungal activity, scanning electron microscopy (SEM) was performed. The SEM images confirmed that organoantimony compound treatment affects the *C. neoformans* cells, with $SbPh_4(ECO)$ treatment resulting in altered morphology and killing of the cells, $SbMe_3(MCO)_2$ treatment resulting in killing of the cells, and $SbPh_4(ACO)$, $SbMe_3(TCO)_2$, and $SbMe_3(ECO)_2$ treatments resulting in the killing of the cells in addition to the presence of an unknown structure. It is unknown whether this extracellular component contributed to the anti-fungal activity, or if it is just an artifact, byproduct, or compound precipitant, so more research will be acquired to determine the importance of this unknown structure. Also unknown is whether or not the cracks in the capsule of cells treated with $SbPh_4(ECO)$ extend through the cell wall and/or membrane of the cryptococcal cells and if they contribute to cell death. Future transmission electron microscopy (TEM) studies can give more insight into these questions and indicate a possible antifungal mechanism of action.

Many anti-microbial treatments that are effective *in-vitro* are not effective *in-vivo* due to complicated interactions in living models (Shi et al., 2019). For this reason, we wanted to test the effectiveness of the organoantimony compounds *in-vivo* using a *G. mellonella* infection model with *C. neoformans*. Only $SbPh_4(ECO)$ at 120 μg/ml was effective at extending the survival of *G. mellonella* larvae infected with *C. neoformans*. This could be because the majority of the organoantimony compounds are not effective *in-vivo*, are not effective in this particular *in-vivo* model, or are toxic at these higher infection model concentrations. The toxicity of these compounds in the *G. mellonella* model can either be confirmed or ruled out via the use of additional control groups that are treated with the compounds alone, but not infected with *C. neoformans*.

Overall, these organoantimony(V) cyanoximates, while not effective *in-vivo* using a *G. mellonella* infection model, can provide valuable information for antifungal research. Through the identification of their mechanism of action, novel anti-fungal molecular targets can be identified for future research and drug production. Future studies include TEM studies to identify the compounds' effects on the fungal cell wall and membrane as well as studies that test compounds against a *C. neoformans* mutant library to further identify specific genes involved in antifungal resistance and point to the antifungal mechanism.

5. Summary:

A series of novel organoantimony compounds exhibited antifungal activity against the fungal pathogen *Cryptococcus neoformans* and were non-toxic to mammalian cells, indicating their potential use as antifungal drugs in the future. Further research began looking into possible antifungal mechanisms of action by identifying several signaling pathways that

were up- or down-regulated following treatment with the compounds and by looking at the effect of the compounds on the morphology of the cryptococcal cells. The overall ineffectiveness of the compounds in an *in-vivo* model (barring $SbPh_4(ECO)$ at 120 μg/ml) indicates that these compounds may not be effective antifungal drugs, however, the compounds can still be studied to provide insight for future drug production through the identification of mechanisms of action and novel molecular targets.

6. Acknowledgments:

This work was supported by the Freshman Research Scholar, Lew Wentz Research Scholar, and Niblack Research Scholar awards from Oklahoma State University Office of Scholar Development as well as Oklahoma State University start-up funds (KLW). Special thanks to Lisa Whitworth and Brent Johnson at the OSU Microscopy Facility for assistance with the electron microscopy experiments and to the Gerasimchuck lab for the production of the organoantimony compounds.

6a. Papers Published:

Gerasimchuk, N.; Pinks, K.; Salpadoru, T.; **Cotton, K**.; Michka, O.; Patrauchan, M.A.; Wozniak, K.L. Non-Antibiotic Antimony-Based Antimicrobials. *Molecules* **2022**, *27*, 7171. https://doi.org/10.3390/ molecules27217171

Cotton, K.; Nelson, B.N.; Gerasimchuk, N.; Wozniak, K.L. (2023). Effects of Organoantimony Compounds on Fungal Pathogen *Cryptococcus neoformans*. [Manuscript in preparation]

6b. Presentations:

Cotton, K, B.N. Nelson, N. Gerasimchuk, and K.L. Wozniak. "Effects of Organoantimony Compounds on Fungal Pathogens *Cryptococcus neoformans* and *Candida albicans*." Joint Meeting of the Missouri and Missouri Valley Branches of the American Society for Microbiology, March 19-20, 2021. Virtual. **Poster.**

Cotton, K, B.N. Nelson, N. Gerasimchuk, and K.L. Wozniak. "Effects of Organoantimony Compounds on Fungal Pathogens *Cryptococcus neoformans* and *Candida albicans*." Oklahoma State University College of Arts & Sciences 3-Minute Thesis Competition, April 5-9, 2021. Virtual. **Talk.**

Cotton, K, B.N. Nelson, N. Gerasimchuk, and K.L. Wozniak. "Effects of Organoantimony Compounds on Fungal Pathogens *Cryptococcus neoformans* and *Candida albicans*." Oklahoma Center for Respiratory and Infectious Diseases (OCRID), April 6-7, 2021. Virtual. **Talk (Undergraduate best student abstract)**

Cotton, K, B.N. Nelson, N. Gerasimchuk, and K.L. Wozniak. "Effects of Organoantimony Compounds on Fungal Pathogens *Cryptococcus neoformans* and *Candida albicans*." Oklahoma State University Freshman Research Scholars Symposium, April 12-24, 2021. Virtual. **Poster (One of the runner ups).**

Cotton, K, B.N. Nelson, N. Gerasimchuk, and K.L. Wozniak. "Effects of Organoantimony Compounds on Fungal Pathogens *Cryptococcus neoformans* and *Candida albicans*." Oklahoma State University Microbiology and Molecular Genetics Departmental Spring Symposium, April 23, 2021. Virtual. **Talk.**

Cotton, K, B.N. Nelson, N. Gerasimchuk, and K.L. Wozniak. "Effects of Organoantimony Compounds on Fungal Pathogens *Cryptococcus neoformans* and *Candida albicans*." Oklahoma State University Summer Research Expo, July 28, 2021. Oklahoma State University, Stillwater, OK. **Poster.**

Cotton, K, B.N. Nelson, N. Gerasimchuk, and K.L. Wozniak. "Effects of Organoantimony Compounds on Fungal Pathogens *Cryptococcus neoformans* and *Candida albicans*." Joint Meeting of the Missouri and Missouri Valley Branches of the American Society for Microbiology, March 18-19, 2022. Oklahoma State University, Stillwater, OK. **Poster (Undergraduate best poster presentation).**

Cotton, K, B.N. Nelson, N. Gerasimchuk, and K.L. Wozniak. "Effects of Organoantimony Compounds on Fungal Pathogens *Cryptococcus neoformans* and *Candida albicans*." Oklahoma State University College of Arts & Sciences 3-Minute Thesis Competition, March 29, 2022. Oklahoma State University, Stillwater, OK. **Talk.**

Cotton, K, B.N. Nelson, N. Gerasimchuk, and K.L. Wozniak. "Effects of Organoantimony Compounds on Fungal Pathogens *Cryptococcus neoformans* and *Candida albicans*." South Central Medical Mycology Meeting, April 1-2, 2022. San Antonio, TX. **Talk.**

Cotton, K, B.N. Nelson, N. Gerasimchuk, and K.L. Wozniak. "Effects of Organoantimony Compounds on Fungal Pathogens *Cryptococcus neoformans* and *Candida albicans*." National Conference on Undergraduate Research, April 4-8, 2022. Virtual. **Poster.**

Cotton, K, B.N. Nelson, N. Gerasimchuk, and K.L. Wozniak. "Effects of Organoantimony Compounds on Fungal Pathogens *Cryptococcus neoformans* and *Candida albicans*." Oklahoma Center for Respiratory and Infectious Diseases (OCRID), April 5-6, 2022. Virtual. **Talk (Undergraduate best student abstract).**

Cotton, K, B.N. Nelson, N. Gerasimchuk, and K.L. Wozniak. "Effects of Organoantimony Compounds on Fungal Pathogens *Cryptococcus neoformans* and *Candida albicans*." Oklahoma State University Lew Wentz Research Scholars Symposium, April 15, 2022. Oklahoma State University, Stillwater, OK. **Poster.**

Cotton, K, B.N. Nelson, N. Gerasimchuk, and K.L. Wozniak. "Effects of Organoantimony Compounds on Fungal Pathogens *Cryptococcus neoformans* and *Candida albicans*." Oklahoma State University Microbiology and Molecular Genetics Departmental Spring Symposium, April 15, 2022. Oklahoma State University, Stillwater, OK. **Poster (Second place in undergraduate poster presentations).**

Cotton, K, B.N. Nelson, N. Gerasimchuk, and K.L. Wozniak. "Effects of Organoantimony Compounds on Fungal Pathogens *Cryptococcus neoformans* and *Candida albicans*." Oklahoma State University Undergraduate Research Symposium, April 19, 2022. Oklahoma State University, Stillwater, OK. **Poster.**

Cotton, K, B.N. Nelson, N. Gerasimchuk, and K.L. Wozniak. "Effects of Organoantimony Compounds on Fungal Pathogens *Cryptococcus neoformans* and *Candida albicans*." Gulf Coast Undergraduate Research Symposium, October 8, 2022. Rice University, Houston, TX. **Talk.**

Cotton, K, B.N. Nelson, N. Gerasimchuk, and K.L. Wozniak. "Effects of Organoantimony Compounds on Fungal Pathogens *Cryptococcus neoformans* and *Candida albicans*." Oklahoma State University Microbiology and Molecular Genetics Departmental Spring Symposium, February 10, 2023. Oklahoma State University, Stillwater, OK. **Poster.**

Cotton, K, B.N. Nelson, N. Gerasimchuk, and K.L. Wozniak. "Effects of Organoantimony Compounds on Fungal Pathogens *Cryptococcus neoformans* and *Candida albicans*." World Congress on Undergraduate Research, April 4-6, 2023. Warwick University, Coventry, UK. **Talk.**

Cotton, K, B.N. Nelson, N. Gerasimchuk, and K.L. Wozniak. "Effects of Organoantimony Compounds on Fungal Pathogens *Cryptococcus neoformans* and *Candida albicans*." Oklahoma Center for Respiratory and Infectious Diseases (OCRID), April 11, 2023. Oklahoma State University, Stillwater, OK. **Poster (Best undergraduate student poster).**

Cotton, K, B.N. Nelson, N. Gerasimchuk, and K.L. Wozniak. "Effects of Organoantimony Compounds on Fungal Pathogens *Cryptococcus neoformans* and *Candida albicans*." Oklahoma State University Undergraduate Research Symposium, April 18, 2023. Oklahoma State University, Stillwater, OK. **Poster.**

6c. References:

BADIEE, P. & HASHEMIZADEH, Z. 2014. Opportunistic invasive fungal infections: diagnosis & clinical management. *Indian J Med Res*, 139, 195-204.

BONGOMIN, F., GAGO, S., OLADELE, R. O. & DENNING, D. W. 2017. Global and Multi-National Prevalence of Fungal Diseases—Estimate Precision. *Journal of Fungi*, 3, 57.

CLEARE, W. & CASADEVALL, A. 1999. Scanning electron microscopy of encapsulated and non-encapsulated Cryptococcus neoformans and the effect of glucose on capsular polysaccharide release. *Medical Mycology*, 37, 235-243.

FRIEDMAN, D. Z. P. & SCHWARTZ, I. S. 2019. Emerging Fungal Infections: New Patients, New Patterns, and New Pathogens. *Journal of Fungi*, 5, 67.

GERASIMCHUK, N., PINKS, K., SALPADORU, T., COTTON, K., MICHKA, O., PATRAUCHAN, M. A. & WOZNIAK, K. L. 2022. Non-Antibiotic Antimony-Based Antimicrobials. *Molecules*, 27.

HOLE, C. R., BUI, H., WORMLEY, F. L. & WOZNIAK, K. L. 2012. Mechanisms of Dendritic Cell Lysosomal Killing of Cryptococcus. *Scientific Reports*, 2, 739.

HOUŠŤ, J., SPÍŽEK, J. & HAVLÍČEK, V. 2020. Antifungal Drugs. *Metabolites,* 10, 106.

KETT, D. H., AZOULAY, E., ECHEVERRIA, P. M. & VINCENT, J. L. 2011. Candida bloodstream infections in intensive care units: analysis of the extended prevalence of infection in intensive care unit study. *Crit Care Med*, 39, 665-70.

KOLLEF, M., MICEK, S., HAMPTON, N., DOHERTY, J. A. & KUMAR, A. 2012. Septic shock attributed to Candida infection: importance of empiric therapy and source control. *Clin Infect Dis*, 54, 1739-46.

LEVITZ, S. M. 1991. The Ecology of Cryptococcus neoformans and the Epidemiology of Cryptococcosis. *Reviews of Infectious Diseases*, 13, 1163-1169.

PERLIN, D. S., RAUTEMAA-RICHARDSON, R. & ALASTRUEY-IZQUIERDO, A. 2017. The global problem of antifungal resistance: prevalence, mechanisms, and management. *The Lancet Infectious Diseases*, 17, e383-e392.

POULAIN, D. 2015. Candida albicans, plasticity and pathogenesis. *Crit Rev Microbiol*, 41, 208-17.

RAJASINGHAM, R., SMITH, R. M., PARK, B. J., JARVIS, J. N., GOVENDER, N. P., CHILLER, T. M., DENNING, D. W., LOYSE, A. & BOULWARE, D. R. 2017. Global burden of disease of HIV-associated cryptococcal meningitis: an updated analysis. *Lancet Infect Dis*, 17, 873-881.

REPENTIGNY, L. D., LEWANDOWSKI, D. & JOLICOEUR, P. 2004. Immunopathogenesis of Oropharyngeal Candidiasis in Human Immunodeficiency Virus Infection. *Clinical Microbiology Reviews*, 17, 729-759.

ROBBINS, N., WRIGHT, G. D. & COWEN, L. E. 2016. Antifungal Drugs: The Current Armamentarium and Development of New Agents. *Microbiology Spectrum*, 4, 4.5.19.

SABIITI, W. & MAY, R. C. 2012. Mechanisms of infection by the human fungal pathogen Cryptococcus neoformans. *Future Microbiol*, 7, 1297-313.

SHI, D., MI, G., WANG, M. & WEBSTER, T. J. 2019. In vitro and ex vivo systems at the forefront of infection modeling and drug discovery. *Biomaterials,* 198, 228-249.

SOBEL, J. D. 2007. Vulvovaginal candidosis. *The Lancet*, 369, 1961-1971.

WILLIAMSON, P. R. 2017. The relentless march of cryptococcal meningitis. *The Lancet Infectious Diseases*, 17, 790-791.

Effects of Organoantimony Compounds on Fungal Pathogen *Cryptococcus neoformans*

Kaitlyn Cotton, Brittney Conn, Benjamin N. Nelson, Nikolay Gerasimchuk, and Karen L. Wozniak

Oklahoma State University, Stillwater, OK

Introduction

- *Cryptococcus neoformans*
  - Opportunistic fungal pathogen found in soil and bird droppings
  - Causes pulmonary cryptococcosis and cryptococcal meningitis

- Antifungal Drugs
  - Low quantity
  - High cytotoxicity
  - Increased resistance in recent years

- Novel Organoantimony compounds

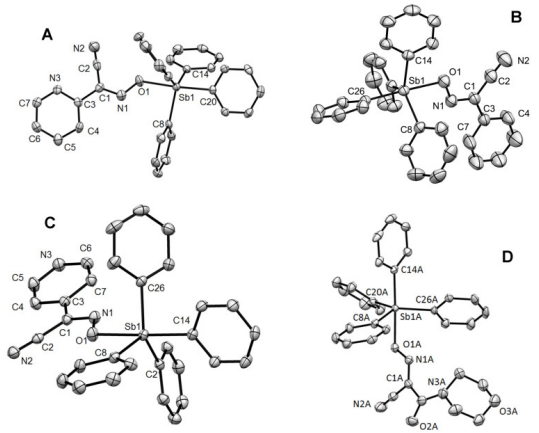

(Gerasimchuk, 2022)

Compounds Consist of a Common Backbone Joined to Different Side Groups

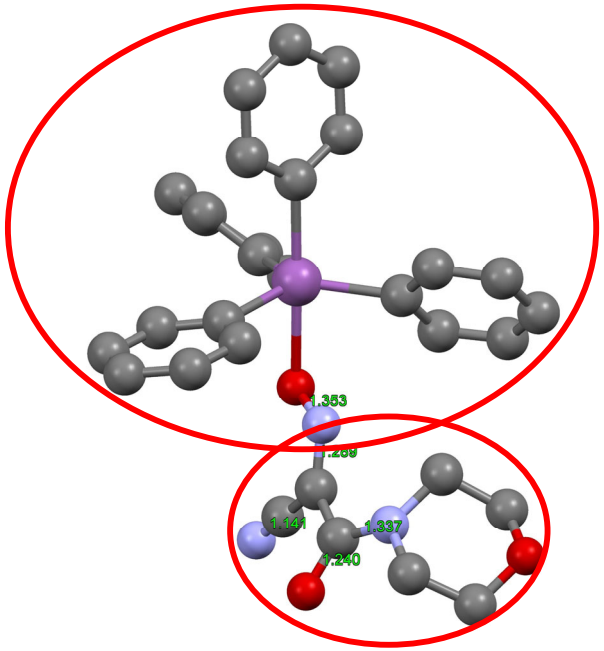

$SbPh_4(MCO)$

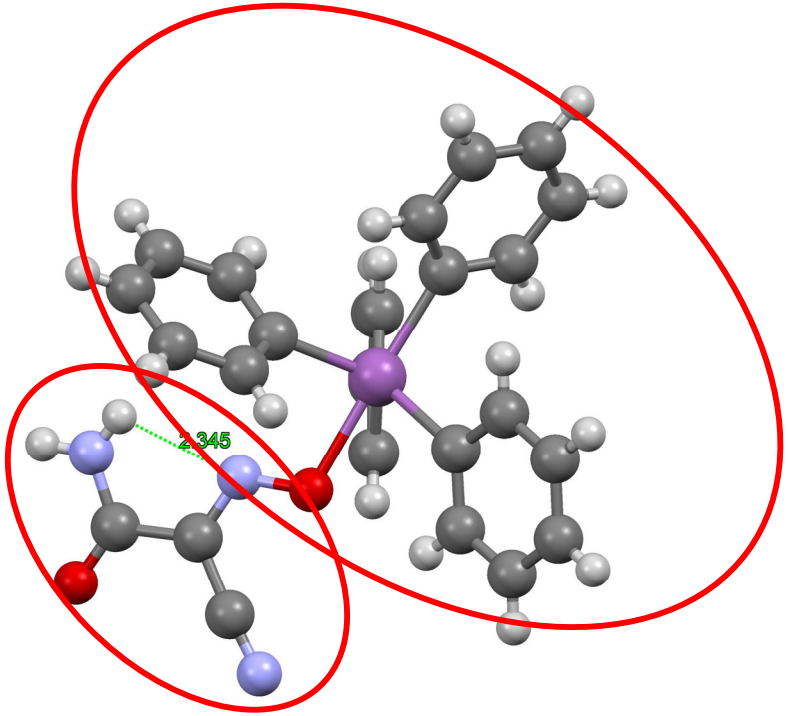

$SbPh_4(ACO)$

(Gerasimchuk, 2022)

Compounds Exhibit Antibacterial Activity

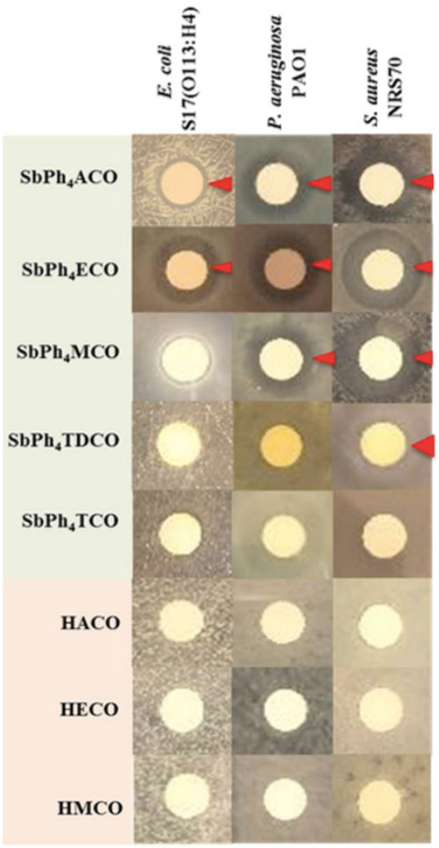

Compound/Clearance Zone, mm	*E. coli*	*P. aeruginosa*	*S. aureus*
Sb Compounds			
$SbPh_4$(ACO)	2.5 ± 0.2	5.6 ± 0.7	4.7 ± 0.7
$SbPh_4$(ECO)	4.7 ± 0.2	2.2 ± 0.3	9.4 ± 0.1
$SbPh_4$(MCO)	ND	5.7 ± 0.2	6.1 ± 0.1
$SbPh_4$(TDCO)	ND	ND	2.0 ± 0.5
$SbPh_4$(TCO)	ND	ND	ND
Controls			
H(ACO)	ND	ND	ND
H(ECO)	ND	ND	ND
H(MCO)	ND	ND	ND

(Gerasimchuk, 2022)

Compounds Exhibit Antifungal Activity

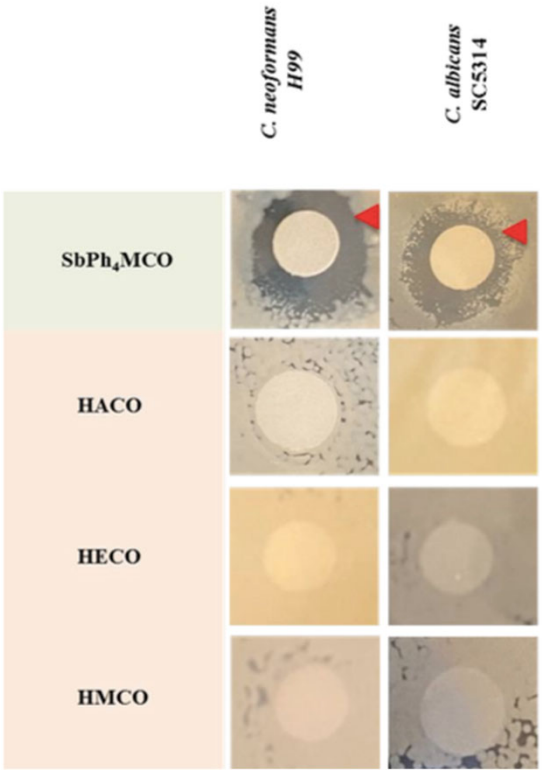

Compound/Clearance Zone, mm	*C. neoformans*	*C. albicans*
Sb Compounds		
$SbPh_4$(ACO)	6.7 ± 1.3	ND
$SbPh_4$(ECO)	9.7 ± 4.4	ND
$SbPh_4$(MCO)	5.0 ± 1.3	2.9 ± 1.2
$SbPh_4$(TDCO)	2.0 ± 1.0	ND
$SbPh_4$(TCO)	2.7 ± 1.3	ND
Controls		
H(ACO)	ND	ND
H(ECO)	ND	ND
H(MCO)	ND	ND

(Gerasimchuk, 2022)

Compounds A, B, E, I, F, and G Exhibited Highest Antifungal Activity

C. neoformans					
	MIC (μg/ml)	MFC (μg/ml)		MIC (μg/ml)	MFC (μg/ml)
Compound A	10.94 ± 3.13	100 ± 0.0	Control 1	41.67 ± 14.43	>100
Compound B	19.79 ± 16.02	100 ± 0.0	Control 2	>100	>100
Compound C	33.33 ± 14.43	>100			
Compound D	25 ± 0.0	>100	Control 3A/3F	>100	>100
Compound E	18.75 ± 7.22	100 ± 0.0	Control 3B/3G	>100	>100
Compound F	20.83 ± 7.22	>100	Control 3C/3H	-	-
Compound G	2.60 ± 0.9	33.33 ± 14.43	Control 3D/3I	33.33 ± 14.43	50 ± 0.0
Compound H	>100	>100	Control 3E	>100	>100
Compound I	12.5 ± 0.0	50 ± 0.0	Control 3J	25 ± 0.0	>100
Compound J	>100	>100	Control 3K	25 ± 0.0	100 ± 0.0
Compound K	>100	>100	Control 3L	50 ± 0.0	>100
Compound L	100 ± 0.0	>100			

Compound A, B, E, I, F, and G are Non-toxic

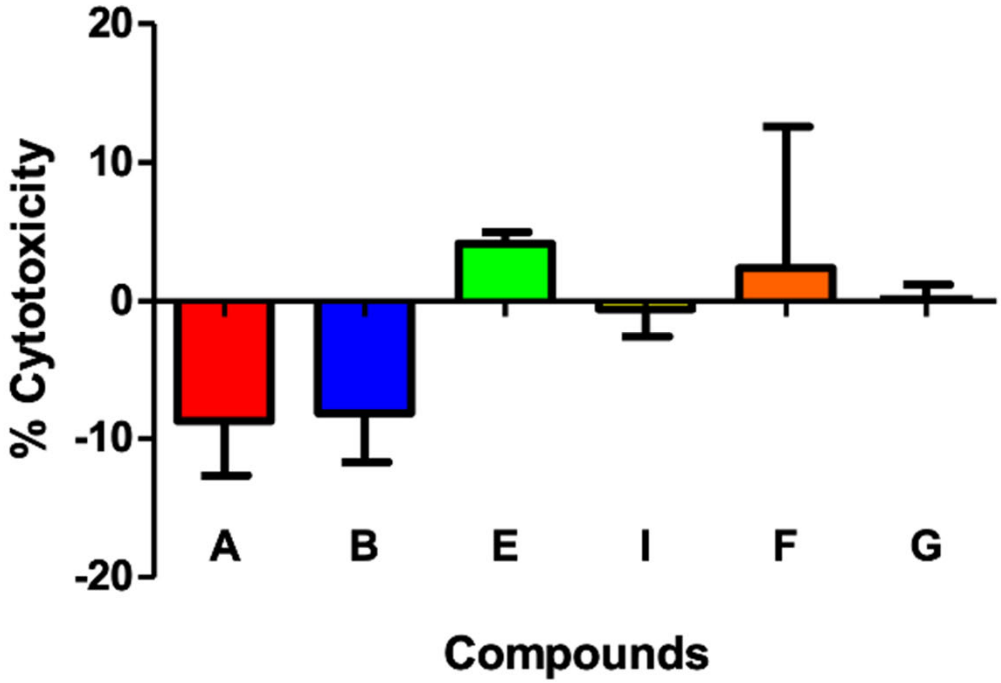

Compound A

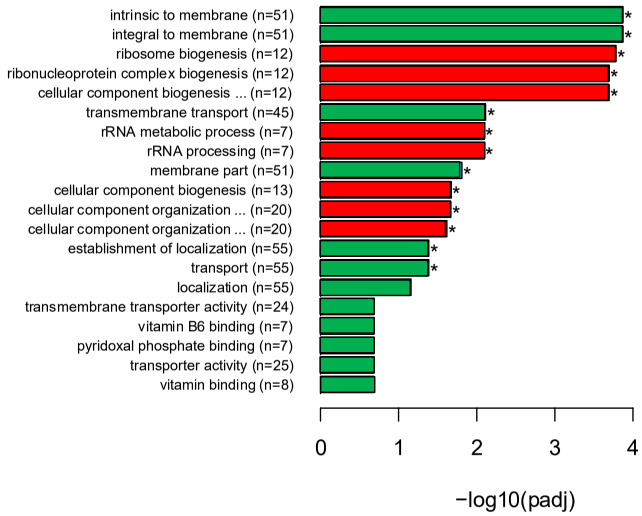

Compound B

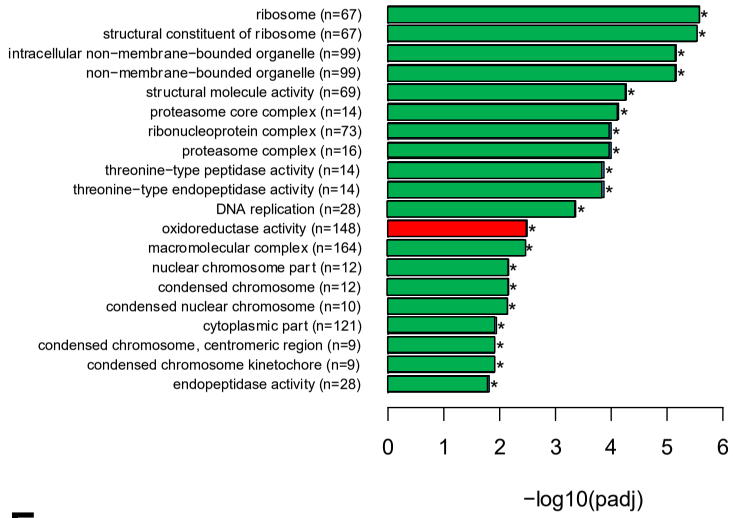

Compound E

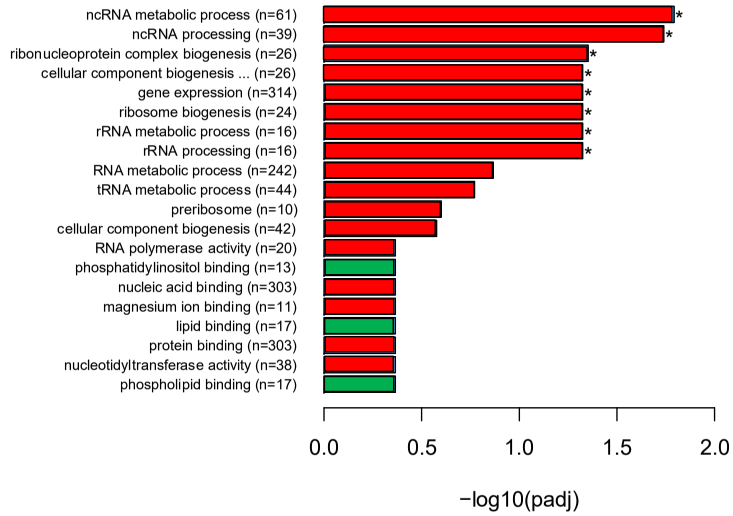

Legend:

- Down-regulated
- Upregulated

Compound A Results in Altered Morphology and Killing

	4 Hours	8 Hours	12 Hours
H99 Control	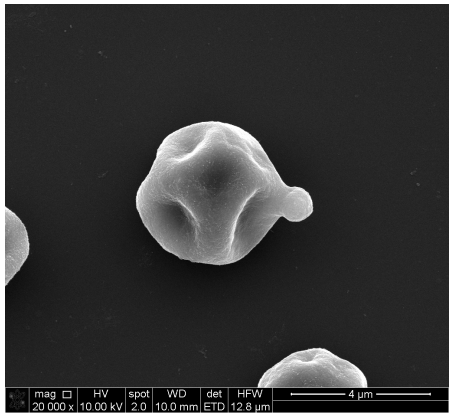	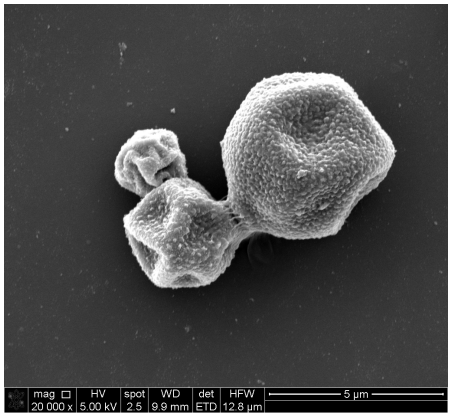	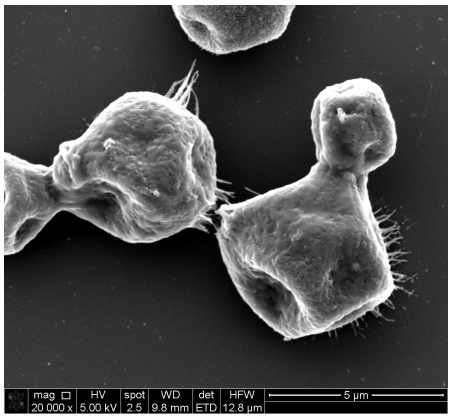
H99 + Compound A	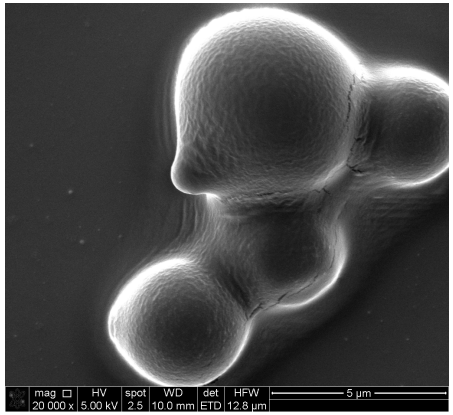	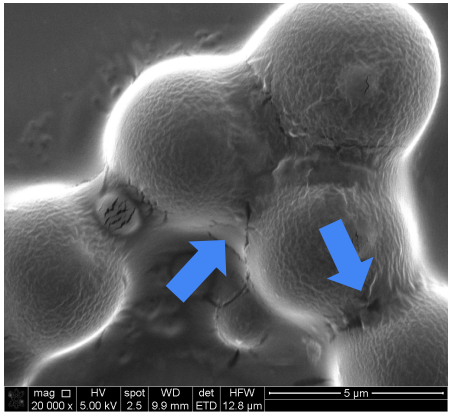	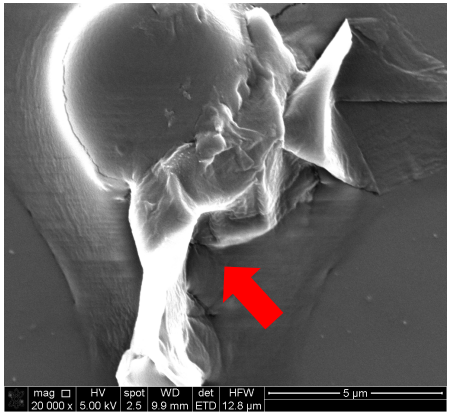

Compound E Results in Killing and Extracellular Components

	4 Hours	8 Hours	12 Hours
H99 Control	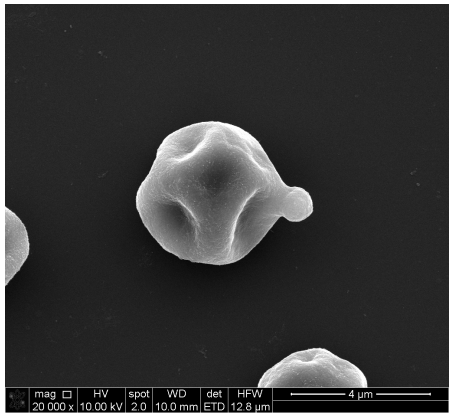	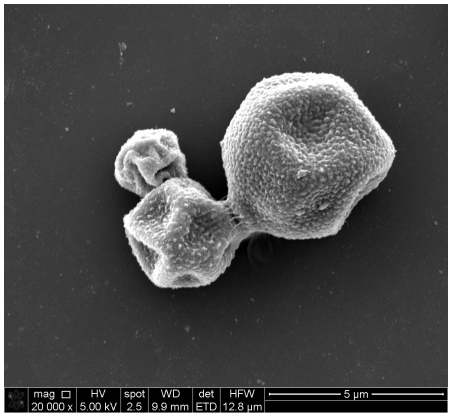	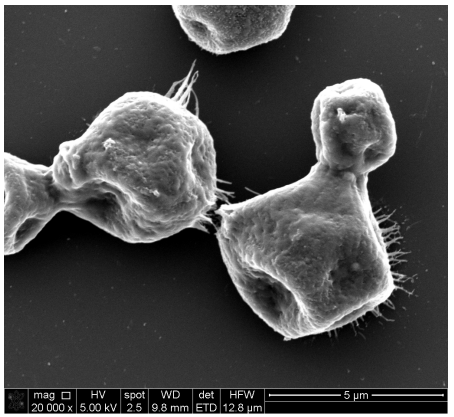
H99 + Compound E	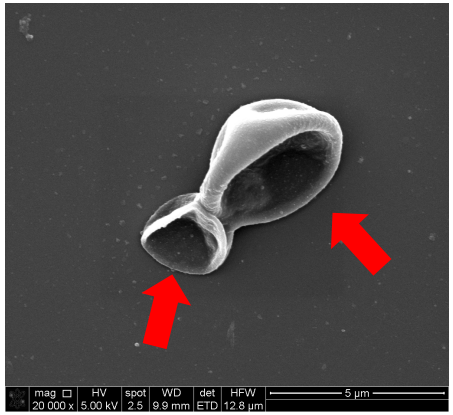	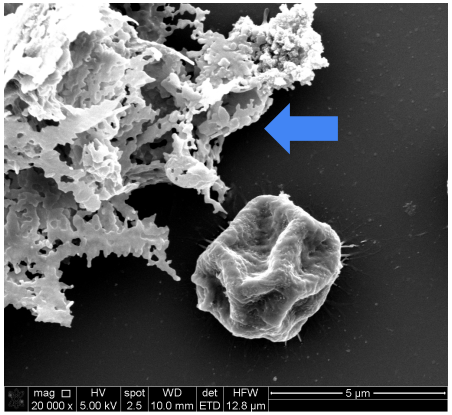	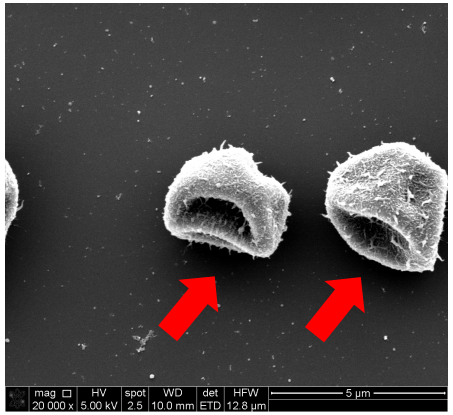

Compound F Results in Killing and Extracellular Components

	4 Hours	8 Hours	12 Hours
H99 Control	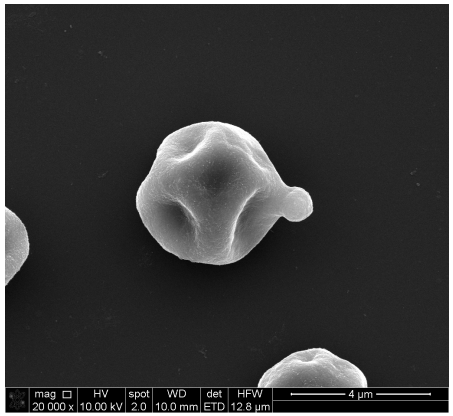	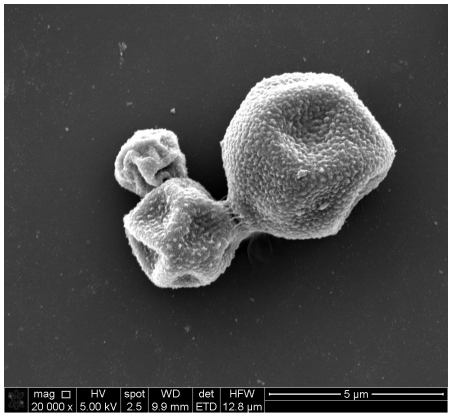	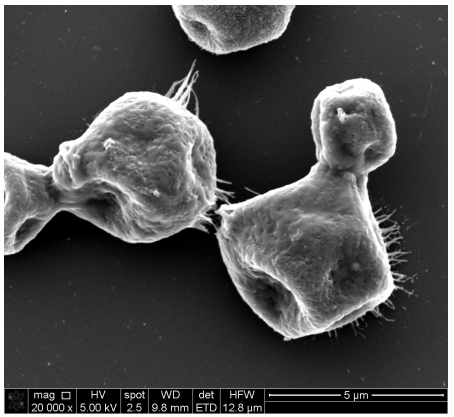
H99 + Compound F	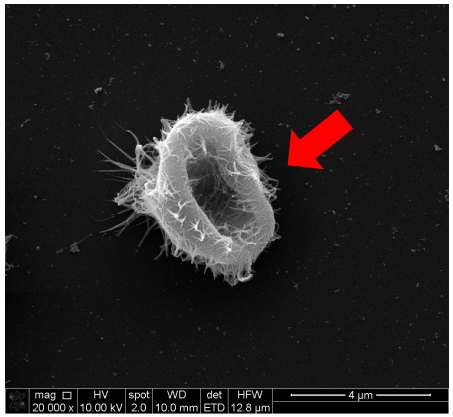	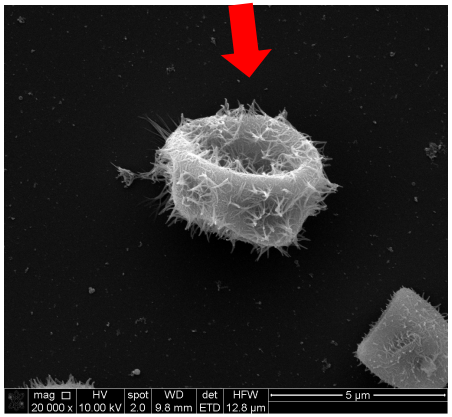	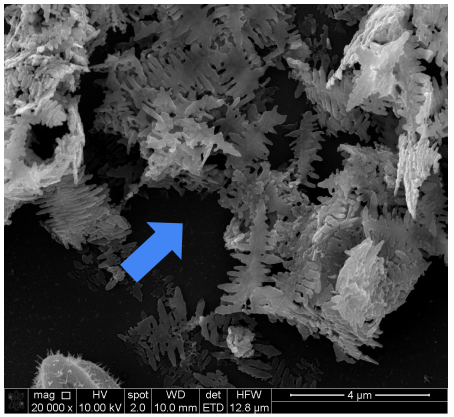

Compound G Results in Killing

	4 Hours	8 Hours	12 Hours
H99 Control	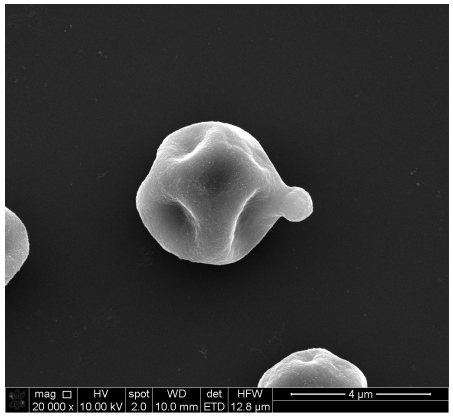	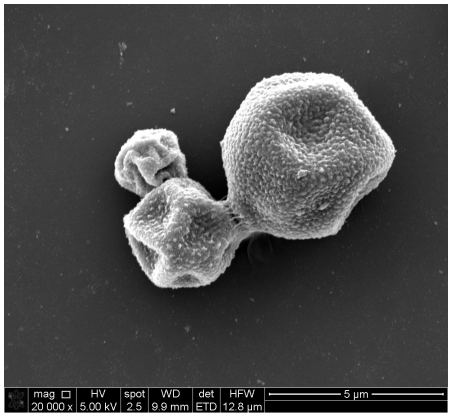	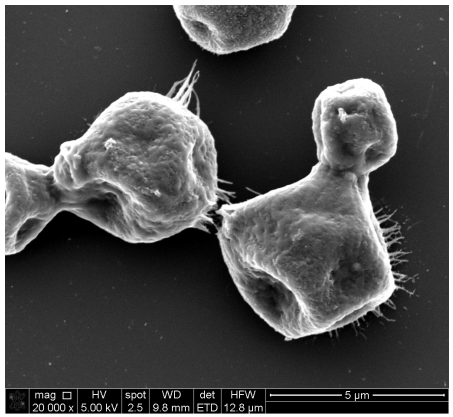
H99 + Compound G	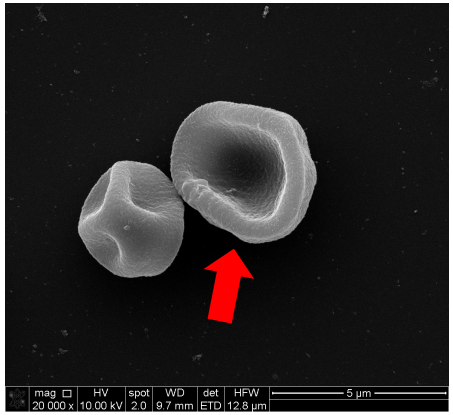	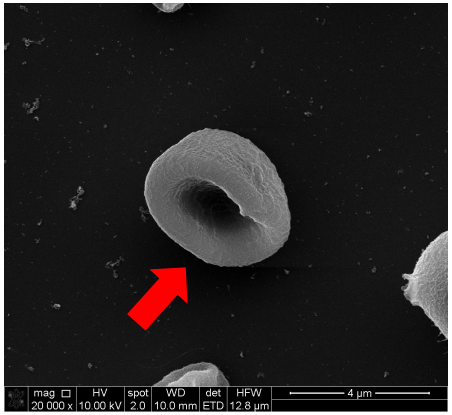	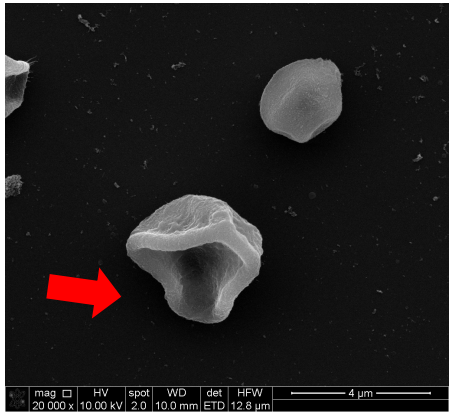

Compound I Results in Killing and Extracellular Components

	4 Hours	8 Hours	12 Hours
H99 Control	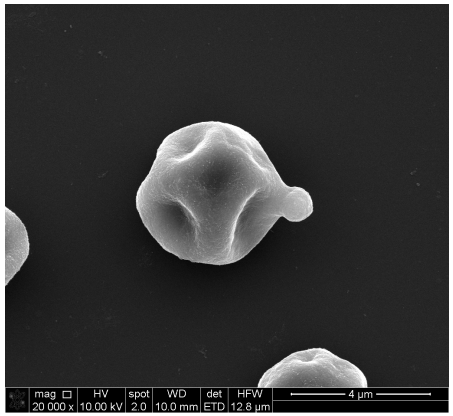	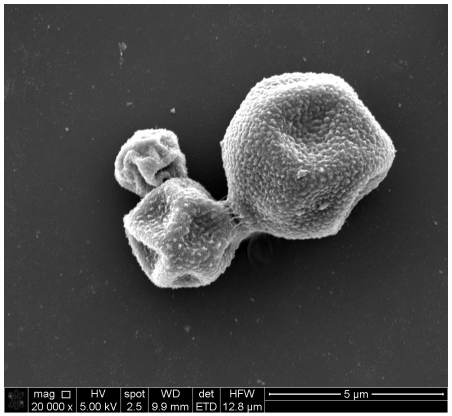	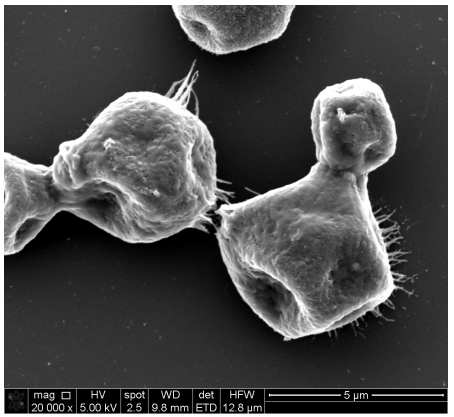
H99 + Compound I	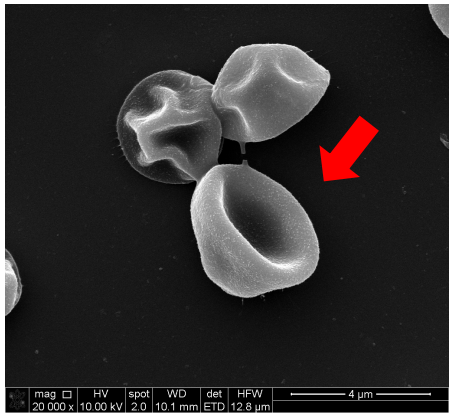	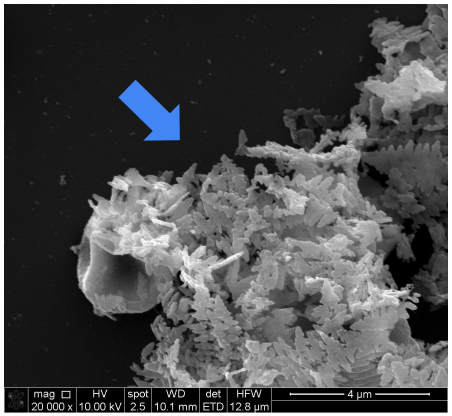	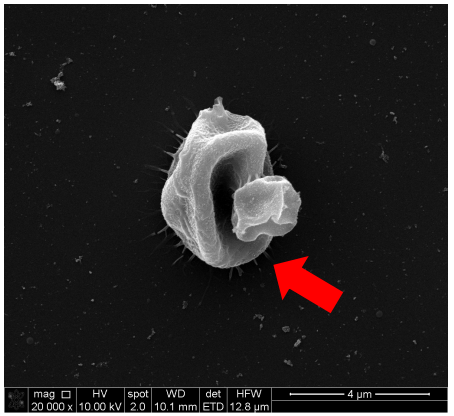

Compound A is Effective in a *G. mellonella* model at 120 μg/ml

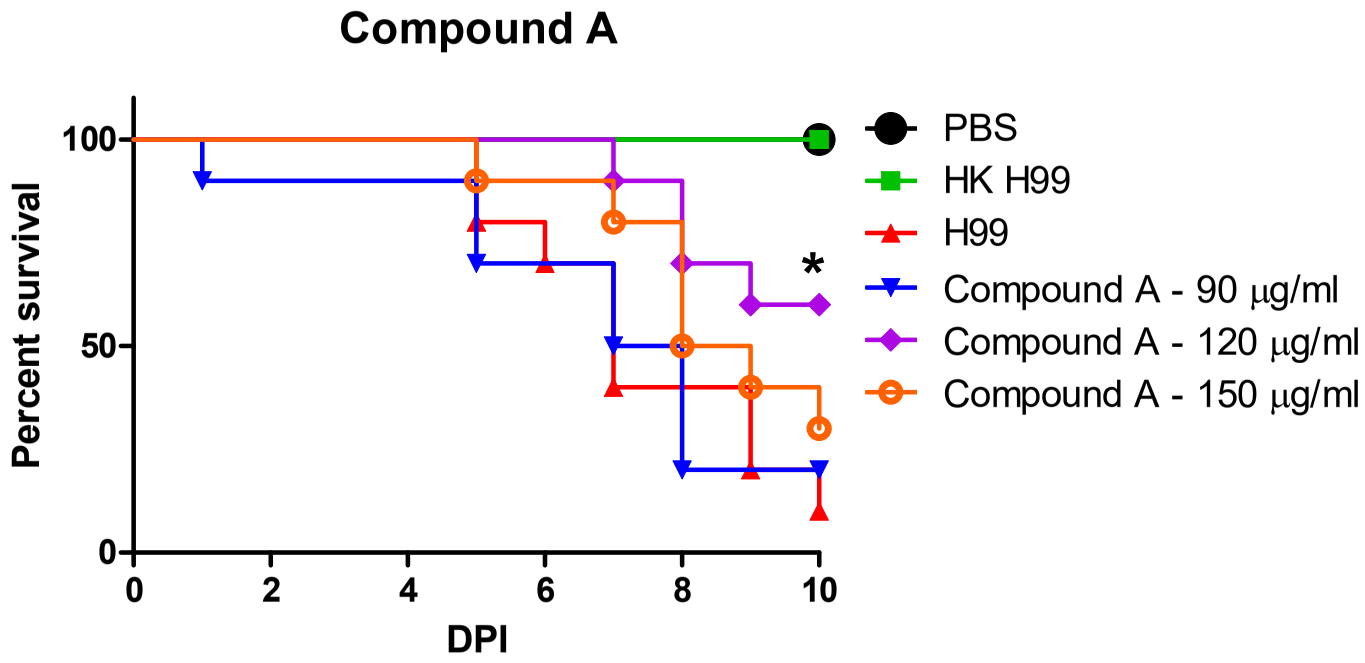

Compound E, I, F, and G Were Not Effective in a *G. mellonella* model

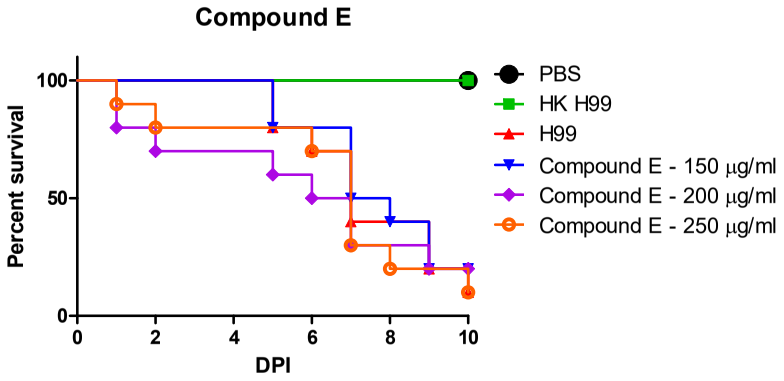

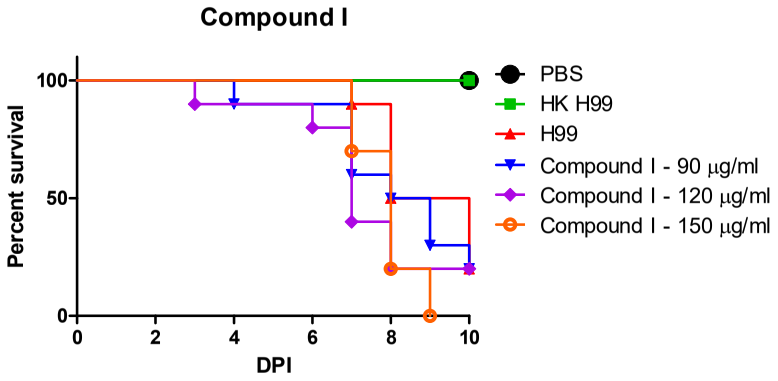

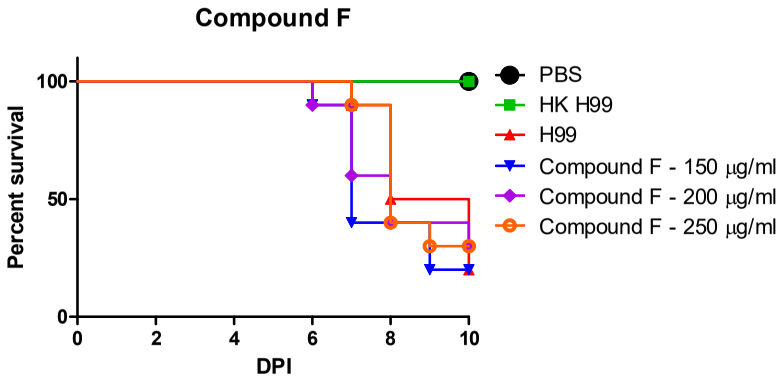

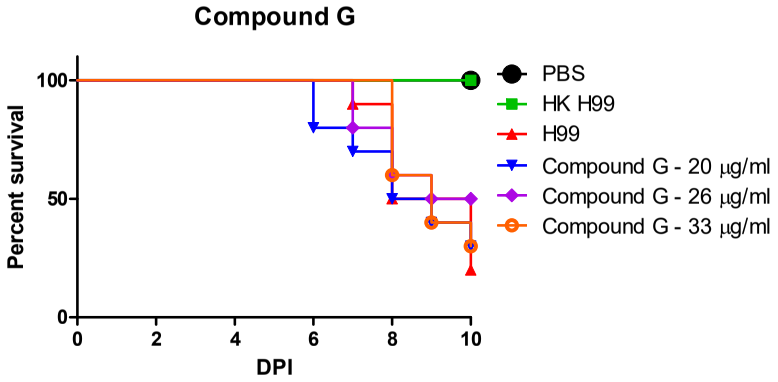

Conclusions

MIC Assays:

- Compounds A, B, E, I, F, and G were most effective at inhibiting *C. neoformans* growth
  - Compounds I and G exhibited fungicidal activity against *C. neoformans* at 50 µg/ml and 25 µg/ml

Cytotoxicity Assays:

- Compounds A, B, E, I, F, and G are non-toxic

RNA Sequencing:

- Identified genes and pathways associated with membrane transport, membrane formation, metabolism, or gene expression that have been up- or down-regulated in *C. neoformans* cells treated with Compounds A, B, or E

SEM:

- Compounds A, E, F, G, and I treatments result in altered morphology and/or killing of *C. neoformans* cells

Galleria Mellonella Infection Model:

- Only Compound A at 120 µg/ml extended the life of *G. mellonella* in a *C. neoformans* infection model

Future Studies

- TEM with compounds A, B, E, I, F, and G against *C. neoformans*
- Further toxicity studies with *G. mellonella*
- Synergistic studies with existing drugs such as Amphotericin B and caspofungin
- Test compounds against drug resistant strains of *C. neoformans*
- Test compounds against mutant strains of *C. neoformans*

Amphotericin B

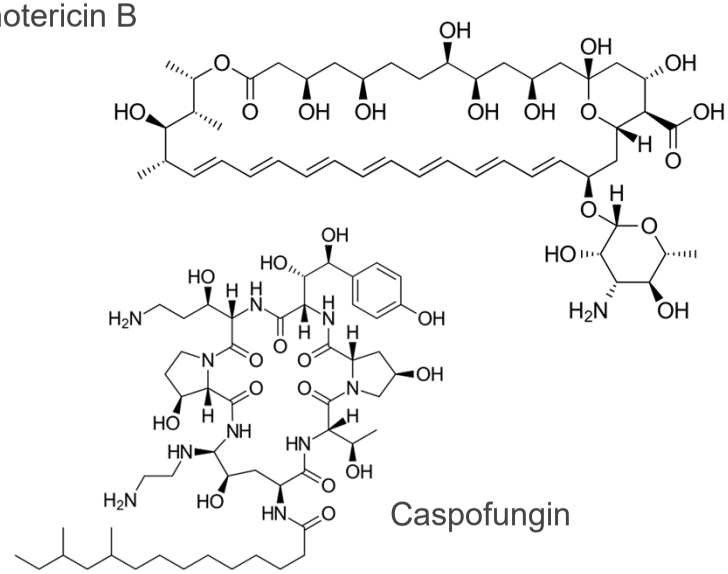

Caspofungin

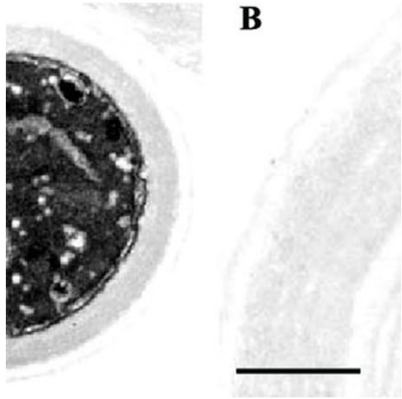

Differences in the cell wall architecture of melanin lacking and melanin producing Cryptococcus neoformans clinical isolates from India: An electron microscopic study - Scientific Figure on ResearchGate.

Acknowledgements

Lab PI:

- Karen Wozniak Ph.D.

Lab Members:

- Ben Nelson
- Savannah Beakley
- Brittney Conn
- Priscilla Chatman
- Ayesha Nair
- Jacob Lieberman
- Megan Roach
- Elyse Cronic

DEPARTMENT OF Microbiology & Molecular Genetics
COLLEGE OF ARTS AND SCIENCES

the Lew Wentz Foundation

Dr. & Mrs. Niblack

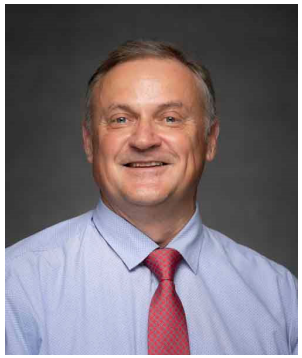

Dr. Nikolay Gerasimchuk and his lab at Missouri State University

Questions?

Compounds

$SbPh_4(ECO)$ → **Compound A**

$SbPh_4(MCO)$ → **Compound B**

$SbPh_4(TDCO)$ → **Compound C**

$SbPh_4(TCO)$ → **Compound D**

$SbPh_4(ACO)$ → **Compound E**

$SbMe_3(ECO)_2$ → **Compound F**

$SbMe_3(MCO)_2$ → **Compound G**

$SbMe_3(TDCO)_2$ → **Compound H**

$SbMe_3(TCO)_2$ → **Compound I**

$SbMe_3(2\text{-}ClPhCO)_2$ → **Compound J**

$SbMe_3(2,4\text{-}diClPhCO)_2$ → **Compound K**

$SbMe_3(2.6\text{-}diClPhCO)_2$ → **Compound L**

$SbPh_4Br$ → **Control 1**

$SbMe_3Br_2$ → **Control 2**

$H(ECO)$ → **Control 3A/3F**

$H(MCO)$ → **Control 3B/3G**

$H(TDCO)$ → **Control 3C/3H**

$H(TCO)$ → **Control 3D/3I**

$Na[H(ACO)_2]$ → **Control 3E**

$H(2\text{-}ClPhCO)$ → **Control 3J**

$H(2,4\text{-}diClPhCO)$ → **Control 3K**

$H_3(2.6\text{-}diClPhCO)$ → **Control 3L**

Regulation of the Type III Secretion System by PtsN in *Pseudomonas aeruginosa*

Mary Erdmann

Microbiology and Molecular Genetics
Faculty Sponsor: Dr. Matthew Cabeen
Graduate Student Mentor: Somalisa Pan

ABSTRACT

There are many virulence factors in *Pseudomonas aeruginosa* that contribute to this opportunistic pathogen's ability to evade the immune system and persist during drug therapy. Previous studies recognized the protein PtsN of the nitrogen-related phosphotransferase system (Nitro-PTS) as having a connection to virulence in *P. aeruginosa* by impacting biofilm levels through an unknown mechanism. Preliminary transcriptomic sequencing data identified that PtsN differentially regulates another virulence factor: the Type III Secretion System (T3SS). The T3SS is a needle-like protein structure embedded in the membrane of many Gram-negative, pathogenic bacteria. This protein complex gives bacteria the ability to inject effector proteins directly into host cells' cytoplasm, increasing the pathogen's ability to colonize the host. My research utilizes luciferase reporter strains to measure the activity of promoters of T3SS genes identified in transcriptome data. These experiments will observe the effect of PtsN on T3SS gene expression, help determine if PtsN is a novel regulator of T3SS in *P. aeruginosa* and develop a hypothesis for how PtsN interacts with the regulatory proteins that control the expression levels of the T3SS.

1. Introduction

Pseudomonas aeruginosa is an opportunistic pathogen that commonly causes nosocomial infections due to its antibiotic resistance, posing an ongoing medical threat. The *P. aeruginosa* strain studied here, PA14, is a highly virulent isolate that is frequently encountered in clinical settings (Mikkelsen, et al., 2011). Its virulence has been attributed to drug therapy resistance via virulence factors, including the production of biofilm—a self-secreted substance made of polysaccharides, DNA, and proteins that binds cells together, shielding colonies from their environment (Iglewski, 1996). Previous work identified PtsN, part of a phosphorelay called the Nitro-PTS, as a negative regulator of biofilm formation when PtsN is unphosphorylated (Cabeen, et al., 2016) (Lüttmann, et al., 2012). Wild-type (phosphorylated) PtsN displays high wrinkling (high biofilm production). In contrast, deleting an upstream kinase, PtsP, shows a smooth (low biofilm) morphology. Although PtsN shows striking phenotypic changes, few gene targets of PtsN regulation are known.

Because PtsN does not contain a DNA binding domain, it is hypothesized that PtsN imposes its effect on gene expression and protein function on a post-translational level or post-transcriptionally.

Transcriptomic sequencing was utilized to find genes differentially expressed when comparing the absence of PtsN (PA14Δ*ptsP*Δ*ptsN*) versus an unphosphorylated version of PtsN (PA14Δ*ptsP*). Again, the unphosphorylated PtsN background was utilized due to its ability to be a negative regulator of biofilm formation. Additionally, this comparison exposes the impact of deletion of PtsN versus in reference to an unphosphorylated PtsN background. Due to the previous studies which observed PtsN having an impact on biofilm, it was expected to see biofilm related genes in the transcriptomic data. However, transcriptomic data did not suggest any known biofilm genes to be differentially regulated when PtsN is not phosphorylated versus when it is absent. Instead, transcriptome sequencing analysis uncovered other virulence genes that were differentially regulated in the PA14Δ*ptsP*Δ*ptsN* versus PA14Δ*ptsP* comparison. Among these were genes constituting the Type III Secretion System (T3SS).

The T3SS is a virulence determinant of PA14 and other Gram-negative bacteria. The T3SS forms a needle complex that can inject, deliver proteins, and therefore manipulate host cells. The PA14 T3SS is under two levels of regulation: 1) signals which initiate T3SS endotoxin secretion and 2) gene transcription (Williams McMackin, 2019). The mechanism of the regulatory proteins of the T3SS is displayed by **Figure 1**. Gene transcription regulation is activated by a protein called ExsA. This protein is bound to an anti-activator called ExsD in a 1:1 complex. For ExsD to release ExsA, it will preferentially bind to ExsC which is in a 2:1 complex with a protein called ExsE. When environmental signals (such as low environmental Ca^{2+}) are sensed by the cell, ExsE disassociates from ExsC, allowing ExsD to preferentially bind to EsxC in a 2:2 complex (Williams McMackin, 2019). This releases ExsA to bind to the promoter of T3SS genes and activate transcription. Transcriptomic data showed that expression of *exsE*, *exsC*, and *exsD* is increased in PA14Δ*ptsP*Δ*ptsN* in the comparison to PA14Δ*ptsP*. Perhaps PtsN is interacting with one or more of these regulatory

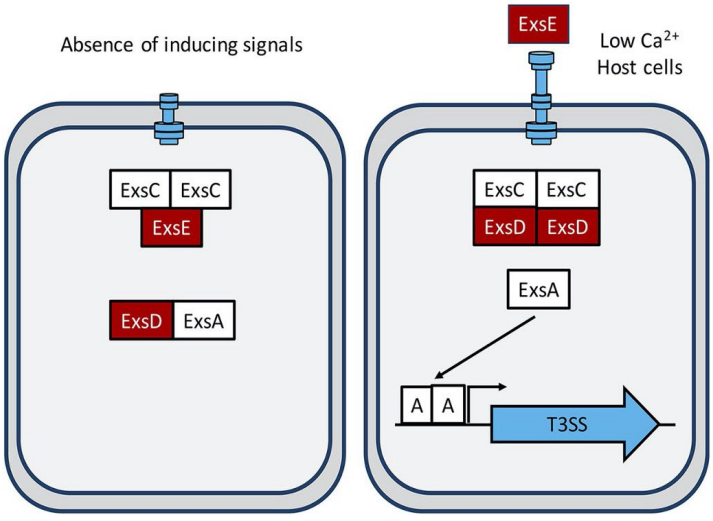

Figure 1: This image describing the regulatory protein mechanism of the T3SS is from the paper "Fitting Pieces into the Puzzle of *Pseudomonas aeruginosa* Type III Secretion System Gene Expression" by Williams McMackin, et.al. It shows ExsA as the T3SS activator, ExsD as the antiactivator, ExsC as the antiantiactivator, and ExsE as the secreted protein.

proteins to have an impact on T3SS expression. A sample of genes upregulated when PtsN is deleted is shown in Table 1.

Table 1: Sample of Upregulated Genes from the PA14Δ*ptsP*Δ*ptsN* versus PA14Δ*ptsP* Transcriptomic Data Analysis

GeneID	Product	P value	logFC	Product ID
PA14_RS17140	SctL family type III secretion system stator protein PscL	2.66E-17	2.472381088	WP_003087735.1
PA14_RS17145	type III secretion system sorting platform protein PscK	7.66E-24	3.200645447	WP_003087734.1
PA14_RS17150	SctJ family type III secretion inner membrane ring lipoprotein Psc	5.98E-27	2.602528845	WP_003120329.1
PA14_RS17155	SctI family type III secretion system inner rod subunit PscI	7.40E-22	2.547524495	WP_003120330.1
PA14_RS17160	YopR family T3SS polymerization control protein PscH	1.86E-29	3.045112514	WP_003100725.1
PA14_RS17165	YscG family type III secretion system chaperone PscG	2.22E-18	2.852697727	WP_003140037.1
PA14_RS17170	type III secretion system needle filament protein PscF	1.79E-17	2.08267887	WP_003087729.1
PA14_RS17175	YscE family type III secretion system co-chaperone PscE	4.16E-15	2.017600326	WP_003100751.1
PA14_RS17180	SctD family type III secretion system inner membrane ring subunit PscD	4.81E-25	2.766198974	WP_003132859.1
PA14_RS17185	SctC family type III secretion system outer membrane ring subunit PscC	3.62E-30	2.377287965	WP_003140040.1
PA14_RS17190	YscB family type III secretion system chaperone PscB	3.70E-21	2.506663586	WP_003109510.1
PA14_RS17255	type III secretion system chaperone PscY	2.28E-05	2.188767872	WP_003113547.1
PA14_RS17260	type III secretion system protein PscX	2.31E-19	3.907969927	WP_003140044.1
PA14_RS17280	SctN family type III secretion system ATPase PscN	6.91E-25	3.473114914	WP_003100796.1
PA14_RS17285	type III secretion system central stalk protein PscO	8.13E-13	2.90035456	WP_003140046.1
PA14_RS17295	SctQ family type III secretion system cytoplasmic ring protein PscQ	2.86E-35	3.76232678	WP_003140061.1
PA14_RS17300	SctR family type III secretion system export apparatus subunit PscR	7.22E-21	3.520844904	WP_003087674.1
PA14_RS17305	SctS family type III secretion system export apparatus subunit PscS	6.17E-13	2.972934615	WP_003087672.1
PA14_RS17310	SctT family type III secretion system export apparatus subunit PscT	5.71E-17	2.822693488	WP_003132884.1
PA14_RS00230	T3SS effector bifunctional cytotoxin exoenzyme T	2.90E-27	2.811925579	WP_003136948.1

Table 1: This list highlights the *pscN-T* operon genes that were upregulated when comparing the transcriptome data of PA14Δ*ptsP*Δ*ptsN* versus PA14Δ*ptsP.* The *pscN-T* operon was utilized to construct luminescent reporters to track T3SS gene expression. The *pscN-T* operon comprises genes that are part of the T3SS machinery.

2. Experimental Details

Transcriptome sequencing data was analyzed by sorting through genes in a PA14Δ*ptsP*Δ*ptsN* versus PA14Δ*ptsP* comparison which had a $\log_2$ fold change ($\log_2$ FC) value larger than ± 2.00. A $\log_2$ fold change of ± 2.00 is a good statistical value to identify genes whose differential expression is due to the deletion of PtsN. Among these candidates were genes responsible for the T3SS. Among these T3SS genes, we selected the *pscN-T* operon—which encodes parts of the secretion machinery—to drive a luminescent reporter for T3SS expression detection. The luminescent reporter is encoded on a CTX-1 plasmid. To create an insert for this plasmid, the first gene in the *pscN-T* operon was determined and the 200 nucleotides before this position was used for the insert. Using these nucleotides for the insert would ensure that the promoter for the *pscN-T* operon was present, since promoters tend to be within 100 bp upstream of the first gene in an operon.

Luciferase luminescence assays ran for 24 hours with continual shaking. Cultures were placed into the 96 well plate around an OD of approximately 0.1. Readings for luminescence and OD_{600} were read every 10 minutes. For each strain we performed 3 biological replicates and 3 technical replicates for each condition. LB with 25 μg/ml of tetracycline was the media used for the luminescence assays because our strains have the CTX-1 plasmid with a tetracycline resistant gene cassette and our luminescent reporter integrated into the genome. Our LB with 25 μg/ml of tetracycline media has a low Ca^{2+} concentration, which is a favorable environment for inducing the T3SS and provides cells with enough nutrients to have strong growth rates (Williams McMackin, 2019). A BioTek Synergy H1 Multi-Mode Microplate Reader was used to measure OD_{600} and luminescence.

Luminescent reporters (CTX-1-*pscN-T-lux*) were constructed and put into *E. coli* strain SM10 for mating with PA14 strains. The following strains were made: PA14 *attB*::*CTX-1-pscN-T-lux*, PA14Δ*ptsP attB*::*CTX-1-pscN-T-lux*, PA14Δ*ptsN attB*::*CTX-1-pscN-T-lux*, and PA14Δ*ptsP*Δ*ptsN attB*::*CTX-1-pscN-T-lux*. A luminescence assay was conducted with these strains to confirm the transcriptomic data.

Deletions of *exsC* and *exsE* were made to create a strain with a constitutively off and a strain with a constitutively on T3SS, respectively. Luminescence assays were conducted with the PA14 PscN-T-lux, PA14Δ*ptsP attB*::*CTX-1-pscN-T-lux*, PA14Δ*ptsN attB*::*CTX-1-pscN-T-lux*, PA14Δ*ptsP*Δ*ptsN attB*::*CTX-1-pscN-T-lux*, PA14Δ*exsC attB*::*CTX-1-pscN-T-lux*, PA14Δ*exsE attB*::*CTX-1-pscN-T-lux*, PA14Δ*ptsN*Δ*exsC attB*::*CTX-1-pscN-T-lux*, and PA14Δ*ptsN*Δ*exsE attB*::*CTX-1-pscN-T-lux*.

3. Results

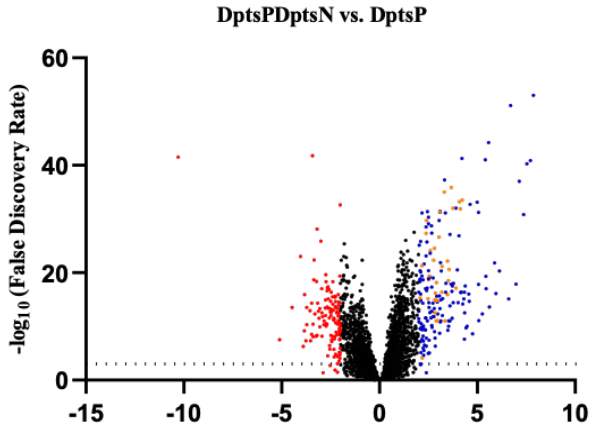

Figure 2: This volcano plot visualizes the genes upregulated and down regulated when comparing a *ptsN* deletion to an unphosphorylated PtsN form. Genes with a log fold change (logFC) value larger than ± 2.00 were considered differentially regulated.
Blue dots are upregulated by PtsN deletion, red dots are downregulated by PtsN deletion, and the orange dots are the genes of the T3SS. The black dots are genes that are not differentially regulated.

To discover genes that PtsN differentially regulates in its absence and presence and in its phosphorylated and nonphosphorylated states, transcriptomic sequencing data in the PA14 Δ*ptsP*Δ*ptsN* versus PA14 Δ*ptsP* comparison was analyzed. **Figure 2** is a volcano plot which displays genes that were upregulated and downegulated. These data suggest that the deletion of *ptsN* increases the expression of the T3SS genes, indicating that PstN might impact T3SS regulation as a repressor. To continue investigating how PtsN is differentially regulating these genes, we used luminescence reporters.

Initial luminescence assays were conducted to validate transcriptome sequencing data that suggested PtsN could be a regulator of T3SS genes. A luminescence reporter for the *pscN-T* operon—which codes for T3SS machinery—was constructed and mated with PA14, PA14Δ*ptsP*, PA14Δ*ptsN*, and PA14Δ*ptsP*Δ*ptsN*. To test the hypothesis that PtsN is a novel regulator of the T3SS, we measured T3SS expression in the presence and absence of PstN and when PtsN is phosphorylated versus unphosphorylated.

The data in **Figure 3** distinctly shows how the deletion of *ptsN* causes a significant increase in T3SS expression in comparison to the WT and the unphosphorylated-PtsN strain (PA14Δ*ptsP*). PtsN increases the maximum promoter signal activity by a factor of approximately 4. This observation confirms the transcriptome data we collected and further supports our hypothesis that PtsN can act as a repressor of the T3SS.

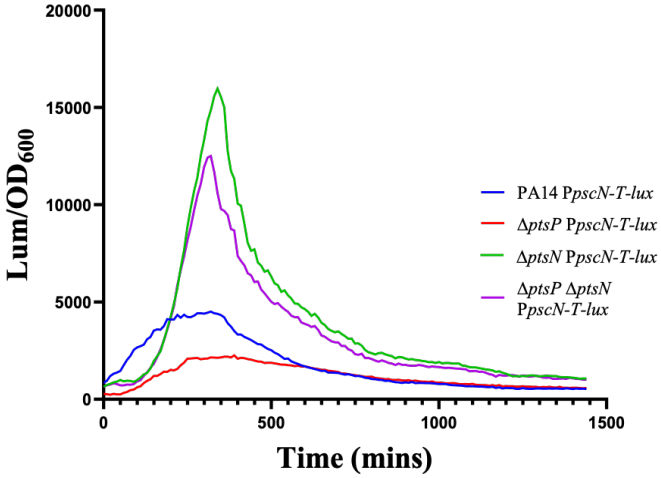

Figure 3: Luciferase assay displays the effect of *ptsN* deletion on the expression level on the T3SS operon PscN-T. We normalize the Luminescence data with OD to ensure that the data we see is not due to one strain having more cells than the other, but due to the level of T3SS expression.

To further understand how PtsN is impacting T3SS regulation, we wanted to observe PtsN's effect in the absence of known T3SS regulators. Figure 4 shows that when PstN is deleted in a ΔexsC background (when the system is constitutively inactive) there is no substantial change in expression. This indicates that deletion of ptsN does not recover T3SS expression when ExsC is absent and T3SS is inactive. Because PtsN is known to increase T3SS, it is surprising that PtsN would not be able to recover an inactive T3SS due to a deletion of exsC.

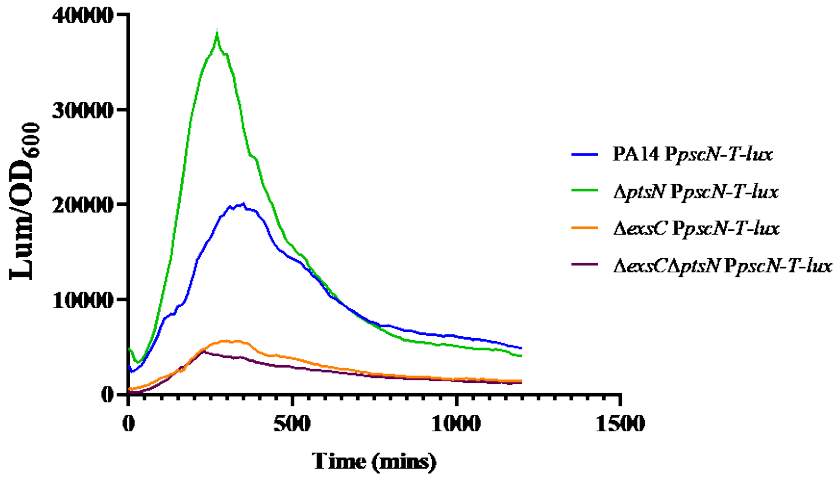

Figure 4: Luciferase assay for the effect of a *ptsN* deletion when the T3SS is constitutively inactive (due to a deletion of *exsC).*

It is possible that ExsC must be present for PtsN to have its effect, but this hypothesis cannot be determined with the current collection of data. Details of future studies to further examine this observation are discussed later in this paper. This observation piqued our

interest for examining the effect of PtsN on a constitutively active T3SS and if it will show no significant impact on expression, as in **Figure 4** with the constitutively off system.

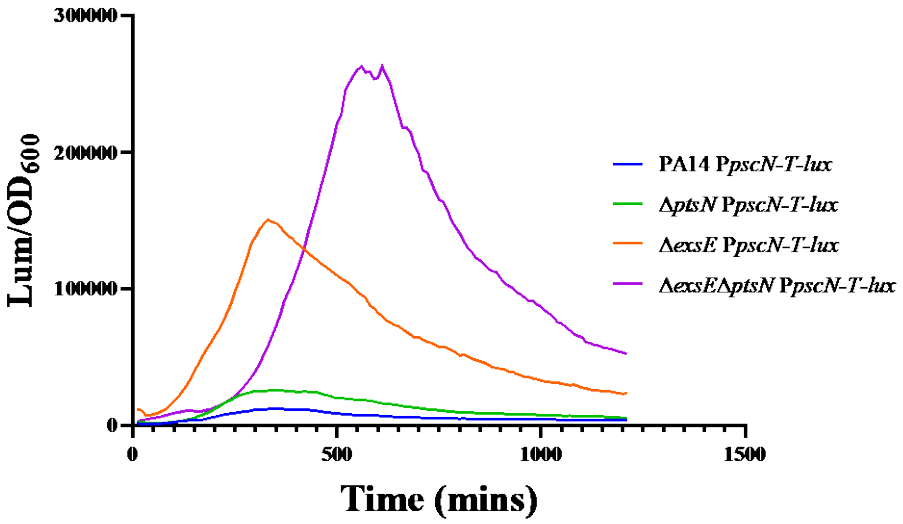

Figure 5: Luciferase assay shows the impact of a *ptsN* deletion when the T3SS is constitutively active due to deletion of *exsE.*

Figure 5 implies that deletion of *pstN* in a Δ*exsE* background (when the T3SS is constitutively active) causes the T3SS to be even more highly expressed. It is also seen that the Δ*exsE* and Δ*exsE*Δ*ptsN* strain have significantly higher expression levels than previously seen with the Δ*ptsN* strain. The delayed curve of the Δ*exsE*Δ*ptsN* strain is reproducible because the Δ*exsE*Δ*ptsN* strain is a slow grower.

4. Discussion and Conclusion

Initially, luciferase assays seen in **Figure 3** determined that the deletion of *ptsN* causes an increase in T3SS expression. Before the results reported here, PtsN was not known to impact regulation of T3SS genes. Furthermore, constitutively inactive (Δ*exsC*) and active (Δ*exsE*) T3SS systems were created to determine whether deleting *ptsN* continued to have an effect when the T3SS is "turned off" and "turned on." In other words, can PtsN expression recover an "off" system or further amplify expression in an active system? Deletion of *ptsN* could not recover a constitutively inactive T3SS (Δ*exsC*). However, a *ptsN* deletion in a constitutively active T3SS strain caused expression beyond the intrinsic limits of the T3SS. The intrinsic limit of the T3SS is seen by creating a system that is constitutively active in the wild-type presence of PtsN (deletion of *exsE*). The deletion of *ptsN* can bring T3SS expression to levels that are even higher than a wild-type condition expression limit. It is possible that there is no effect on T3SS expression when *ptsN* is deleted in a Δ*exsC* background because the protein that PtsN is interacting with is absent (ExsC). The phosphorylated PtsN form could be lowering the affinity of ExsC for ExsD, keeping ExsD bound to ExsA, or PtsN could play a

role in keeping ExsE bound to ExsC until the cell receives signaling for T3SS gene expression.

Future studies that delete *exsD* will provide more understanding on the intrinsic expression limits of the T3SS (ensuring that the *exsE* deletion is showing the maximum intrinsic expression for T3SS) and on which regulatory proteins PtsN is interacting with. Based on our current data, it is possible that PtsN could be interacting with ExsC, ExsD or ExsA to impact T3SS expression levels.

Future studies should aim to discover which T3SS regulatory protein has an interaction with PtsN. This can be deduced from further luciferase assays with an *exsD* and *exsA* deletions, which provide different versions of an active and inactive T3SS – deleting *exsD* would create an active system while deleting *exsA* would inactivate the system. Seeing the impact on expression when deleting *ptsN* in these strains with the presence of ExsC and ExsE will provide more evidence to suggest a regulatory protein that PtsN is regulating. Interaction studies such as co-immunoprecipitation or fluorescence resonance energy transfer can be performed to see if PtsN is directly interacting with T3SS regulatory proteins on a post-translational level. Additionally, PtsN could be impacting the activity of these regulatory proteins via phosphorylation. Therefore, western blotting could visualize phosphorylation states of T3SS regulatory proteins in the absence and presence of PtsN. If a protein sample is phosphorylated, the protein band will "shift up," or have a higher band location on the gel, than an unphosphorylated control protein.

Additionally, since deletion of *ptsN* increases T3SS expression, thus identifying PtsN as a negative regulator of T3SS expression, future experiments can test the expectation that overexpressing *ptsN* will lower T3SS expression levels. To that end, an SM10 strain with pJN105-*ptsN*, a plasmid containing an arabinose-inducible promoter that will express *ptsN*, can be constructed and mated with experimental strains: PA14 *attB*::*CTX-1-pscN-T-lux*, PA14Δ*ptsN attB*::*CTX-1-pscN-T-lux*, PA14Δ*exsE attB*::*CTX-1-pscN-T-lux*, and PA14Δ*ptsN*Δ*exsE attB*::*CTX-1-pscN-T-lux*. The PA14Δ*exsC attB*::*CTX-1-pscN-T-lux* and PA14Δ*ptsN*Δ*exsC attB*::*CTX-1-pscN-T-lux* strains would not be used because it is expected that *ptsN* overexpression will drive down T3SS expression, and these strains already show minimal T3SS expression so overexpression of *ptsN* would likely have little effect. These overexpression experiments will further clarify how PtsN is regulating the T3SS.

5. Summary

This study aimed to investigate the ability of PtsN to impact T3SS expression levels. Initial data suggests that PtsN is a repressor of the T3SS system, meaning its presence suppresses T3SS gene expression and its absence allows the T3SS to increase expression levels. Future studies, as proposed in this paper, will clarify exactly how PtsN is impacting

T3SS expression, furthering our knowledge of PA14 and its key virulence factors that allow this bacterium to have a substantial reputation amongst opportunistic pathogens.

6. Appendices

6a. Acknowledgements

Thank you, Mr. and Mrs. Niblack, for giving me the opportunity to develop and test my own research proposal. Thank you, Dr. Cabeen, for letting me join your lab four years ago and allowing me to be a part of the Cabeen lab. Somalisa Pan, thank you for being with me every step of the way on my research journey and teaching me how to be a researcher. To all the members of the Cabeen lab, thank you for the constant support you showed me throughout my entire undergraduate career.

6b. Papers Published

Papers:

PtsN in Pseudomonas aeruginosa Is Phosphorylated by Redundant Upstream Proteins and Impacts Virulence-Related Genes. *Journal of bacteriology*, e0045322. Underhill, S. A. M., Pan, S., Erdmann, M., & Cabeen, M. T. (2023).

Presentations:

American Society of Microbiology Regional Meeting, March 2022

Oklahoma Research Day, March 2022

Oklahoma Research Day, March 2022

6c. Literature Cited

Cabeen, M. T., Leiman, S. A., & Losick, R., 2016, Colony-morphology screening uncovers a role for the Pseudomonas aeruginosa nitrogen-related phosphotransferase system in biofilm formation. Molecular microbiology, 99(3), 557–570.

Hauser A. R., 2009, The type III secretion system of Pseudomonas aeruginosa: infection by injection. Nature reviews. Microbiology, 7(9), 654–665.

Iglewski, B. H., 1996, Pseudomonas. In S. Baron (Ed.), Medical Microbiology. (4th ed.). University of Texas Medical Branch at Galveston.

Lüttmann, D., Göpel, Y., & Görke, B., 2012, The phosphotransferase protein EIIA(Ntr) modulates the phosphate starvation response through interaction with histidine kinase PhoR in Escherichia coli. Molecular microbiology, 86(1), 96–110.

Mikkelsen, H., McMullan, R., & Filloux, A., 2011, The Pseudomonas aeruginosa reference strain PA14 displays increased virulence due to a mutation in ladS. *PloS one*, *6*(12), e29113.

Williams McMackin, E. A., Djapgne, L., Corley, J. M., & Yahr, T. L., 2019, Fitting Pieces into the Puzzle of *Pseudomonas aeruginosa* Type III Secretion System Gene Expression. *Journal of bacteriology*, *201*(13), e00209-19.

Regulation of the Type III Secretion System by PtsN in *Pseudomonas aeruginosa*

MARY ERDMANN
DR. CABEEN & SOMALISA PAN

PSEUDOMONAS AERUGINOSA (PA14)

- Gram-negative, rod-shaped bacteria
- Multi-drug resistance
- Common in nosocomial infections
- Nitro-Pts system in PA14 shown to impact virulence factors in previous studies.

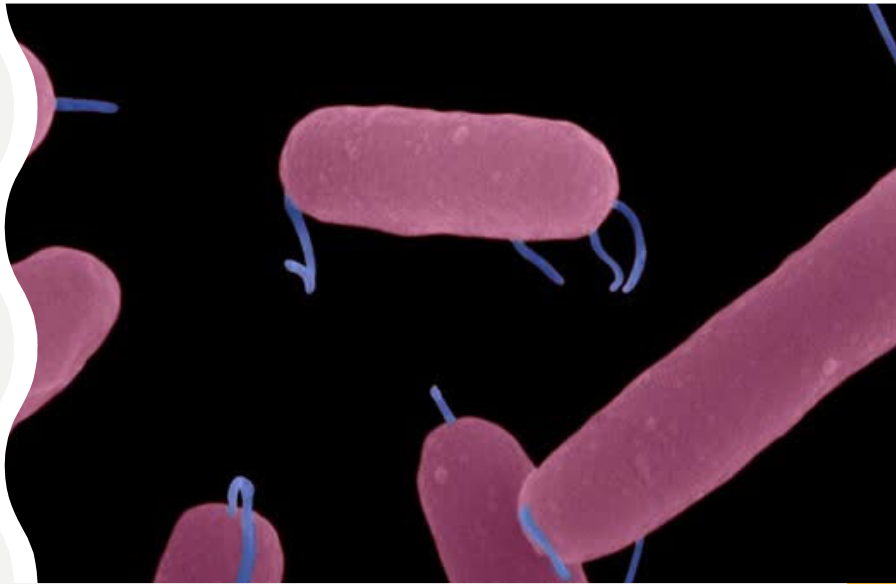

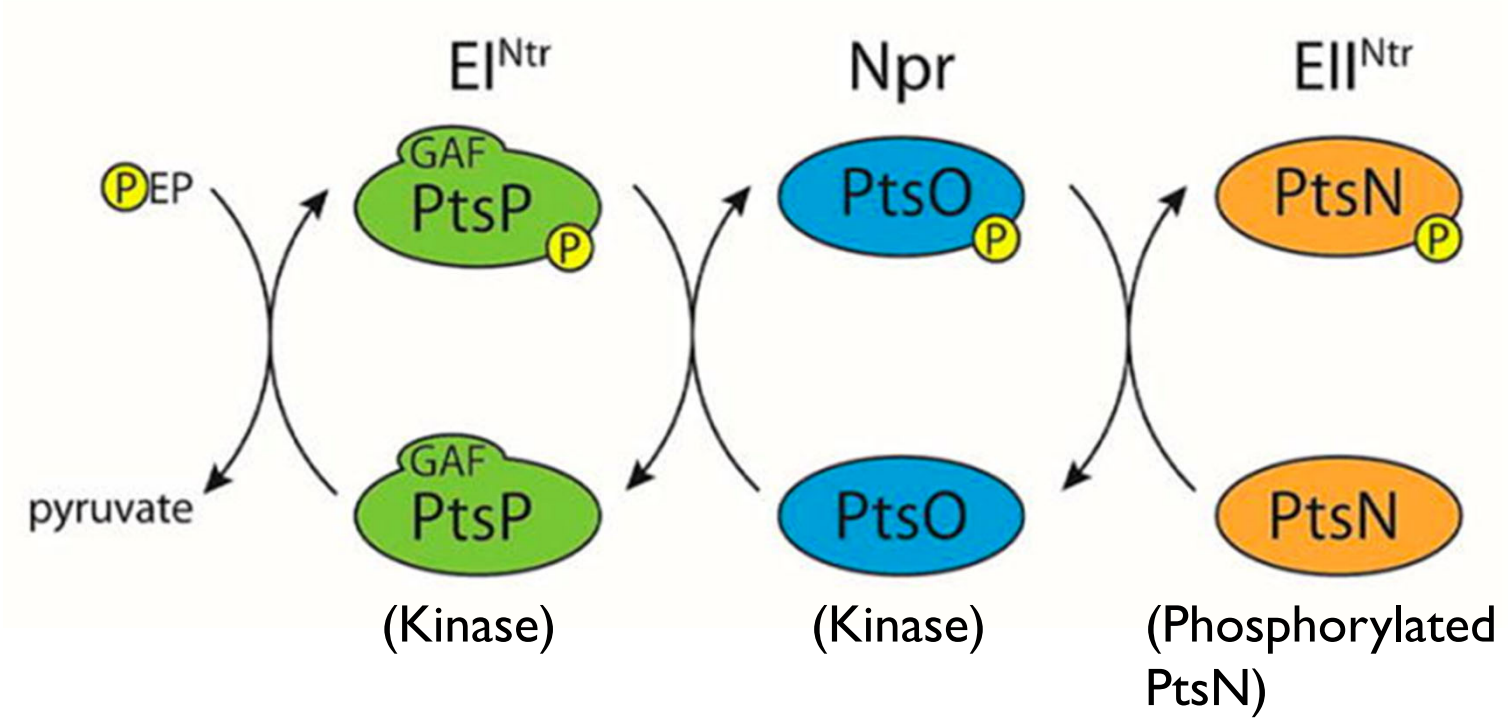

WHAT IS THE NITRO-PTS SYSTEM?

WHAT VIRULENCE-RELATED GENES DOES THE NITRO-PTS SYSTEM INFLUENCE?

RNA SEQUENCING DATA & DIFFERENTIAL GENE REGULATION

- Compared ΔPtsp ΔPtsN versus ΔPtsP
  - Shows genes differentially regulated by presence of unphosphorylated PtsN and absence of PtsN
- Among others virulence factors … T3SS genes are differentially regulated

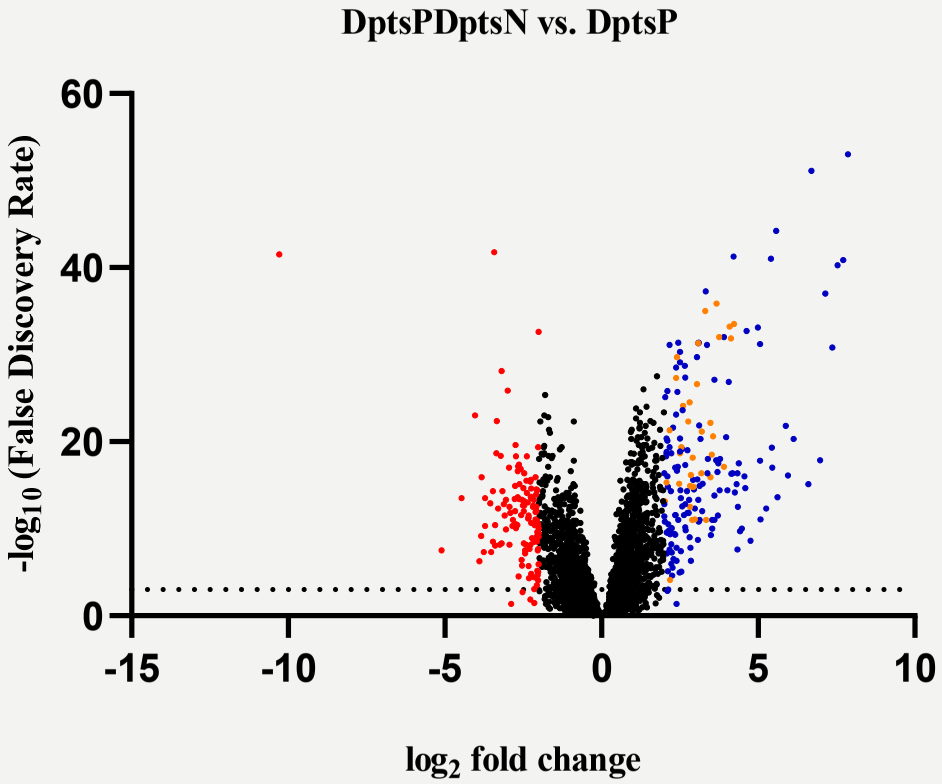

WHAT IS THE T3SS?

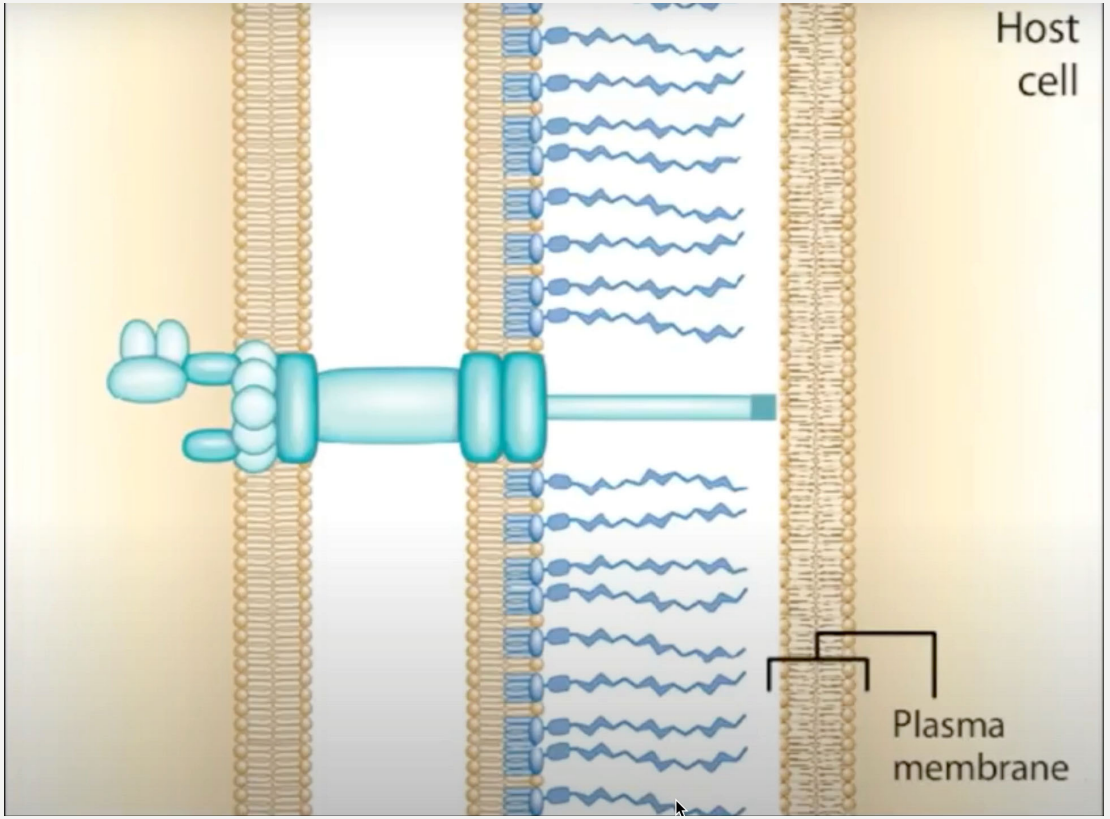

HOW IS PTSN AFFECTING T3SS EXPRESSION?

LUCIFERASE ASSAYS TRACK T3SS EXPRESSION

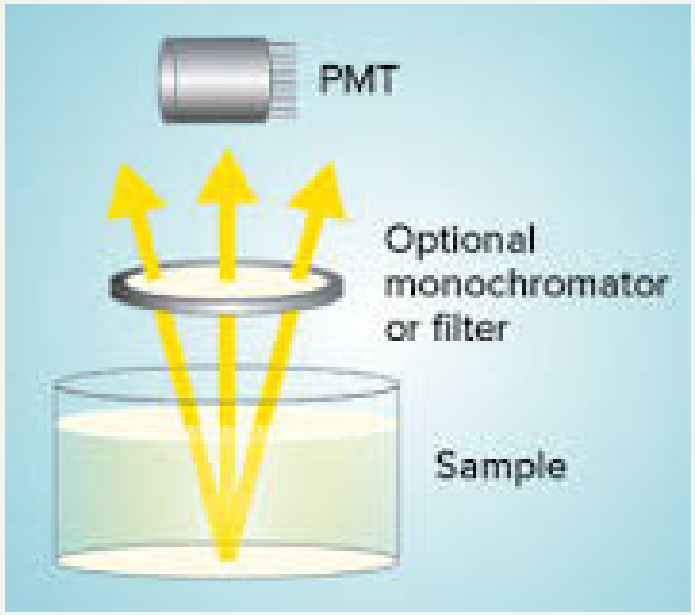

- Luminescence reporter strains made by encoding luminescent protein downstream of the promoter of the operon of interest.
- PscN-T encodes T3SS machinery
- When the PscN-T operon is expressed, the luminescent protein is expressed as well.
- Use a machine to read intensity of light given off from sample to quantify T3SS expression levels.

INITIAL LUCIFERASE ASSAY & CONFIRMING RNA SEQ DATA

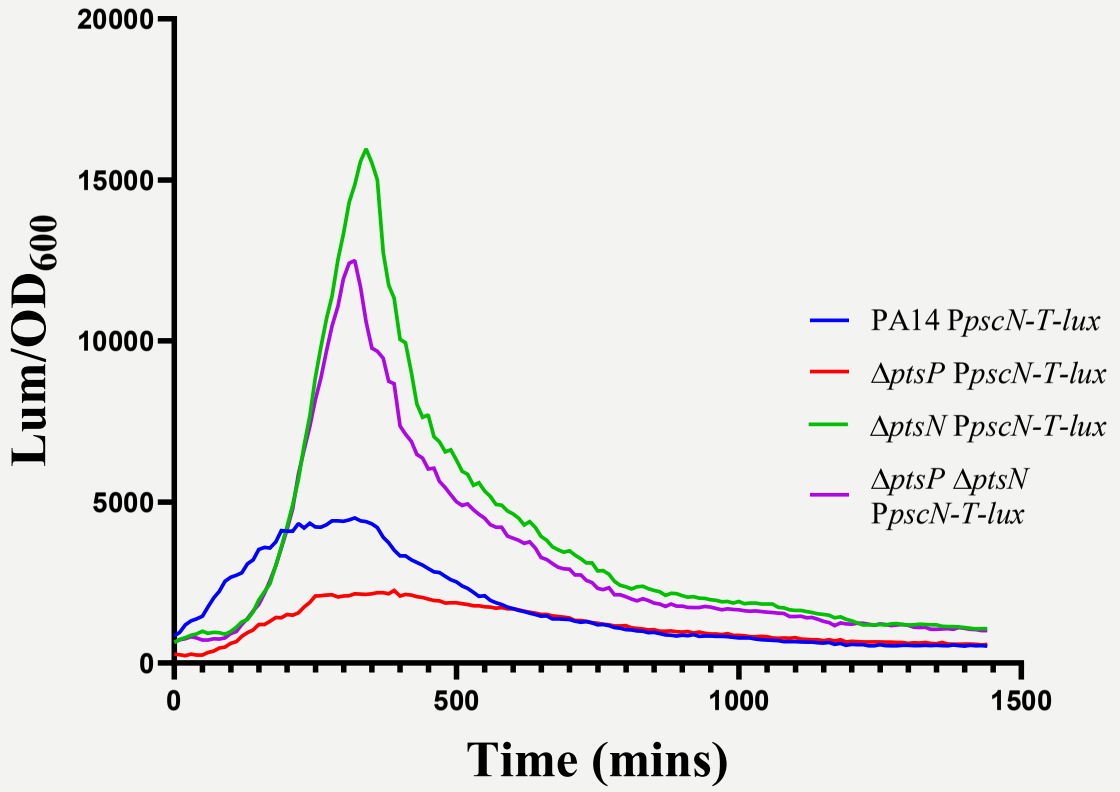

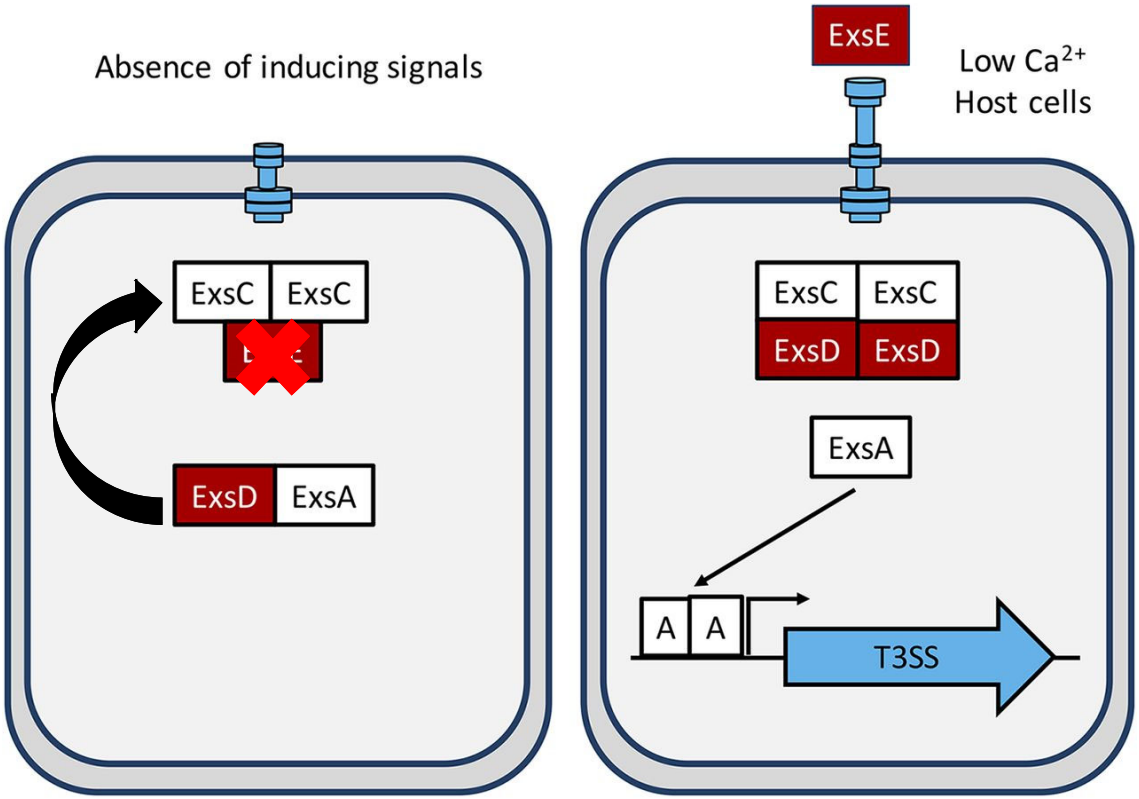

T3SS ACTIVATION MECHANISM

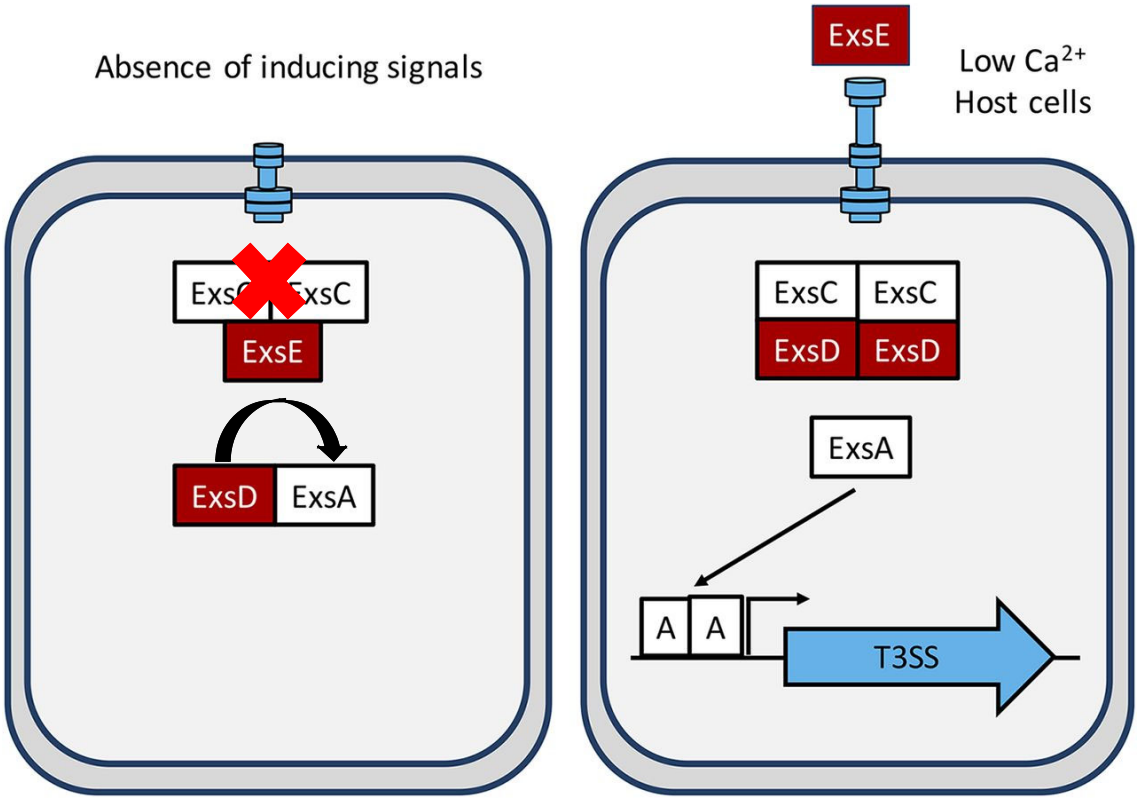

T3SS ACTIVATION MECHANISM

T3SS ACTIVATION MECHANISM

ΔExsC = OFF
ΔExsE = ON

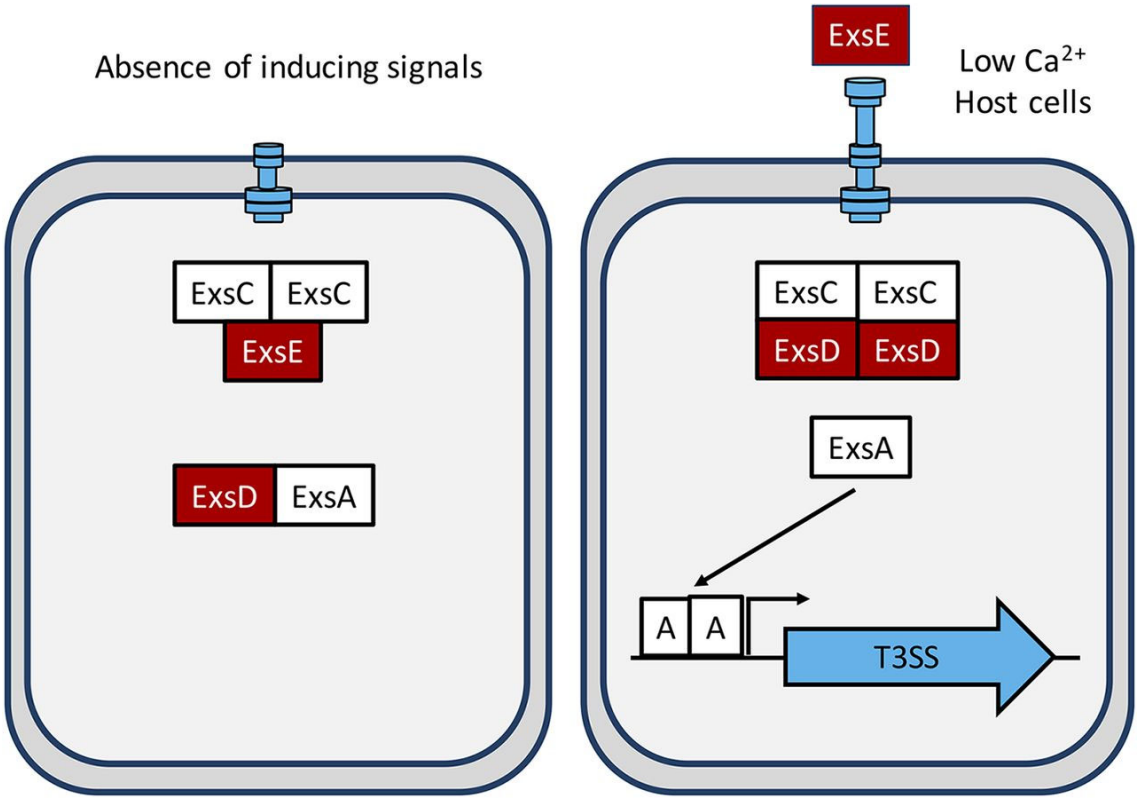

CAN A PTSN DELETION (PREVIOUSLY SHOWN TO INCREASE T3SS EXPRESSION) RECOVER EXPRESSION OF A ΔEXSC (OFF) T3SS?

ΔPTSN DOES NOT RECOVER ΔEXSC T3SS ACTIVITY

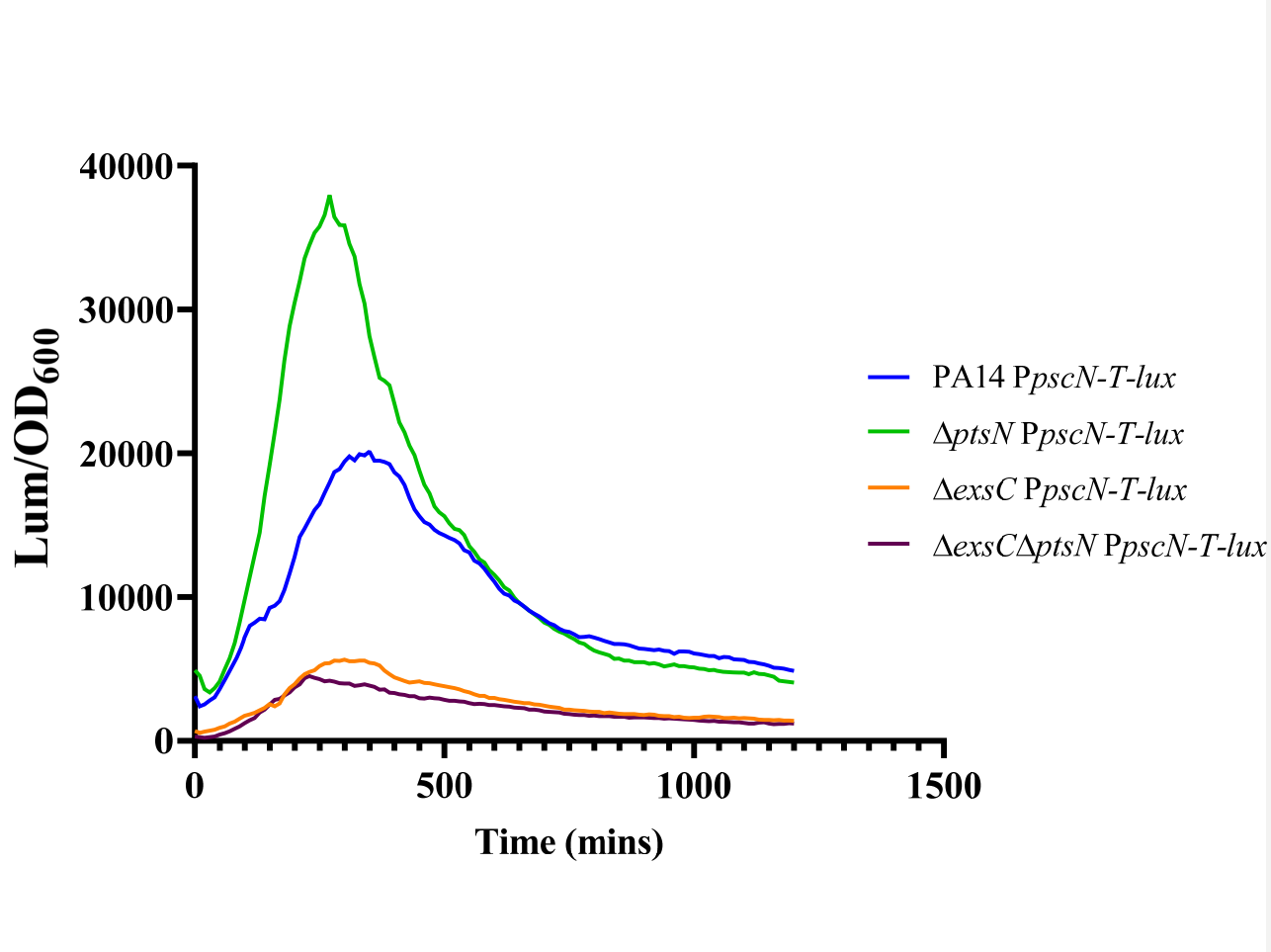

CAN A PTSN DELETION FURTHER AMPLIFY EXPRESSION OF A ΔEXSE (ON) T3SS?

ΔPTSN AMPLIFIES ΔEXSE EXPRESSION

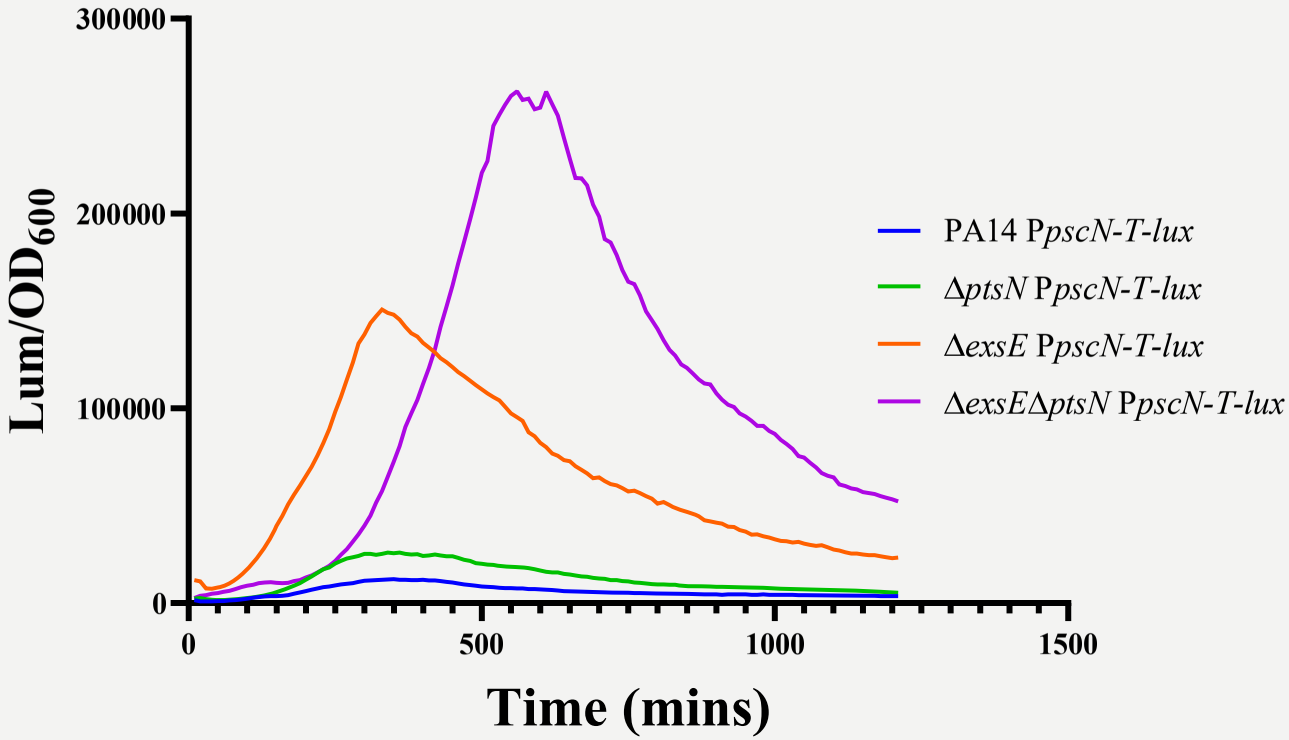

FUTURE RESEARCH

- Overexpressing PtsN to observe if PtsN overexpression will drive down the T3SS.
- Deleting ExsD to see if this causes higher T3SS expression than the ExsE mutant and if expression changes in the absence of PtsN (perhaps Δ*exsE* did not reach full potential of T3SS expression and there was some ExsA still bound to anti-activator ExsD?)
  - If there is no change between Δ*exsD* and Δ*exsD* Δ*ptsN* T3SS expression, then PtsN is most likely interacting with ExsD, ExsC, or ExsE.
    - With no change seen in a Δ*exsC* background and a significant change of expression in the Δ*exsE* background, could PtsN impact the ExsC-ExsD interaction?
  - If there is a change in T3SS expression between Δ*esxD* and Δ*exsD* Δ*ptsN* then PtsN is most likely interacting with ExsA.
    - Follow up with coimmunoprecipitation assays.

ACKNOWLEDGEMENTS:

Thank you, Somalisa for all your support and guidance!

Thank you, Dr. Cabeen for being a great mentor and inviting me be a part of the Cabeen Crew!

Thank you, Dr. Niblack for giving me this incredible research and academic opportunity.

SESSION TWO:

Charlie Vermeire

"*Mycobacterium abscessus* Infection Upregulates Exosome Biogenesis in Macrophages and Induces Proinflammatory Responses to Mycobacterial Infection *in vitro*"
Research Area: Biochemistry and Molecular Biology
Faculty Sponsor: Dr. Yong Cheng
Graduate Student Mentor: Stephen Kotey

Natalee Richardson

"*in vivo* Assay: Bacterial Small RNAs May Regulate Eukaryotic Gene Expression"
Research Area: Animal and Food Sciences
Faculty Sponsor: Dr. Darren Hagen
Graduate Student Mentor: Anna Goldkamp

Mycobacterium abscessus Infection Upregulates Exosome Biogenesis in Macrophages and Induces Proinflammatory Responses to Mycobacterial Infection *in vitro*

Charlie Vermeire

Biochemistry and Molecular Biology
Faculty Sponsor: Dr. Yong Cheng
Graduate Student Mentor: Stephen K. Kotey

ABSTRACT

Recent studies suggest that exosomes released by infected host cells induce inflammatory responses to intracellular pathogens in recipient cells (Cheng & Schorey, 2013; Schorey et al., 2015; Cheng & Schorey, 2019; Cheng et al., 2020). Further investigation into the mechanisms by which these exosomes modulate host immune function may promote the development of more effective treatments for intracellular infections, such as those caused by *Mycobacterium abscessus* (*M.abscessus*), a non-tuberculous Mycobacterium frequently identified in the lungs of cystic fibrosis patients with respiratory infections (Cheng et al., 2020). To determine the role of *M.abscessus*-infected-macrophage-released exosomes on host immune responses, we prepared exosomes from macrophage cell culture *in vitro*, then analyzed the vesicles using biochemical and immunological tools. Exosomes from uninfected and *M.abscessus*-infected macrophages were characterized using nanoparticle tracking analysis and electron microscopy. Bacterial survival assays and qRT-PCR were employed to assess the impact of macrophage-derived exosomes on mycobacterial killing and macrophage polarization in recipient cells. To further elucidate the mechanisms of vesicle function, mass spectrometry and protein pathway analysis were performed. We observed that *M.abscessus* infection did not affect exosome size or morphology, but did increase exosome yield. Furthermore, both uninfected and *M.abscessus*-infected macrophage-released exosomes promoted mycobacterial killing by stimulating proinflammatory pathways in recipient macrophages. In whole, our data indicate that *M.abscessus* infection induces host immune responses to mycobacterial infection by inducing exosome biogenesis.

1. Introduction

Non-tuberculous Mycobacteria (NTM) are a group of opportunistic pathogens that are commonly identified in water and soil (Gardner et al., 2019). Although environmental exposure to NTM rarely causes infection in healthy individuals, exposure to NTM often results in serious respiratory infections in immunodeficient patients (Cheng et al., 2020). Individuals living with cystic fibrosis (CF), a genetic disorder that inhibits lung function, are particularly vulnerable to NTM infections (Cheng et al., 2020; Shteinberg et al., 2021). The NTM

Mycobacterium abscessus (*M.abscessus*), for instance, is frequently identified in the lungs of CF patients and has been linked to a marked decline in the lung function of infected individuals (Esther et al., 2010; Gardner et al., 2019).

Unfortunately, treatment of such infections is difficult and extended courses of several antibiotics are often required (Gardner et al., 2019). The treatment of NTM infections is complicated not only by the expanding antibiotic tolerance of NTM, but also by the ability of NTM to reside within alveolar macrophages, a survival mechanism that promotes immune system evasion (Schorey et al., 2015). Though the host immune response may follow several avenues of defense against invading pathogens, including the production of proinflammatory cytokines, phagocytosis by non-specific leukocytes, and activation of adaptive immune cells, all require host immune cell access to components of invading pathogens (Schorey et al., 2015; Cheng & Schorey, 2020). Antigens of extracellular pathogens are readily available to host immune cells during infection, but those of intracellular NTM are not so easily accessed (Cheng & Schorey, 2020).

To compensate, recent studies suggest intracellular pathogenic material is delivered to immune cells via the formation and release of extracellular vesicles (EVs), such as exosomes, by infected host cells (Cheng & Schorey, 2019). These membrane-enclosed packages contain mycobacterial cell wall antigens, RNAs, proteins, and lipids and appear to modulate host immune responses (Schorey et al., 2015). Notably, exosomes released by *Mycobacterium tuberculosis*-infected macrophages have been shown to illicit cytokine production in non-infected recipient cells, and macrophages infected by *Mycobacterium avium* (*M.avuim*) have been observed to release exosomes containing *M.avium* components that promote pro-inflammatory responses in naïve macrophages (Bhatnagar & Schorey, 2007; Cheng & Schorey, 2019). Understanding these interactions may promote the development of more effective treatments for NTM infections, but the mechanism by which macrophage-released exosomes modulate the host-pathogen interactions of mycobacterial infections currently remains unclear.

In the current study, we examined the functional role of exosomes released from *M.abscessus*-infected macrophages in *M.abscessus*-host interactions and explored the mechanisms of these functions using an *in vitro* mouse macrophage cell culture model. Our results suggest that *M.abscessus* infection induces host immune responses to mycobacterial infection by stimulating the production of proinflammatory exosomes by infected macrophages.

2. Materials and Methods

Mammalian Cell Culture. RAW 264.7 ATCC TIB-71 macrophages were cultured at 37ºC and 5% CO_2 in Dulbecco's Modified Eagle Medium (DMEM) (Cat. No. SH30243.01; HyClone) supplemented with 10% (v/v) fetal bovine serum (Cheng & Schorey, 2019).

Streptomycin and penicillin were added at 100 U/mL to uninfected cultures (Cat. No. SV30010; HyClone) (Cheng & Schorey, 2019).

Bacterial Culture. *M.abscessus* ATCC 19977 was cultured to mid-log phase in Middlebrook 7H9 broth (Cat. No. M198; HiMedia Laboratories) supplemented with 10% (v/v) OADC (oleic acid-albumin-dextrose-catalase, 0.05% Tween 80) and 0.2% glycerol at 37ºC and 5% CO_2, as done previously (Sullivan et al., 2021; Cheng et al., 2020; Cheng & Schorey, 2013). Before use, culture was passed through a 27-gauge syringe a minimum of 10 times.

Exosome Isolation and NanoSight Analysis. RAW 264.7 macrophages were cultured in exosome-free DMEM. The macrophages were uninfected or infected with *M.abscessus* at a multiplicity of infection (MOI) of 5 for 4 hours, then washed three times with pre-warmed 1x PBS and incubated for 72 hours at 37ºC and 5% CO_2. Culture supernatant was harvested following low speed centrifugation at 10,000 x g and 4ºC, then passed through a 0.2 μm filter unit (Cat. No. FB12566506; Fisher Scientific) to remove cell debris. EVs were isolated from the filtered supernatant via ultracentrifugation at 100,000 x g and 4ºC for 3 hours, as we did previously, then washed three times at 100,000 x g and 4ºC and resuspended in 0.5 mL 1x PBS (Cheng & Schorey, 2019). The isolated EVs were subjected to immunoaffinity chromatography using an Exosome Isolation Kit (Cat. No. 130-117-039; Miltenyi Biotec) according to manufacturer instruction to separate macrophage-derived exosomes from *M. abscessus*-derived EVs and other nanoscale particles. Exosome concentrations and protein loads were then determined for each sample by Pierce Micro BCA assay (Cat. No. 23227; ThermoFischer Scientific) and NanoSight NS300 (Malvern Panalytical, UK) nanoparticle analysis. Samples were stored at -80 ºC.

Transmission Electron Microscopy (TEM) Analysis. To examine vesicle morphology, exosomes were viewed via electron microscopy. Samples were placed on carbon-film TEM grids (Electron Microscopy Sciences, Hatfield, PA, USA) for 1 minute. Excess liquid was blotted away with filter paper and the sample on the grid was stained with a drop of 2.5% uranyl acetate for 45 seconds. Excess stain was blotted away, and the samples were imaged using a transmission electron microscope (JEOL Ltd., Akishima, Tokyo, Japan) at the Oklahoma State University microscopy core facility.

Survival Assay of *M.abscessus* in RAW 264.7 Macrophages. RAW 264.7 macrophages were treated with purified exosomes *in vitro* at 100 exosomes/cell for 24 hours, then infected with *M.abscessus* at an MOI of 5 for 1 hour at 37ºC and 5% CO_2 (Cheng & Schorey, 2019). After infection, macrophages were washed three times with pre-chilled 1x PBS to remove remaining extracellular *M.abscessus*, incubated for 1 and 24 hours at 37ºC and 5% CO_2, washed 3 times with cold 1x PBS, and lysed with 0.05% SDS (Cheng & Schorey, 2019). Cell lysates were serially diluted in 1x PBS and plated on Middlebrook 7H10 agar plates (Cat. No. 61000-050; HiMedia) supplemented with 10% (v/v) OADC and 0.2% glycerol. Resulting *M.abscessus* colonies were then counted after 3-5 days of incubation at 37ºC and 5% CO_2 to

assess the impact of macrophage-derived exosomes on mycobacterial survival within recipient macrophages.

qRT-PCR. To assess the effect of *M.abscessus*-infected macrophage-released exosomes on macrophage polarization, the expression of TNFα, IL6, IL10, and Arg1 were measured in exosome-treated RAW 264.7 macrophages (Bardi et al., 2018). Cells were treated with exosomes *in vitro* at 100 exosomes/cell for 24 hours, then total RNA was isolated using a Monarch's Total RNA Miniprep Kit (T20105; New England Biolabs) according to manufacturer instruction. RNA integrity was confirmed via gel electrophoresis, and cDNA was synthesized using AMV reverse transcriptase (Cat. No. B0277A; New England Biolabs) (Cheng & Schorey, 2019). qRT-PCR was then conducted on the Roche LightCycler 480 real-time PCR system (Qiagen) using luna universal master mix (Cat. No. M3003E; New England Biolabs) and the forward and reverse primers for TNFα, IL6, IL10, Arg1, and GAPDH (control).

Proteomic Analysis of RAW 264.7 Exosomes. The protein profiles of purified exosomes were determined via mass spectrometry in collaboration with the Oklahoma State University genomics and proteomics core facility. Raw data were analyzed using Perseus (version 2.0.7.0) to determine differentially regulated proteins. Protein pathway analysis was then conducted to elucidate the biological functions of the differentially regulated proteins using Metascape custom analysis-*Mus musculus* GO: biological processes (Zhou et al., 2019).

Statistical Analysis. Data were analyzed via Student's paired t-tests, and $p \leq 0.05$ was considered significant. Analyses were conducted with Excel (but will be repeated with GraphPad prior to publication).

3. Results

***M.abscessus* infection induces exosome biogenesis in murine macrophages.** To assess the role of mycobacterial infection on exosome biogenesis in macrophages, exosomes isolated from uninfected or *M.abscessus*-infected murine macrophage cell culture were characterized using NanoSight analysis, electron microscopy, and BCA assay as described above. Though *M.abscessus i*nfection was observed to have no effect upon exosome size distribution (**Fig. 1A**), infection increased macrophage exosome production approximately 3-fold (**Fig. 1B**). NanoSight nanoparticle tracking analysis and transmission electron microscopy further confirmed that exosomes produced by uninfected or *M.abscessus*-infected macrophages exhibit similar sizes and morphologies (**Fig. 1C**) (**Fig. 1D**). Similarly, BCA assay results revealed that the total concentration of exosome-carried proteins released by macrophages is comparable in uninfected and *M.abscessus*-infected macrophage cultures (**Fig. 1E**) (**Fig. 1F**).

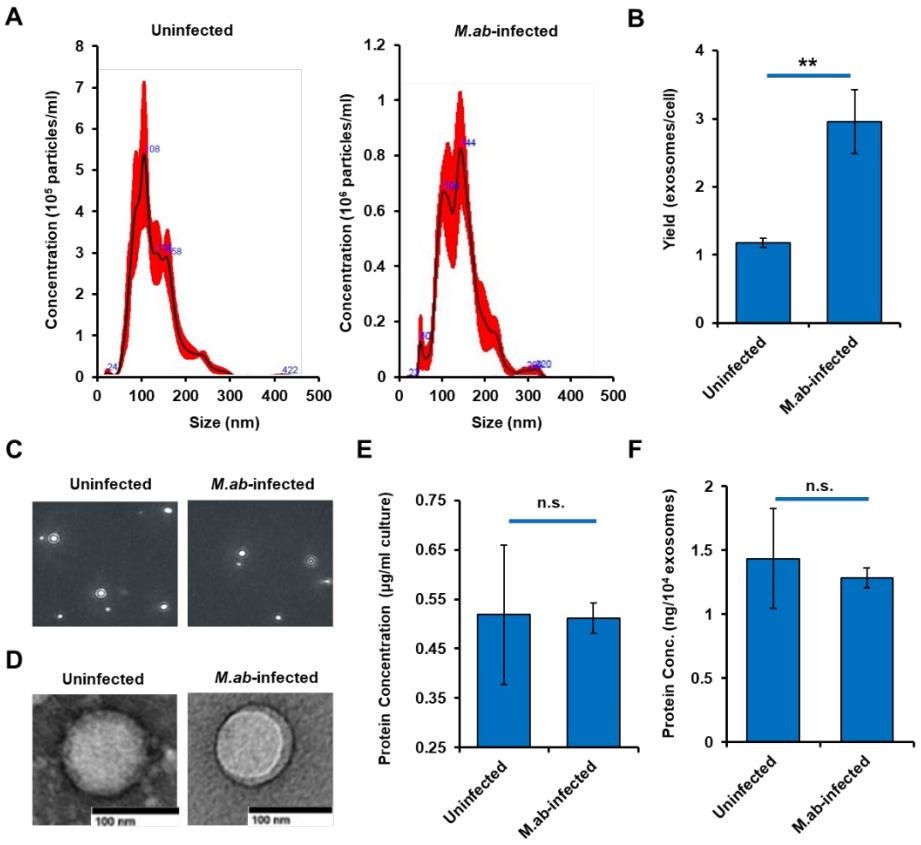

Figure 1. Concentration and morphology of purified exosomes. A) NanoSight nanoparticle analysis for exosomes isolated from uninfected (Uninfected) or *M.abscessus*-infected (*M.ab*-infected) mouse macrophages. **B)** Yield of exosomes isolated from uninfected or *M.abscessus*-infected mouse macrophage culture. Total exosome yield was measured via NanoSight NS300 nanoparticle analysis and values were ratioed to the number of macrophages used for exosome isolation. **C)** Images captured of exosomes during NanoSight analysis for measurement of exosome concentration and size distribution. **D)** Transmission electron microscopy analysis for purified exosomes. Scale bar, 100 nm. **E)** Protein concentrations for exosomes isolated from the same volume of macrophage culture, as determined by BCA assay. **F)** Protein concentration per exosome, determined by BCA assay and NanoSight analysis. Data are representative of at least three independent experiments. Data are Means ±SD; **B)** (n=5); **E)**, **F)** (n=3). n.s., not significant; * $p < 0.05$ and ** $p < 0.01$ by two-tailed Student's t test.

Exosomes promote mycobacterial killing *in vitro.* To investigate the modulatory effect of *M.abscessus*-infected macrophage-released exosomes on host immune response to NTM infection, bacterial survival assays and qRT-PCR were employed. While bacterial uptake was comparable in murine macrophages untreated or pretreated with exosomes purified from uninfected or *M.abscessus*-infected macrophages 1 hour post-infection (**Fig. 2A)**, cultures treated with exosomes prior to *M.abscessus* infection exhibited reduced mycobacterial survival

24 hours post-infection (**Fig. 2B**). No difference was observed between the anti-mycobacterial activities of exosomes isolated from *M.abscessus*-infected macrophages and those isolated from uninfected macrophages (**Fig. 2B**). To assess whether this effect could be attributed to exosome-induced changes in macrophage polarization, the relative expressions of TNFα and IL6 (indicators of proinflammatory M1 polarization) as well as IL10 and Arg1 (indicators of anti-inflammatory M2 polarization) were measured in exosome-treated macrophages. The

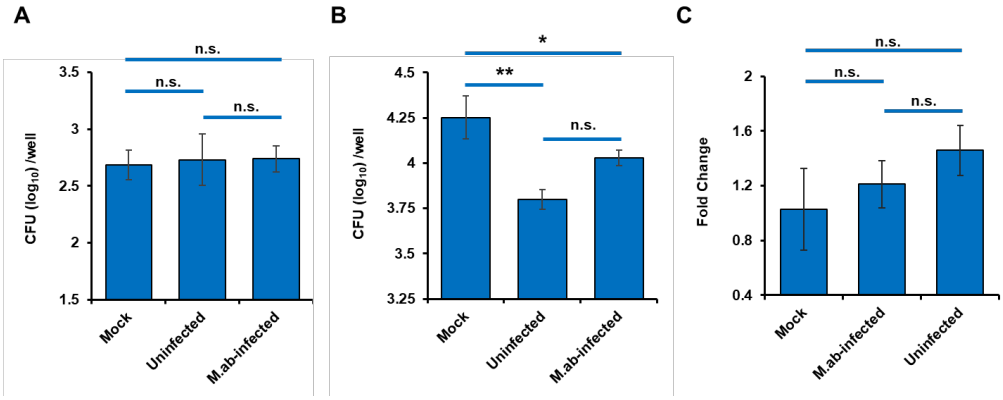

relative expressions of IL 6, IL10, and Arg 1 were too low to be detected, and no difference in TNFα expression was observed between exosome-treated cultures and untreated cultures (this experiment is ongoing) (**Fig. 2C**).

Figure 2. Immunological analysis of macrophage-released exosomes. A) *M.abscessus* uptake 1 hour post-infection in macrophages untreated (Mock) or pretreated with exosomes purified from uninfected (Uninfected) or *M.abscessus*-infected (*M.*ab-infected) mouse macrophages. **B)** *M.abscessus* survival 24 hours post-infection in macrophages untreated or pretreated with exosomes purified from uninfected or *M.abscessus*-infected mouse macrophages. **C)** Relative expression of TNFα in macrophages untreated or pretreated with exosomes purified from uninfected or *M.abscessus*-infected mouse macrophages. Values were normalized to the expression of GAPDH. Data are representative of at least three independent experiments. Data are Means ± SD; n=3. n.s., not significant; * $p < 0.05$ and ** $p < 0.01$ by two-tailed Student's t test.

Proteins in macrophage-derived exosomes are differentially regulated by infection. To explore the mechanism by which exosomes promote mycobacterial killing in recipient macrophages, the protein profiles of macrophage-released exosomes were analyzed as described above. Of the 934 proteins identified by mass spectrometry, 85 were detected only in exosomes from *M.abscessus*-infected macrophages and 75 were detected only in exosomes from uninfected macrophages (**Fig. 3A**). In total, 141 proteins were upregulated in exosomes from *M.abscessus*-infected macrophages relative to exosomes from uninfected macrophages and 153 proteins were downregulated (**Fig. 3B**) (**Fig. 3C**). Pathway analysis of these differentially regulated proteins revealed that proinflammatory pathways are upregulated in exosomes isolated from *M.abscessus*-infected macrophages as well as those isolated from

uninfected macrophages. Interestingly, a greater number of pathways involved in exosome biogenesis and uptake were upregulated in exosomes isolated from *M.abscessus*-infected

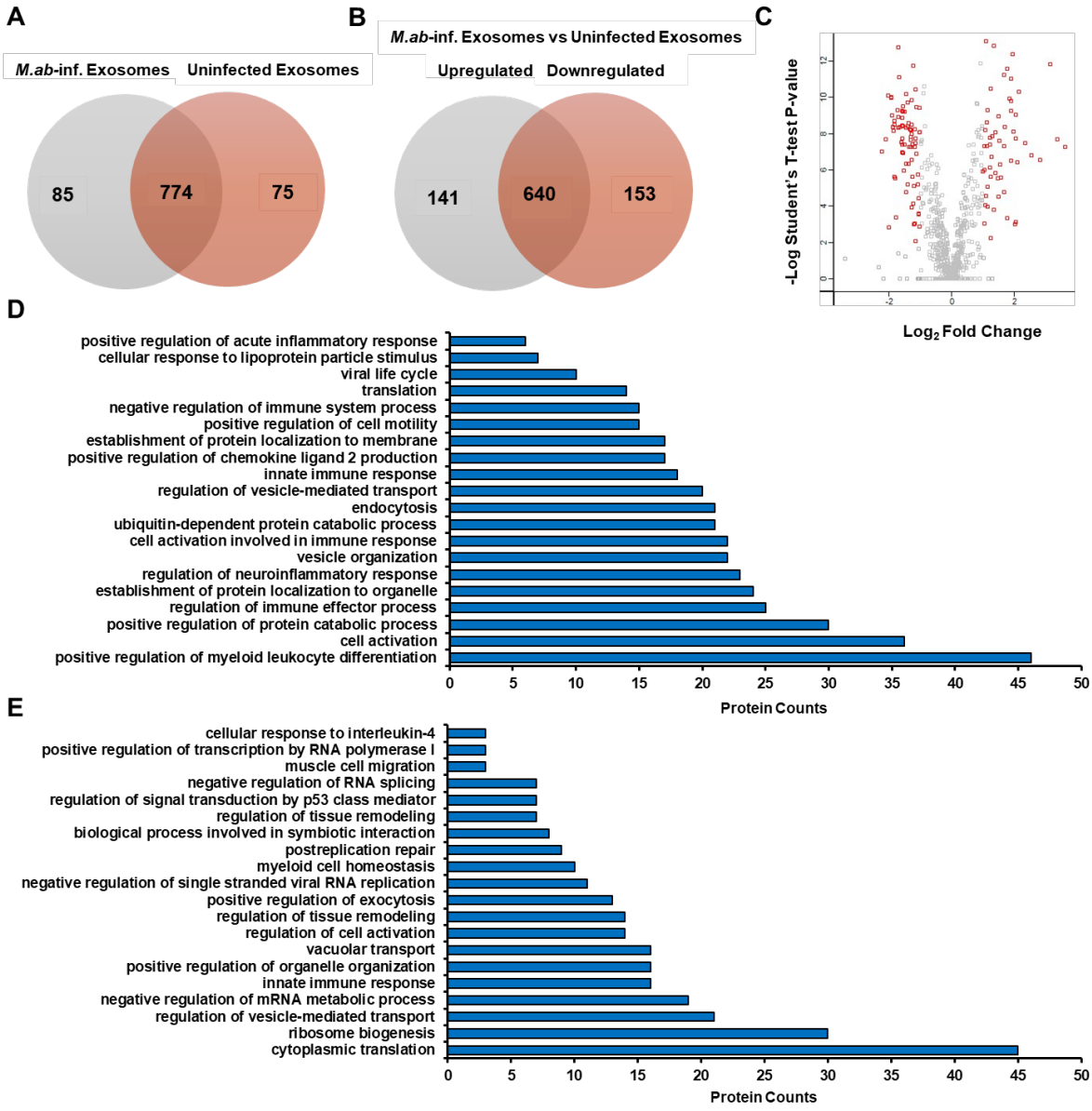

macrophages compared to those isolated from uninfected macrophages (**Fig. 3D**) (**Fig. 3E**).

Figure 3. Protein pathway analysis for purified exosomes. A) Venn diagram of proteins identified in exosomes isolated from uninfected or *M.abscessus*-infected macrophages. **B)** Venn diagram of proteins differentially regulated in exosomes isolated from uninfected or *M.abscessus*-infected macrophages (fold change > 2 and $p < 0.0086$, BH false discovery rate < 0.05). **C)** Volcano plot of proteins differentially regulated in exosomes isolated from uninfected or *M.abscessus*-infected macrophages (fold change > 2 and $p < 0.0086$, BH false discovery rate < 0.05). **D)** Metascape pathway analysis of proteins upregulated in exosomes

isolated from *M.abscessus*-infected macrophages ($p < 0.01$). **E)** Metascape pathway analysis of proteins upregulated in exosomes isolated from uninfected macrophages ($p < 0.01$).

4. Discussion and Conclusions

M.abscessus is frequently identified in the lungs of CF patients with microbial lung infections (Cheng et al., 2020). These infections result in significant lung function decline and are difficult to resolve due to the ability of NTM to tolerate antibiotics and survive within alveolar macrophages (Esther et al., 2010; Schorey et al., 2015; Gardner et al., 2019). In response, NTM-infected host cells have been observed to release exosomes that modulate cellular function in recipient cells. Exosomes isolated from *M.avuim*-infected murine macrophages, for instance, have been found to containin *M.avium* components that promote pro-inflammatory responses in naïve macrophages (Bhatnagar & Schorey, 2007).

Consistent with these findings, our data indicate that macrophage-released exosomes upregulate proinflammatory pathways in recipient macrophages (**Fig. 3**) and reduce mycobacterial survival in macrophages during *M.abscessus* infection (**Fig. 2**). Interestingly, *M.abscessus* infection does not appear to impact the proinflammatory activity of exosomes produced by macrophages (**Fig. 2**) (**Fig. 3**). *M.abscessus* infection does, however, appear to increase exosome yield via the upregulation of pathways involved in exosome biogenesis and uptake (**Fig. 1**) (**Fig. 3**). We subsequently suggest that macrophages upregulate host immune responses to *M.abscessus* infection by increasing the production of proinflammatory exosomes.

Further investigation into the mechanisms by which exosomes promote inflammation is warranted, as these mechanisms may have therapeutic applications. Treatment of *M.abscessus*-infected CF mice, for instance, may reveal whether exogenous exosome treatment promotes inflammatory responses *in vivo*. Additionally, because epithelial exosomes have been found to modulate macrophage polarization, the effect of macrophage-derived exosomes on macrophage polarization should be explored via qRT-PCR (Bardi et al., 2018).

5. Summary

We investigated the functional role of exosomes released from *M.abscessus*-infected macrophages in the regulation of proinflammatory responses to NTM infection using biochemical and immunological tools. We further explored the mechanisms of these functions in an *in vitro* mouse macrophage cell culture model using proteomic approaches. We observed that *M.abscessus* infection did not impact exosome size or morphology, but did increase exosome production. Additionally, we found that both uninfected and *M.abscessus*-infected macrophage-released exosomes promote mycobacterial killing by stimulating proinflammatory pathways in recipient macrophages. Taken together, our data indicate that *M.abscessus*-infection stimulates proinflammatory responses to NTM infection by inducing exosome biogenesis in recipient cells. Considering the proinflammatory action of exosomes,

we propose that these vesicles may be a target for the development of more effective treatments for NTM infections.

6. Appendices

6a. Acknowledgments

This work was made possible by Dr. and Mrs. Niblack, Dr. Y. Cheng, Dr. L. Liu, Dr. X. Tan, Dr. S. Hartson, S. Kotey, and A. Ramos by their provision of opportunity, funding, education, and technical support. Funding for this project was received from the Oklahoma State University Startup Fund (YC), Oklahoma Center for Respiratory and Infectious Diseases, National Institute of General Medical Sciences of the National Institutes of Health under Award Number P20GM103648 (LL), Oklahoma Center for the Advancement of Science & Technology under Award Number HR21-050 (YC), and National Institute of Allergy and Infectious Diseases under Award Number R21AI166118 (YC and LL) and R01AI173180 (YC and LL). A continuation of this project will be further supported by Neil Purdie and Barry Goldwater research fellowships.

6b. Publications/Posters

Vermeire, C., Tan, X., Liang, Y., Kotey, S.K., Rogers, J., Hartson, S.D., Liu, L., & Cheng, Y. *Mycobacterium abscessus* extracellular vesicles increase Mycobacterial resistance to clarithromycin *in vitro*. (Submitted July 2023). *Journal of Proteomics*.

Vermeire, C., Tan, X., Liang, Y., Kotey, S., Liu, L., Hartson, S., & Cheng, Y. Exosomes Released by *Mycobacterium abscessus*-Infected Macrophages Facilitate Mycobacterial Intracellular Survival within Host Cells**.** Oklahoma State University Undergraduate Research Symposium (04/2023).

Vermeire, C., Tan, X., Liang, Y., Kotey, S., Liu, L., Hartson, S.D., & Cheng, Y. Exosomes Released by *Mycobacterium abscessus*-Infected Macrophages Facilitate Mycobacterial Intracellular Survival within Host Cells**.** Oklahoma Center for Respiratory and Infectious Disease (04/2023).

Vermeire, C., Tan, X., Liang, Y., Kotey, S., Liu, L., Hartson, S., & Cheng, Y. Exosomes Released by *Mycobacterium abscessus*-Infected Macrophages Facilitate Mycobacterial Intracellular Survival within Host Cells**.** Oklahoma State University Biochemistry and Microbiology Symposium (02/2023).

Vermeire, C., Tan, X., Liang, Y., Kotey, S., Liu, L., & Cheng, Y. The Role of *Mycobacterium abscessus*-Infected-Macrophage-Released Exosomes on Host Immune Responses. Oklahoma State University Undergraduate Research Symposium (04/2022).

6c. References

Bardi, G.T., Smith, M.A., & Hood, J.L. (2018). Melanoma exosomes promote mixed M1 and M2 macrophage polarization. *Cytokine*, 105: 63-72.

Bhatnagar, S., & Schorey, J.S. (2007). Exosomes released from infected macrophages contain Mycobacterium avium glycopeptidolipids and are proinflammatory. *The Journal of Biological Chemistry,* 282: 25779–89.

Cheng, Y., Kiene, N.J., Tatarian, A., Eix, E.F., & Schorey, J.S. (2020). Host cytosolic RNA sensing pathway promotes T Lymphocyte-mediated mycobacterial killing in macrophages. *PLOS Pathogens*, 16: e1008569.

Cheng, Y., & Schorey, J.S. (2013). Exosomes carrying mycobacterial antigens can protect mice against *Mycobacterium tuberculosis* infection. *European Journal of Immunology*, 43: 3279-3290.

Cheng, Y., & Schorey, J.S. (2019). Extracellular vesicles deliver Mycobacterium RNA to promote host immunity and bacterial killing. *EMBO reports*, 20: e46613.

Cheng, Y., & Schorey, J.S. (2020). Chapter 6 - The function and therapeutic use of exosomes in bacterial infections. In: Edelstein, L., Smythies, J., Quesenberry, P., & Noble, D., editors. *Exosomes*. (pp. 123–46). Academic Press.

Esther, C.R., Esserman, D.A., Gilligan, P., Kerr, A., & Noone, P.G. (2010). Chronic Mycobacterium abscessus infection and lung function decline in cystic fibrosis. *Journal of Cystic Fibrosis,* 9:117–23.

Gardner, A.I., McClenaghan, E., Saint, G., McNamara, P.S., Brodlie, M., & Thomas, M.F. (2019). Epidemiology of Nontuberculous Mycobacteria infection in children and young people with cystic fibrosis: Analysis of UK cystic fibrosis registry. *Clinical Infectious Diseases,* 68(5):731–737.

Schorey, J.S., Cheng, Y., Singh, P.P., & Smith, V.L. (2015). Exosomes and other extracellular vesicles in host-pathogen interactions. *EMBO Reports*, 16(1): 24–43.

Shteinberg, M., Haq, I.J., Polineni, D., & Davies, J.C. (2021). Cystic fibrosis. *The Lancet*, 397:2195-2211.

Sullivan, J.R., Lupien, A., Kalthoff, E., Hamela, C., Taylor, L., Munro, K.A., Schmeing, T.M., Kremer, L., & Behr, M.A. (2021). Efficacy of epetraborole against *Mycobacterium abscessus* is increased with norvaline. *PLOS Pathogens*, 17(10): e1009965.

Zhou, Y., Zhou, B., Pache, L., Chang, M., Khodabakhshi, A.H., Tanaseichuk, O., Benner, C., & Chanda, S.K. (2019). Metascape provides a biologist-oriented resource for the analysis of systems-level datasets. *Nature Communications*, 10(1):1523.

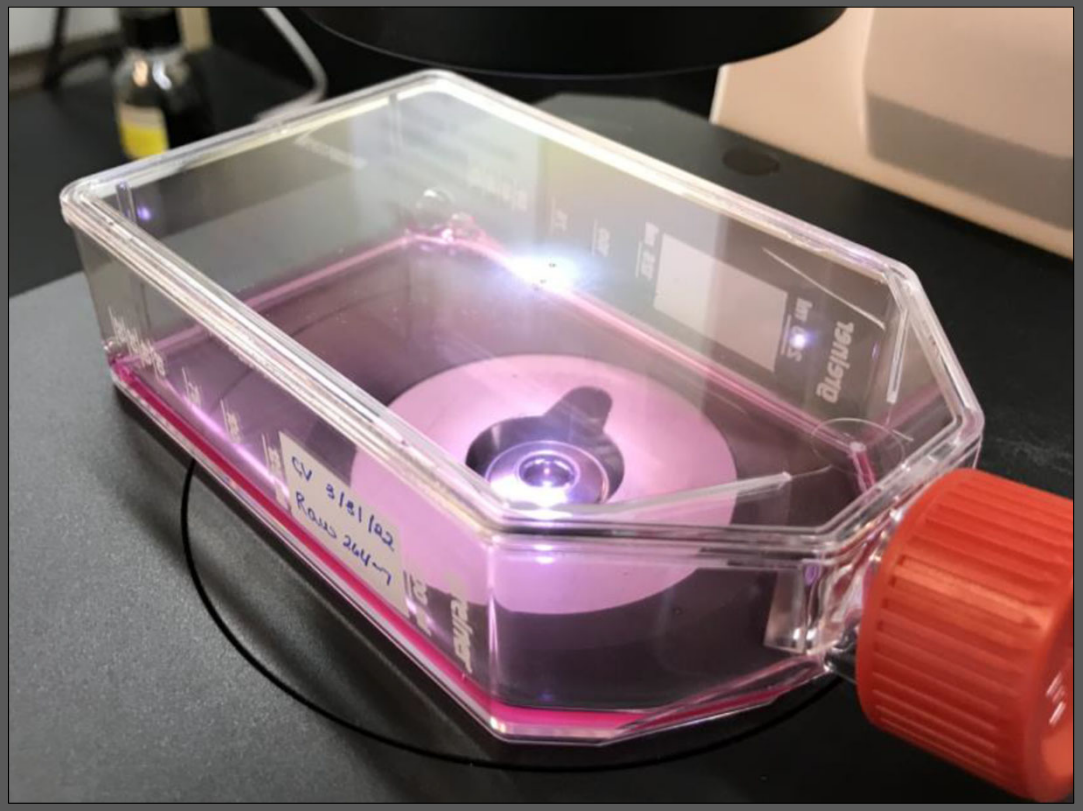

Mycobacterium abscessus Infection Upregulates Proinflammatory Exosome Biogenesis in Macrophages *in vitro*

Charlie Vermeire

Department of Biochemistry and Molecular Biology

Nontuberculous Mycobacteria (NTM) and Cystic Fibrosis (CF)

-Exposure to NTM results in **serious respiratory infections in individuals living with CF** (Shteinberg et al., 2021; Cheng et al., 2020)

-***Mycobacterium abscessus* is responsible for lung function decline** in infected CF patients (Gardner et al., 2019; Esther et al., 2010)

-**Treatment** of NTM infection is **difficult** (Gardner et al., 2019)

-Intracellular pathogenic material is **delivered to immune cells via the formation and release of exosomes** (Cheng & Schorey, 2019).

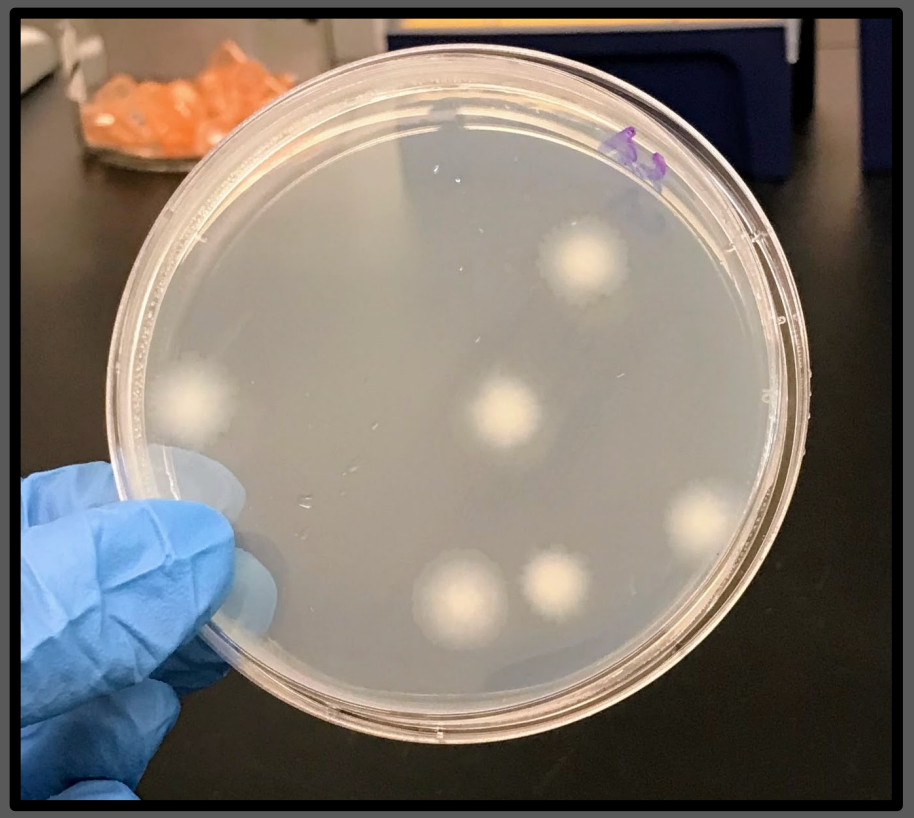

Objectives

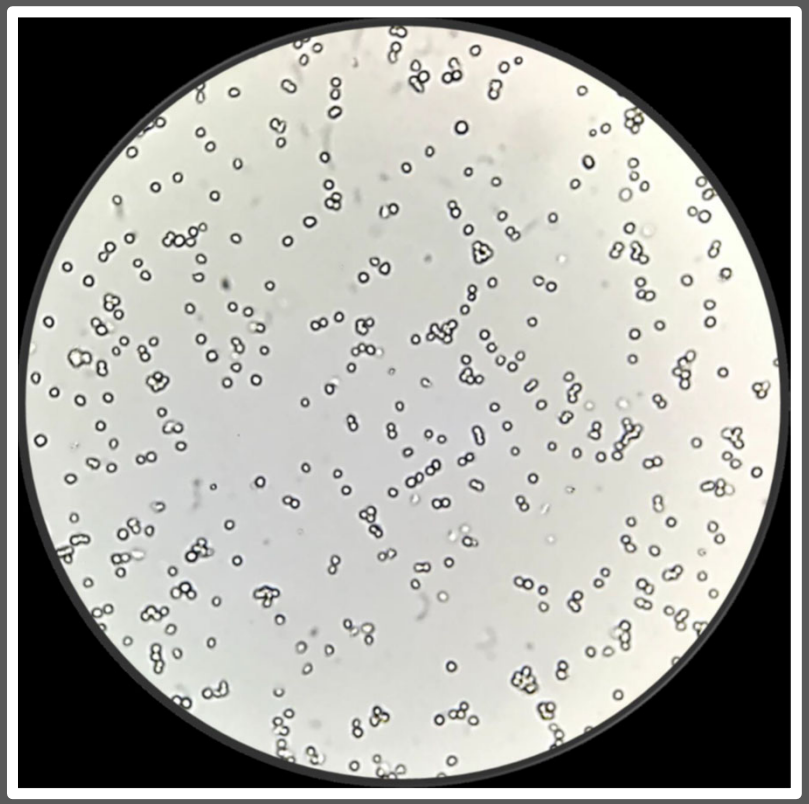

I. **Isolate and characterize exosomes** released from *M.abscessus*-infected macrophages

II. Examine the **functional role of exosomes** released from *M.abscessus*-infected macrophages in ***M.abscessus*-host interactions**

III. Explore the **mechanisms of function** using an *in vitro* mouse macrophage cell culture model

Exosome Isolation and Characterization

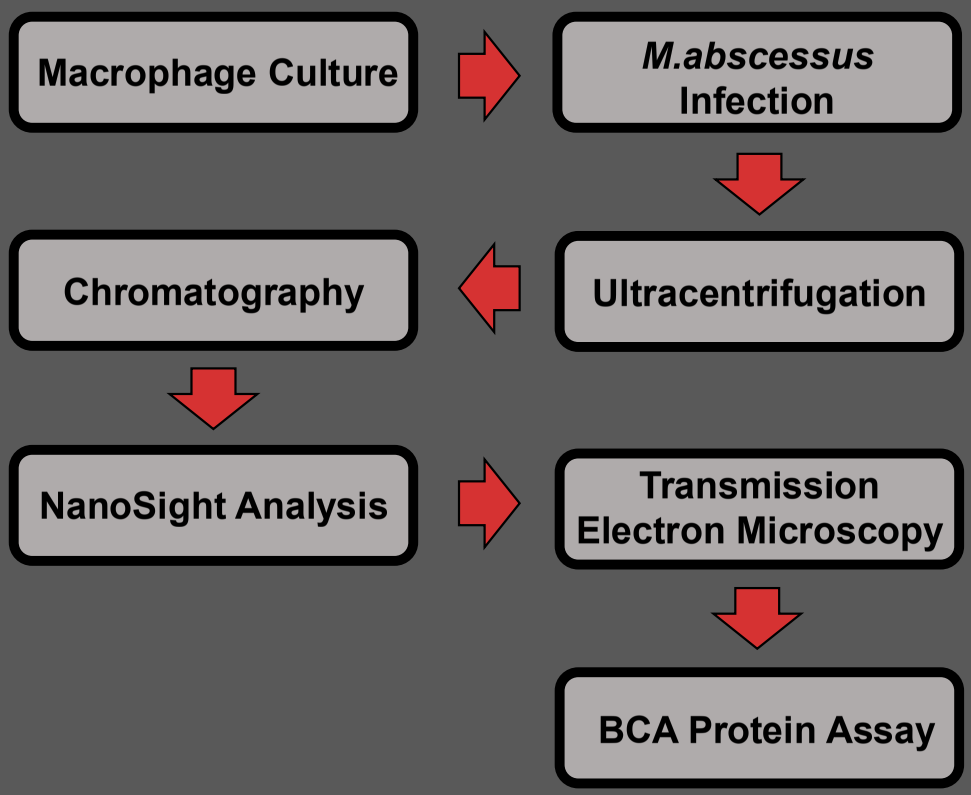

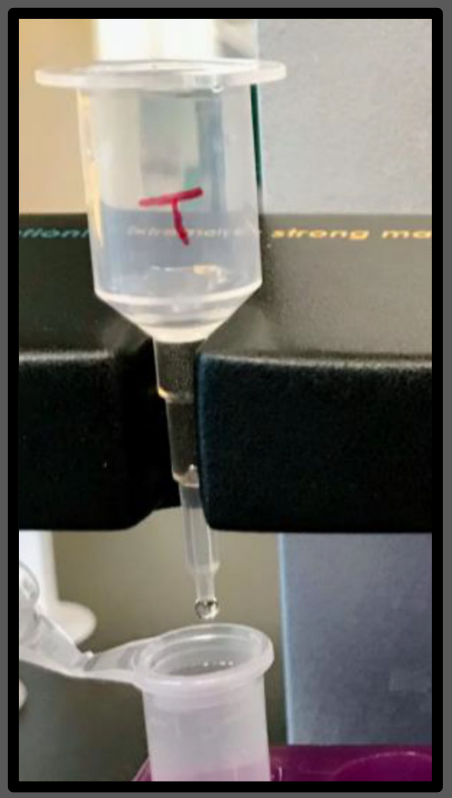

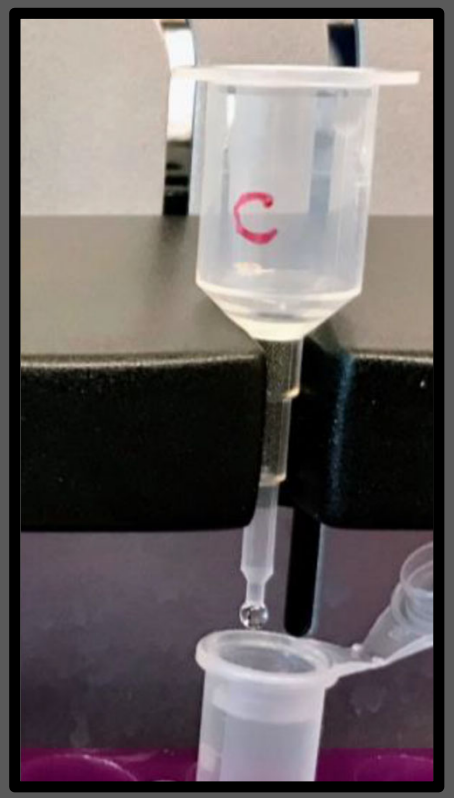

Functional Analysis

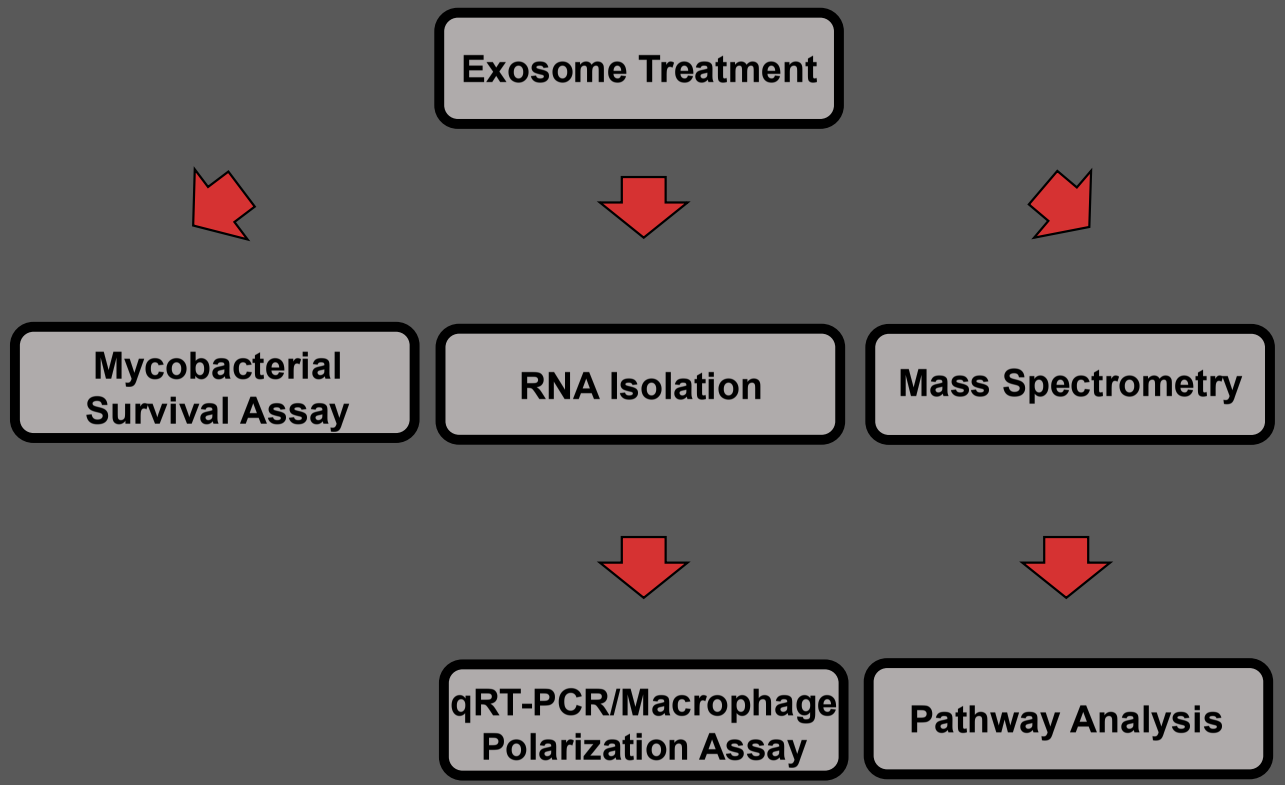

M.abscessus infection induces exosome biogenesis in murine macrophages

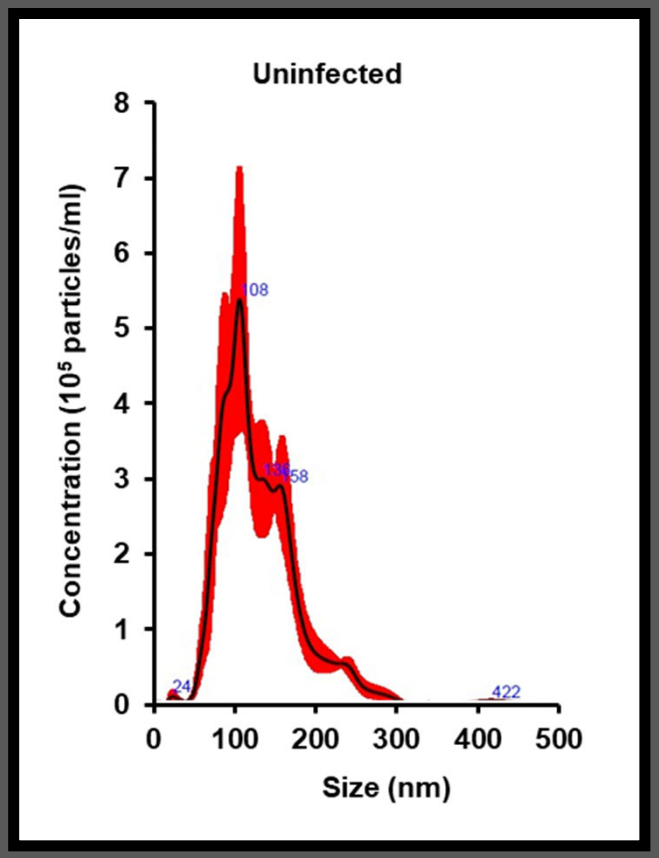

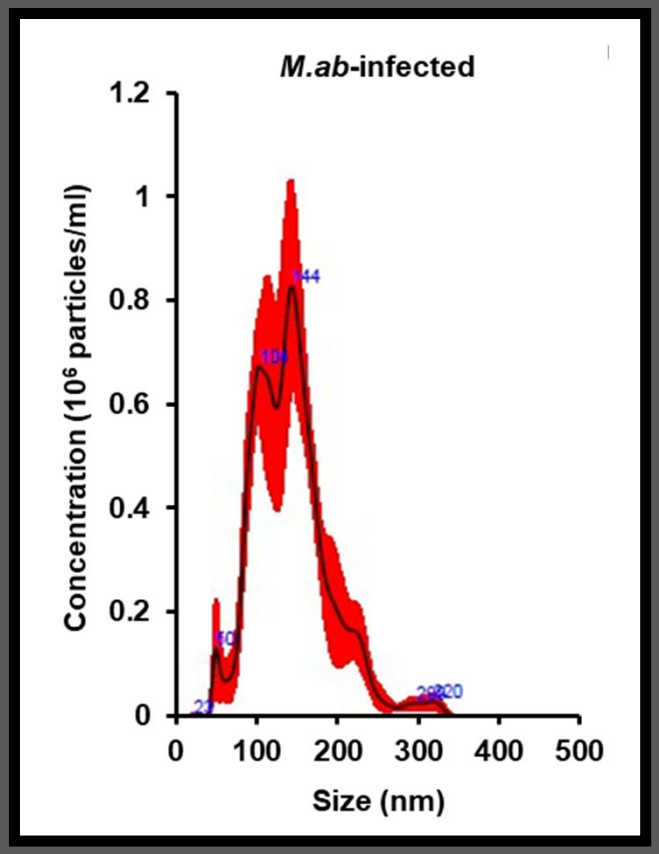

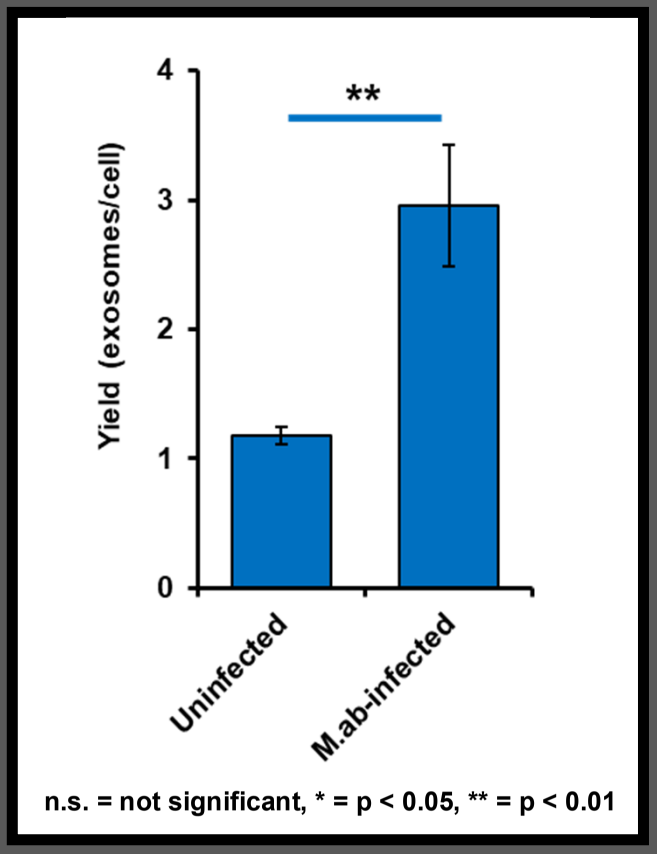

Exosomes produced by uninfected or *M.abscessus*-infected macrophages exhibit similar sizes and morphologies

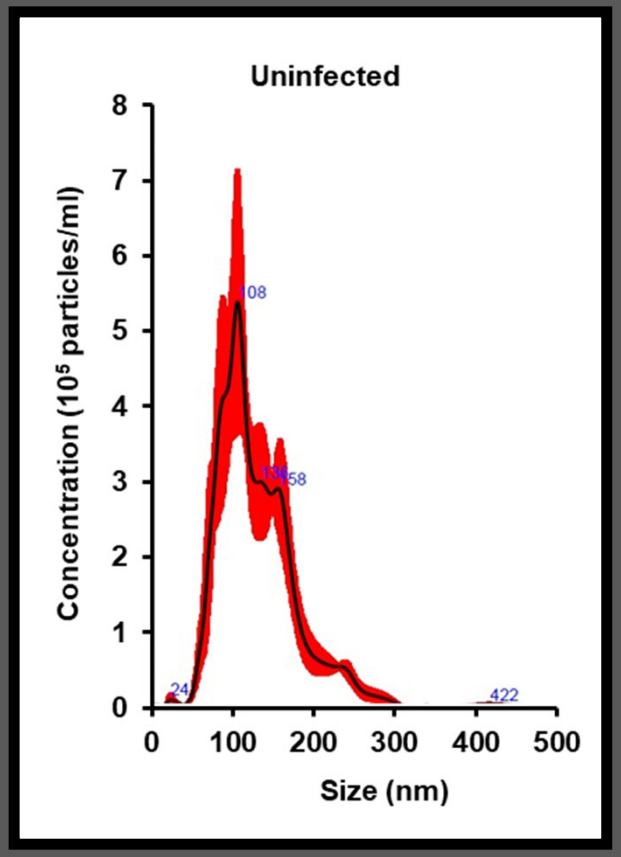

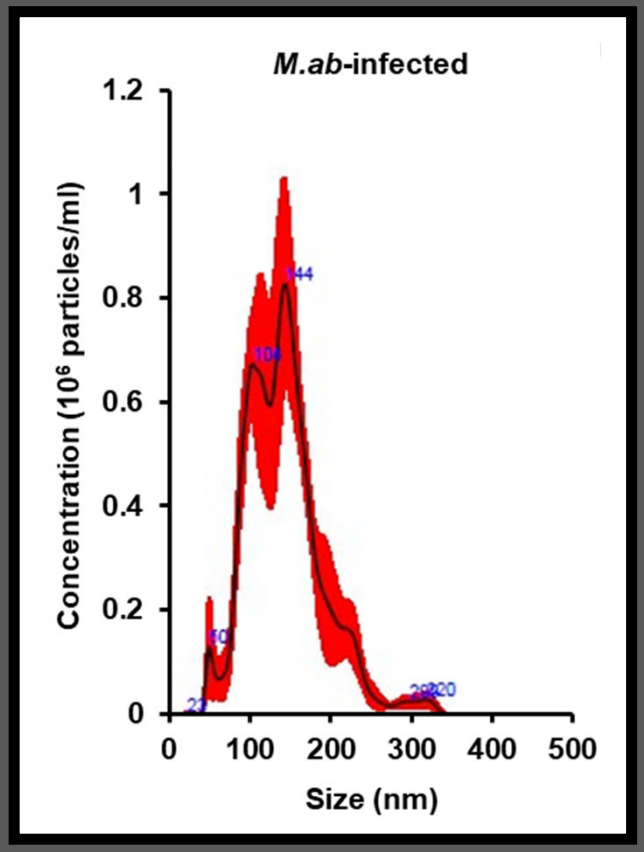

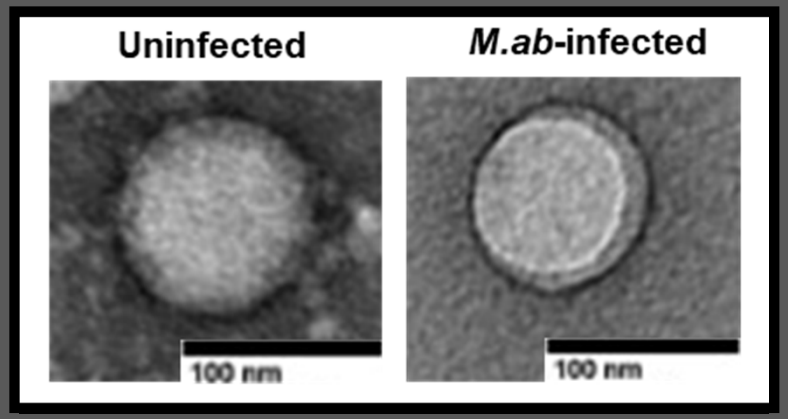

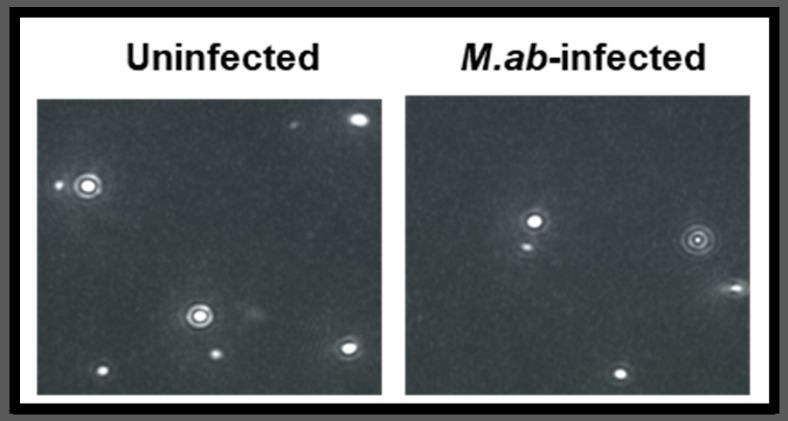

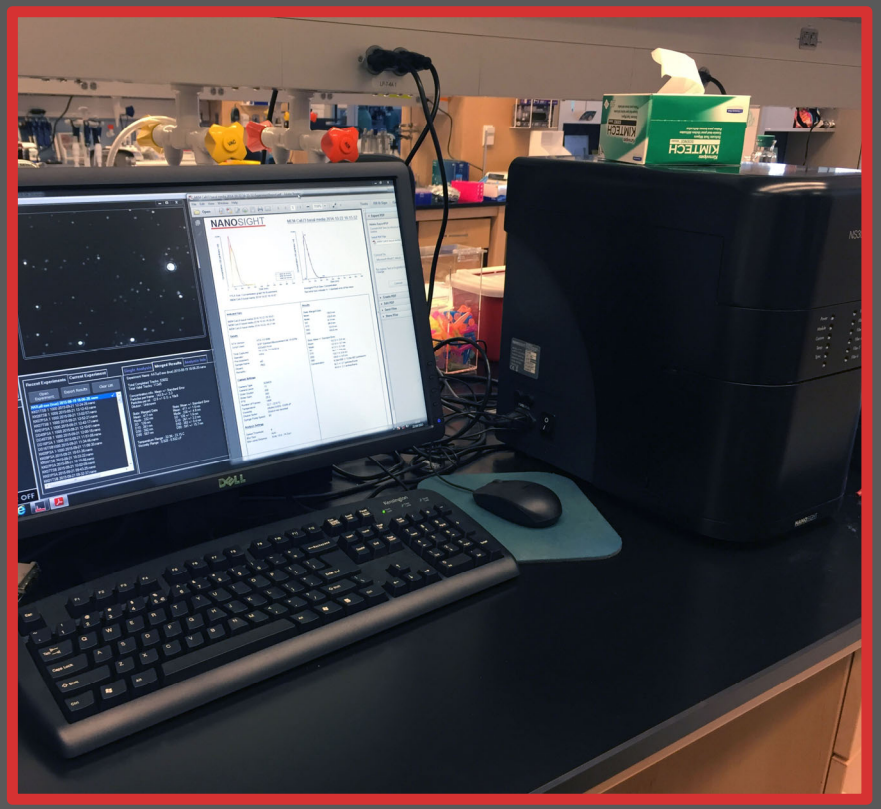

https://encrypted-tbn0.gstatic.com/images?q=tbn:ANd9GcTyvY7HnPOSjj07FjUCNN0ZA6hc-udknPMs2A&usqp=CAU

Total concentration of exosome-carried proteins is comparable in uninfected and *M.abscessus*-infected macrophage cultures

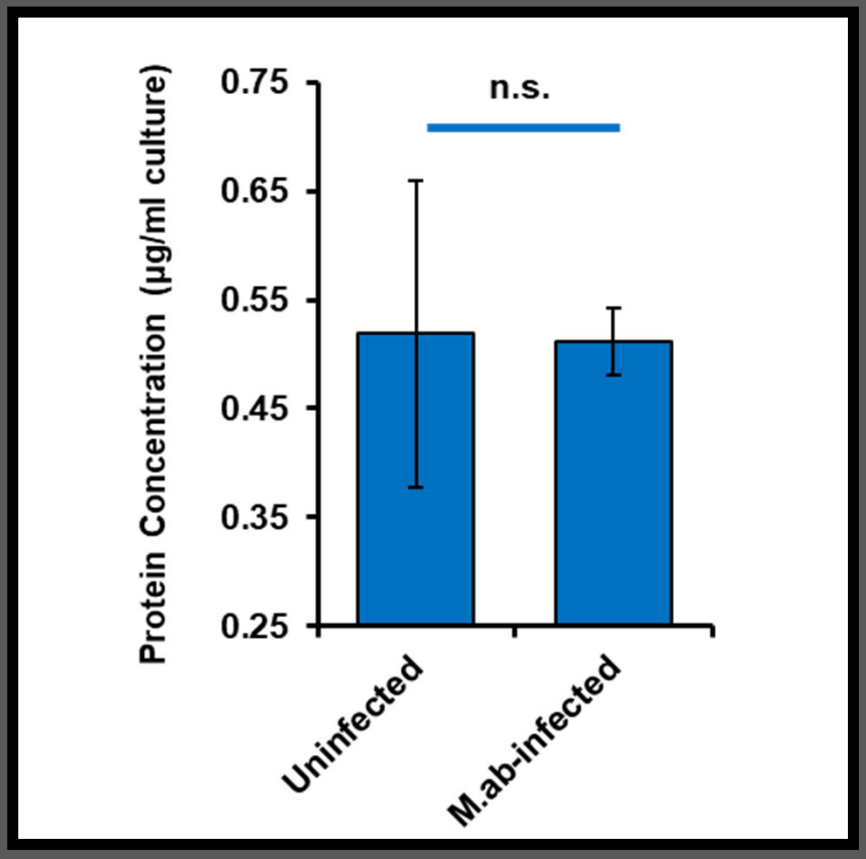

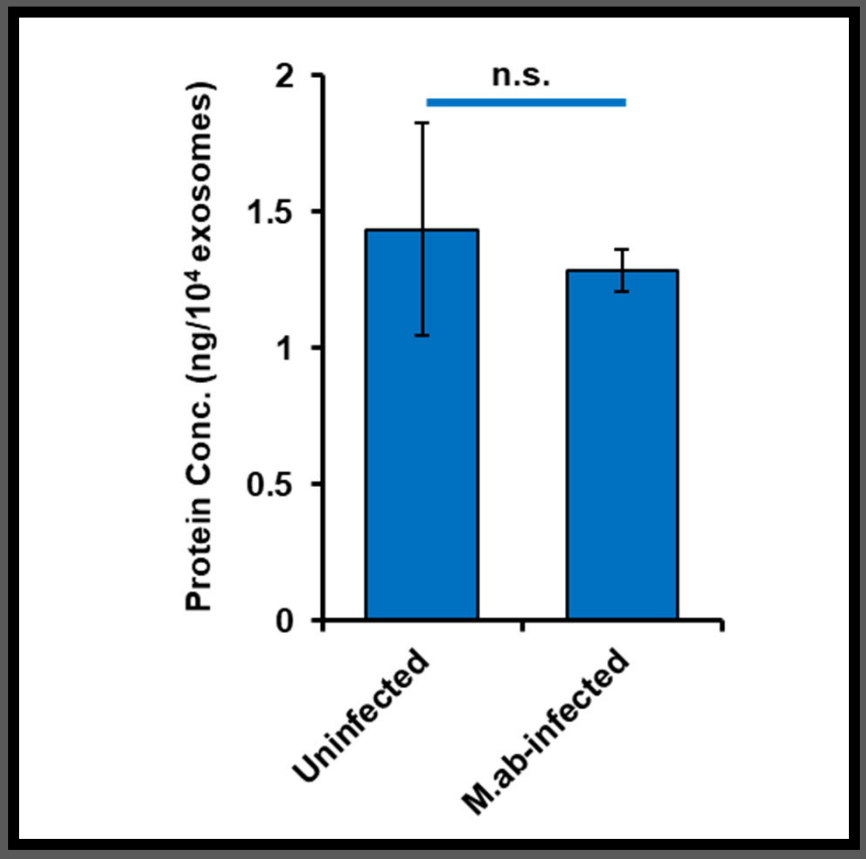

Exosomes promote mycobacterial killing *in vitro*

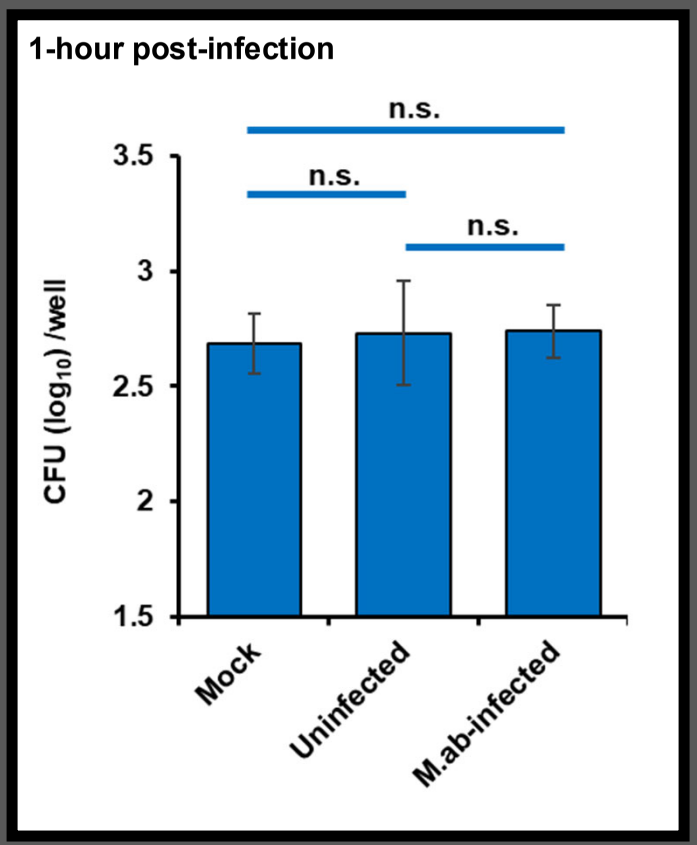

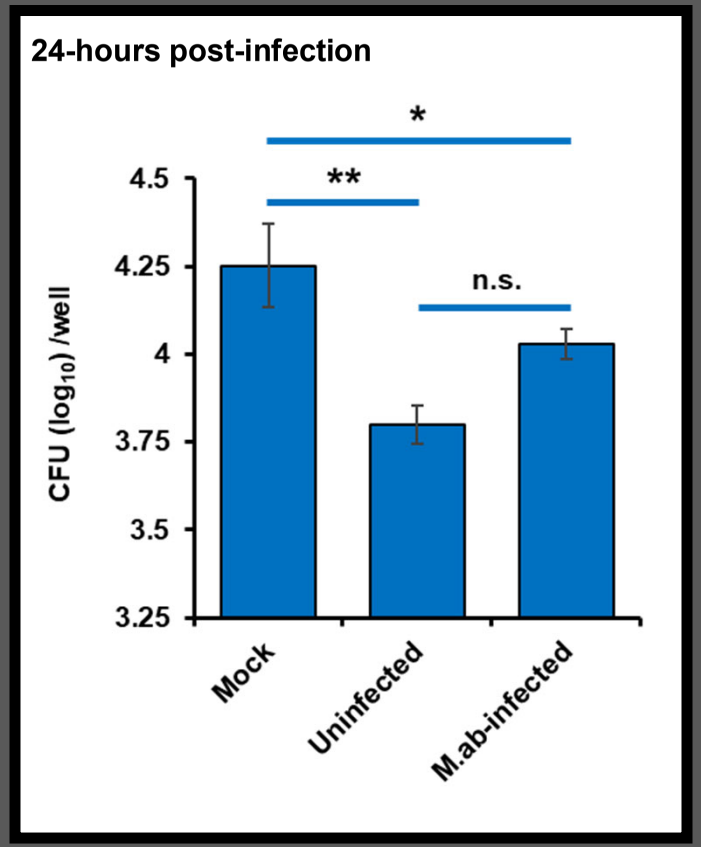

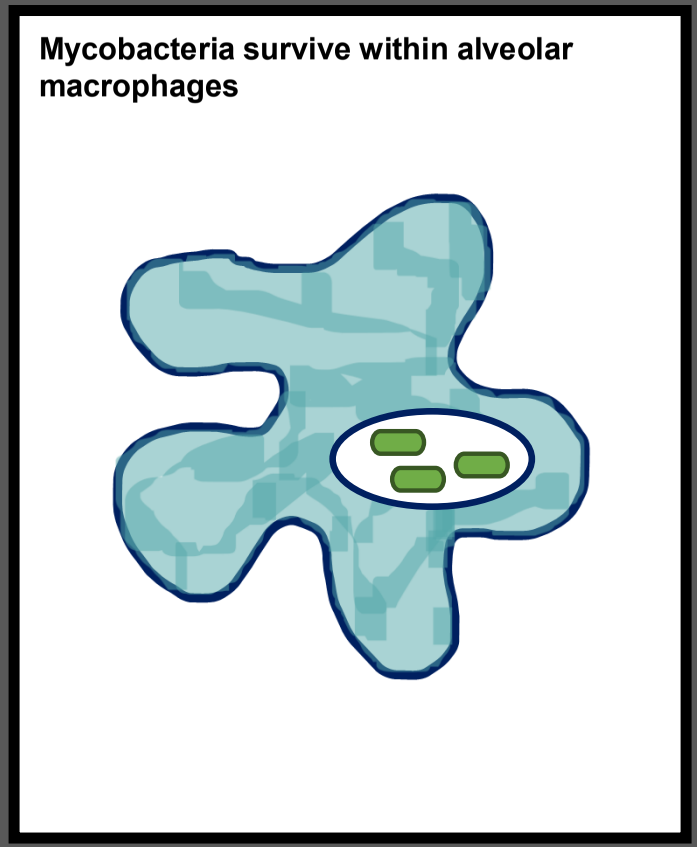

The impact of exosome treatment on macrophage polarization remains unclear

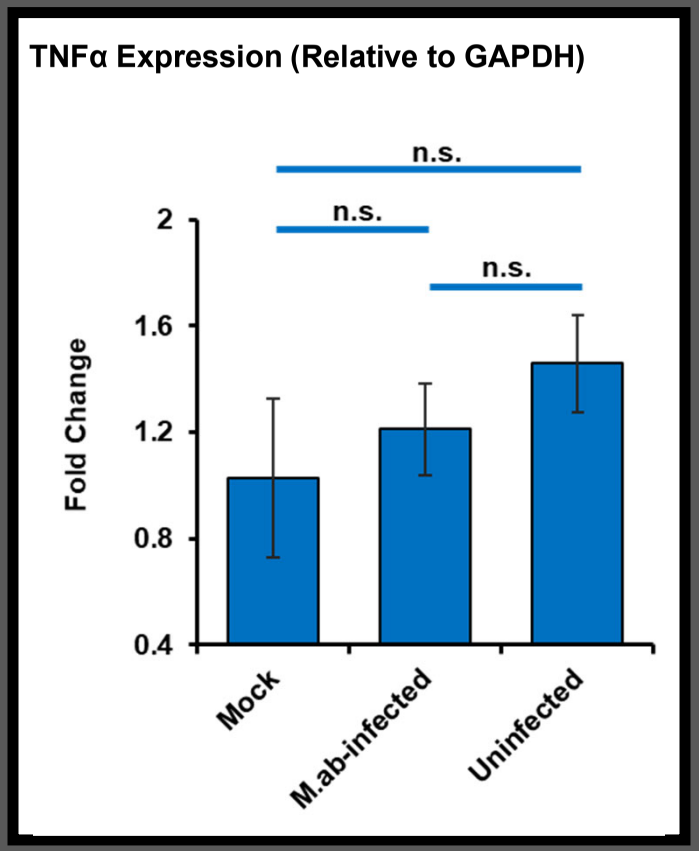

The protein profiles of macrophage-derived exosomes are altered by *M.abscessus* infection

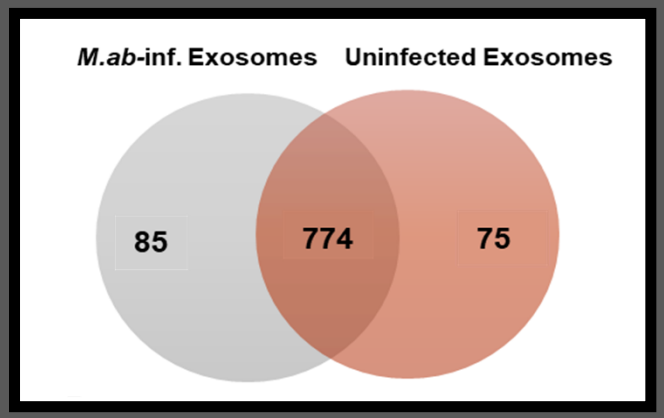

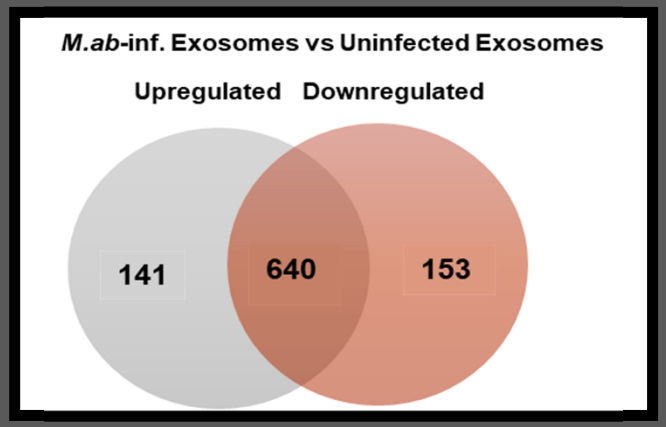

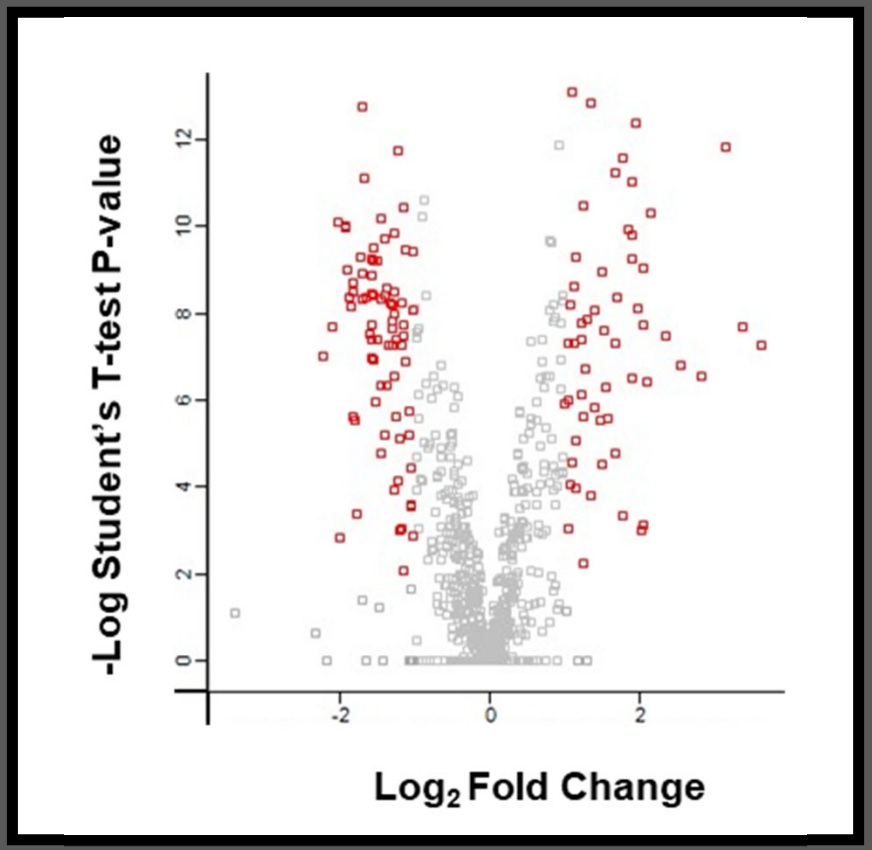

M.abscessus infection enriches proteins involved in exosome biogenesis and uptake in macrophage-derived exosomes

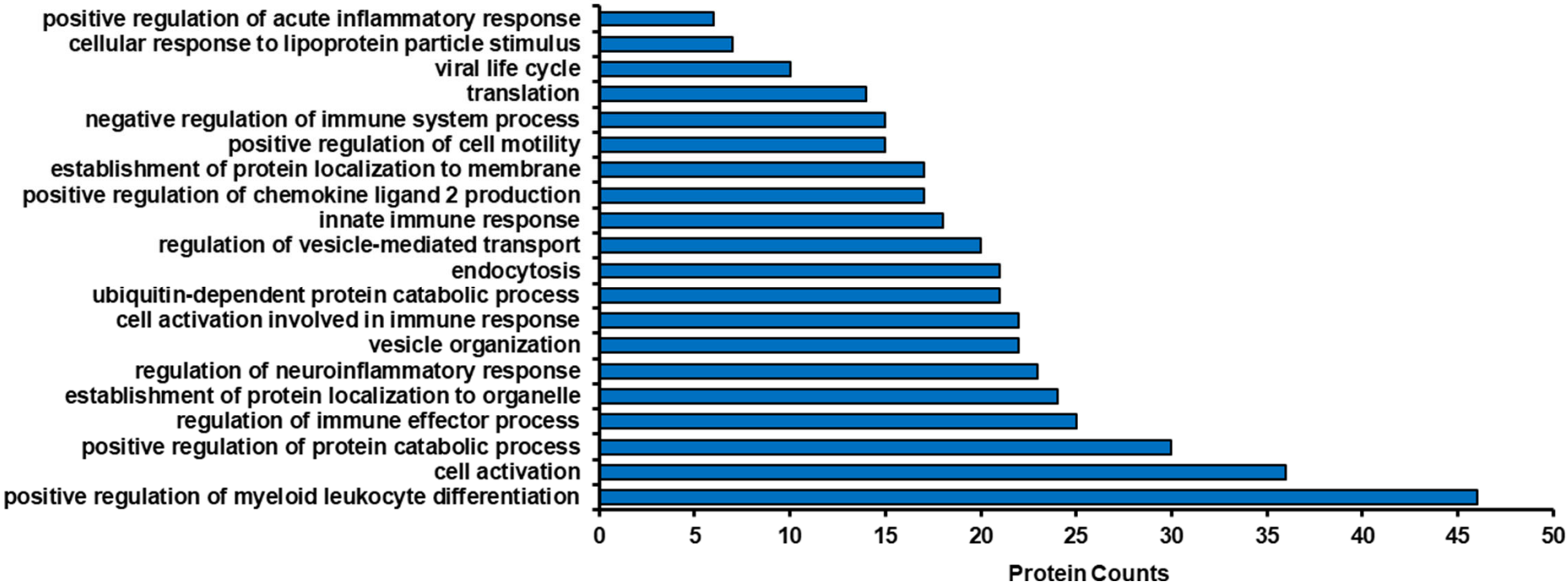

Proinflammatory pathways are upregulated in exosomes isolated from both *M.abscessus*-infected macrophages and uninfected macrophages

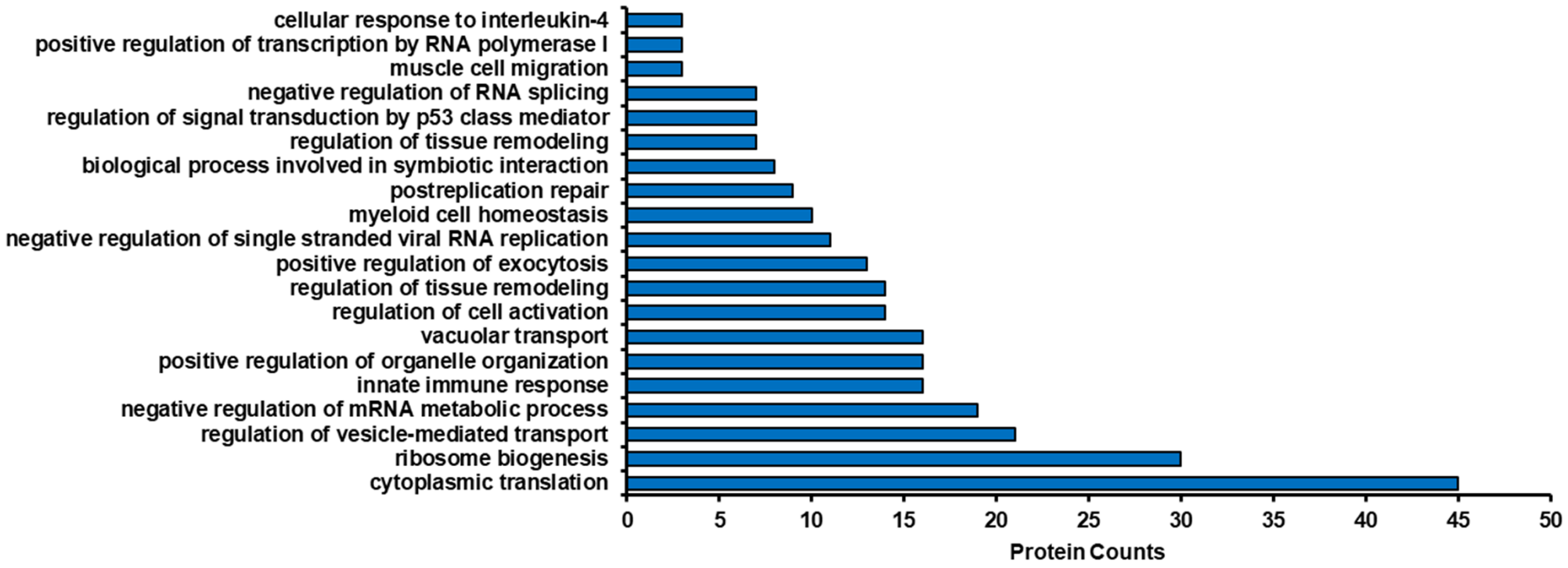

Conclusions

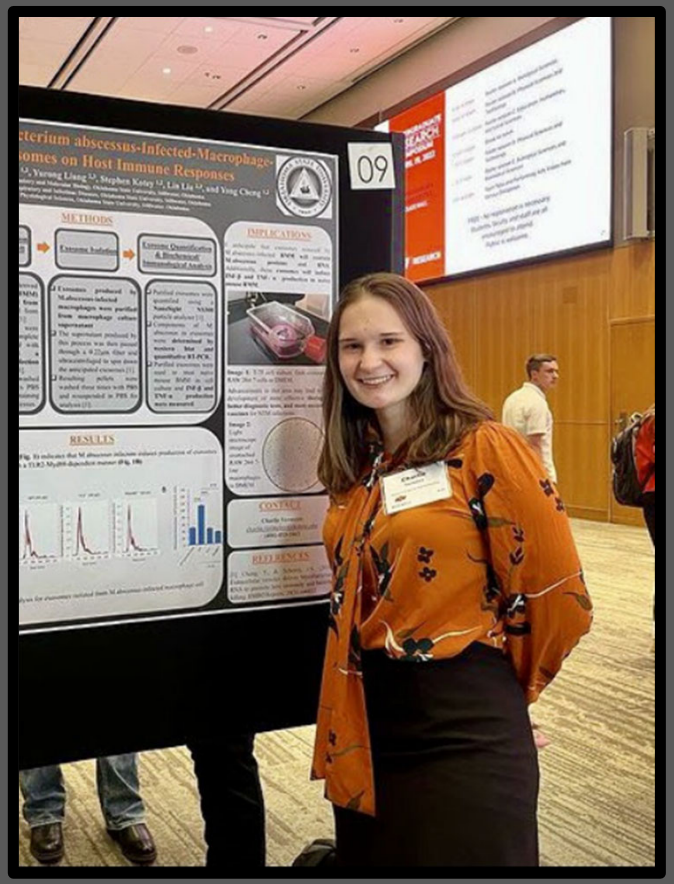

-Macrophage-released exosomes **upregulate proinflammatory pathways** in recipient macrophages and **reduce mycobacterial survival**

-*M.abscessus* infection **does not** impact inflammatory activity of exosomes

-*M.abscessus* infection **increases exosome yield** via the upregulation of exosome biogenesis

-Macrophages **upregulate host immune responses** to *M.abscessus* infection by **increasing the production of proinflammatory exosomes**.

-Further investigation may yield **therapeutic developments**

Acknowledgements

Thank You:

- Dr. and Mrs. Niblack
- OSU Division of the Vice President for Research
- Dr. Y. Cheng, Dr. L. Liu, Dr. X. Tan, Dr. S. Hartson, S. Kotey, and A. Ramos
- J. Sullins, L. Tasci, and Dr. K. Garbutt

https://www.google.com/imgres?imgurl=https%3A%2F%2Fpbs.twimg.com%2Fprofile_images%2F1145840553927593984%2FPOsHXvlH_400x400.p
ng&tbnid=8Ctly5x3gUyJ2M&vet=12ahUKEwj6pbPMt76AAxUqM94AHetgA00QMygJegUIARD9AQ..i&imgrefurl=https%3A%2F%2Ftwitter.com%2FOS
UWBB&docid=7C4DkBLHQKe83M&w=400&h=400&q=osu&client=firefox-b-1-d&ved=2ahUKEwj6pbPMt76AAxUqM94AHetgA00QMygJegUIARD9AQ

References

Cheng, Y., Kiene, N.J., Tatarian, A., Eix, E.F., & Schorey, J.S. (2020). Host cytosolic RNA sensing pathway promotes T Lymphocyte-mediated mycobacterial killing in macrophages. PLOS Pathogens, 16: e1008569.

Cheng, Y., & Schorey, J.S. (2019). Extracellular vesicles deliver Mycobacterium RNA to promote host immunity and bacterial killing. EMBO reports, 20: e46613.

Esther, C.R., Esserman, D.A., Gilligan, P., Kerr, A., & Noone, P.G. (2010). Chronic Mycobacterium abscessus infection and lung function decline in cystic fibrosis. Journal of Cystic Fibrosis, 9:117–23.

Gardner, A.I., McClenaghan, E., Saint, G., McNamara, P.S., Brodlie, M., & Thomas, M.F. (2019). Epidemiology of Nontuberculous Mycobacteria infection in children and young people with cystic fibrosis: Analysis of UK cystic fibrosis registry. Clinical Infectious Diseases, 68(5):731–737.

Shteinberg, M., Haq, I.J., Polineni, D., & Davies, J.C. (2021). Cystic fibrosis. The Lancet, 397:2195-2211.

in vivo Assay: Bacterial Small RNAs May Regulate Eukaryotic Gene Expression

Natalee Richardson

Animal and Food Sciences
Faculty Sponsor: Dr. Darren Hagen
Graduate Student Mentor: Anna Goldkamp

ABSTRACT

Wolbachia is present in 70% of insects because of this it is widely studied. Research suggests that one or more small RNAs, made by the *Wolbachia* bacteria is responsible for initiating and maintaining the ability to manipulate its host's reproduction which is a phenomenon called cytoplasmic incompatibility (CI). Early evidence suggests that some *Wolbachia*- derived small RNAs hybridize to *Drosophila* protein-coding genes, which regulate protein expression. If the small RNAs are produced in enough volume to bind to *Drosophila* targets with enough strength they could regulate protein expression. The bacterial small RNA sequences have been derived from RNA library pools sequenced using RNA-Seq. A plasmid was designed from two existing plasmids. The pHd-DsRed plasmid and the act5c plasmid, which each contain specific pieces that were needed to complete the designed plasmid. For the pHd-DsRed plasmid, restriction enzyme digestion was used to cut the section of the plasmid needed and a gel electrophoresis was used to separate the piece from the rest of the plasmid. For the act5c plasmid, PCR was used to amplify and isolate a section of the plasmid. The pac5-DsRed plasmid, containing the ACT5C promoter, a fluorescence gene, and an ampicillin resistance gene, is transformed into cells and selected for using ampicillin plates.

1. Introduction

Gene expression can be affected by several different factors, external and internal. For example, you might have the gene that Usain Bolt has that indicates you run fast, however, you may run really slow simply because that gene is not activated. In recent years, microRNAs (miRNAs) have become a topic of research for geneticists and other scientists, as well. They are not a well-researched topic, therefore, there are many questions floating around about these small RNAs. The question I will be focusing on in my research will pertain to small RNA interactions with DNA. I will be using Drosophila cell culture and *Wolbachia* bacteria to determine if small RNAs from bacteria affect the host's gene expression.

Small noncoding RNAs, 18-30 nucleotides in length, are one of those factors that affect gene expression. MiRNAs are a class of small RNAs that are around 20 nucleotides in

length. MiRNAs only exist in Eukaryotic organisms and are known to affect gene expression. They are a relatively new discovery in the genetics field so there has not been much research done on the subject. Their basic structure and a little about how they work is known, however, not much is known about how they affect their surroundings. They are involved in almost every cellular process and are a critical part of animal development, cell differentiation, and homeostasis (Gerbert, 2019). These factors and their abundance make them a great resource for research and show a need for more studies on the subject. A 'hairpin' structure, which is where the miRNA sequences are embedded, develops as mRNAs are transcribed by RNA polymerase II (Ha, 2014). This hairpin is cut by enzymes making the miRNAs, which then float around in the cytoplasm until they bind to a target sequence at the 3' untranslated region. We are proposing that the bacterial small noncoding RNA mechanism is similar to the miRNA mechanism.

There is also evidence that small RNAs produced by viruses and the host are involved with each other (Kabekkodu, 2018). This intercellular communication opens up the question which began my project: 'Can these small RNAs from bacteria and viruses affect host gene expression?' If this is the case it would have to change the way antibiotics are used and designed. If the bacteria that live in us naturally affect gene expression in the body, then antibiotics that kill all bacteria in the area are in turn affecting which genes are expressed or inhibited.

Drosophila melanogaster is often used to model genetic research because of its rapid life cycle, short life span, small size, easy generation of mutant animals, and they share about 40% of the nucleotide and protein sequence in their homologs with mammalian species (Baena, 2019). This project will be using Drosophila cell cultures instead of a live model. Cell cultures was chosen because in previous projects conducted by former students there were complications with live models. I, also, have previous experience working with cell cultures, which opened the opportunity for this project. Cell cultures are a very straightforward way to determine the results of this project. Drosophila were chosen for this project because it has 466 known miRNAs (Ha, 2014) and usually approval for experimental settings from animal welfare ethical review boards is not needed (Baena, 2019). All of these factors have led to Drosophila being well researched which leaves few unknown variables that could affect this research outside of what is being tested.

This project will use two types of Drosophila cultures, one infected with *Wolbachia* and one uninfected. *Wolbachia* is a part of the order Rickettsiales, which is a group of intracellular bacteria that is made up of species with parasitic, mutualistic and commensal relationships with their hosts (Werren, 2008). There were several factors that made *Wolbachia* the choice bacteria for this project. The first reason, *Wolbachia* have a unique feature called cytoplasmic incompatibility (CI) which is when one or more small RNAs made by the bacteria is responsible for initiating and maintaining the ability to manipulate its host's reproduction which is a phenomenon. The second reason, Wolbachia usually do not infect

vertebrates (Werren, 2008). The third reason, Dr. Hagen had a contact that could provide Drosophila cultures infected and uninfected with *Wolbachia.*

Once cultures are grown plasmids will be transformed into them. Plasmids are rings that have three key features: an antibiotic resistance gene, an origin of replication site, and multiple cloning sites. The plasmid used in this project is the pHD-DsRed plasmid (Figure 1). It contains the DsRed fluorescent gene. The pHD-DsRed plasmid is designed for rapid generation of gene-specific donor templates and are custom synthesized (Gratz, 2014). There is evidence that this plasmid is very compatible with Drosophila. It has also been used in Dr. Hagen's lab previously, which provided an advantage in jump starting this research project. The pHD-DsRed plasmid's multiple cloning sites were designed to conserve as many restriction sites as possible to make the vector compatible with homology arms (Gratz, 2014). This plasmid will have to be manipulated slightly to be completely applicable to this research project. The promoter will have to be replaced and a target sequence will need to be added as well.

The promoter on the plasmids have been changed to a promoter that is more applicable to Drosophila systems. The decision was between two promoters, copia transposon promoter (COPIA) and actin 5C promoter (ACT5C). When comparing the two in both price and quality of the promoter the decision was made to get the ACT5C promoter. Both produce similar fluorescence signals in Drosophila (Qin, 2010), but when comparing prices, the ACT5C promoter made the most sense for this project. Promoters act as on and off switches. For this project, a promoter that is on at all times was required. This allows us to limit the influences of other cellular factors on our results. The complete plasmid will consist of several pieces. The piece will include: the ACT5C promoter, the body of the pHD-DsRed, and the 3' UTR sequences will be stitched together using this kit. The full plasmid will then be transformed into the cell culture and go through an electrical shock process to trigger the absorption of the plasmid into the cells.

The goal of the project I am proposing is to identify interactions between small noncoding RNAs from *Wolbachia* bacteria and protein-coding genes in *Drosophila* JW cells. This project will allow continued research of molecular relations between bacteria and host interactions. I will generate a DNA plasmid that contains the promoter, ACT5C, which acts as an on or off switch that is driving the DsRed gene, a fluorescent gene, and a 3' UTR target sequence, which the small noncoding RNAs will attach to. I will then insert the plasmid into the lung cells, one uninfected culture and one infected with *Wolbachia*. If the small noncoding RNAs generated by *Wolbachia* are complementary to the target sequences in the plasmids, are produced and hybridized with sufficient strength, there is expected to be a visual reduction or inactivity of fluorescence expression. Picture it like a flashlight that is always turned on and shining. If a piece of paper blocks the light, then it will shine less or not at all. If the small RNAs are not produced in sufficient quantity or strongly connected, the small RNAs will be able to be identified as non-targeting. The correctly assembled transgenic

plasmid will lead to CRISPR being able to identify small RNAs influenced by *Wolbachia* within lung cell lines.

This project will lead to a better understanding of the relationship between *Wolbachia* bacteria and their Drosophila hosts. This project will help determine whether the bacteria in our bodies, either helpful or harmful, affects the expression of our genes. Which in turn will lead to a greater understanding of how antibiotics and bacteria affect us at the genetic level. Antibiotics currently kill all bacteria in an area, not just the good or the bad. Therefore, my project could bring that characteristic into question and allow us to consider ways to limit the bacteria affected by antibiotics, specifically to infectious or harmful bacteria. It also has the potentially to limit the expression of genetic cancers or stop them altogether. Cancer researchers and antibiotic developers will have new questions to research, and it will show other scientists valuable information about how outside forces can affect the genome.

This project will combine the use of Drosophila cultures, one group infected with *Wolbachia* and one group uninfected, to determine if small noncoding RNAs from bacteria affect gene expression in the host. The DNA plasmid will consist of a pHD-DsRed with an added ACT5C promoter replacing the original and added 3'UTR sequences that was found in data from RNA library pools that were created. The DNA plasmid will be used to insert the fluorescent gene, DsRed, and the 3'UTR sequence the small RNA will attach to. This project will lead to a better understanding of interactions between bacteria and hosts at the molecular level and genetics as a whole.

2. Experimental Details

Two groups of *Drosophila* cells were purchased, one infected with *Wolbachia* and the other uninfected. Eight small RNA library pools were created from the two groups of *Drosophila* cells, four from the uninfected and four from the *Wolbachia* infected, using the NEBNext Small RNA Library Prep Set. The first step is to ligate the 3' SR adaptor, to do this use 1 µg of total RNA from each sample, 1 µl of 3'SR adaptor for Illumina, and nuclease-free water to bring the total volume to 7 µl were combined. The samples are incubated in a preheated thermal cycler for 2 minutes at 70℃ and then is transferred to ice. The following components were added to the samples: 10 µl of 3' Ligation Reaction Buffer (2X) and 3 µl of 3' Ligation Enzyme Mix. The samples were vortexed and incubated for one hour at 25℃ in a thermal cycler. The second step is to hybridize the reverse transcription primer, to do this add 4.5 µl of nuclease-free water and 1 µl of SR RT primer for Illumina and then mix the solution. Place the tube in a thermocycler with a heated lid and run it for 5 minutes at 75℃ then 15 minutes at 37℃ then 15 minutes at 25℃ then hold at 4℃. The third step is to ligate the 5' SR adaptor, which was briefly denatured at 70℃ for two minutes. Add 1 µl of the denatured 5' SR adapter for Illumina, 1 µl 5' ligation reaction buffer (10x), and 2.5 µl 5' ligation enzyme mix to bring the total volume to 30 µl for each sample. Mix the solution and incubate for one hour at 25℃ in a thermal cycler. The fourth step is to perform reverse

transcription to do this add 8 µl of the first strand synthesis reaction buffer, 1 µl of the murine RNase inhibitor, and 1 µl of the ProtoScript II reverse transcriptase and mix the solution. Next, incubate the solution for 60 minutes at 50℃ and immediately after start step five. The fifth step is to perform PCR amplification. Add and mix well 50 µl of LongAmp Taq 2X master mix, 2.5 µl SR primer for Illumina, 2,5 µl Index (X) primer, and 5 µl nuclease-free water. Use the recommended cycling conditions for the PCR program. The final step is to perform a quality control check and size selection, in this experiment, a bioanalyzer high-sensitivity DNA chip was used to evaluate quality.

To obtain plasmids cells needed to be grown. Plasmid-containing bacteria were grown in glycerol and quadrant streaked on ampicillin-coated LB Agar plates. To make the LB agar selection plates add 12.5g of LB Broth to 500 mL of deionized distilled water and stir until the clumps are gone. Then add 7.5g of agar, it will not dissolve, and autoclave for a 30-minute liquid cycle. Once the agar has cooled to the touch, use a serological pipet to transfer 25 µl to each plate and let them solidify. After the plates have solidified add 25 µl of ampicillin as you use them. The plates growing plasmid-containing bacteria are incubated overnight at 37℃ and several colonies are selected from those plates to be grown in 3 ml of LB broth with 3 µl of ampicillin overnight. LB broth is made by adding 12.5g of LB broth to 500 mL of deionized distilled water and stirring until the clumps are dissolved. Once the plasmid-containing bacteria has been grown in liquid culture use the Monarch Plasmid DNA Miniprep Kit to purify plasmid DNA. Using the Monarch Plasmid DNA Miniprep Kit pellet 1 ml of the bacterial culture by centrifuging for 30 seconds at 13,000 RPM and discard the supernatant after. Then mix the pellet with 200 µl of the plasmid resuspension buffer by vortexing. To lyse the cells, add 200 µl of the plasmid lysis buffer, invert the tubes until the solution changes to dark pink, and incubate for one minute. Add 400 µl of the plasmid neutralization buffer to neutralize the lysate. Invert the tubes until the color of the solution is yellow and a precipitate forms and incubate for two minutes. Centrifuge the solution for five minutes and transfer the supernatant to a spin column. Centrifuge the spin column for one minute and discard the flow-through. Add 200 µl of plasmid wash buffer 1 to the spin column and centrifuge for one minute. Then add 400 µl of plasmid wash buffer 2 and centrifuge for one minute. Transfer the column to a new tub and add 30 µl of elution buffer, let the elution buffer saturate the filter for one minute then centrifuge for one minute.

In order to isolate the DsRed fluorescence gene, the ampicillin resistance gene, and the origin of repliation pieces from the pHd-DsRed plasmid a double restriction enzyme digest was used. A double digest was conducted using 2 mg of plasmid DNA, 1 µl of NCOI, 1 µl of BamHI, 2 µl 10x tango buffer, and then water is added to reach a total volume of 20 µl. Incubate the solution at 37℃ for one hour and heat kill the enzymes at 70℃ for 20 minutes. The next step is to purify using agarose gel electrophoresis. The agarose gel should be a 0.8% gel with 60 ml of TBE that runs for an hour and 45 minutes. The final step to obtain the cut pHd-DsRed plasmid is to extract the isolated piece of the plasmid by cutting the band out of

the gel and extracting the DNA using the QIAquick Gel Extraction Kit. The first step when using the QIAquick Gel Extraction Kit is to weigh the gel slice and add three volumes of that amount in QG buffer. Once the QG buffer is added incubate the solution at 50℃ for 10 minutes, shaking occasionally. After the gel slice is melted add the weight of the gel slice in isopropanol to the solution and mix. Add the entire solution into the spin column and centrifuge – all centrifuge steps are one minute, then add 500 µl of QG buffer to the spin column and centrifuge, then add 750 µl of PE buffer to the spin column and incubate at room temperature for four minutes then centrifuge. Spin briefly in a tabletop centrifuge before transferring the spin column to a new tube and adding 30 µl of buffer EB. Once buffer EB is added let it incubate at room temperature for one minute then centrifuge.

To obtain the promoter from the ACT5C plasmid two PCR amplification reactions were used. The promoter was too large for one PCR amplification reaction to work successfully. Multiple smaller amplifications with overlapping primers allowed for successful amplification. The first reaction has 2 µl of template DNA in it with a concentration of 87.3 ng/ µl, 5 µl of 5x Green GoTaq Flexi buffer, 2 µl of dNTPs, 1.5 µl of $MgCl_2$, 0.5 µl of the AC5_DsRed_1F primer, 0.5 µl of the AC5_DsRed_1R primer, 0.5 µl of Taq, and enough deionized distilled water to reach a total of 25 µl in the reaction. The second reaction has 2 µl of template DNA in it with a concentration of 87.3 ng/ µl, 5 µl of 5x Green GoTaq Flexi buffer, 2 µl of dNTPs, 1.5 µl of $MgCl_2$, 0.5 µl of the AC5_DsRed_2F primer, 0.5 µl of the AC5_DsRed_2R primer, 0.5 µl of Taq, and enough deionized distilled water to reach a total of 25 µl in the reaction. Run the reactions through a PCR program with the following parameters: initial denaturation at 95℃ for one minute; for 35 cycles have denaturation at 95℃ for 30 seconds, annealing at 47℃ for 30 seconds, and extension at 72℃ for one minute and 30 seconds; final extension at 72℃ for 10 minutes; and to finish out the program set it to 4℃ for infinity. After the PCR program finishes, run the reaction through agarose gel electrophoresis to check for the proper size of the promoter and to purify the DNA from the gel using the QIAquick Gel Extraction Kit.

The next step is ligating the pieces from each plasmid, the pHd-DsRed and ACT5C, together to build the final plasmid, the pAc5 plasmid. In order to ligate the pieces together the NEBuilder HiFi DNA Assembly Kit is used. To reach a total of 0.06 pmols of DNA when using 2 fragments, 0.02 pmols of the vector, the pHd-DsRed plasmid, and 0.04 pmols of the insert, the ACT5C plasmid, according to the ratio and recommended pmols of DNA fragments as described in the reaction protocol. The vector needs to have a concentration of 60 ng added to the tube. The insert needs to have a concentration of 75 ng added to the tube. The amount of µl needed for the vector and insert is determined on an individual basis by the concentration of the DNA sample you have at the time. Add 10 µl of Assembly Master Mix to the tube and add the amount of water required to make the total volume reach 20 µl. Incubate the sample(s) in a thermocycler at 50℃ for 60 minutes then store on ice.

The next step is continuing to use the NEBuilder HiFi DNA Assembly Kit to transform the cells. First, thaw the competent cell tube from New England Biolabs on ice and add 2 µl of the assembly mix to the cells. Pipet gently to mix and place the mixture on ice for 30 minutes, then heat shock at 42℃ for 30 seconds. After heat shock, transfer the tubes to ice for 2 minutes and add 950 µl of room temperature SOC medium to the tube. Incubate the tube at 37℃ for 60 minutes while shaking at 250 rpm. While the tube is incubating, warm the selection plates to 37℃ and add 25 µl of ampicillin to the plates. After the selection plates are warmed, light a Bunsen burner to sterilize the air and the spread bar then spread 100 µl of the cells onto the selection plates and incubate overnight at 37℃. The next day, warm the selection plates to 37℃ and add 25 µl of ampicillin to the plates. Once the plates are warmed draw 3 lines horizontally and 3 lines vertically on the bottom of the plate to make a 12-space grid. Label the spaces and label 12 PCR tubes 1-12. Remove the spread plates from the incubator from the day before and select 12 random colonies. Use an autoclaved toothpick to pick up one of the selected colonies and swap the PCR tube with the toothpick. Next, stab the toothpick into the agar plate in the coordinating space and repeat this process for the other 11 colonies with different toothpicks. Once all 12 colonies have been selected and stab cultured, incubate the plate overnight at 37℃. The next day, remove the plate from the incubator and wrap the plate in parafilm to store at 4℃.

To check the proper assembly and ligation of the plasmid pieces we run a specific PCR program to check the binding sites. Using the PCR tubes that have the stab culture samples in them add a master mix containing 5 µl of 5x Green GoTaq Flexi buffer, 2 µl of dNTPs, 1.5 µl of $MgCl_2$, 0.5 µl of the red_ac5_junction_ F primer, 0.5 µl of the red_ac5_junction_R primer, 0.5 µl of Taq, and 15 µl deionized distilled water for each of the samples you are running, in this case, 12. Place the 12 samples in the thermocycler and start the program. The program consists of three stages. The first stage, initial denaturation, runs at 95℃ for two minutes. The second stage, consists of denaturation which runs at 95℃ for 30 seconds, annealing which runs at 50℃ for 30 seconds, and extension which runs at 72℃ for 30 seconds. The third stage, final extension, runs at 72℃ for five minutes and then drops to 4℃ and lasts forever. After the PCR program finishes gel electrophoresis needs to be set up and run to check for the proper sizing, 218 bps, and that the pieces are properly assembled in the pAc5 plasmid.

3. Results

Successful restriction enzyme digestion was conducted on the pHd-DsRed. The NCOI enzyme cut at 1552 bp mark. The BamHI enzyme cut at the 1376 mark. When run on a gel the expected band size was seen (Figure 2) and cut from the band for purification using the QIAquick Gel Extraction Kit.

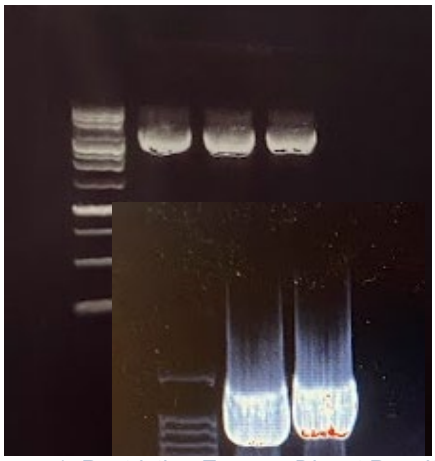

Figure 1: Restriction Enzyme Digest Results from NCOI and BamHI double digest.

Figure 2: AC5 Promoter Amplification Result

Successful amplification of the promoter from ACT5C was conducted. These are gel images from the AC5 promoter amplification. From figure 3 you can see that there was amplification and that it was the size we expected to see. The reaction run with the 1f and 1R primers is on the right of the gel image. The reaction run with the 2F and 2R primers is on the left of the gel image. The primers amplified the correct sequence and expected sizes were seen when run on a gel. The correctly sized bands were cut from the gel and DNA was extracted using the QIAquick Gel Extraction Kit.

These gel images (Figure 4 and Figure 5) depict the successful ligation and transformation of the pAc5 plasmid. We know the ligation was successful because the primers used in this PCR reaction straddle one of the spots where the plasmid pieces connected, and the product is the expected 218 bps in length. We know the transformation was successful because the PCR was run using the cells we transfected with the ligated plasmid. These images prove the pAc5 plasmid was built correctly and is performing its intended role thus far.

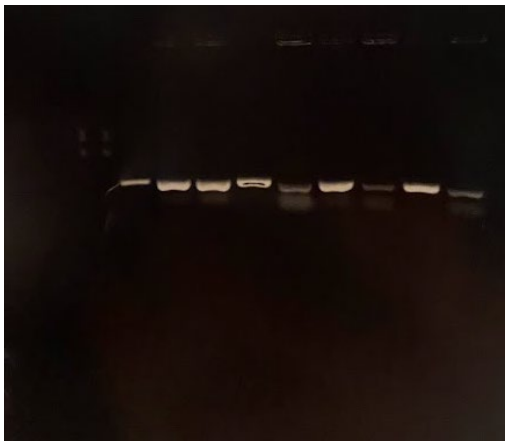

Figure 3: Ligation and Transformation Results Samples 1-9

Figure 4: Ligation and Transformation Results Samples 10-12

4. Discussion and Conclusions

The pAc5 plasmid was successfully assembled to contain the constituently active promoter, AC5, and the fluorescence gene and the ampicillin resistance gene, pHd-DsRed. This plasmid can now be used in the next phase of the *Drosophila* project, which includes adding 3' UTR target sponges to the plasmid and transforming the plasmids into infected and uninfected *Drosophila* cells. The building of the pAc5 plasmid had several complications. For example, the PCR product to check for the proper assembly was never amplified in gels, with many changes. (insert gel images) It was assumed that the assembly was not happening properly because the pHd-DsRed plasmid was not digested well. This was assumed because cells were growing on ampicillin-coated plates and the ampicillin resistance gene came from the pHd-DsRed plasmid. However, it was not realized until later in the project that both the plasmids used to construct the pAc5 contained ampicillin resistance genes. This was discovered when DNA from cells that were run through PCR to check for the assembly was sequenced. It became very apparent that the pHd-DsRed plasmid was nowhere in the DNA sequence of those cells. It was quickly realized the primers used to amplify the promoter from the ACT5C plasmid were amplifying much more than the promoter alone. New primers were designed to target the promoter more specifically through the use of the DNA sequences we obtained.

This project will lead to a better understanding of the relationship between *Wolbachia* bacteria and their *Drosophila* hosts. The results of this project will help determine whether the bacteria in our bodies, either helpful or harmful, is affecting the expression of our genes. This will lead to a greater understanding of how antibiotics and bacteria affect us at the genetic level. Antibiotics currently kill all bacteria in an area, not just the good or the bad. Therefore, my project could bring that characteristic into question and allow us to consider

ways we can limit the bacteria affected by antibiotics, specifically to infectious or harmful bacteria. It also can potentially limit the expression of genetic cancers or stop them altogether. Cancer researchers and antibiotic developers will have new research questions, showing other scientists valuable information about how outside forces can affect the genome.

5. Summary

In conclusion, gene expression can be affected by various factors, possibly including bacterial small non-coding RNAs. *Drosophila* cell culture and *Wolbachia* bacteria were used to investigate whether small RNAs from bacteria affect gene expression in the host. MiRNAs are involved in almost every cellular process, and the bacterial small non-coding RNA mechanism is believed to be similar to the miRNA mechanism. The project used two existing types of plasmids to build a new plasmid that will be transformed into *Drosophila* calls after the addition of a target sequence. There is a need for further research on small RNAs and the potential impact on antibiotics if bacteria naturally affect gene expression in the body.

6. Appendices

6a. Acknowledgments

I would like to acknowledge and thank Dr. and Mrs. Niblack for their generous contribution. I would also like to thank Dr. Darren Hagen for his support and assistance, in and out of the laboratory over the past two years. I would also like to thank Anna Goldkamp for her help, enthusiasm, and support over the last two years.

6b. Literature Cited

Addgene: pHD-DsRed. (n.d.). https://www.addgene.org/51434/

Baenas, N., & Wagner, A. E. (2019c). Drosophila melanogaster as an alternative model organism in nutrigenomics. *Genes &Amp; Nutrition*, *14*(1).

Gebert, L.F.R. and I.J. MacRae, *Regulation of microRNA function in animals.* Nat Rev Mol Cell Biol, 2019. **20**(1): p. 21-37.

Gratz, S. J., Ukken, F. P., Rubinstein, C. D., Thiede, G., Donohue, L. K., Cummings, A. M., & O'Connor-Giles, K. M. (2014). Highly Specific and Efficient CRISPR/Cas9-Catalyzed Homology-Directed Repair in *Drosophila*. *Genetics*, *196*(4), 961–971. https://doi.org/10.1534/genetics.113.160713

Ha, M. and V.N. Kim, *Regulation of microRNA biogenesis.* Nat Rev Mol Cell Biol, 2014. **15**(8): p. 509-24.

Kabekkodu, S.P., et al., *Clustered miRNAs and their role in biological functions and diseases.* Biol Rev Camb Philos Soc, 2018. **93**(4): p. 1955-1986. https://doi.org/10.1186/s12263-019-0641-y

Qin, J. Y. (2010, May 12). *Systematic Comparison of Constitutive Promoters and the Doxycycline-Inducible Promoter*. PLOS ONE. Werren, J., Baldo, L. & Clark, M. *Wolbachia:* master manipulators of invertebrate biology. *Nat Rev Microbiol* 6, 741–751 (2008). https://doi.org/10.1038/nrmicro1969

In Vivo Assay: Bacterial Small Non-coding RNAs May Regulate Eukaryotic Gene Expression

Natalee Richardson
Faculty Mentor: Dr. Darren Hagen, Ph.D.
Dept. of Animal and Food Science
Oklahoma State University, Stillwater

Agenda

1. Cover the Overarching Question
2. Background Information and Introduction
3. Experimental Details
4. Results
5. Discussion
6. Conclusion
7. Acknowledgements
8. References

Over-Arching Question

The goal of this project is to identify interactions between bacterial small noncoding RNAs and host protein coding genes.

Small Non-Coding RNAs

- Non-coding regions makes up 98% of our genome
- Small RNAS are 18-30 nucleotides
- Noncoding RNAs produced by bacteria/viruses and the host may be involved

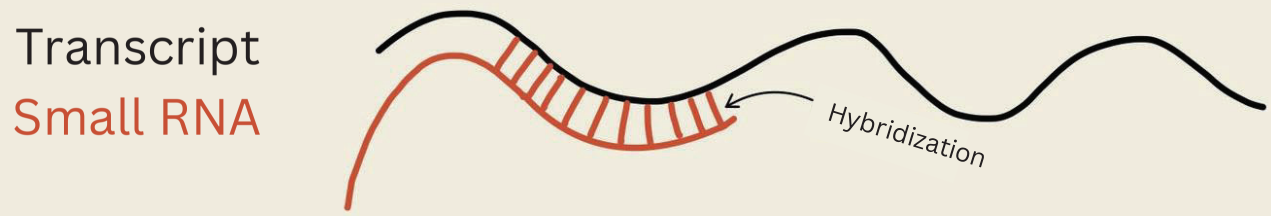

Drosophila

Chosen because of:

- Rapid life cycle
- easy generation of mutant animals
- share 40% of the nucleotide and protein sequence with mammalian species (Baena, 2019)

Wikimedia Commons

Wolbachia

- Wolbachia are an intercellular bacteria
- Wolbachia usually do not infect vertebrates
- Naturally effects Drosophila

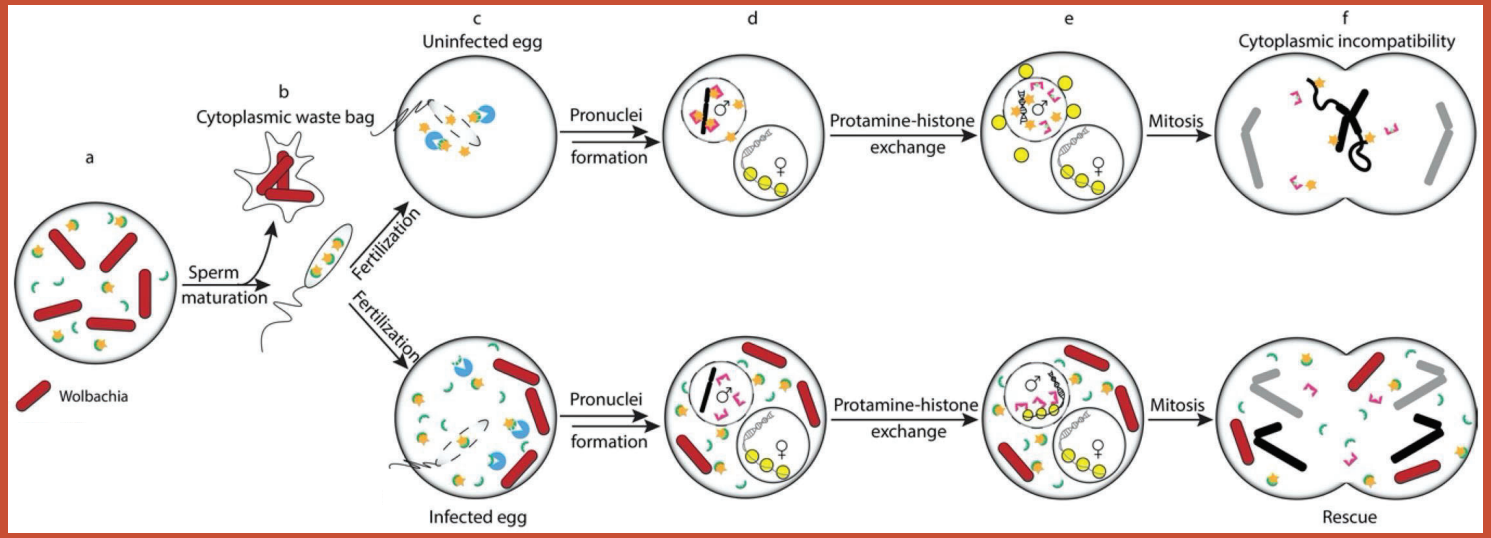

Chen, et al., 2020

Background and Introduction Information

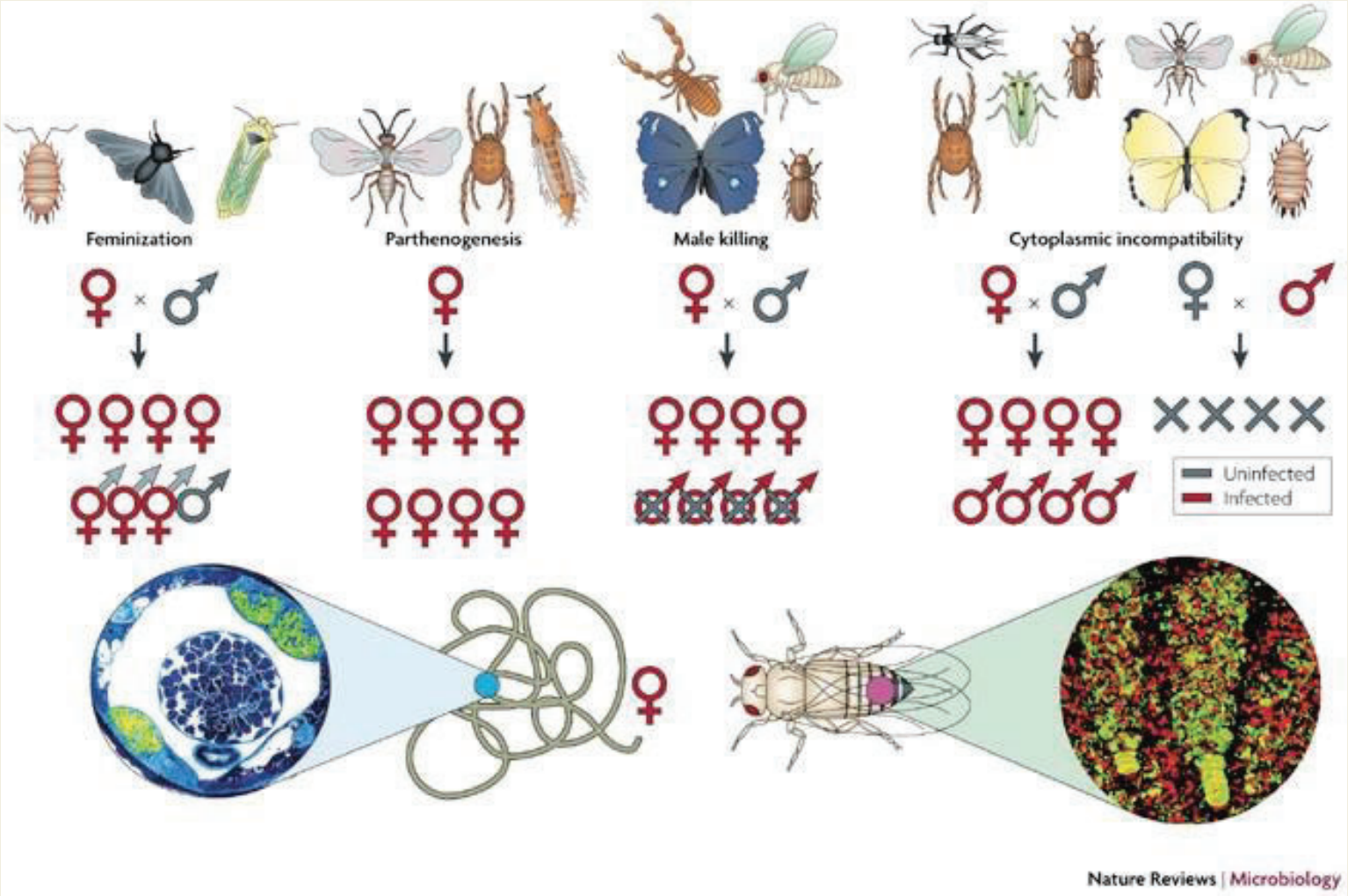

Cytoplasmic Incompatibility

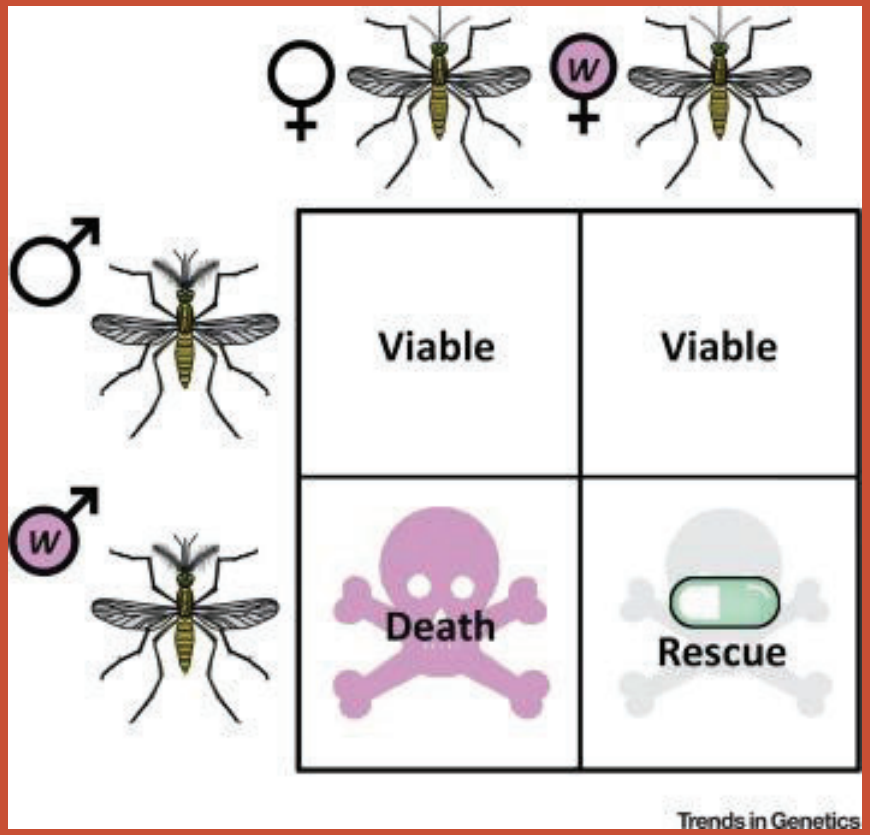

Background and Introduction Information

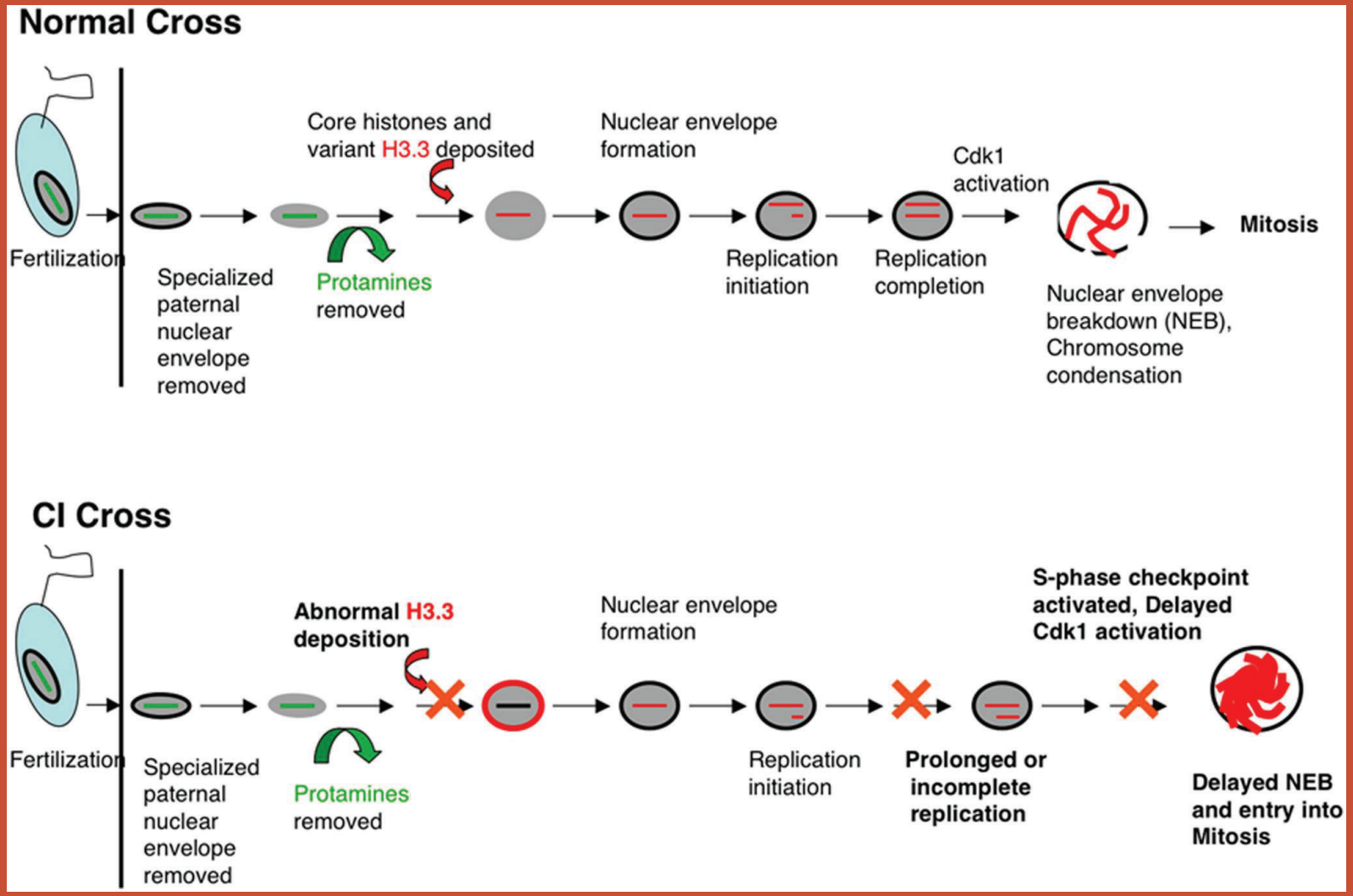

Proposed Mechanism

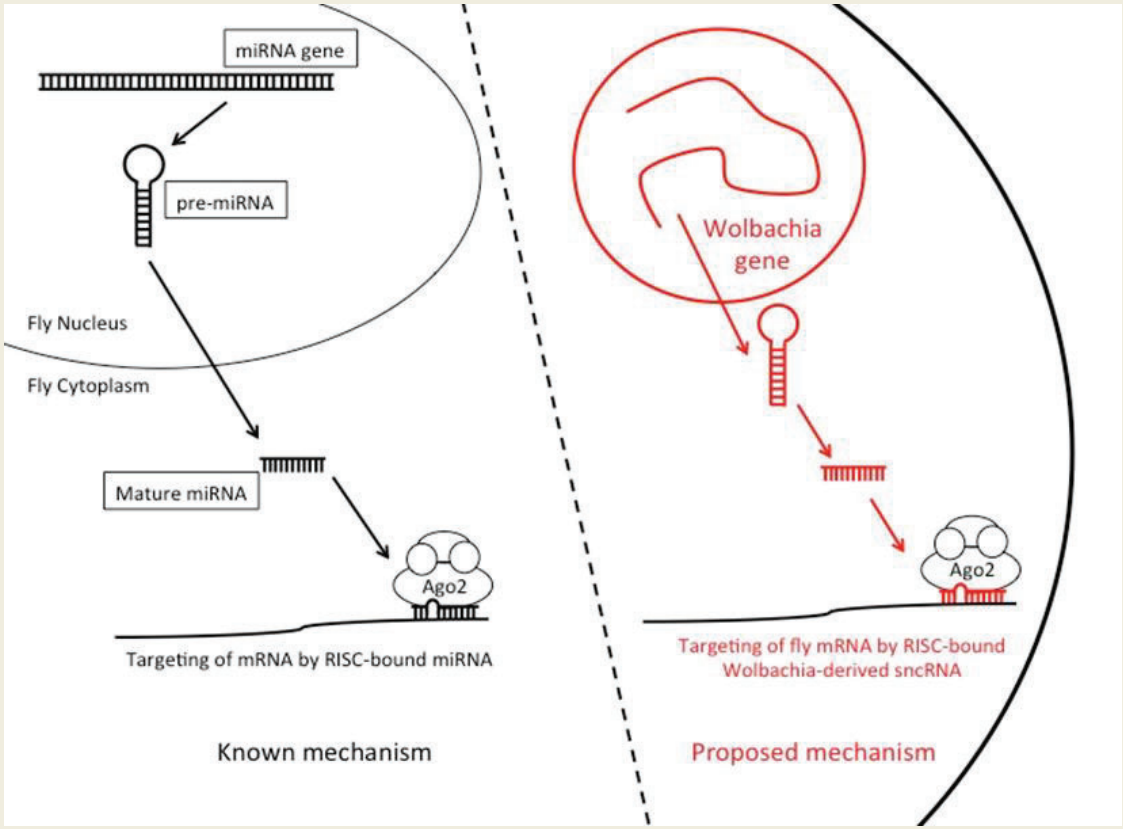

Plasmids

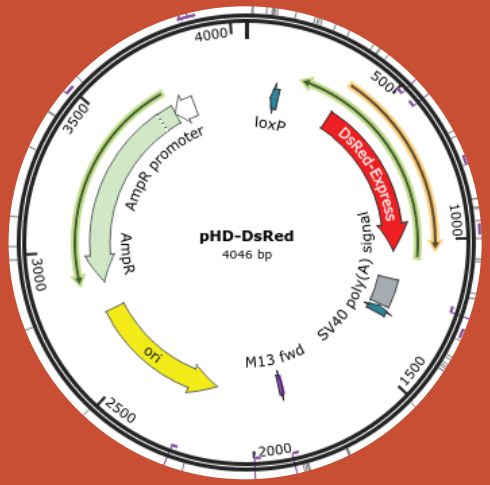

pHd-DsRed

+

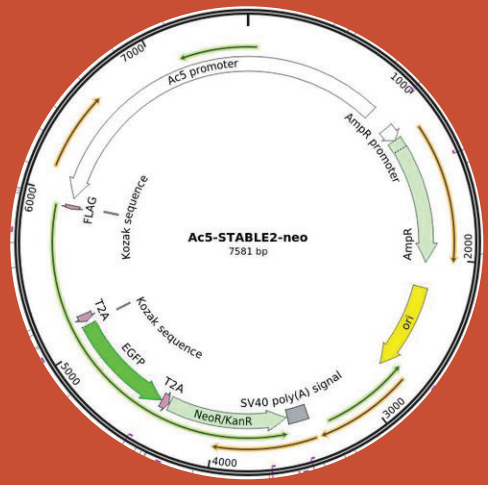

ACT5C

Experimental Details

Experimental Details

Create Small RNA Library Pools (NEBNext Small RNA Library Prep Kit)
Making Broths and Agars
Purifying Plasmid DNA (Monarch Plasmid DNA Miniprep Kit)
Isolation of specific pieces of the pHd-DsRed Plasmid (Restriction Enzyme Digest, AGE, Gel Cutting and Extraction
Isolation of the Promoter from the ACT5C Plasmid (Making PCR Reactions to Target the Promoter, Run a PCR Program, AGE and Gel Extraction)
Ligation and Transfection of Plasmid Pieces (Using NEBuilder HiFi DNA Assembly Kit)
Plating Transfected Cells
Check for Proper Assembly and Ligation of the pAC5 Plasmid (Stab culture, PCR, AGE)

Plasmids

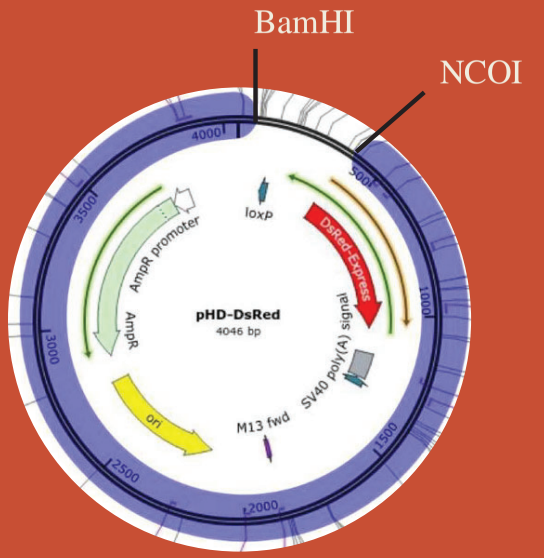

pHd-DsRed

+

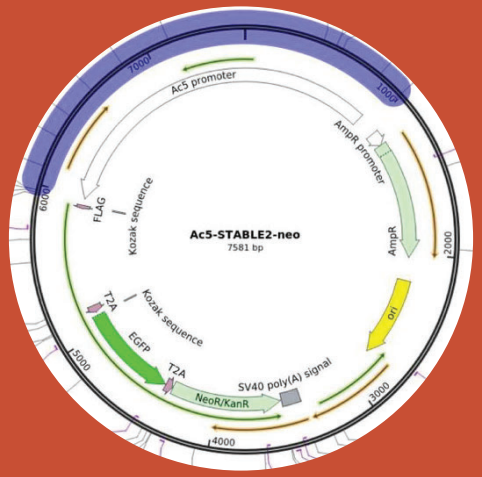

ACT5C

=

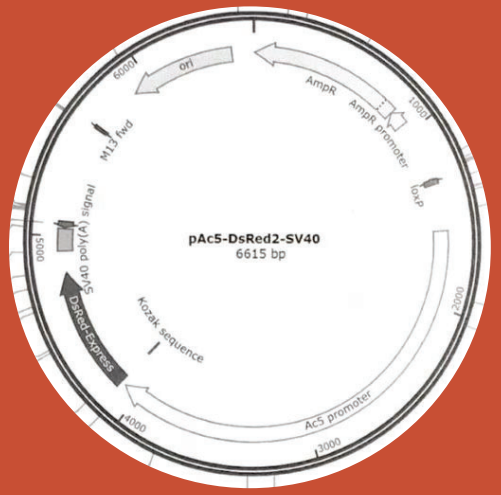

pAc5

Experimental Details

Create Small RNA Library Pools (NEBNext Small RNA Library Prep Kit)
Making Broths and Agars
Purifying Plasmid DNA (Monarch Plasmid DNA Miniprep Kit)
Isolation of specific pieces of the pHd-DsRed Plasmid (Restriction Enzyme Digest, AGE, Gel Cutting and Extraction
Isolation of the Promoter from the ACT5C Plasmid (Making PCR Reactions to Target the Promoter, Run a PCR Program, AGE and Gel Extraction)
Ligation and Transfection of Plasmid Pieces (Using NEBuilder HiFi DNA Assembly Kit)
Plating Transfected Cells
Check for Proper Assembly and Ligation of the pAC5 Plasmid (Stab culture, PCR, AGE)

Transfection

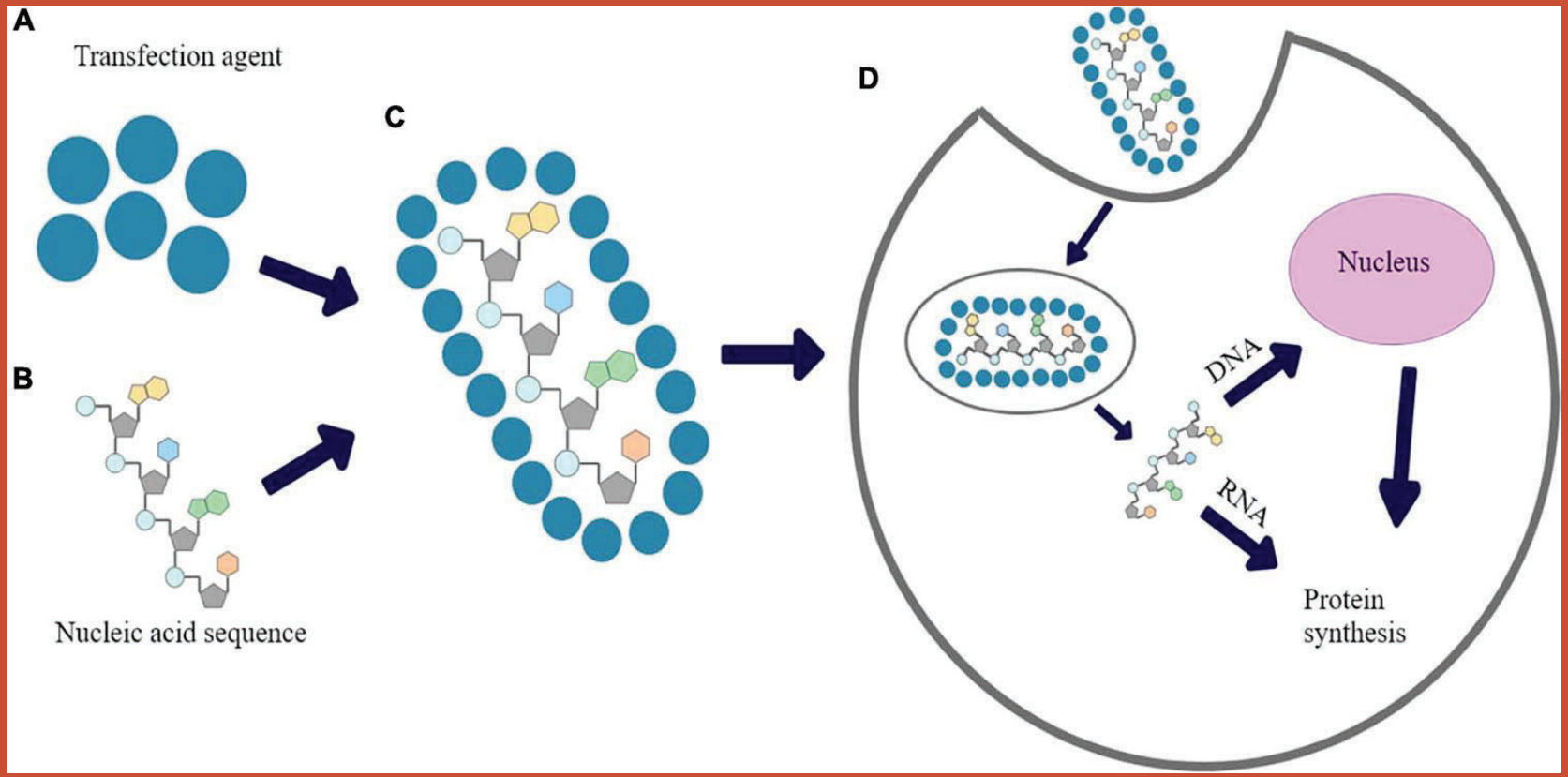

Fus-Kujawa, et al., 2021

Experimental Details

Create Small RNA Library Pools (NEBNext Small RNA Library Prep Kit)
Making Broths and Agars
Purifying Plasmid DNA (Monarch Plasmid DNA Miniprep Kit)
Isolation of specific pieces of the pHd-DsRed Plasmid (Restriction Enzyme Digest, AGE, Gel Cutting and Extraction)
Isolation of the Promoter from the ACT5C Plasmid (Making PCR Reactions to Target the Promoter, Run a PCR Program, AGE and Gel Extraction)
Ligation and Transfection of Plasmid Pieces (Using NEBuilder HiFi DNA Assembly Kit)
Plating Transfected Cells
Check for Proper Assembly and Ligation of the pAC5 Plasmid (Stab culture, PCR, AGE)

Experimental Details

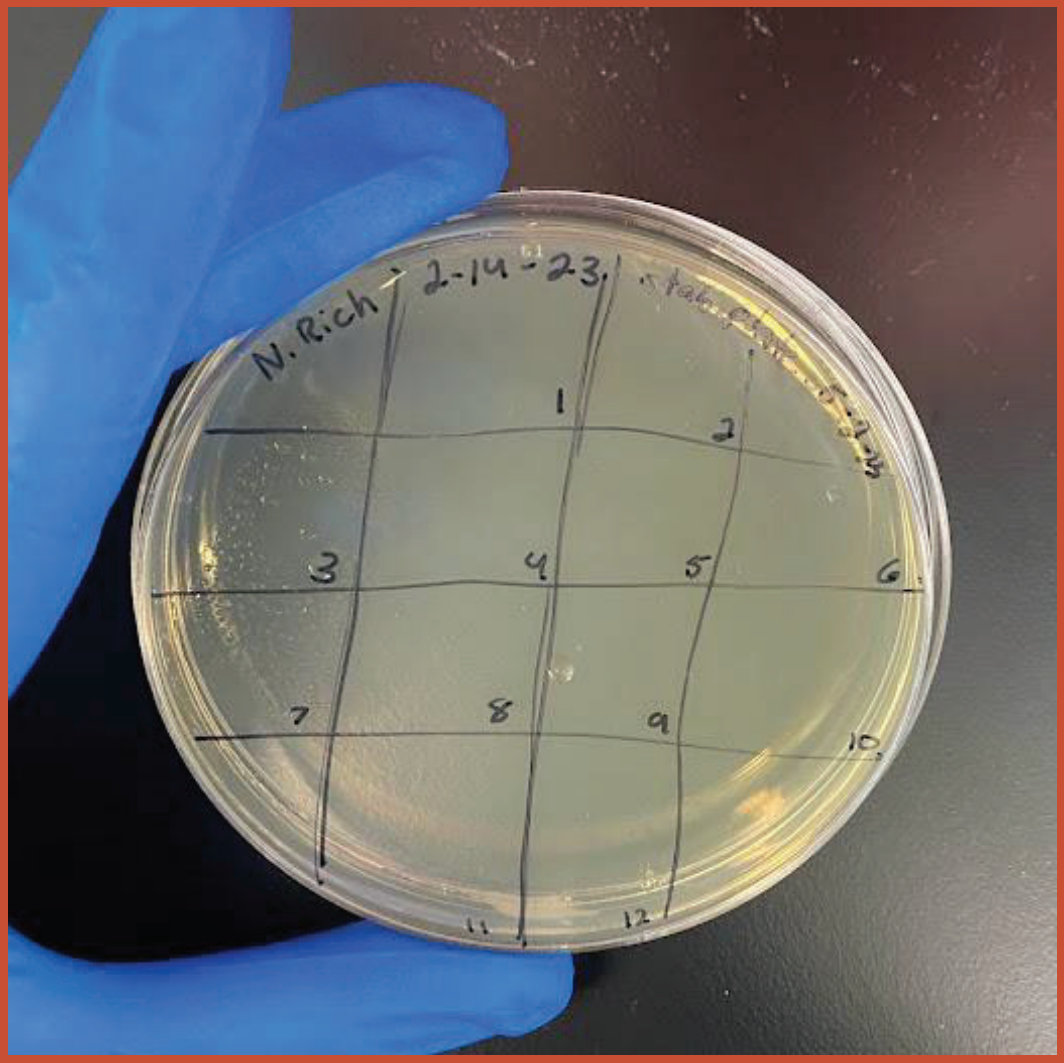

Experimental Details

Create Small RNA Library Pools (NEBNext Small RNA Library Prep Kit)
Making Broths and Agars
Purifying Plasmid DNA (Monarch Plasmid DNA Miniprep Kit)
Isolation of specific pieces of the pHd-DsRed Plasmid (Restriction Enzyme Digest, AGE, Gel Cutting and Extraction
Isolation of the Promoter from the ACT5C Plasmid (Making PCR Reactions to Target the Promoter, Run a PCR Program, AGE and Gel Extraction)
Ligation and Transfection of Plasmid Pieces (Using NEBuilder HiFi DNA Assembly Kit)
Plating Transfected Cells
Check for Proper Assembly and Ligation of the pAC5 Plasmid (Stab culture, PCR, AGE)

Results

Restriction Enzyme Digest Results

AC5 Promoter Amplification Results

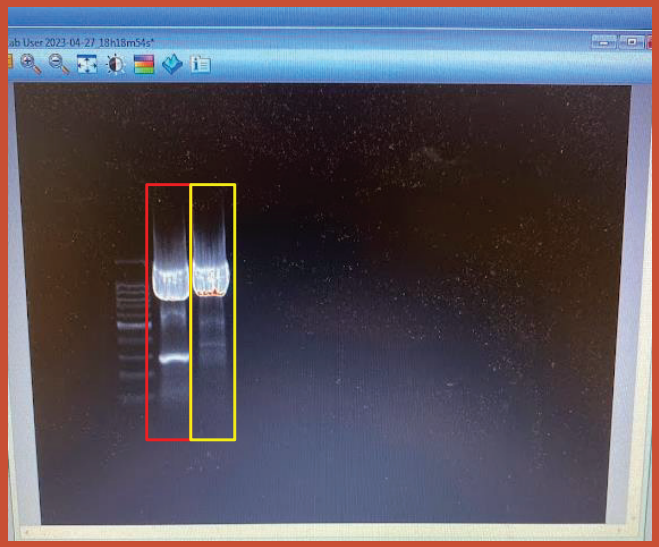

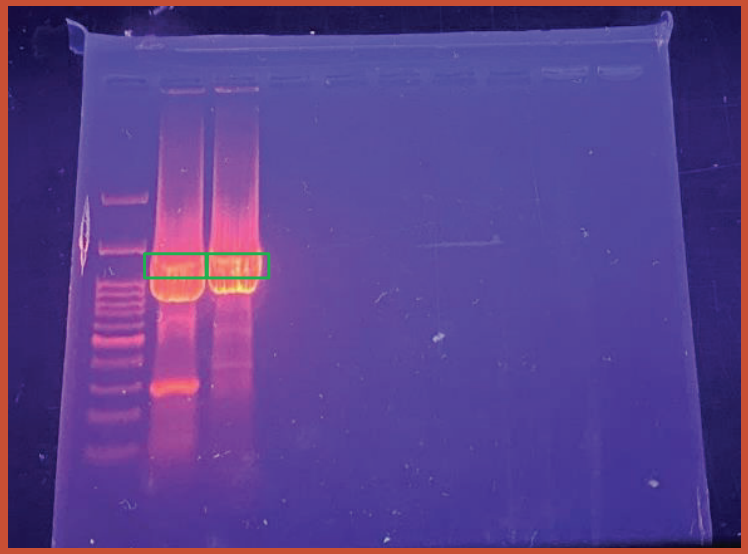

Ligation and Transfection Results

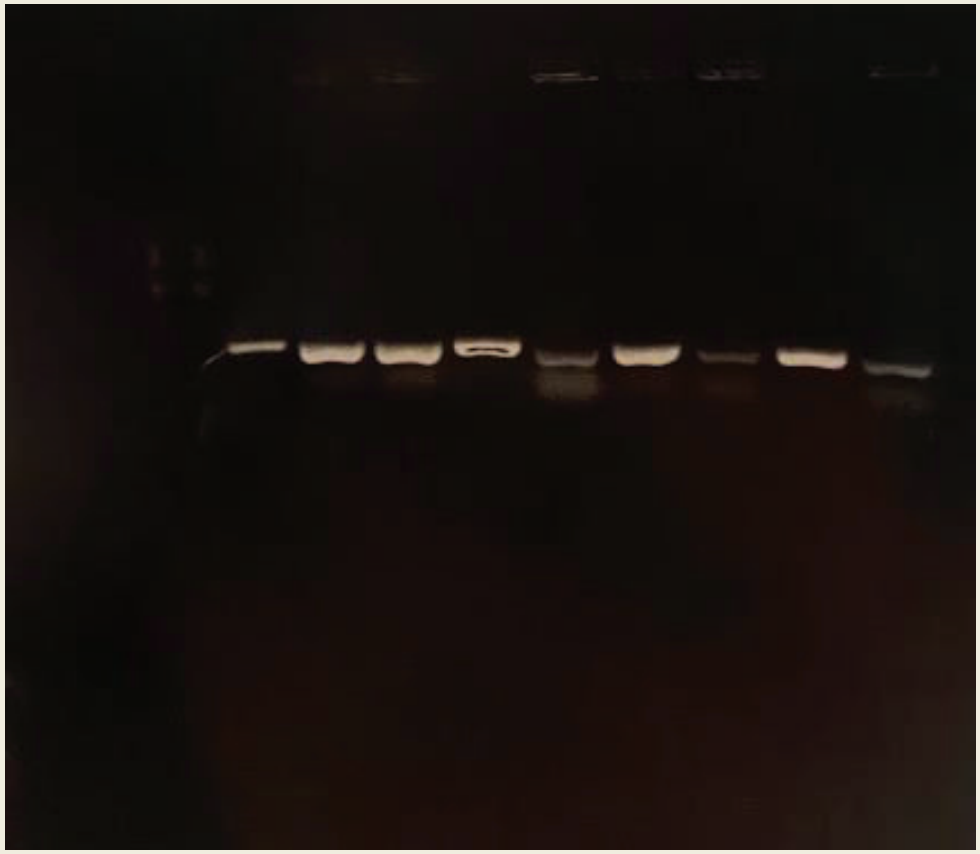

Future Directions

The Next Steps

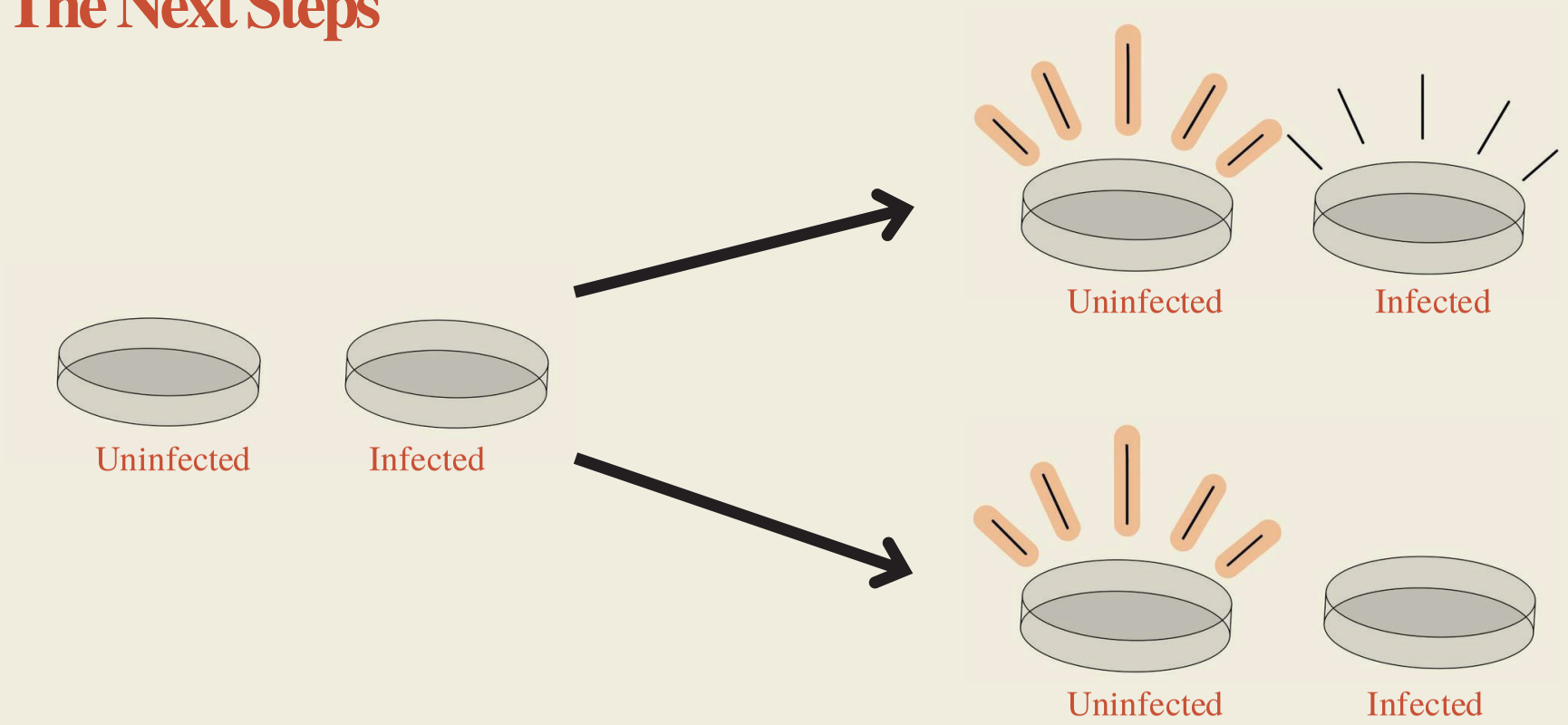

Discussion

- Complications:
  - The PCR product to check for the proper assembly was not being amplified in gels
  - Thought the pHd-DsRed plasmid was not digested well.
  - Realized that both the plasmids used to construct the pAc5 contained ampicillin resistance genes.
  - The pHd-DsRed plasmid was nowhere in the DNA sequence of those cells.
  - The primers used to amplify the promoter from the ACT5C plasmid were amplifying much more than the promoter alone.

Discussion

- Better understanding of the relationship between bacteria and hosts
- Determine if bacteria affects the expression of our genes
- Potential to affect the way we think about antibiotics and other medical treatments

Conclusion

Combined use of:

- Drosophila cultures
  - infected culture
  - uninfected culture
- pAc5 DNA plasmid
  - Fluorescent gene
  - Ampicillin Resistance gene
  - Actin 5 Promoter
  - 3'UTR "sponge" sequence
- Transfection of plasmids into cells

Will lead to better understanding of bacteria and host interactions.

What this Project has Meant to Me

- Many opportunities to present research
- Allowed me the chance to work towards my Master's of Science
- Allowed me the chance to attend the University of Guelph

Acknowledgements

I would like to thank:

- Dr. And Mrs. Niblack
- Dr. Darren Hagen
- Anna Goldkamp
- The Members of Hagen Lab

References

Baenas, N., & Wagner, A. E. (2019c). Drosophila melanogaster as an alternative model organism in nutrigenomics. Genes &Amp; Nutrition, 14(1).

Gebert, L.F.R. and I.J. MacRae, Regulation of microRNA function in animals. Nat Rev Mol Cell Biol, 2019. 20(1): p. 21-37.

Gratz, S. J., Ukken, F. P., Rubinstein, C. D., Thiede, G., Donohue, L. K., Cummings, A. M., & O'Connor-Giles, K. M. (2014). Highly Specific and Efficient CRISPR/Cas9-Catalyzed Homology-Directed Repair in Drosophila. Genetics, 196(4), 961–971.https://doi.org/10.1534/genetics.113.160713

Ha, M. and V.N. Kim, Regulation of microRNA biogenesis. Nat Rev Mol Cell Biol, 2014. 15(8): p. 509-24.

Kabekkodu, S.P., et al., Clustered miRNAs and their role in biological functions and diseases. Biol Rev Camb Philos Soc, 2018.93(4): p. 1955-1986.https://doi.org/10.1186/s12263-019-0641-y

Landmann, Frédéric, et al. "Wolbachia-Mediated Cytoplasmic Incompatibility Is Associated with Impaired Histone Deposition in the Male Pronucleus." *PLOS Pathogens*, vol. 5, no. 3, Mar. 2009, p. e1000343. *PLoS Journals*, https://doi.org/10.1371/journal.ppat.1000343.

Qin, J. Y. (2010, May 12). Systematic Comparison of Constitutive Promoters and the Doxycycline-Inducible Promoter. PLOSONE.

Werren, J., Baldo, L. & Clark, M. Wolbachia: master manipulators of invertebrate biology. Nat Rev Microbiol 6, 741–751 (2008). https://doi.org/10.1038/nrmicro1969

Any Questions?

SESSION THREE:

Brinkli Abbitt

"Identifying Efficient Methods of Determining the Electrochemical Window of Ionic Liquids"
Research Area: Chemical Engineering
Faculty Sponsor: Dr. Jindal Shah
Graduate Student Mentor: Sudip Das

Samantha Stobbe

"Visible Light-Driven C-C Coupling Reaction of Terminal Alkynes at Atmospheric Temperature and Pressure Reaction Conditions using Hybrid Cu2O-Pd Nanostructures"
Research Area: Chemical Engineering
Faculty Sponsor: Dr. Marimuthu Andiappan
Graduate Student Mentor: Ravi Teja Tirumala; Sundaram Bhardwaj Ramakrishnan

Sam Glenn

"Morphological Characterization of Wing Shapes of Tiny Insects"
Research Area: Mechanical and Aerospace Engineering
Faculty Sponsor: Dr. Arvind Santhanakrishnan
Graduate Student Mentor: Mitchell Ford

Identifying Efficient Methods of Determining the Electrochemical Window of Ionic Liquids

Brinkli Abbitt

Chemical Engineering
Faculty Sponsor: Jindal Shah
Graduate Mentor: Sudip Das

ABSTRACT
This study aims to present an investigation into the methods employed to determine the electrochemical window (ECW) of 50 distinct ionic liquids, employing density functional theory (DFT) calculations. Key parameters in quantum mechanics including the Gibbs free energy, total energy, and the energies of the highest occupied molecular orbital (HOMO) and lowest unoccupied molecular orbital (LUMO) were evaluated. These calculations were performed with the functionals B3LYP and M06L at a fixed basis set 6-311+g(2d,p), and were subject to both vacuum and solvent conditions.

1. Introduction

As the world shifts towards more renewable energy sources to aide in the fight against climate change, offering a cleaner and more sustainable future has become a necessity; however, the unpredictable nature of renewable energy, such as solar and wind, presents a unique set of challenges. Traditional nonrenewable energy sources like coal, fossil fuels, and natural gas have long been favored partially due to their reliability, a trait that renewable sources sometimes lack and as we transition towards renewable energy, the concern for efficient and safe energy storage is important to address. Anxiety for the future is only further fueled by both the unreliability of this new source and the volatility of the available energy storage options.

Modern batteries, while efficient, harbor significant safety concerns that are important to take into consideration. The electrolytes used within today's aqueous batteries can be volatile, prone to short-circuiting, local heating, and even ignition at elevated temperatures. This precarious nature of existing storage technology has spurred an urgent quest for innovative, clean, and safe electrolytes, steering the focus towards the world of ionic liquids.

Ionic liquids, also referred to as "designer solvents," have recently emerged as as attractive substitutes for conventional electrolytes in batteries, fuel cells, and supercapacitors. Ionic liquids are significantly safer due to their nearly nonexistent volatility, good thermal stability, and minimal flammability. They avoid efficiency problems related to the limited Electrochemical Potential Windows (EPWs) of many modern electrolytes by having

excellent conductivity and broad EPWs. (Brennecke, n.d.) This adaptability sets them apart, allowing their properties to be fine-tuned by manipulating their respective anion and cation components.

Ionic liquids' adaptability allows for a wide range of applications, but it also indicates a complex landscape of potential uses, making experimental investigation expensive and time-consuming. It takes a lot of time and resources to carefully investigate each cation and anion pairing to evaluate its characteristics and applicability. In this context, the role of quantum chemical calculations becomes paramount. Quantum computing, being faster, more accessible, and more cost-effective, offers a pragmatic approach to explore the vast and uncharted territory of ionic liquids. By employing quantum chemical calculations, researchers can predict beneficial ionic liquid combinations rather than relying on random selection and laborious experimentation.

To deepen our understanding of these unique substances, this study explores quantum chemical computations to examine the electrochemical characteristics of 50 ionic liquids. We aim to provide insightful contributions to the developing field of energy storage and stimulate a more comprehensive transition to renewable energy by explaining the most effective approach to ascertain the Electrochemical Window (ECW) of an ionic liquid. Similar research only further highlights the urgent need for novel energy storage solutions that resonate with the global ambition to develop a more robust and sustainable future.

2. Experimental Details

Density Functional Theory (DFT) Calculations: Quantum chemical calculations were performed using Density Functional Theory (DFT), a computational modeling method that utilizes the Schrödinger's equation to describe the electronic structure of a system. By solving this equation, DFT aids in determining a molecule's optimum geometric structure and electron distribution. This optimization is essential to ascertain the system's ground state energy, offering insight into its stability and reactivity. Identifying the ground state energy is synonymous with locating the molecule's optimum geometric structure, where the forces between the atoms are balanced, and the system's energy is at its minimum.

Structure optimization was carried out to locate the most stable geometric conformation of the molecules, ensuring that the energy is at a minimum. Following the optimization, frequency calculations were performed to validate that the structures reside at energy minima, a prerequisite for the accurate assessment of thermodynamic properties.

The calculations were conducted employing two different functionals, M06L and B3LYP. A functional in DFT provides the exchange-correlation energy, governing the interactions between electrons. Comparisons were made for ionic liquids (ILs) both in vacuum and in a solvent possessing a dielectric constant analogous to the average IL. The use of the solvent 1,2-Dichloroethane with a similar dielectric constant to that of the average

ionic liquid which essentially simulates ion interactions, as the dielectric constant quantifies a material's ability to reduce the electrostatic force between charges. (Weingärtner, 2006)

Fifty IL calculations were conducted with both cation and anion present, from which the Highest Occupied Molecular Orbital (HOMO) and Lowest Unoccupied Molecular Orbital (LUMO) energies were collected from the optimized structures. These calculations were performed on the Pete supercomputer, utilizing the Gaussian 09 suite of programs.

Methods Employed:

Koopmans' Theorem with IL Pairs: According to Koopmans' theorem, the negative of the energy of the HOMO is equal to the ionization energy (IE) of the system. Similarly the negative of the energy of the lowest unoccupied molecular orbital (LUMO) can be used to approximate the electron affinity (EA) of the system. (Tsuneda et al., 2010) The Electrochemical Window (ECW) was then computed as the difference between IE and EA. These calculations were run in solvent and vacuum (using M06L and B3LYP functionals).

$$\mathrm{IE} = -\mathrm{E}HOMO \tag{1}$$

$$EA = -\mathrm{E}LUMO \tag{2}$$

$$ECW = IE - EA \tag{3}$$

Koopmans' Theorem with Ion Pairs: In this method the ionic liquid cations and anions were calculated separately to better observe the individual ion properties. The IE and EA of ions were obtained from the HOMO and LUMO energies. The maximum IE of both cations and anions, and the minimum EA of both charged and neutral cations and anions were used to calculate the ECW as ECW = IE − EA.

$$IE = max < -E_{HOMO,cation}, -E_{HOMO,anion} > \tag{4}$$

$$EA = min < -E_{LUMO,cation}, -E_{LUMO,anion} > \tag{5}$$

These methods, incorporating DFT, structural optimization, functional and solvent selection, provide an analysis of the ECW for ionic liquids. By understanding the potentials, HOMO and LUMO energies, the total energy, and the Gibbs free energy, we can deepen our insights into the electrochemical properties of ionic liquids. The integration of these concepts fosters a robust exploration of the ECW, contributing vital knowledge to the field of efficient and safe energy storage.

3. Results

The application of the Koopman method for IL pairs yielded significant errors in the calculation of the ECW. The experimental and theoretical ECWs are reported along with the mean errors associated with this approach in Appendix A and highlight the inconsistencies

inherent in this methodology. The observed discrepancies are likely attributable to the approximations and assumptions embedded within Koopman's theorem such as the assumption that the removal of an electron does not affect remaining electrons or the molecular orbitals. This suggests that the method's current configuration may not be suited for accurate determination of the ECW for IL pairs. Further refinements or alternative approaches may be necessary to enhance its applicability and precision. It is important to note the out of all the IL characteristics considered, Vacuum M06L presented least mean error %, which means that it was the most accurate of the four types listed.

The results for the Koopman method applied to individual ions were even more pronounced in their inaccuracies, as documented in Appendix B. The theoretical ECW reported indicate a significant divergence from the expected values, emphasizing the limitations of this method in its present form. The probable explanation is that Koopmans theorem is too generalized of an assumption. The Ions when paired together, like in the IL method, have interactions that were considered when the IL's structure was optimized. This method; however, takes no interactions into consideration. Two graphs were constructed to visualize the trend lines for both methods found in Appendix C and D, underscoring the disparities observed.

4. Discussion and Conclusion

The investigation into the approximation of the ECW of an ionic liquid reveals the complexities and challenges associated with quantum chemical calculations. While Koopman's theorem appears to be an enticingly simple approach to predicting the ionization energies and electron affinities, the underlying assumptions lead to significant inaccuracies. When engaging in quantum chemical calculations, it is important to remember that every slight change makes a big difference. Isomers, molecular orbitals, and even a single electrons movement can change the entire structural optimization of a molecule or molecules. The calculation of the electrochemical window of an ionic liquid is not a mere computational exercise as it requires a comprehensive understanding of the underlying quantum mechanics.

5. Summary

These results and findings present more as a warning to not approach the approximating of the electrochemical window using a generalized theorem such as Koopmans'. Further investigations must be made into the usage of other methods such as the Delta SCF method (Pandian et al., 2015; Tian et al., 2012) which takes into consideration the total energy of a neutral and charged ion and the thermodynamic cycle method which focuses solely on the Gibbs free energy which has a direct correlation to the redox potentials of an electrolyte. The molecule files for 50 ionic liquids, in solvent and vacuum, as well as each individual anion and cation (neutral and charged) have been run under M06L and B3LYP functionals and have been computationally optimized. When exploring for another method of

determining the ECW, no new calculations shall be required unless they require data outside of the bounds just listed, which is unlikely. These 50 ionic liquids will be placed into a machine learning model that will learn from their coordinates, connectivity, molecular orbitals, and thermochemistry data to better predict future ionic liquid properties.

6. Appendix

Appendix A. Koopmans theorem of ILs; theoretical and experimental ECW and mean error

Ionic Liquid	Theoretical ECW VB3LYP	Theoretical ECW VM06L	Theoretical ECW SB3LYP	Theoretical ECW SM06L	Experiemental ECW
1-2-butyl-3-methylpyrrolidinium_Bistrifluoromethanesulfonylimide	6.60	4.61	7.65	6.23	5.67
12-dimethyl-3-ethylimidazolium_Bistrifluoromethanesulfonylimide	6.06	3.90	6.62	5.39	4.4
12-Dimethyl-3-propylimidazolium_hexafluorophosphate	6.60	5.35	5.81	5.00	4.3
12-Dimethyl-3-propylimidazolium_hexafluoroarsenate	6.64	4.27	6.59	5.38	5.37
12-Dimethyl-3-propylimidazolium_tristrifluoromethylsulfonylmethide	5.56	4.66	6.66	5.36	4.4
12-Dimethyl-4-fluoropyrazolium_tetrafluoroborate	6.13	4.52	6.24	4.89	4.1
1-butyl-3-methylimidazolium_2-cyanopyrrolide	3.16	2.51	4.50	3.35	3
1-butyl-3-methylimidazolium_124-triazolide	3.96	3.55	4.44	2.98	3.2
1-butyl-3-methylimidazolium_hexafluorophosphate	6.86	5.53	6.66	4.45	6.35
1-butyl-3-methylimidazolium_trifluoroacetate	5.02	3.52	5.73	5.47	5.7
1-butyl-3-methylimidazolium_tetrafluoroborate	6.20	4.30	6.69	5.58	4.6
1-butyl-3-methylpiperidinium_Bistrifluoromethanesulfonylimide	6.32	5.85	7.91	6.79	4.44
1-butyl-3-methylpyrrolidinium_Bistrifluoromethanesulfonylimide	6.97	5.84	7.86	6.55	6
1-Butylpyridinium_tetrafluoroborate	5.38	4.82	5.96	4.69	3.4
1-ethyl-23-dimethylimidazolium_Bistrifluoromethanesulfonylimide	5.90	4.27	6.57	5.38	4.4
1-ethyl-3-methylimidazolium_Bistrifluoromethanesulfonylimide	4.72	4.32	6.74	5.45	4.7
1-Ethyl-3-methylimidazolium_acetate	3.33	3.10	4.97	3.85	3.6
1-ethyl-3-methylimidazolium_2-cyanopyrrolide	3.04	2.50	4.36	3.50	2.4
1-ethyl-3-methylimidazolium_124-triazolide	3.64	4.56	4.49	2.86	3
1-Ethyl-3-methylimidazolium_fluoride	6.76	2.73	6.79	4.44	3.1
1-ethyl-3-methylimidazolium_Chloride	3.09	3.46	5.62	4.15	5
1-ethyl-3-methylimidazolium_trifluoromethanesulfonate	4.38	3.66	6.15	4.60	4.1
1-ethyl-3-methylimidazolium_trifluoroacetate	5.04	3.12	6.09	4.54	3.8
1-ethyl-3-methylimidazolium_tetrafluoroborate	6.90	5.45	6.78	5.56	4.3
1-Ethyl-3-methylimidazolium_bispentafluoroethylsulfonylimide	5.83	4.32	6.68	5.49	4.1
1-Ethyl-3-methylimidazolium_tetrachloroaluminate	5.53	4.13	6.71	5.51	4.8
1-methyl-3-propylpiperidinium_Bistrifluoromethanesulfonylimide	5.76	4.87	7.73	6.69	5.6
1-propyl-23-dimethylimidazolium_Bistrifluoromethanesulfonylimide	5.83	4.54	6.60	5.34	4.2
1-propyl-23-dimethylimidazolium_Hexafluoroarsenate	6.60	5.35	5.81	4.79	4.4
1-propyl-23-dimethylimidazolium_tristrifluoromethanesulfonylmethide	5.45	5.41	6.61	5.36	4.3
1-propyl-23-dimethylimidazolium_Hexafluorophosphate	6.56	4.52	6.60	5.39	5.4
1-propyl-3-methylimidazolium_Bistrifluoromethanesulfonylimide	5.70	4.28	6.74	5.40	4.3
1-propyl-3-methylpyrrolidinium_Bistrifluoromethanesulfonylimide	7.27	4.90	7.68	6.41	5.3
2-methyl-2-butylpyrrolidinium_2-cyanopyrrolide	5.62	4.42	5.77	4.35	3.6
2-methyl-2-butylpyrrolidinium_124-triazolide	5.91	4.47	5.36	4.30	4.1
Methoxytrimethylammonium_Bistrifluoromethanesulfonylimide	6.47	4.60	7.71	6.28	5.6
N-methyl-N-propylpiperidinium_Bistrifluoromethanesulfonylimide	6.19	5.34	7.78	6.69	5.6
N-methyl-N-propylpyridinium_Bistrifluoromethanesulfonylimide	4.74	2.93	5.16	3.94	5.9
N-methyl-N-propylpyrrolidinium_tetrafluoroborate	7.57	5.81	9.15	8.02	5
N-propyltrimethylammonium_Bistrifluoromethanesulfonylimide	6.38	5.25	7.74	6.66	5.6
Tetrabutylammonium_Bistrifluoromethanesulfonylimide	6.02	5.26	7.43	6.70	6
Tetraethylammonium_Bistrifluoromethanesulfonylimide	6.46	5.19	7.70	6.74	5.8
tetramethylammonium_Bistrifluoromethanesulfonylimide	6.30	5.15	7.79	6.68	4.11
tetra-methylarsenic_Bistrifluoromethanesulfonylimide	6.11	5.00	7.44	6.52	4.5
tetraethylphosphonium_Bistrifluoromethanesulfonylimide	6.30	5.21	7.51	6.40	4.93
triethyl2-methoxyethylphosphonium_Bistrifluoromethanesulfonylimide	6.06	5.02	7.01	5.91	4.7
triethyl-hexylammonium_Bistrifluoromethanesulfonylimide	6.23	5.06	7.72	6.68	5.2
triethyl-n-pentylphosphonium_Bistrifluoromethanesulfonylimide	6.08	5.12	7.50	6.55	5.3
Triethylsulfonium_Bistrifluoromethanesulfonylimide	6.28	4.91	7.56	6.29	5.07
Trimethylmethoxyethylammonium_Bistrifluoromethanesulfonylimide	6.54	4.97	7.36	6.19	5.12
trimethylpropylammonium_Bistrifluoromethanesulfonylimide	6.14	5.15	7.78	6.70	6
Mean error by method	Error%(VB3LYP)	Error%(VM06L)	Error%(SB3LYP)	Error%(SM06L)	
	28.99	15.07	46.41	22.07	

(VB3LYP): Vacuum B3LYP; (VM06L): Vacuum M06L; (SB3LYP):Solvent B3LYP; (SM06L): Solvent M06L

Experimental Data (Galiński et al., 2006; Li et al., 2016; Sánchez-Ramírez et al., 2017; Shi et al., 2013; Sun et al., 1998; Zhang et al., 2021; Zhang and Bond, 2005; Sakaebe and Matsumoto, 2003; Dupont et al., 2002; Forsyth et al., 2001; Howlett et al., 2006; De Vos et al., 2014)

Appendix B. Koopmans theorem for Ions; theoretical and experimental ECW and mean error

KOOPMANS THEOREM IONs					
Ionic Liquid	Theoretical ECW VB3LYP	Theoretical ECW VM06L	Theoretical ECW SB3LYP	Theoretical ECW SM06L	Experiemental ECW
1-2-butyl-3-methylpyrrolidinium_Bistrifluoromethanesulfonylimide	16.24	15.25	10.01	8.82	5.67
12-dimethyl-3-ethylimidazolium_Bistrifluoromethanesulfonylimide	14.53	13.84	10.09	8.85	4.4
12-Dimethyl-3-propylimidazolium_hexafluorophosphate	16.10	14.85	12.26	11.01	4.3
12-Dimethyl-3-propylimidazolium_hexafluoroarsenate	15.11	13.84	12.52	11.11	5.37
12-Dimethyl-3-propylimidazolium_tristrifluoromethylsulfonylmethide	13.86	13.18	9.75	8.76	4.4
12-Dimethyl-4-fluoropyrazolium_tetrafluoroborate	17.22	15.79	12.46	11.78	4.1
1-butyl-3-methylimidazolium_2-cyanopyrrolide	15.14	14.46	8.19	7.54	3
1-butyl-3-methylimidazolium_124-triazolide	15.10	14.41	8.57	7.89	3.2
1-butyl-3-methylimidazolium_hexafluorophosphate	16.10	15.26	12.26	11.01	6.35
1-butyl-3-methylimidazolium_trifluoroacetate	15.90	15.21	8.63	10.20	5.7
1-butyl-3-methylimidazolium_tetrafluoroborate	17.22	15.78	12.46	11.78	4.6
1-butyl-3-methylpiperidinium_Bistrifluoromethanesulfonylimide	15.62	14.68	10.03	8.92	4.44
1-butyl-3-methylpyrrolidinium_Bistrifluoromethanesulfonylimide	16.01	15.11	10.08	8.89	6
1-Butylpyridinium_tetrafluoroborate	17.22	16.14	12.46	11.78	3.4
1-ethyl-23-dimethylimidazolium_Bistrifluoromethanesulfonylimide	14.53	13.84	10.02	8.85	4.4
1-ethyl-3-methylimidazolium_Bistrifluoromethanesulfonylimide	15.04	14.37	10.06	8.83	4.7
1-Ethyl-3-methylimidazolium_acetate	15.69	15.02	10.11	8.04	3.6
1-ethyl-3-methylimidazolium_2-cyanopyrrolide	15.28	14.61	8.23	7.56	2.4
1-ethyl-3-methylimidazolium_124-triazolide	15.24	14.57	8.59	7.92	3
1-Ethyl-3-methylimidazolium_fluoride	24.22	22.88	17.55	16.22	3.1
1-ethyl-3-methylimidazolium_Chloride	18.11	17.44	11.22	10.50	5
1-ethyl-3-methylimidazolium_trifluoromethanesulfonate	15.74	15.07	11.18	10.05	4.1
1-ethyl-3-methylimidazolium_trifluoroacetate	16.03	15.36	8.66	10.20	3.8
1-ethyl-3-methylimidazolium_tetrafluoroborate	17.22	15.78	12.46	11.78	4.3
1-Ethyl-3-methylimidazolium_bispentafluoroethylsulfonylimide	14.69	14.02	10.06	8.84	4.1
1-Ethyl-3-methylimidazolium_tetrachloroaluminate	14.94	14.27	9.29	8.85	4.8
1-methyl-3-propylpiperidinium_Bistrifluoromethanesulfonylimide	15.21	14.37	10.03	8.90	5.6
1-propyl-23-dimethylimidazolium_Bistrifluoromethanesulfonylimide	14.46	13.77	10.08	8.83	4.2
1-propyl-23-dimethylimidazolium_Hexafluoroarsenate	15.11	13.84	12.63	11.16	4.4
1-propyl-23-dimethylimidazolium_tristrifluoromethanesulfonylmethide	13.84	13.15	9.85	8.81	4.3
1-propyl-23-dimethylimidazolium_Hexafluorophosphate	16.10	14.85	12.26	11.01	5.4
1-propyl-3-methylimidazolium_Bistrifluoromethanesulfonylimide	14.94	14.26	10.01	8.83	4.3
1-propyl-3-methylpyrrolidinium_Bistrifluoromethanesulfonylimide	16.35	15.35	10.03	8.85	5.3
2-methyl-2-butylpyrrolidinium_2-cyanopyrrolide	15.46	14.66	9.30	8.39	3.6
2-methyl-2-butylpyrrolidinium_124-triazolide	15.42	14.62	9.65	8.75	4.1
Methoxytrimethylammonium_Bistrifluoromethanesulfonylimide	16.32	15.20	9.98	8.83	5.6
N-methyl-N-propylpiperidinium_Bistrifluoromethanesulfonylimide	16.16	15.27	9.98	8.82	5.6
N-methyl-N-propylpyridinium_Bistrifluoromethanesulfonylimide	14.13	13.50	9.98	8.82	5.9
N-methyl-N-propylpyrrolidinium_tetrafluoroborate	17.67	16.79	12.46	11.78	5
N-propyltrimethylammonium_Bistrifluoromethanesulfonylimide	16.58	15.69	10.07	9.12	5.6
Tetrabutylammonium_Bistrifluoromethanesulfonylimide	15.27	14.36	9.98	8.82	6
Tetraethylammonium_Bistrifluoromethanesulfonylimide	16.74	15.79	10.01	8.99	5.8
tetramethylammonium_Bistrifluoromethanesulfonylimide	18.98	18.05	11.80	11.20	4.11
tetra-methylarsenic_Bistrifluoromethanesulfonylimide	17.39	16.63	10.10	9.35	4.5
tetraethylphosphonium_Bistrifluoromethanesulfonylimide	16.19	15.37	9.98	8.82	4.93
triethyl2-methoxyethylphosphonium_Bistrifluoromethanesulfonylimide	13.75	12.79	9.98	8.82	4.7
triethyl-hexylammonium_Bistrifluoromethanesulfonylimide	14.73	13.96	9.98	8.82	5.2
triethyl-n-pentylphosphonium_Bistrifluoromethanesulfonylimide	15.06	14.29	9.98	8.82	5.3
Triethylsulfonium_Bistrifluoromethanesulfonylimide	16.00	15.29	9.98	8.85	5.07
Trimethylmethoxyethylammonium_Bistrifluoromethanesulfonylimide	14.39	13.41	10.07	9.02	5.12
trimethylpropylammonium_Bistrifluoromethanesulfonylimide	16.58	15.69	10.07	9.12	6
Mean error by method	Error%(VB3LYP)	Error%(VM06L)	Error%(SB3LYP)	Error%(SM06L)	
	257.4141091	237.808967	134.8229562	114.1318356	

Appendix C

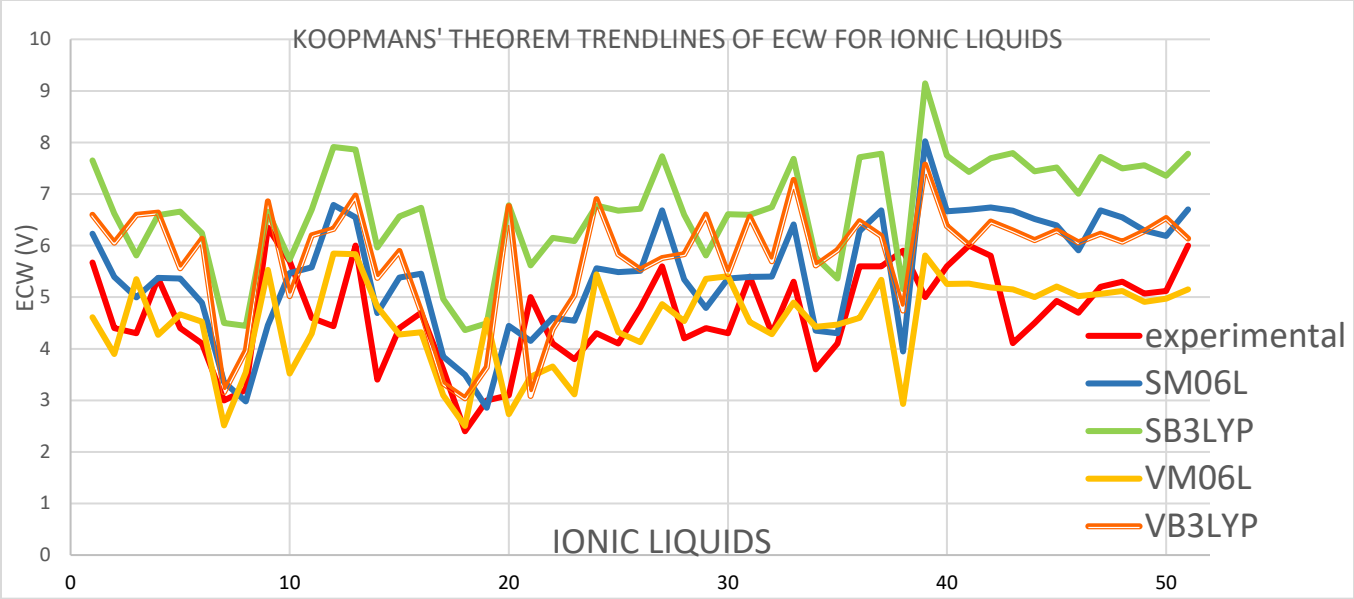

Appendix D

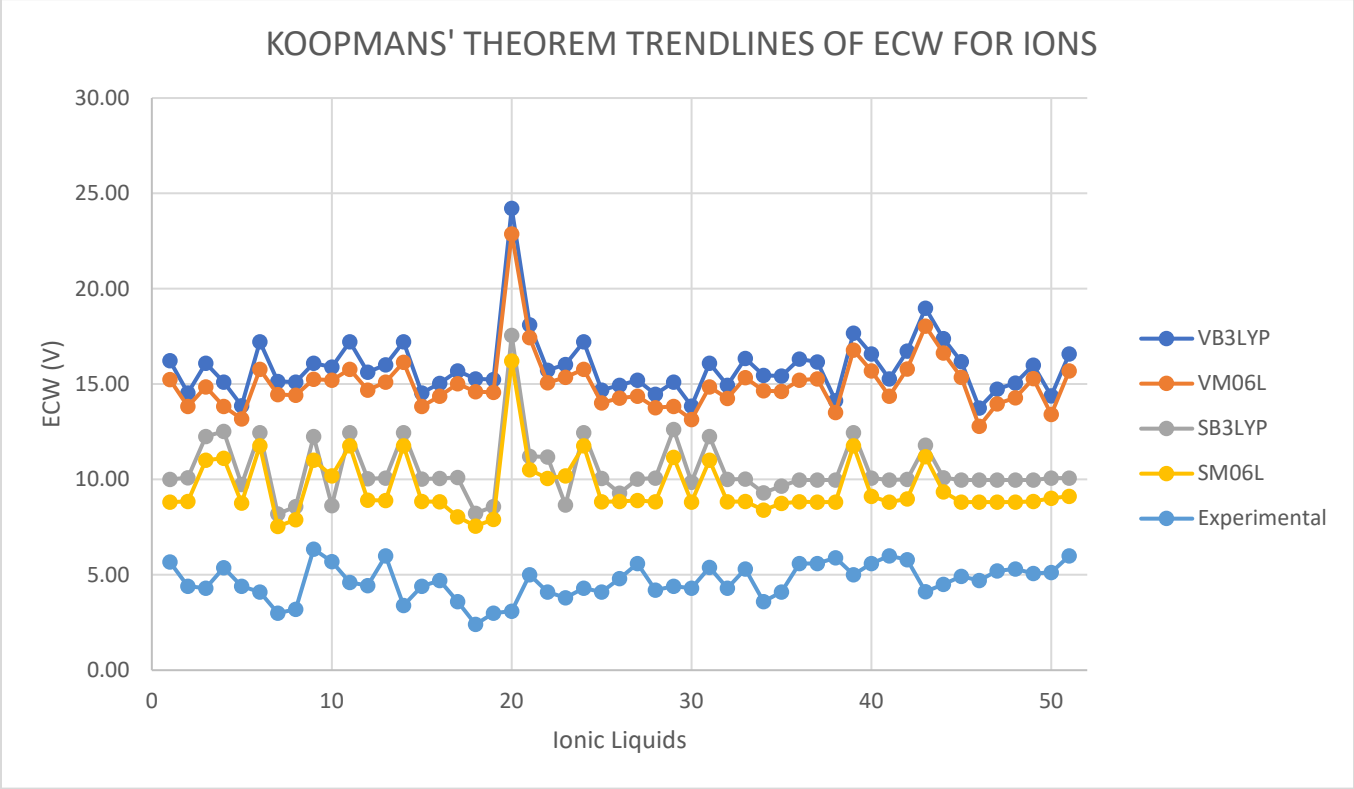

6a. Acknowledgements

I would like to firstly thank Dr. and Mrs. Niblack for this scholarship opportunity, it has brought me closer to my research partners and allowed me to explore further out into the world of computation.

I would like to thank my sponsor Dr. Shah for teaching me to push past my limits and for always providing me with unique and amazing opportunities such as this one.

I would also like to thank the Pete and Tiger team at Okstate, and specifically Jesse Schafer and Evan Linde of whom were able to greatly help me in my long and arduous quest to automate this researching process.

And finally thank you to my mentor Sudip Das, I am proud of the man you are and who you are becoming. Thank you for all your help and congratulations on the baby.

6b Literature Cited

Brennecke, J.F., n.d. Energy Applications of Ionic Liquids 55.

De Vos, N., Maton, C., Stevens, C.V., 2014. Electrochemical Stability of Ionic Liquids: General Influences and Degradation Mechanisms. ChemElectroChem 1, 1258–1270. https://doi.org/10.1002/celc.201402086

Dupont, J., De Souza, R.F., Suarez, P.A.Z., 2002. Ionic Liquid (Molten Salt) Phase Organometallic Catalysis. Chem. Rev. 102, 3667–3692. https://doi.org/10.1021/cr010338r

Forsyth, S., Golding, J., MacFarlane, D.R., Forsyth, M., 2001. N-methyl-N-alkylpyrrolidinium tetrafluoroborate salts: ionic solvents and solid electrolytes. Electrochimica Acta 46, 1753–1757. https://doi.org/10.1016/S0013-4686(00)00781-7

Galiński, M., Lewandowski, A., Stępniak, I., 2006. Ionic liquids as electrolytes. Electrochimica Acta 51, 5567–5580. https://doi.org/10.1016/j.electacta.2006.03.016

Howlett, P.C., Izgorodina, E.I., Forsyth, M., MacFarlane, D.R., 2006. Electrochemistry at Negative Potentials in Bis(trifluoromethanesulfonyl)amide Ionic Liquids. Z. Für Phys. Chem. 220, 1483–1498. https://doi.org/10.1524/zpch.2006.220.10.1483

Li, Q., Jiang, J., Li, G., Zhao, W., Zhao, X., Mu, T., 2016. The electrochemical stability of ionic liquids and deep eutectic solvents. Sci. China Chem. 59, 571–577. https://doi.org/10.1007/s11426-016-5566-3

Pandian, S., Raju, S.G., Hariharan, K.S., Kolake, S.M., Park, D.-H., Lee, M.-J., 2015. Functionalized ionic liquids as electrolytes for lithium-ion batteries. J. Power Sources 286, 204–209. https://doi.org/10.1016/j.jpowsour.2015.03.130

Sakaebe, H., Matsumoto, H., 2003. N-Methyl-N-propylpiperidinium bis(trifluoromethanesulfonyl)imide (PP13–TFSI) – novel electrolyte base for Li battery. Electrochem. Commun. 5, 594–598. https://doi.org/10.1016/S1388-2481(03)00137-1

Sánchez-Ramírez, N., Assresahegn, B.D., Bélanger, D., Torresi, R.M., 2017. A Comparison among Viscosity, Density, Conductivity, and Electrochemical Windows of *N* - *n* -Butyl- *N* -methylpyrrolidinium and Triethyl- *n* -pentylphosphonium Bis(fluorosulfonyl imide) Ionic Liquids and Their Analogues Containing Bis(trifluoromethylsulfonyl) Imide Anion. J. Chem. Eng. Data 62, 3437–3444. https://doi.org/10.1021/acs.jced.7b00458

Shi, C., Quiroz-Guzman, M., DeSilva, A., Brennecke, J.F., 2013. Physicochemical and Electrochemical Properties of Ionic Liquids Containing Aprotic Heterocyclic Anions Doped With Lithium Salts. J. Electrochem. Soc. 160, A1604–A1610. https://doi.org/10.1149/2.116309jes

Sun, J., Forsyth, M., MacFarlane, D.R., 1998. Room-Temperature Molten Salts Based on the Quaternary Ammonium Ion. J. Phys. Chem. B 102, 8858–8864. https://doi.org/10.1021/jp981159p

Tian, Y.-H., Goff, G.S., Runde, W.H., Batista, E.R., 2012. Exploring Electrochemical Windows of Room-Temperature Ionic Liquids: A Computational Study. J. Phys. Chem. B 116, 11943–11952. https://doi.org/10.1021/jp303915c

Tsuneda, T., Song, J.-W., Suzuki, S., Hirao, K., 2010. On Koopmans' theorem in density functional theory. J. Chem. Phys. 133, 174101. https://doi.org/10.1063/1.3491272

Weingärtner, H., 2006. The Static Dielectric Constant of Ionic Liquids. Z. Für Phys. Chem. 220, 1395–1405. https://doi.org/10.1524/zpch.2006.220.10.1395

Zhang, C., Hu, J., Yang, Z., Zheng, Z., Geng, S., Zhong, X., 2021. Effects of the number of imidazoline ring and the length of alkyl group chain of imidazoline derivatives on corrosion inhibition of carbon steel in HCl solution: Molecular simulation and experimental validation. Petroleum S2405656121000171. https://doi.org/10.1016/j.petlm.2021.03.002

Zhang, J., Bond, A.M., 2005. Practical considerations associated with voltammetric studies in room temperature ionic liquids. The Analyst 130, 1132. https://doi.org/10.1039/b504721h

Identifying Efficient Methods of Determining the Electrochemical Window of Ionic Liquids

Brinkli Abbitt

Chemical Engineering

Faculty Sponsor: Jindal Shah

Graduate Mentor: Sudip Das

Worldwide Implications of Climate Change

wildfires

melting ice caps

mass flooding

UNRELIABLE ENERGY

What Can We Change?

Safety

Performance

Environmental Impact

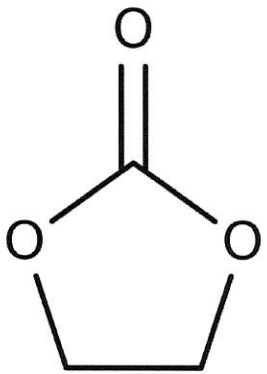

ethylene carbonate

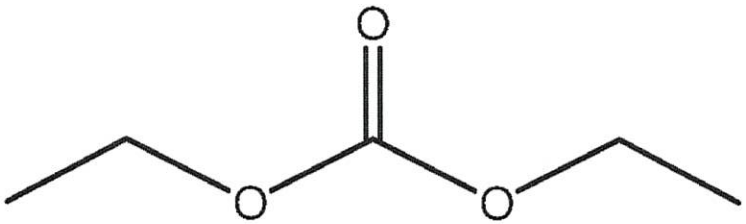

diethyl carbonate

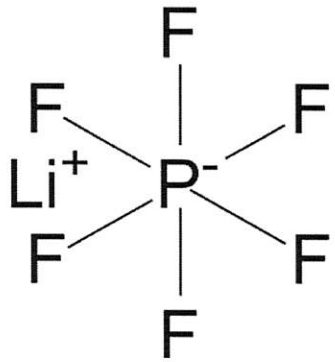

lithium hexafluorophosphate

IONIC LIQUIDS

DESIGNER SOLVENTS

HIGH TERMAL STABILITY

LOW VOLATILITY

WIDE ELECTROCHEMICAL WINDOW

Common Types of Ionic Liquid Cations

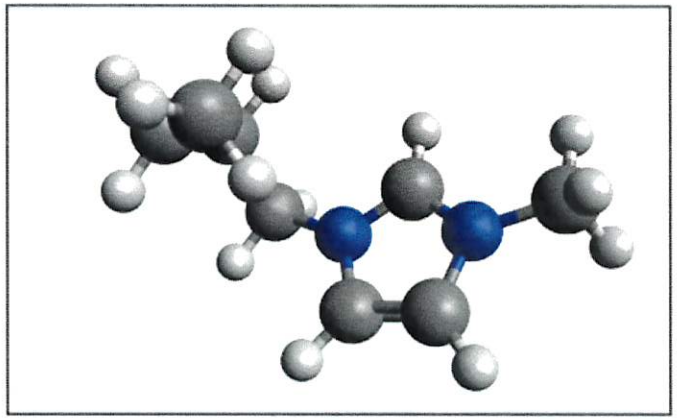
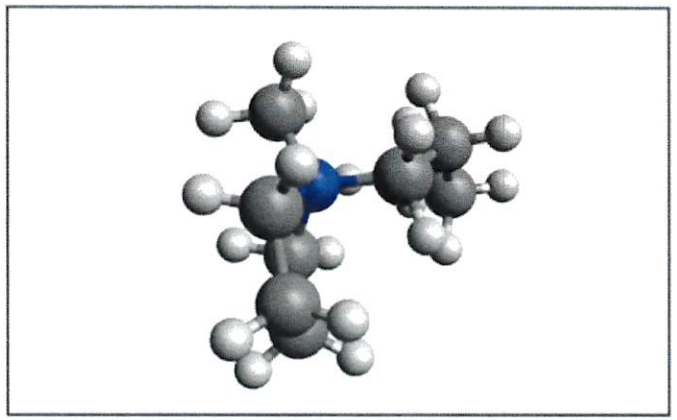
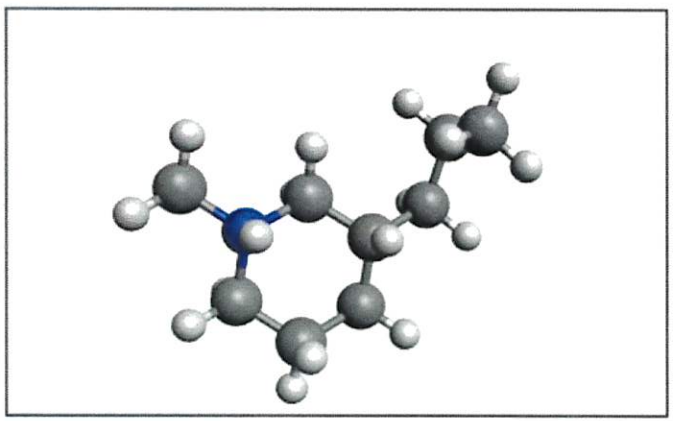
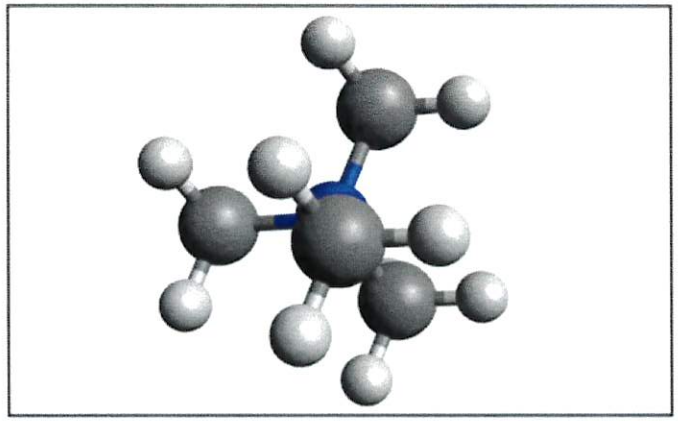
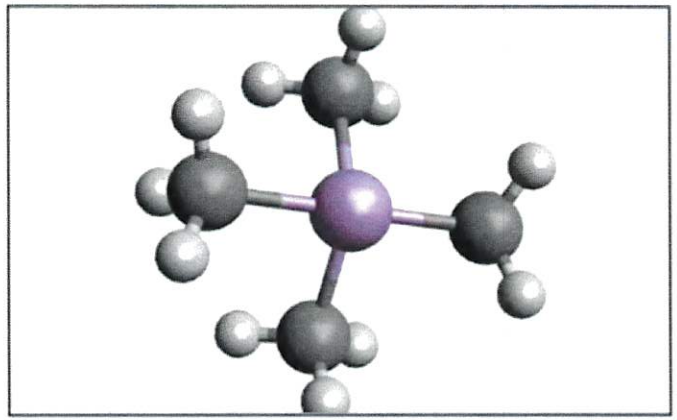
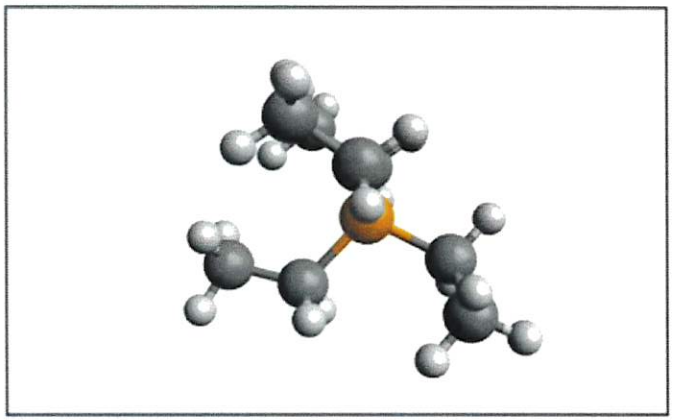

Common Types of Ionic Liquid Anions

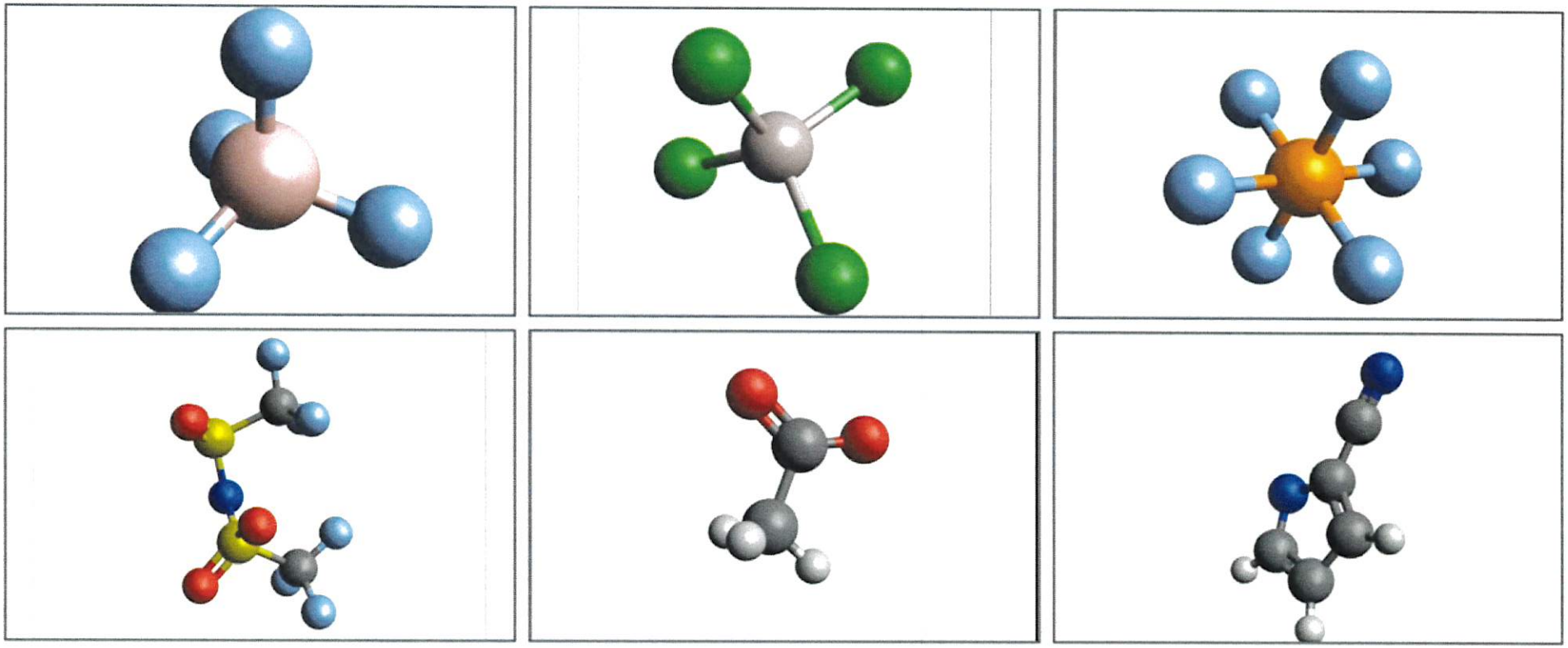

Electrochemical Stability Window (ECW)

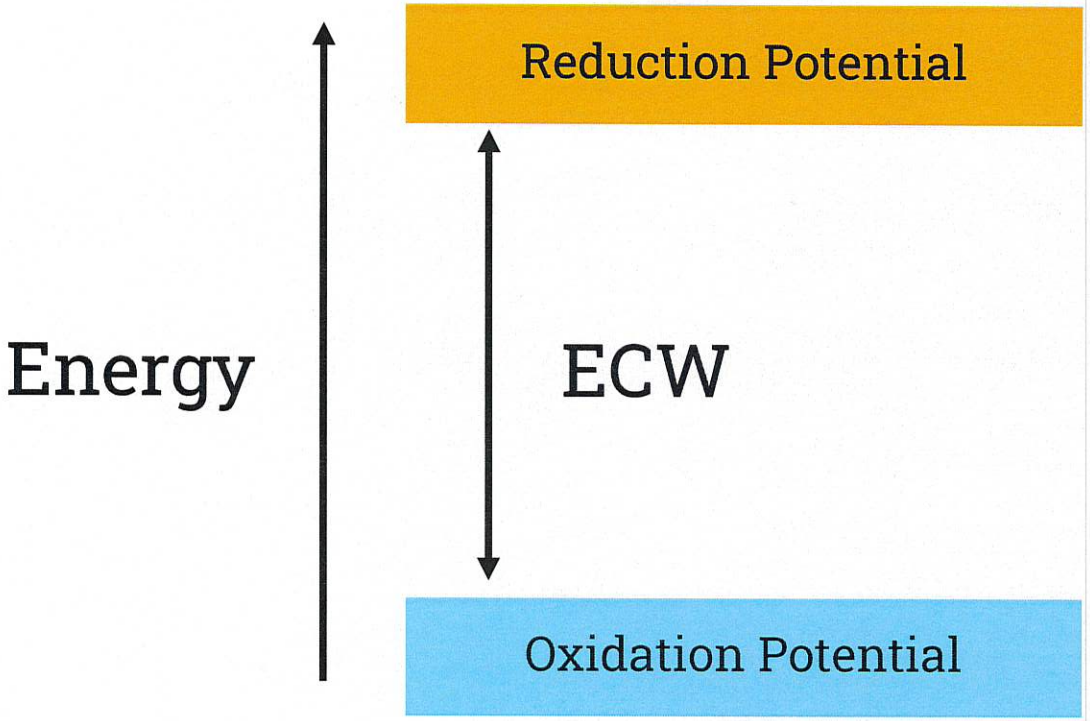

- Decomposition
- Energy Density
- Application

Why Computational ?

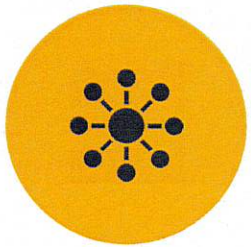

FLEXIBILITY

TIME

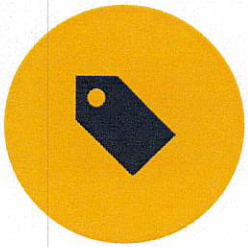

COST

SAFETY

ACCESIBILITY

PREDICITVE POWER

REDUCED WASTE

What is DFT ?

$$H\Psi(\mathrm{r},\mathrm{R}) = E(r,R)\Psi(r,R)$$

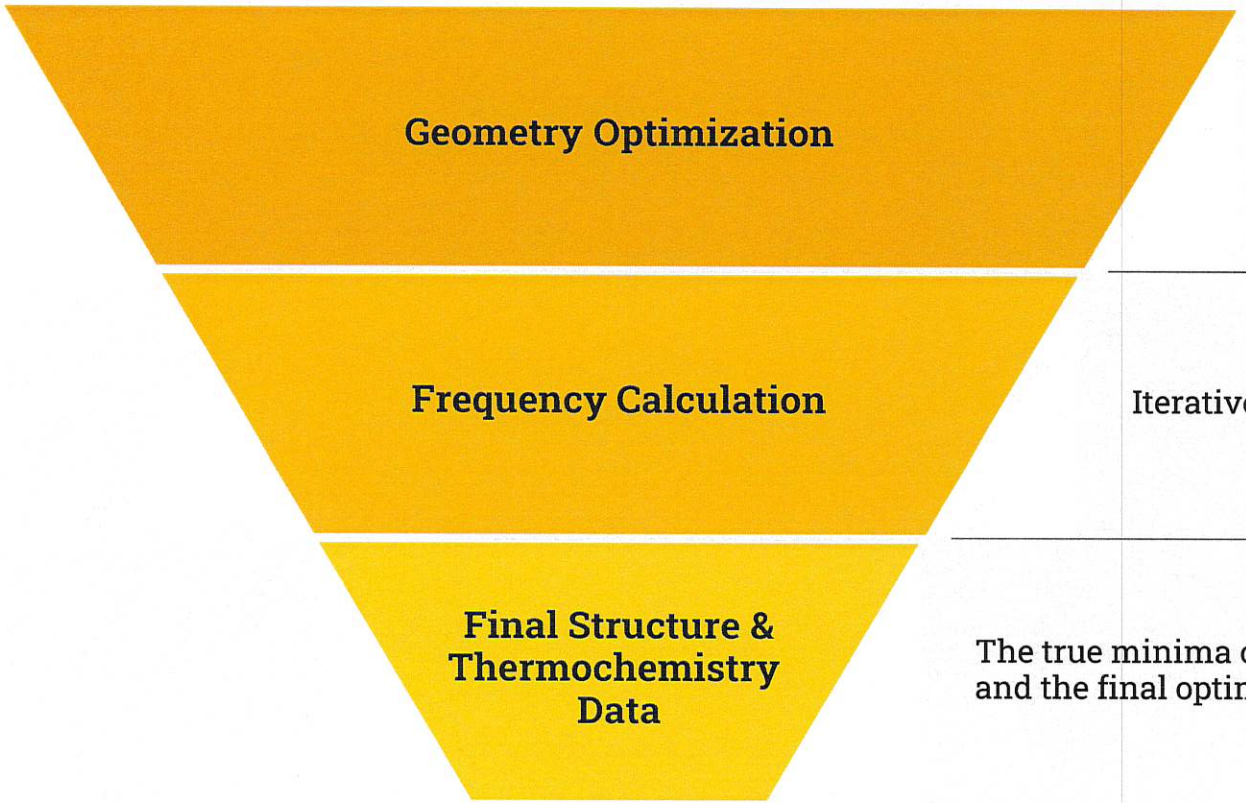

Iteratively determining the most stable geometric structure

Iteratively computes the vibrational frequencies

The true minima of the potential energy surface is determined and the final optimized structure is revealed

Methodology: Initial Process of One Molecule

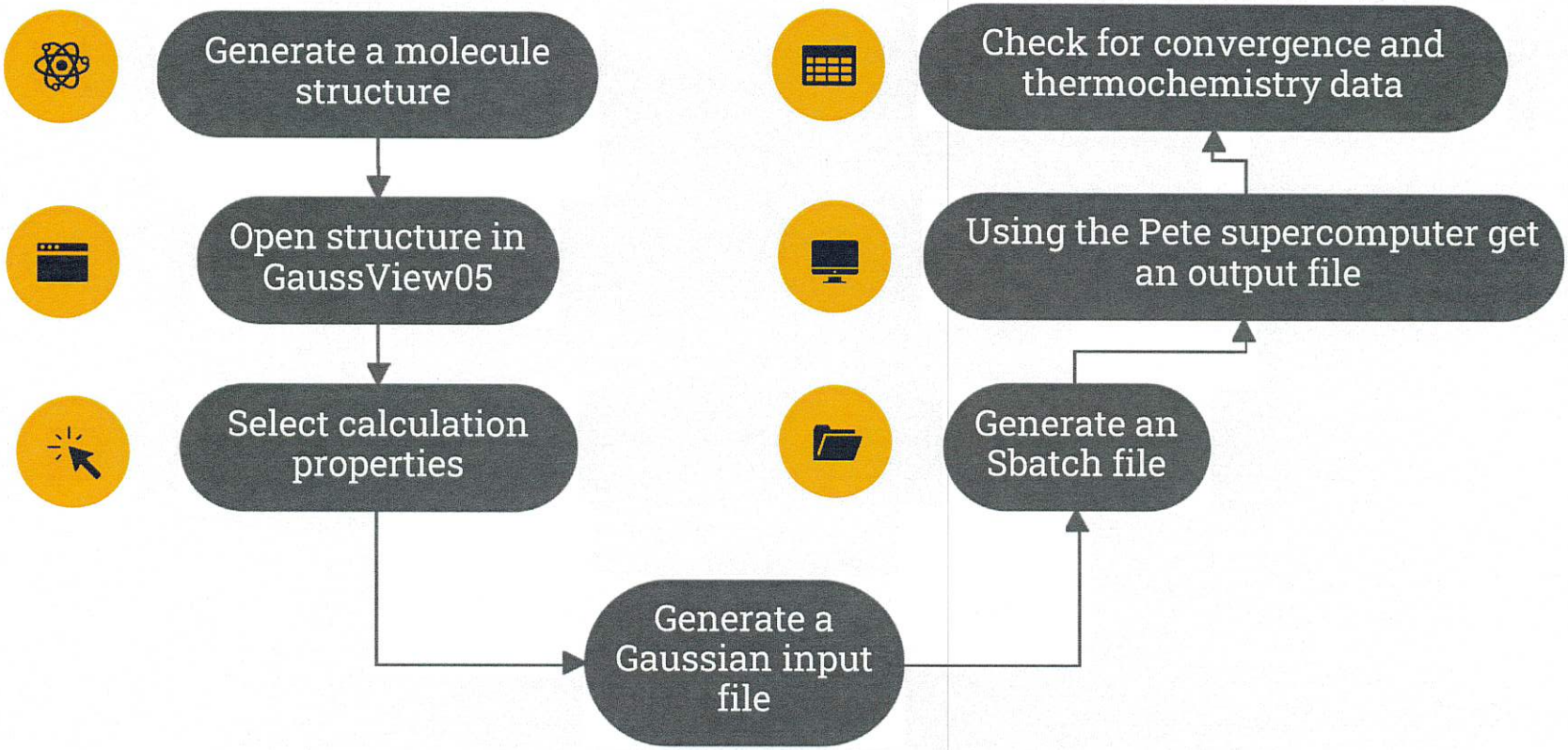

Methodology: New Process of Multiple Molecules

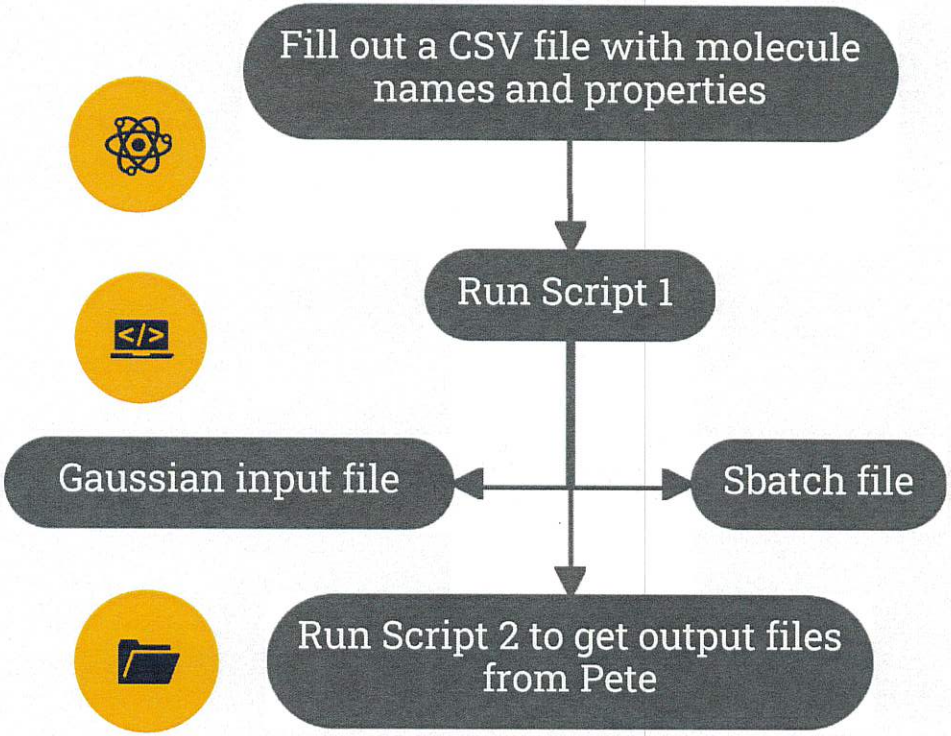

DFT Methods for calculating the ECW

1. Koopmans' Theorem
2. Self Consistent Field Method
3. Gibbs Free Energy Difference
4. Thermodynamic Model

Method 1: Koopmans' Theorem

$$EA = -LUMO$$

$$IE = -HOMO$$

$$ECW = EA - IE$$

- EA= Electron Affinity
- IE: Ionization Energy
- LUMO=Lowest Unoccupied Molecular Orbital
- HOMO = Highest Occupied Molecular Orbital

Method 2: Self Consistent Field Method

- $ECW = E_{ox} - E_{red}$
- $E_{ox}^{\circ} = -\frac{E_{HOMO}}{e}$
- $E_{Red}^{\circ} = -\frac{E_{LUMO}}{e}$
- $IE = E(C) - E(C^{+}) = -E_{HOMO}$
- $EA = E(A^{-}) - E(A) = -E_{LUMO}$

$e = elementary\ charge\ of\ an\ electron$

Method 3: Gibbs Free Energy Difference

- $ECW = V_{ox} - V_{red}$
- $V_{red} = G_{cation+e} - G_{cation}$
- $V_{ox} = G_{anion} - G_{anion-e}$

Method 4: Thermodynamic Model

- $\Delta G^{ox} = \Delta G_g^{ox} + (\Delta G_s^{A-} - \Delta G_s^{A})$
- $\Delta G^{red} = \Delta G_g^{red} + (\Delta G_s^{C} - \Delta G_s^{C+})$
- $E_{ox} = \dfrac{\Delta G^{ox}}{ne}$
- $E_{red} = \dfrac{\Delta G^{red}}{ne}$

$n = number\ of\ electrons$

Data Comparison Issues

- Working Electrode
- Reference Electrode
- Methodological differences
- Errors in the experimental data
- Temperature
- Pressure

Data Analysis: Trendline Data

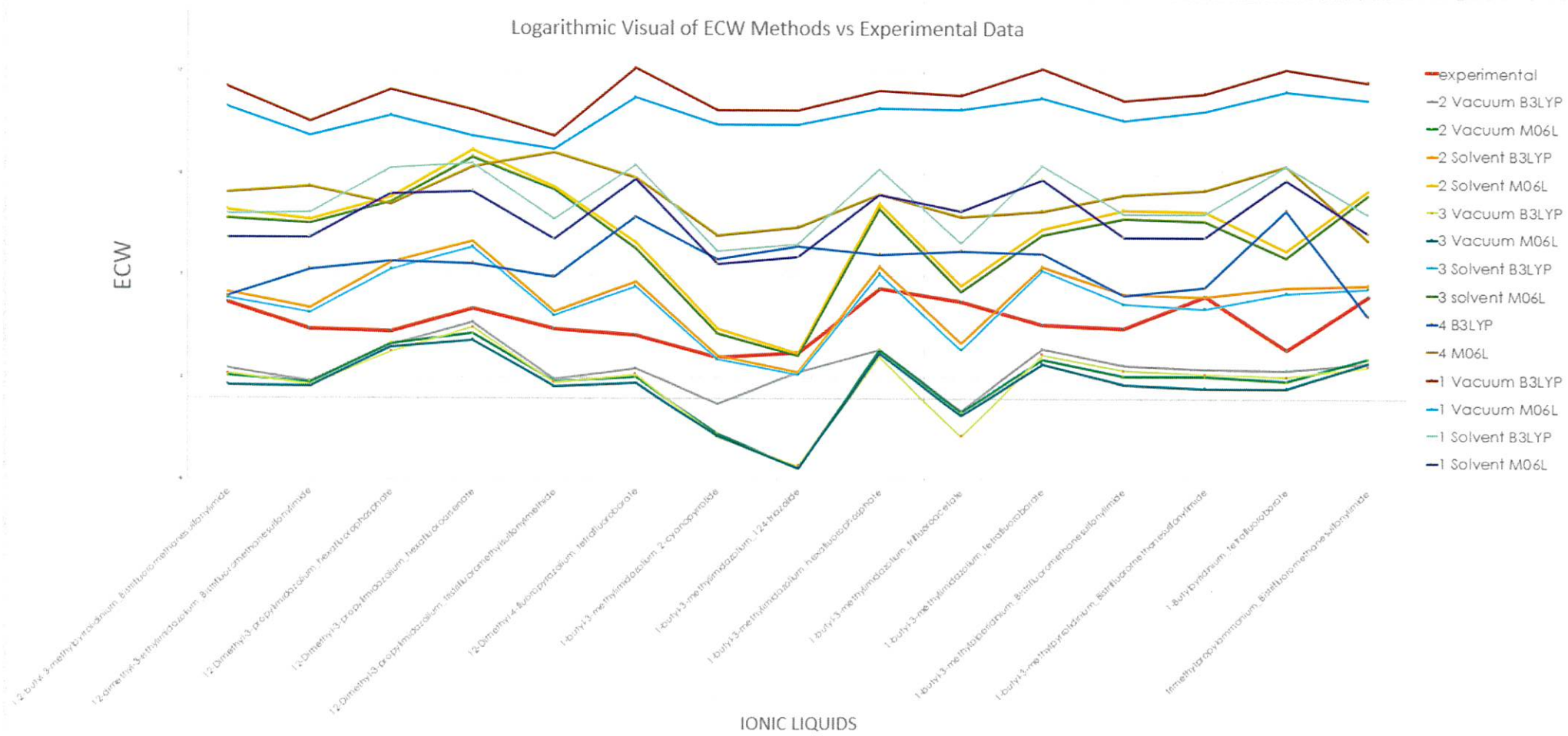

Data Analysis: Trendline Data

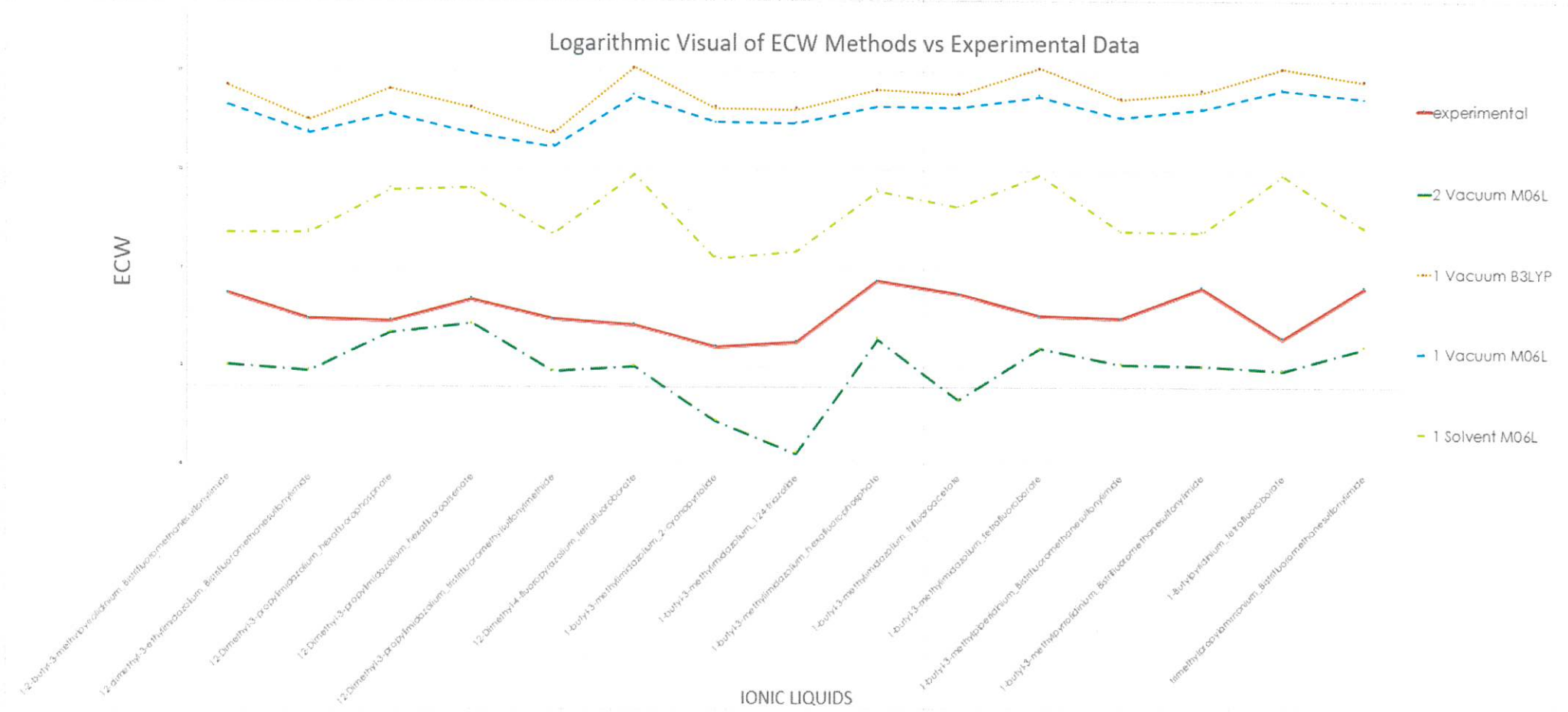

Data Analysis: Methods

Analyze the difference between functionals

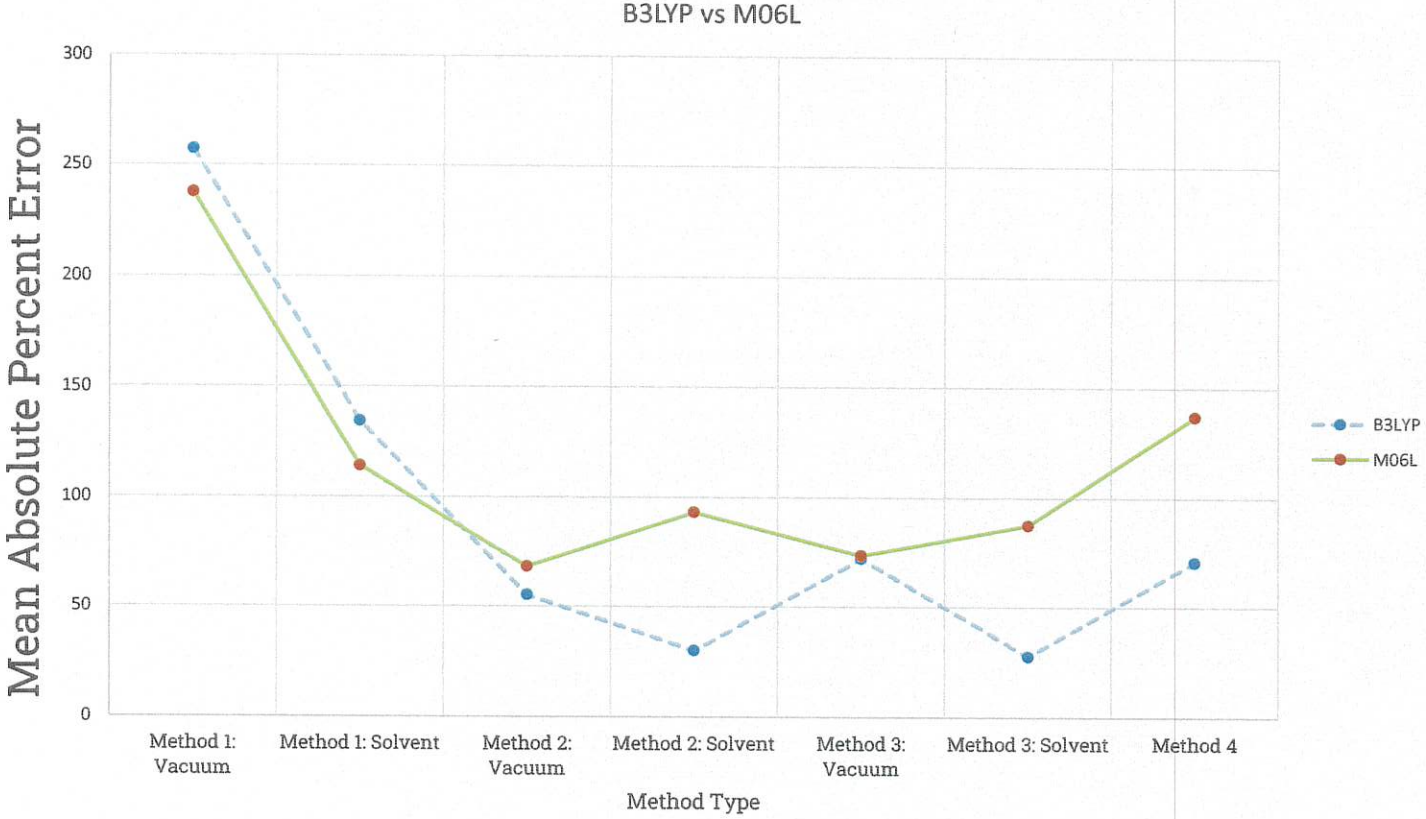

- Method 1: M06L was 1.1x more accurate
- Method 2: B3LYP was 1.89x more accurate
- Method 3: B3LYP was 1.6x more accurate
- Method 4: B3LYP was 1.9x more accurate

Data Analysis: Methods

Analyze the difference between Solvent and Vacuum

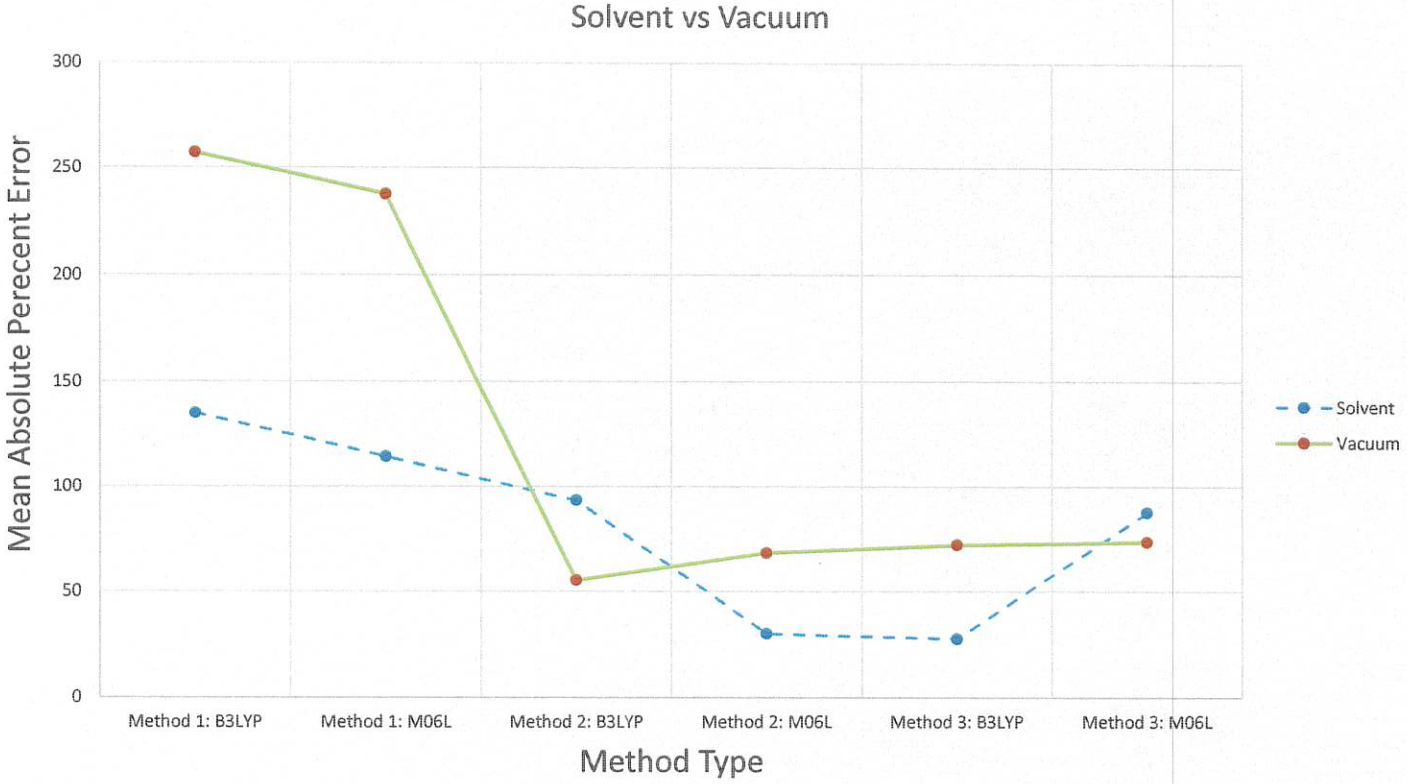

- Method 1: Solvent was 2x more accurate
- Method 2: Solvent was 1.02x more accurate.
- Method 3: Solvent was 1.3x more accurate

Data Analysis: Methods

Overall Accuracy Analysis

- Method 1: M06L in Solvent is 0.91x more accurate
- Method 2: B3LYP in Solvent is 3.46x more accurate
- Method 3: B3LYP in Solvent is 3.77x more accurate
- Method 4: B3LYP is 1.47x more acurate

Conclusions

Overall Analysis

- Method 1 is useful for predicting Ionic Liquids with high ECW's at a fraction of the cost of other methods
- Method 2 B3LYP in Solvent had the highest accuracy compared the average data based on sample errors
- B3LYP on average performed better than M06L
- Further experimentation must be conducted to generate a better method for direct computational and experimental comparison

Future analyses and work

- Comparing Computational Data
- Analyzing specific cation and anion isomers
- Coding Additions
- Working and reference electrode rule of thumb
- Research other ECW methods

References

- Brennecke, J.F., n.d. Energy Applications of Ionic Liquids 55.
- De Vos, N., Maton, C., Stevens, C.V., 2014. Electrochemical Stability of Ionic Liquids: General Influences and Degradation Mechanisms. ChemElectroChem 1, 1258–1270. https://doi.org/10.1002/celc.201402086
- Dupont, J., De Souza, R.F., Suarez, P.A.Z., 2002. Ionic Liquid (Molten Salt) Phase Organometallic Catalysis. Chem. Rev. 102, 3667–3692. https://doi.org/10.1021/cr010338r
- Forsyth, S., Golding, J., MacFarlane, D.R., Forsyth, M., 2001. N-methyl-Nalkylpyrrolidinium tetrafluoroborate salts: ionic solvents and solid electrolytes. Electrochimica Acta 46, 1753–1757. https://doi.org/10.1016/S0013-4686(00)00781-7
- Galiński, M., Lewandowski, A., Stępniak, I., 2006. Ionic liquids as electrolytes. Electrochimica Acta 51, 5567–5580. https://doi.org/10.1016/j.electacta.2006.03.016
- Howlett, P.C., Izgorodina, E.I., Forsyth, M., MacFarlane, D.R., 2006. Electrochemistry at Negative Potentials in Bis(trifluoromethanesulfonyl)amide Ionic Liquids. Z. Für Phys. Chem. 220, 1483–1498. https://doi.org/10.1524/zpch.2006.220.10.1483
- Li, Q., Jiang, J., Li, G., Zhao, W., Zhao, X., Mu, T., 2016. The electrochemical stability of ionic liquids and deep eutectic solvents. Sci. China Chem. 59, 571–577. https://doi.org/10.1007/s11426-016-5566-3 9

References Continued

- Pandian, S., Raju, S.G., Hariharan, K.S., Kolake, S.M., Park, D.-H., Lee, M.-J., 2015. Functionalized ionic liquids as electrolytes for lithium-ion batteries. J. Power Sources 286, 204–209. https://doi.org/10.1016/j.jpowsour.2015.03.130

- Sakaebe, H., Matsumoto, H., 2003. N-Methyl-N-propylpiperidinium bis(trifluoromethanesulfonyl)imide (PP13–TFSI) – novel electrolyte base for Li battery. Electrochem. Commun. 5, 594–598. https://doi.org/10.1016/S1388-2481(03)00137-1

- Sánchez-Ramírez, N., Assresahegn, B.D., Bélanger, D., Torresi, R.M., 2017. A Comparison among Viscosity, Density, Conductivity, and Electrochemical Windows of N - n - Butyl- N -methylpyrrolidinium and Triethyl- n - pentylphosphonium Bis(fluorosulfonyl imide) Ionic Liquids and Their Analogues Containing Bis(trifluoromethylsulfonyl) Imide Anion. J. Chem. Eng. Data 62, 3437–3444. https://doi.org/10.1021/acs.jced.7b00458

- Shi, C., Quiroz-Guzman, M., DeSilva, A., Brennecke, J.F., 2013. Physicochemical and Electrochemical Properties of Ionic Liquids Containing Aprotic Heterocyclic Anions Doped With Lithium Salts. J. Electrochem. Soc. 160, A1604–A1610. https://doi.org/10.1149/2.116309jes

- Sun, J., Forsyth, M., MacFarlane, D.R., 1998. Room-Temperature Molten Salts Based on the Quaternary Ammonium Ion. J. Phys. Chem. B 102, 8858–8864. https://doi.org/10.1021/jp981159p

References Continued

- Tian, Y.-H., Goff, G.S., Runde, W.H., Batista, E.R., 2012. Exploring Electrochemical Windows of Room-Temperature Ionic Liquids: A Computational Study. J. Phys. Chem. B 116, 11943–11952. https://doi.org/10.1021/jp303915c

- Tsuneda, T., Song, J.-W., Suzuki, S., Hirao, K., 2010. On Koopmans' theorem in density functional theory. J. Chem. Phys. 133, 174101. https://doi.org/10.1063/1.3491272

- Weingärtner, H., 2006. The Static Dielectric Constant of Ionic Liquids. Z. Für Phys. Chem. 220, 1395–1405. https://doi.org/10.1524/zpch.2006.220.10.1395

- Zhang, C., Hu, J., Yang, Z., Zheng, Z., Geng, S., Zhong, X., 2021. Effects of the number of imidazoline ring and the length of alkyl group chain of imidazoline derivatives on corrosion inhibition of carbon steel in HCl solution: Molecular simulation and experimental validation. Petroleum S2405656121000171. https://doi.org/10.1016/j.petlm.2021.03.002

- Zhang, J., Bond, A.M., 2005. Practical considerations associated with voltammetric studies in room temperature ionic liquids. The Analyst 130, 1132. https://doi.org/10.1039/b504721h

Acknowledgements

- Thank you, Dr. and Mrs. Niblack for providing this scholarship opportunity.
- I am grateful to my research professor, Dr. Shah, for supporting and backing my research endeavors
- Thank you to my grad student mentor, Sudip Das, for guiding me through the research process
- And a special thanks to Jesse Schafer and Evan Linde, as well as the rest of the HPC team for their help with my coding endeavors.
- Finally thank you Dr. Johnson for organizing and planning this research experience, and thank you for all of your help and understanding.

Visible Light-Driven C-C Coupling Reaction of Terminal Alkynes at Atmospheric Temperature and Pressure Reaction Conditions using Hybrid Cu_2O-Pd Nanostructures

Samantha Stobbe

Chemical Engineering
Faculty Sponsor: Dr. Marimuthu Andiappan
Graduate Student Mentor: Ravi Teja A. Tirumala, Sundaram Bhardwaj Ramakrishnan

ABSTRACT

The field of nanocatalysis has been largely driven by plasmonic metal nanostructures (PMNs). The materials that largely fall into this category are Au, Ag, Cu, and Al. While significant progress has been made in these materials for a wide range of applications such as photovoltaics, photocatalysis, etc. due to their strong enteric-field enhancement with light interaction. However, PMNs suffer from being expensive and scalability issues for high-volume manufacturing. Here, we present an alternative to PMNs with dielectric Mie resonators nanoparticles (MRNPs). All these materials exhibit dielectric Mie resonance resulting in both electric and magnetic field enhancements almost of equal magnitude. In this work, we chose Copper (Cu)-based MRNPs namely Cu_2O for pharmaceutically relevant coupling reactions. The choice of Cu_2O is due to previous work done by Andiappan and coworkers on the same. In this work, we hybridize MRNPs (HMRNPs) with catalytically active materials such as palladium (Pd) to form Cu_2O-Pd. To test the efficacy of these HMRNPs we used an oxidative homocoupling of phenylacetylene (PA) as the probe reaction. We see a much higher rate of enhancement under light compared to dark conditions. This idea can be extended to a wide range of industrially important reactions such as CO_2 reduction, ammonia synthesis, chemicals, and fuels.

1. Introduction

In industry, light manipulation dielectric materials have started to come forward as replacements for the commonly used plasmonic materials. Plasmonic metal nanostructures (PMNs). are known for their high extinction cross sections and Mie resonances. This ability is created due to the localized surface plasmon resonance (LSPR) which can manipulate the geometry and physical environment.[1–6] Due to their high extinction cross sections, PMNs can easily manipulate electromagnetic fields which gives them many real-world applications. Even with all these benefits, PNMs are expensive and have issues scaling up in large-scale semiconductor manufacturing.[7] Therefore, photocatalytic dielectric mie resonator particles have started to become of interest (MRNPs). Unlike plasmonic nanocatalysts, dielectric

materials exhibit both electric and magnetic resonances which allow enchanted optical responses.[7] The magnetic and electric field spatial distributions were observed using Finite Time Difference Domain data. The same data also show that the Cu_2O sphere can exhibit enhancements of up to 25 and 8 times for the near magnetic and electric field intensities, respectively, over the incident far field.[9] This makes them viable photocatalysts for many of the same cross-coupling reactions. Also, various reactions carried out in the industry use thermal energy at relatively high temperatures. The present issue with thermal catalytic technologies is the reaction uses high amounts of heat which can create numerous unwanted results and create many safety issues. Visible light photocatalysts are being offered as a more efficient alternative than the use of thermal energy. Through photocatalysts, industrial processes could be performed using lower temperatures and gaining higher selectivity. Cu_2O has been presented as a promising semiconductor because it is cost-effective, earth-abundant and it holds a small band gap of 2.0-2.2eV.[8,9] We hybridize the cuprous oxide with catalytically active materials such as palladium to form Cu_2O-Pd (HMRNPs). These band structures allow for the absorption of a broad part of the visible light spectrum to be absorbed.

2. Experimental Details

To synthesize the spherical Cu_2O nanoparticles, a microemulsion technique was used at room temperature. This created smaller nanoparticles sized with an average diameter of 30-50 nm.[9–11] The calibration curve was done before by hand from prepared reactant samples. Before the oxidative homocoupling reaction began, the nanoparticles were suspended in a mixture of water and dimethylformamide (DMF, 13.5mL, DI Water, 1.5mL). This was added to a 25mL flask, hooked up to a condenser, and then added a thermocouple if needed. Air constantly flowed throughout the reaction to maintain the oxidative environment needed for OHR reactions. Potassium Carbonate (207mg) was added while stirring. To start the reaction, phenylacetylene (100uL) was added. The reaction was sampled regularly throughout the period to observe the conversion rates. Depending on the intention of the reaction, a white light or heat was added to the reaction.

3. Results

Glaser-type oxidative homo-coupling reaction (OHR) of phenylacetylene (PA) was used to investigate the photocatalytic nature of the Cu_2O-Pd. The nanoparticles used in all reactions were prepared using the microemulsion synthesis method. Since Glaser-type oxidative homo-coupling reaction only has a single reactant and product, the conversion of the reaction was efficient to observe.

The oxidative homo-coupling reactions were carried out in the presence of K_2CO_3 with and without light. The solvent used was a mixture of 90% dimethyl fluoride (DMF) and 10% DI water.

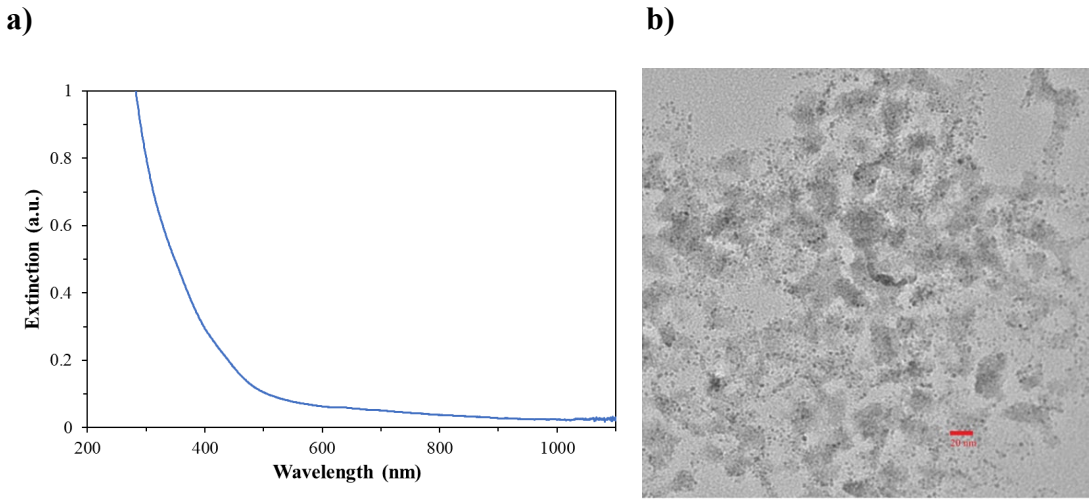

Figure 1. (a) UV-Vis extinction spectra of Cu_2O nanospheres ranging from 30 nm-50 nm diameters Cu_2O spherical nanocatalysts synthesized using the microemulsion technique. **(b)** TEM imaging shows nanospheres sizing at an average of 35nm.

The nanoparticles were then characterized through the UV-Vis and displayed in Figure 1a. To further characterize the nanocatalysts, a sample was put through TEM imaging shown in Figure 1b to confirm the sizing and shape of the nanospheres. Nanoparticles shown on average have a circular shape and rounded edges. Therefore, it can be confirmed that nanospheres around ~35 nm was being synthesized.

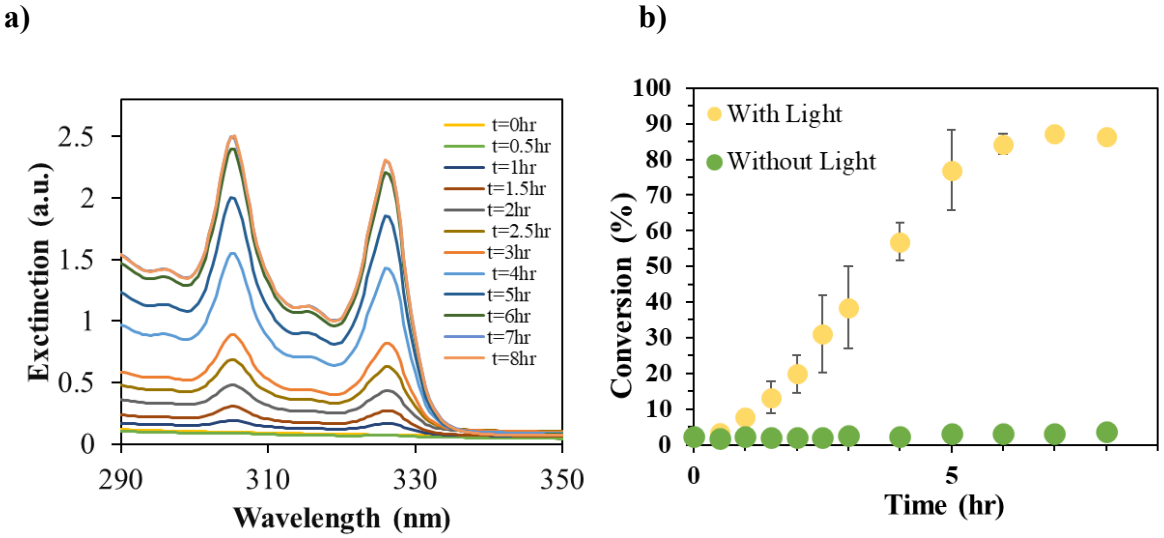

Figure 2. (a) UV-Vis extinction spectra of the reaction mixture after the addition of PA at different samples of time. **(b)** Reaction conversion as a function of reaction time for oxidative homocoupling with and without the effect of light at the primary peak (326 nm) of DPDA.

The DPDA product was observed using characterization through running timed UV-Vis samples. Figure 2a shows primary and secondary extinction peaks for DPDA appear at ~326nm and ~305nm respectively. As the reaction continues, the amount of DPDA available inside the reaction mixture increases with time. The OHR reaction over a period of 8 hours was complete with and without the presence of light. The extinction points of the primary peak (326nm) were used to quantify the conversion and then plotted in comparison to the time as shown in Figure 2b. Observing Figure 2b, it can be noted that with the reaction exposed to white light, the ending conversion is shown to be much higher. It can be concluded that the presence of light magnifies the reaction rate when compared to without light.

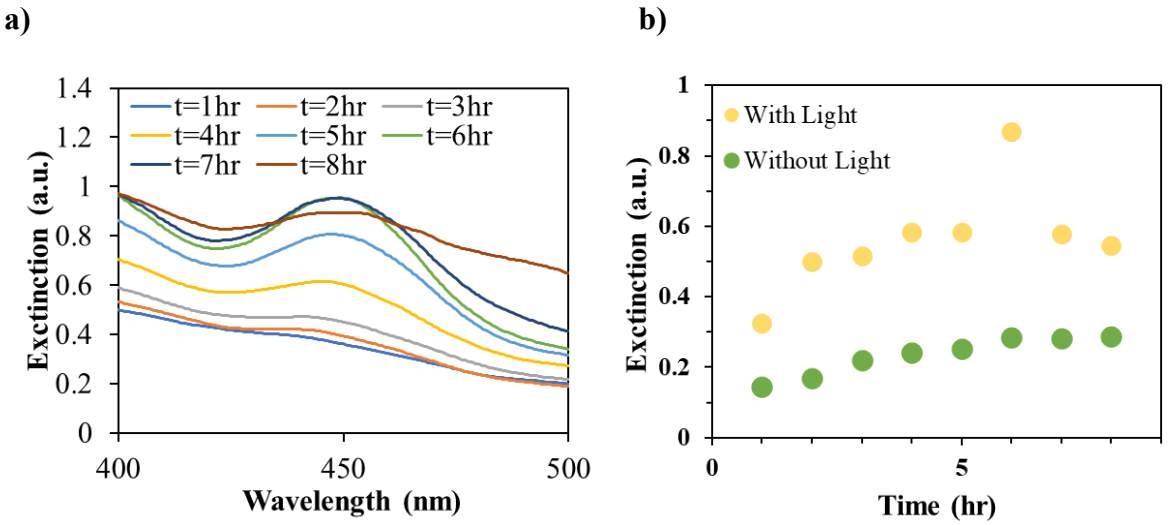

Figure 3. (a) UV-Vis extinction spectra of the reaction mixture after the addition of PA at different samples of time. **(b)** UV-Vis extinction spectra of the reaction mixture at 450nm as a function of time.

During both types of reactions, a peak began to appear at ~450mn. A dilution of 100uL of the mixture of the reaction to 3mL of Ethanol was taken to observe the extinction peak and is displayed in Figure 3a more efficiently. These peaks indicate the formation of homogeneous Cu complexes, the intermediate species created in the reaction mixture between the reactant, PA, and the product, DPDA, while the reaction is taking place. It is expected and shown that there will be no intermediate species at the beginning of the reaction. As the reaction persists, the complex amount should increase and then decrease until there is no complex since the concentration of PA at the end of the reaction is relatively low. PA is a reactant to create the complex and therefore can be attributed to the expected decreasing trends. Figure 3b shows the comparison of the trend of complexes in both types of reactions as a function of time. Without light, the formation of the Cu complex stays relatively linear over the 8-hour period. Because a great increase or the start of a decrease in extinction is never seen, it can be concluded that the rate of the reaction must be extremely slow. With light, the extinction shows the expected

result of increasing and then decreasing extinction. Compared to without light, the rate of reaction must be significantly higher.

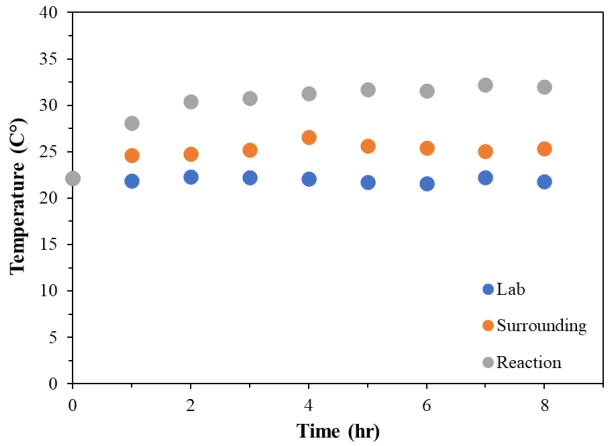

Figure 4. The measured temperature of the lab, surrounding the reaction, and the reaction itself in of the reaction with the effect of light.

Thermal energy is another variable that is highly used inside of industry for many energy and power reactions. The current type of light we are using gives off some amount of heat which is absorbed by the reaction. Knowing that this heat could affect our results, the OHR reaction was done at around ~35°C to observe the reaction rate just using thermal energy. The temperature was recorded using a handheld electronic thermometer throughout each reaction using light and was shown in Figure 4.

a) **b)**

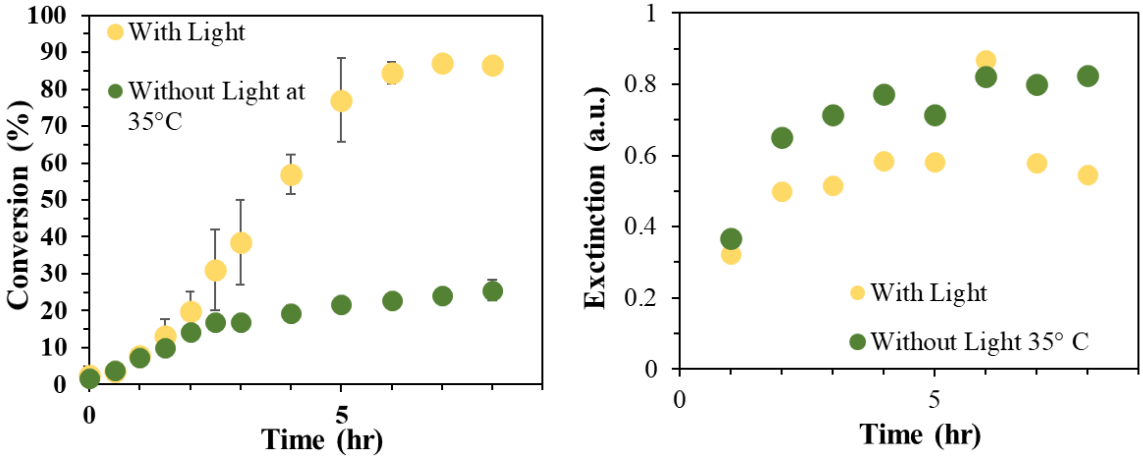

Figure 5. (a) Reaction conversion as a function of reaction time for oxidative homocoupling of PA without light heated to 35° C. **(b)** UV-Vis extinction spectra of the reaction mixture at 450nm as a function of time.

A reaction was done without light while being heated to 35 °C to simulate the effect of the heat coming from the light bulb. As shown by Figure 5a, the reaction when heated shows a similar conversion to that of a reaction with light. Observing the trendline, the conversion rate of the reaction without light seems to be deactivating or decreasing in slope as time increases. Comparing that to the reaction with light, the trendline is still increasing immensely and hypothetically will continue to hold that rate after the 8-hour period. Even though this may show similar conversions after 8 hours the conversion of the reaction with light would show a much greater conversion than the reaction being heated. Figure 5b confirms that the heat coming off the light bulb is not the reason behind the high conversion. The reaction without light shows a very linear complex formation compared to the reaction with light increases and decreases with time. As discussed before, this is an indicator of a slow reaction compared to a much faster reaction, respectively.

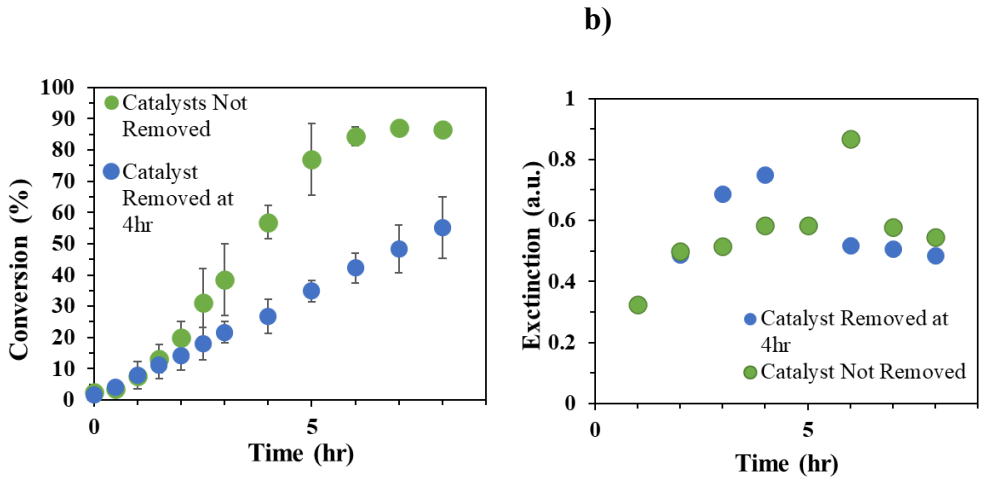

Figure 6. (a) Reaction conversion as a function of reaction time for oxidative homocoupling of PA with and without the catalyst removed. **(b)** UV-Vis extinction spectra of the reaction mixture at 450nm as a function of time.

To observe the efficiency of the photocatalyst on the reaction, an OHR was performed but at 4 hours the catalyst was removed from the experiment. This was done by centrifuging out all the solids in the experiment and only placing the liquid back into the flask. As displayed by Figure 6a, the conversion of the reaction with the catalyst removed did not perform as well. This shows the effect of the Cu_2O-Pd photocatalyst.

4. Discussion and Conclusions

The results obtained by the UV-Vis extinction spectroscopy for the Cu_2O-Pd oxidative homocoupling reaction with and without the presence of light are consistent with the hypothesis presented. The higher calculated conversion rates as well as the consistent Cu complex trends further this statement. It can be stated that using metal oxide semiconductors

for photocatalytic technologies would show to be not only an effective dielectric material but also effective against thermal energy technologies. The work and results presented in our study open the door to more development for solar and pharmaceutical applications.

5. Summary

Dielectric Mie resonators are presented as an alternative to plasmonic metal nanostructures. Cu_2O was chosen because of its small energy band gap as well as its pharmaceutically relevant coupling reactions. To test the efficacy of our chosen dielectric material using light manipulation, we used an oxidative homocoupling of phenylacetylene as the base reaction. We see a much higher rate of enhancement under light compared to dark conditions. To further prove this theory, we compared our data with light to a reaction using only thermal energy. Just like before, we still see a high conversion with light than with additional heat. Finally, we wanted to see how well our catalyst was working. This was observed by removing the catalyst at 4 hours. Since the conversion of the reaction still did not quite reach that of our base reaction, we know our catalyst is excelling the reaction. This idea can be extended to a wide range of industrially important reactions such as CO_2 reduction, ammonia synthesis, chemicals, and fuels.

6. Appendices

6a. Acknowledgements

This research was supported by Oklahoma Centre for the Advancement of Science and Technology (OCAST), NSF, and the Niblack Research Scholars Program. I want to immensely acknowledge my advisor Dr. Andiappan and my mentors Ravi and Sundaram. Lastly, I want to thank Dr. Niblack and his wife for their generosity and dedication.

6b. Papers Published

AIChE Annual Conference November 2022, Phoenix, Arizona
Awarded: 2nd Place Group III Poster Conference - Catalysis and Reaction Engineering

AIChE Midwest Regional Conference March 2023, Columbia, Missouri
Awarded: 2nd Place Poster Conference

6c. Literature Cited

(1) Linic, S.; Christopher, P.; Ingram, D. B. Plasmonic-Metal Nanostructures for Efficient Conversion of Solar to Chemical Energy. *Nature Mater* **2011**, *10* (12), 911–921. https://doi.org/10.1038/nmat3151.
(2) Linic, S.; Aslam, U.; Boerigter, C.; Morabito, M. Photochemical Transformations on Plasmonic Metal Nanoparticles. *Nature Mater* **2015**, *14* (6), 567–576. https://doi.org/10.1038/nmat4281.

(3) Aslam, U.; Rao, V. G.; Chavez, S.; Linic, S. Catalytic Conversion of Solar to Chemical Energy on Plasmonic Metal Nanostructures. *Nat Catal* **2018**, *1* (9), 656–665. https://doi.org/10.1038/s41929-018-0138-x.
(4) Christopher, P.; Xin, H.; Linic, S. Visible-Light-Enhanced Catalytic Oxidation Reactions on Plasmonic Silver Nanostructures. *Nature Chem* **2011**, *3* (6), 467–472. https://doi.org/10.1038/nchem.1032.
(5) Christopher, P.; Ingram, D. B.; Linic, S. Enhancing Photochemical Activity of Semiconductor Nanoparticles with Optically Active Ag Nanostructures: Photochemistry Mediated by Ag Surface Plasmons. *J. Phys. Chem. C* **2010**, *114* (19), 9173–9177. https://doi.org/10.1021/jp101633u.
(6) Brongersma, M.; Halas, N.; Nordlander, P. Plasmon-Induced Hot Carrier Science and Technology. *Nature nanotechnology* **2015**, *10*, 25–34. https://doi.org/10.1038/nnano.2014.311.
(7) Kuznetsov, A. I.; Miroshnichenko, A. E.; Brongersma, M. L.; Kivshar, Y. S.; Luk'yanchuk, B. Optically Resonant Dielectric Nanostructures. *Science* **2016**, *354* (6314), aag2472. https://doi.org/10.1126/science.aag2472.
(8) Hajakbari, F.; Hojabri, A.; Gholami, M.; Ghoranneviss, M. Calculation of Cu2O Thin Film Optical Constants Using the Transmittance Data. 3.
(9) Mohammadparast, F.; Ramakrishnan, S. B.; Khatri, N.; Tirumala, R. T. A.; Tan, S.; Kalkan, A. K.; Andiappan, M. Cuprous Oxide Cubic Particles with Strong and Tunable Mie Resonances for Use as Nanoantennas. *ACS Appl. Nano Mater.* **2020**, *3* (7), 6806–6815. https://doi.org/10.1021/acsanm.0c01201.
(10) Mohammadparast, F.; Dadgar, A. P.; Tirumala, R. T. A.; Mohammad, S.; Topal, C. O.; Kalkan, A. K.; Andiappan, M. C–C Coupling Reactions Catalyzed by Gold Nanoparticles: Evidence for Substrate-Mediated Leaching of Surface Atoms Using Localized Surface Plasmon Resonance Spectroscopy. *J. Phys. Chem. C* **2019**, *123* (18), 11539–11545. https://doi.org/10.1021/acs.jpcc.8b12453.
(11) Addanki Tirumala, R. T.; P. Dadgar, A.; Mohammadparast, F.; Ramakrishnan, S. B.; Mou, T.; Wang, B.; Andiappan, M. Homogeneous *versus* Heterogeneous Catalysis in Cu_2O-Nanoparticle-Catalyzed C–C Coupling Reactions. *Green Chem.* **2019**, *21* (19), 5284–5290. https://doi.org/10.1039/C9GC01930H.

Visible Light-Driven C-C Coupling Reaction of Terminal Alkynes at Atmospheric Temperature and Pressure Reaction Conditions using Hybrid Cu_2O-Pd Nanostructures

Samantha Stobbe, Ravi Teja AT, Sundaram Bhardwaj Ramakrishnan, and Dr. Marimuthu Andiappan

School of Chemical Engineering

Oklahoma State University

Stillwater, OK, USA

Plasmonic Catalysis

Motivation

- Nanomaterials for Photonic and Spectroscopic applications: Plasmonic metal nanostructures (PMN)
- PMN's Unique property: Mie Resonance - Localized Surface Plasmon Resonance (LSPR)
- Limitations of PMNs:
  - Relatively expensive (Au and Ag)
  - Not compatible with conventional semiconductor manufacturing
- **So, what's the alternative to PMN ?**
- **High dielectric nanostructures (e.g., Cu_2O, CuO)**

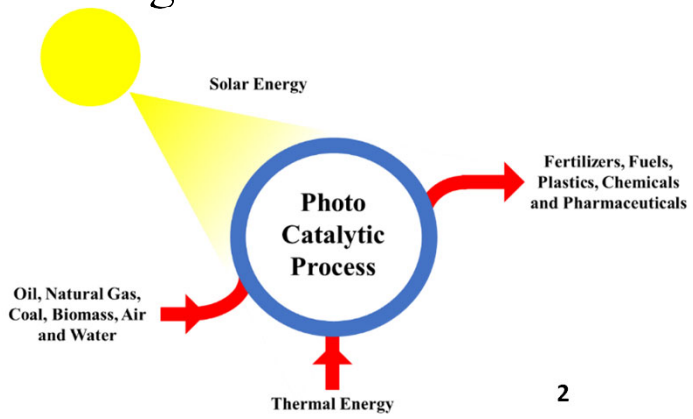

Plasmonic vs Dielectric

Plasmonic Ag sphere – 175nm

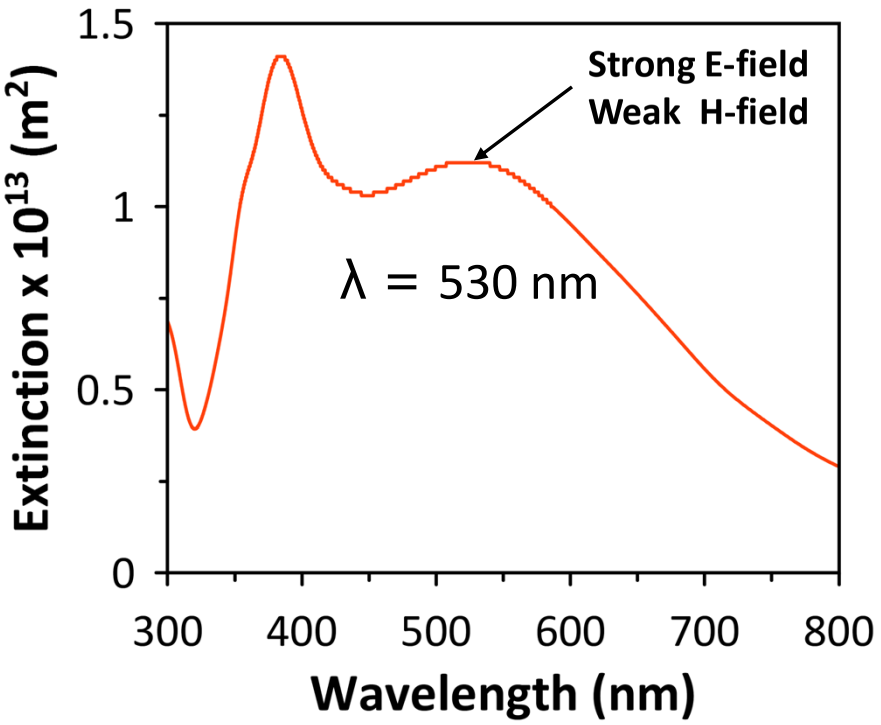

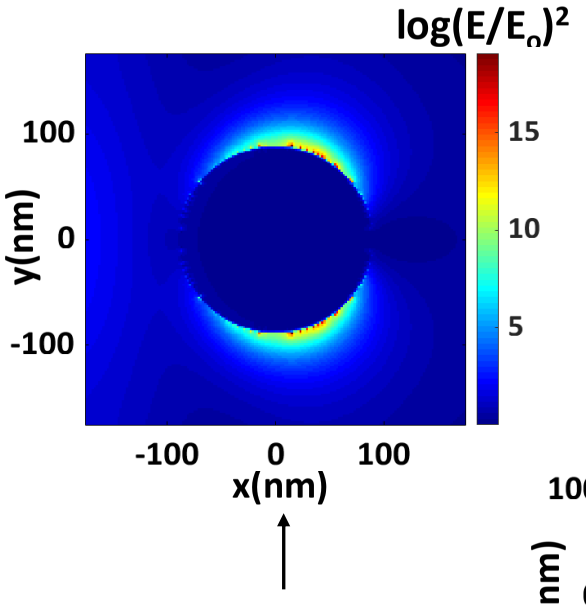

Electric Dipole is stronger

Magnetic Dipole is weaker

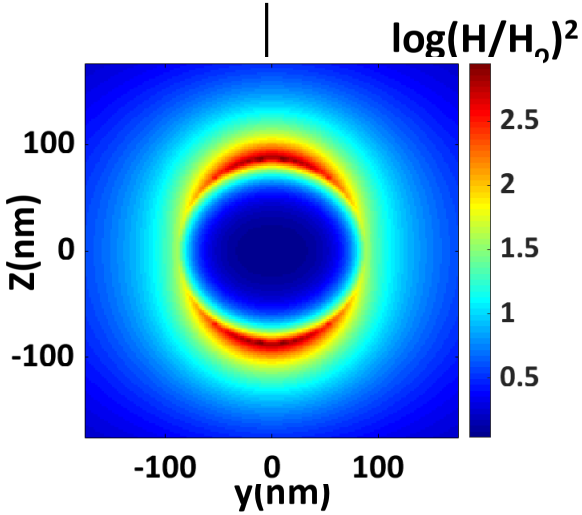

Plasmonic vs Dielectric

Dielectric Cu_2O sphere – 175nm

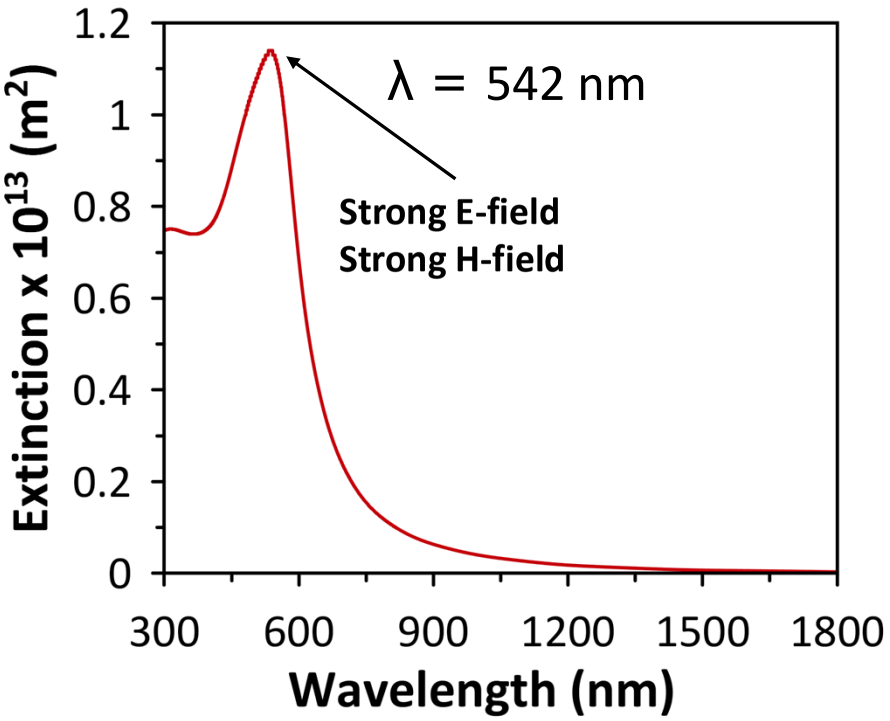

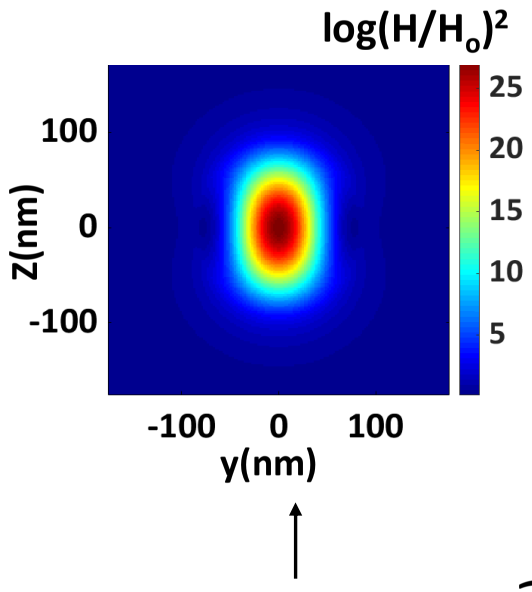

Magnetic Dipole is stronger

Electric Dipole is stronger

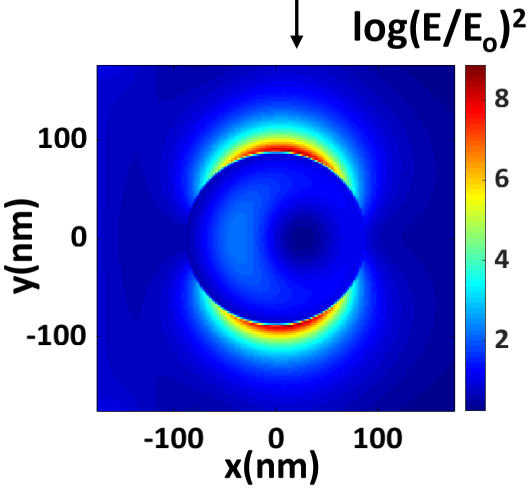

Mohammadparast et al. *ACS Appl. Nano Mater.* **2020**, 3, 7, 6806–6815

Project Challenge

- Dielectric visible light driven Mie resonator nanoparticles as a viable catalyst.
- Cu_2O nanocatalyst is inexpensive, non-toxic, low bandgap semiconductor, and high dielectric in nature.
- Hybridizing MRNPs with catalytic active materials such as palladium to form Cu_2O-Pd.

Challenge: Photocatalytic Activity of Cu_2O is low under conventional light conditions.

Cu_2O Small Spheres – Synthesis

- Micro emulsion technique
- Copper nitrate ($Cu(NO_3)_2$) salt in water is used as a precursor
- Reverse micelle method
- Reverse micelles serve as uniformly sized nanoreactors

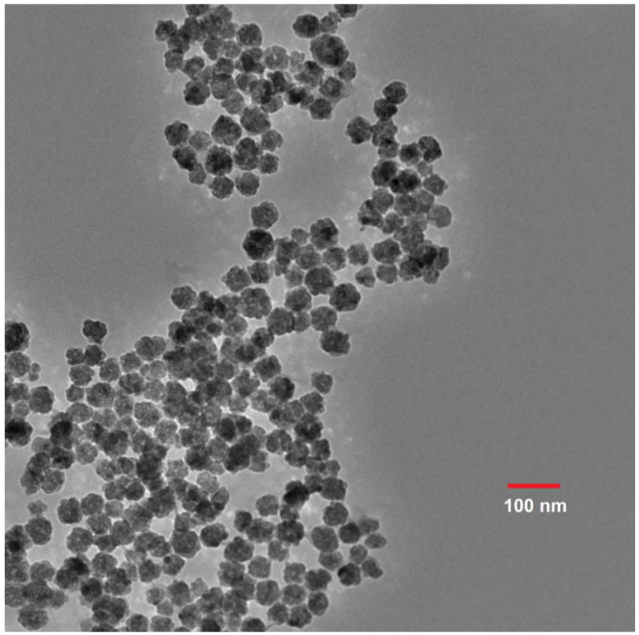

Particle Size: 47 ± 6**

Ravi Teja. AT, Andishaeh P. Dadgar et. al. *Green Chemistry,* **2019** *21* (19), 5284–5290.

Background C-C Coupling

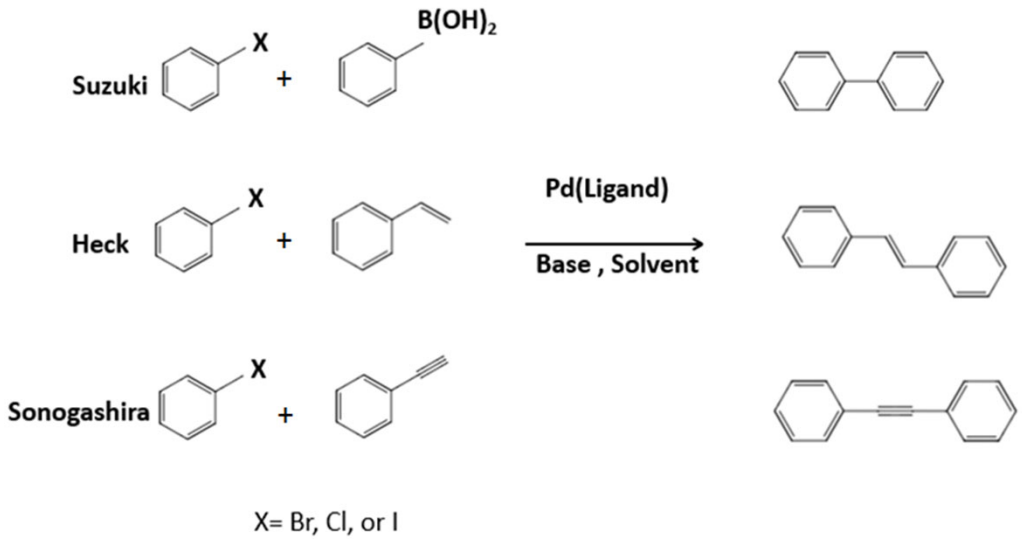

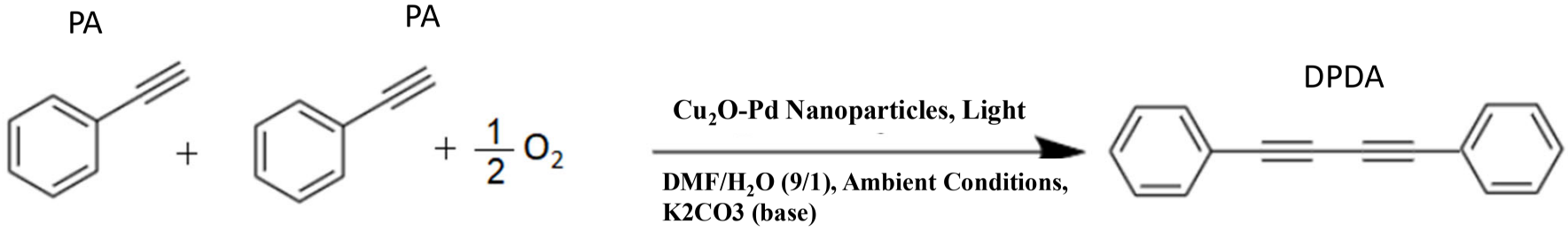

Ravi Teja. AT, Andishaeh P. Dadgar et. al. *Green Chemistry,* **2019** *21* (19), 5284–5290.

Rate Enhancement - Light

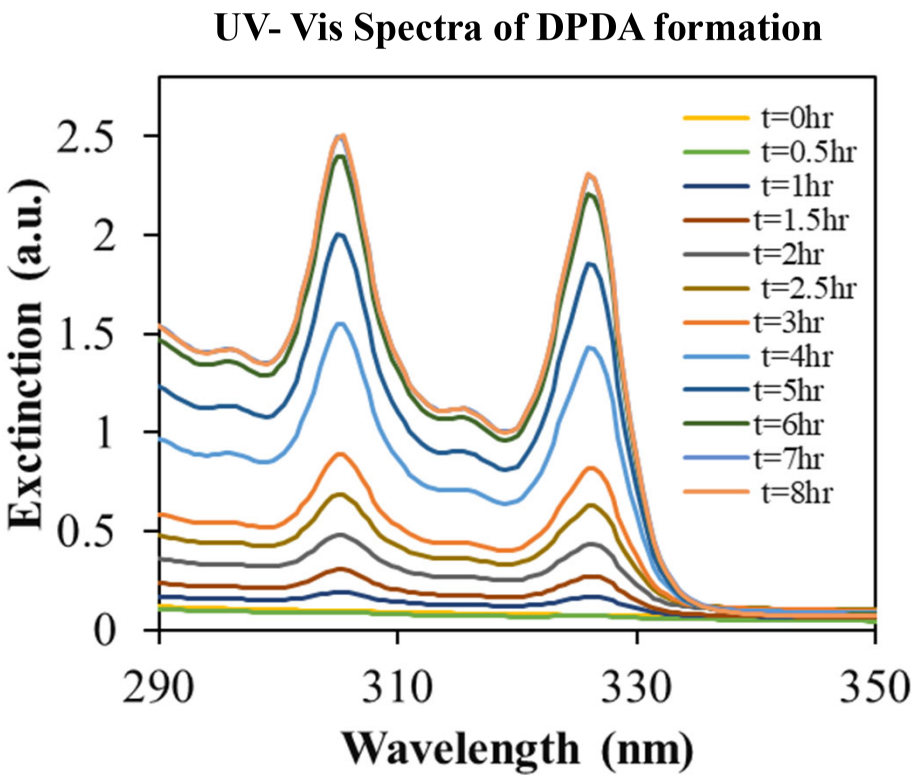

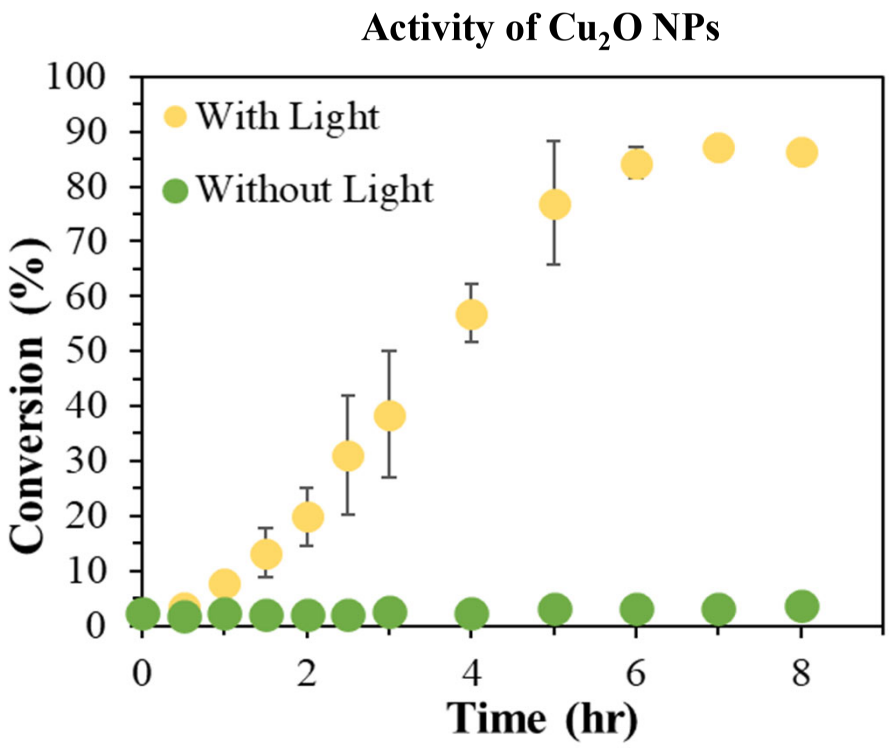

Ravi Teja. AT, Andishaeh P. Dadgar et. al. *Green Chemistry,* **2019** *21* (19), 5284–5290.

Rate Enhancement - Light

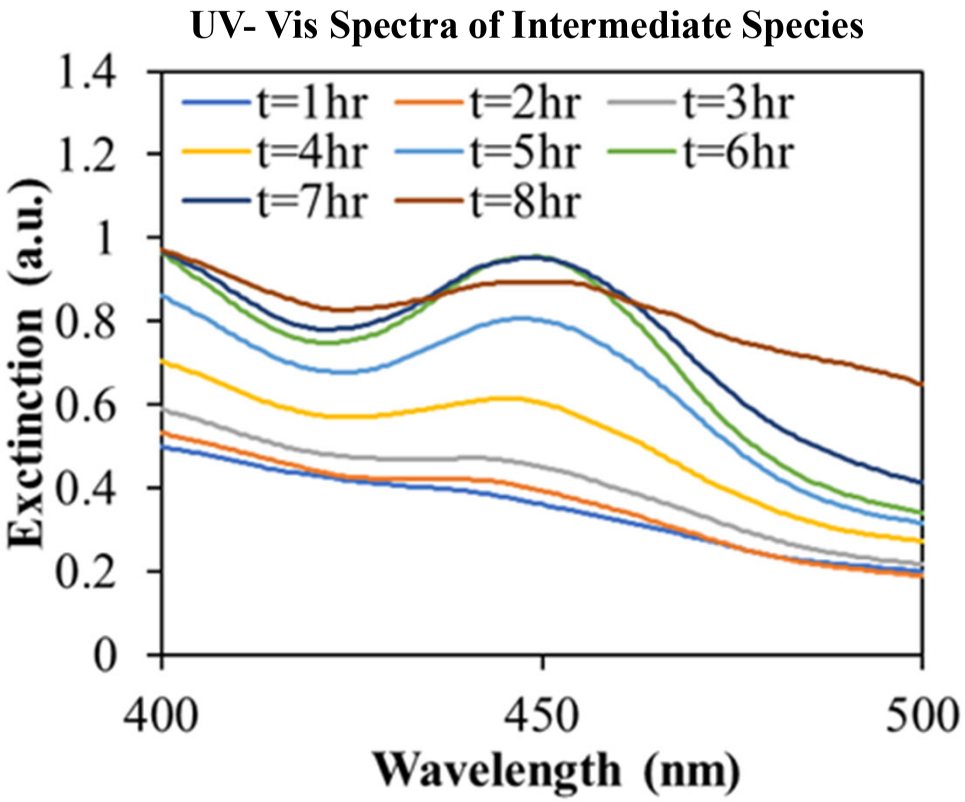

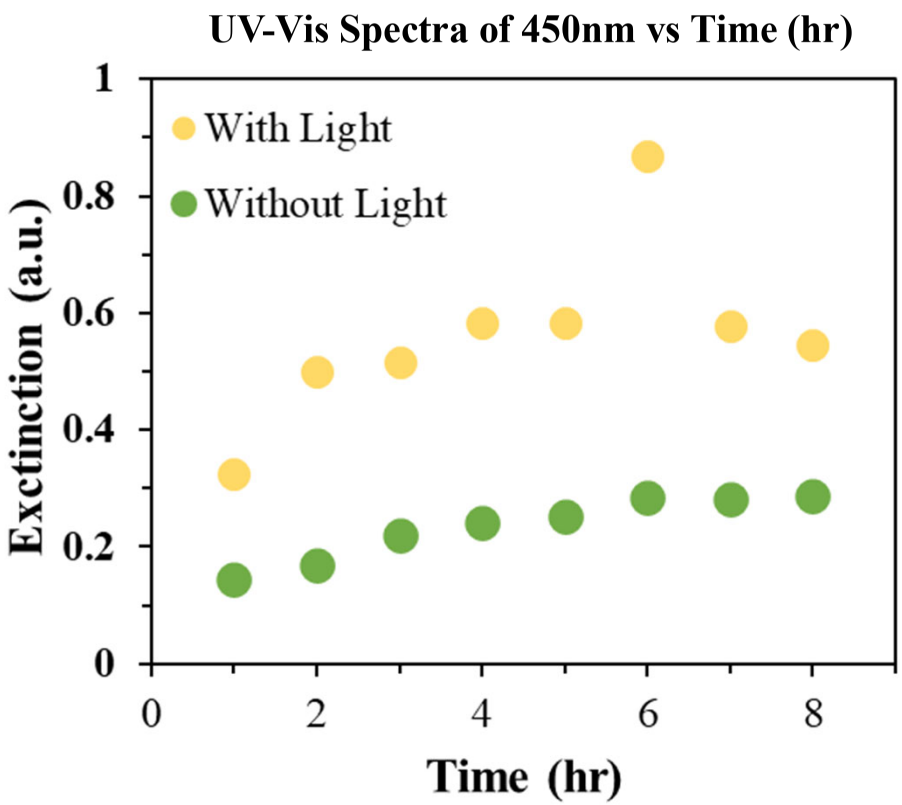

Ravi Teja. AT, Andishaeh P. Dadgar et. al. *Green Chemistry,* **2019** *21* (19), 5284–5290.

Understanding Thermal Effect

- To verify the significance of the thermal effect in the photocatalytic glazer coupling reaction catalyzed by Cu_2O NPs

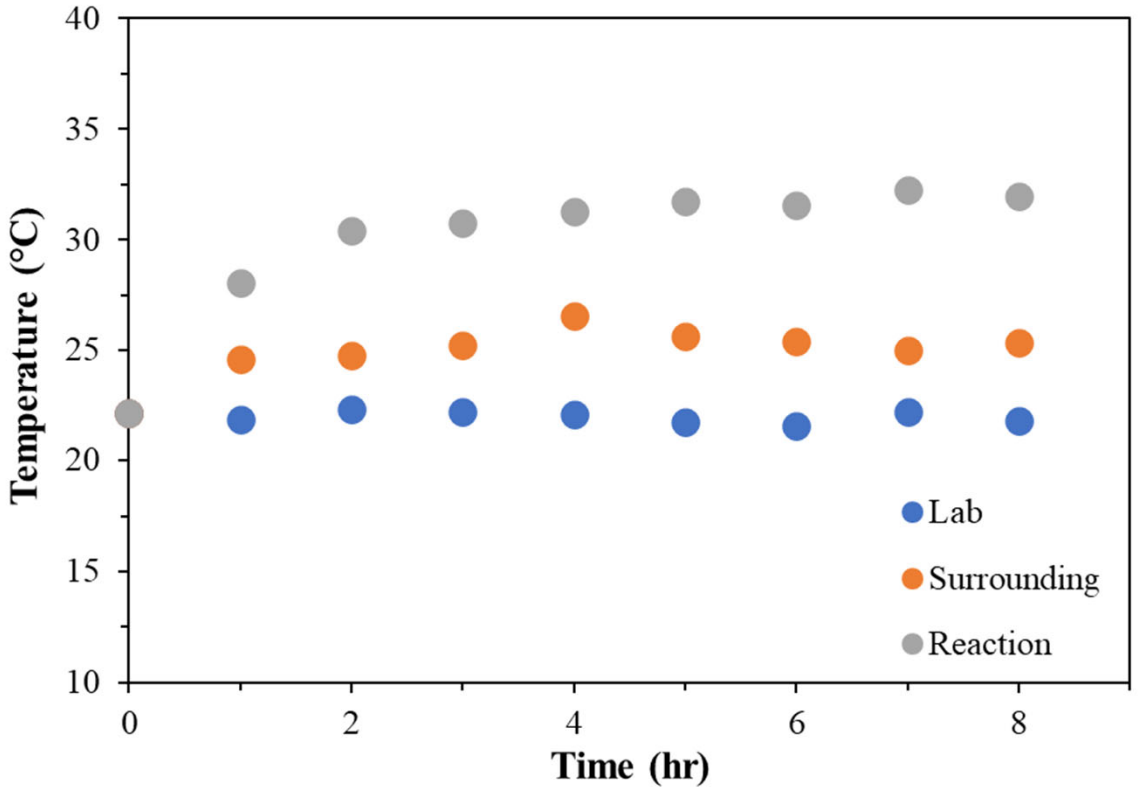

Understanding Thermal Effect

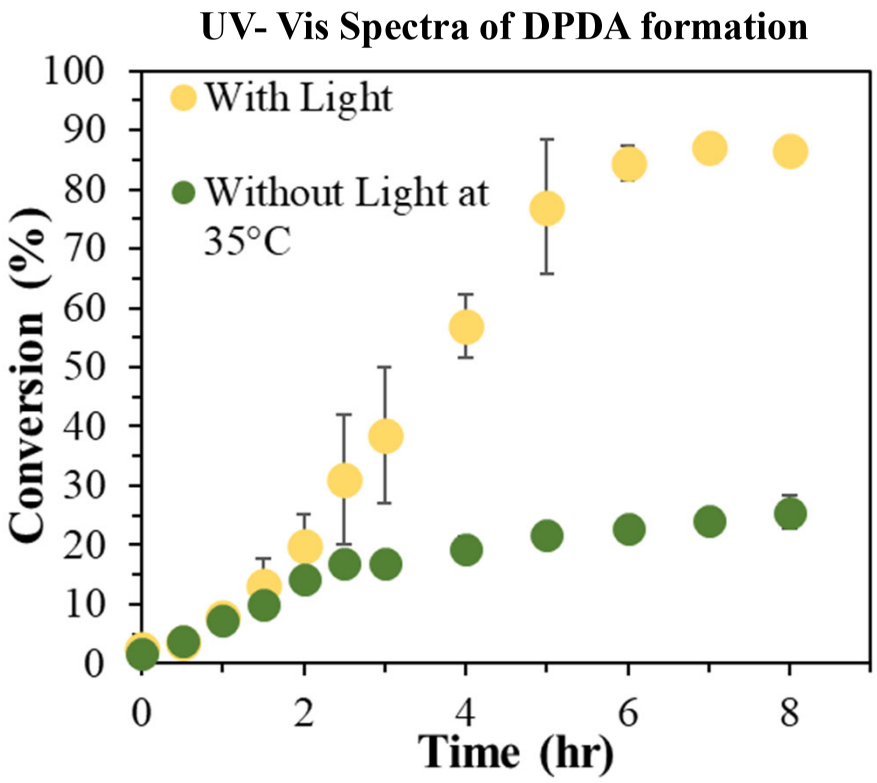

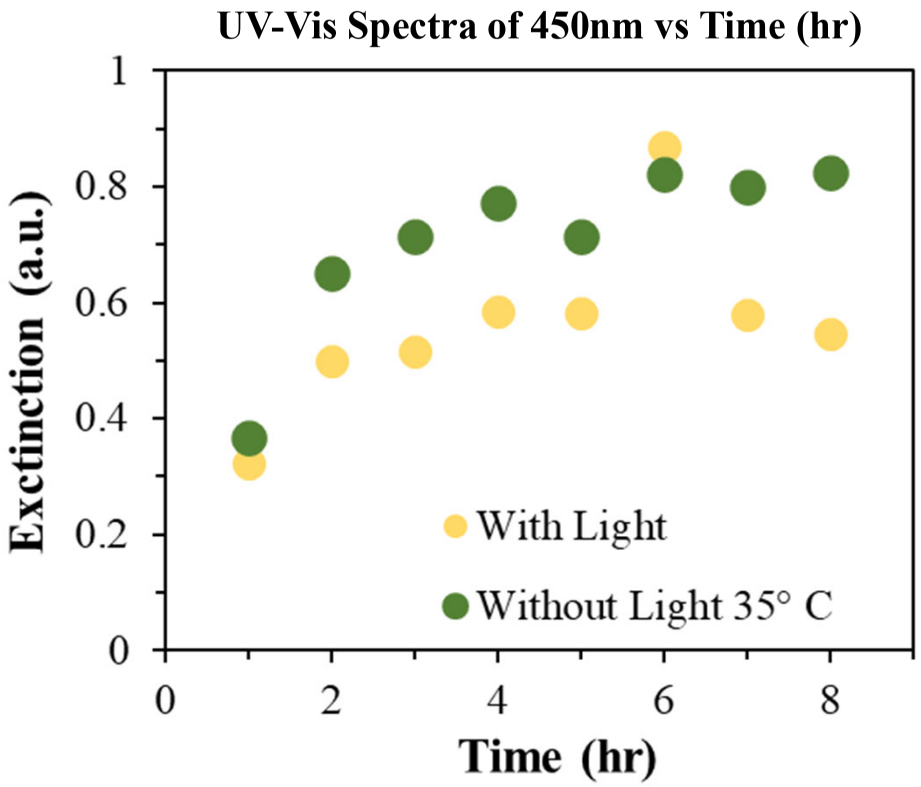

Effect of the Photocatalyst

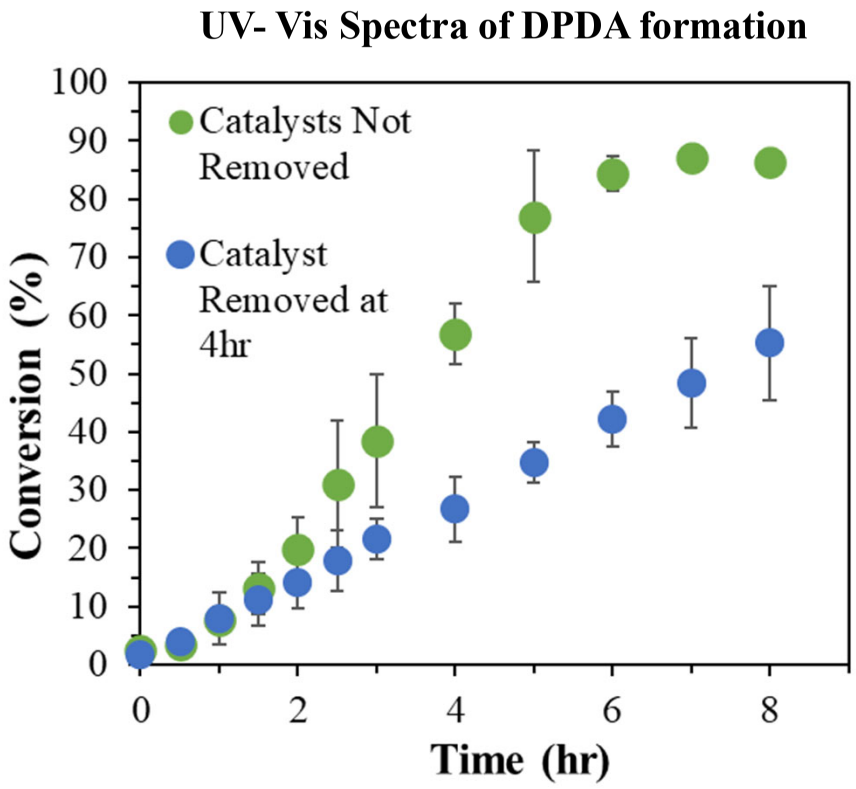

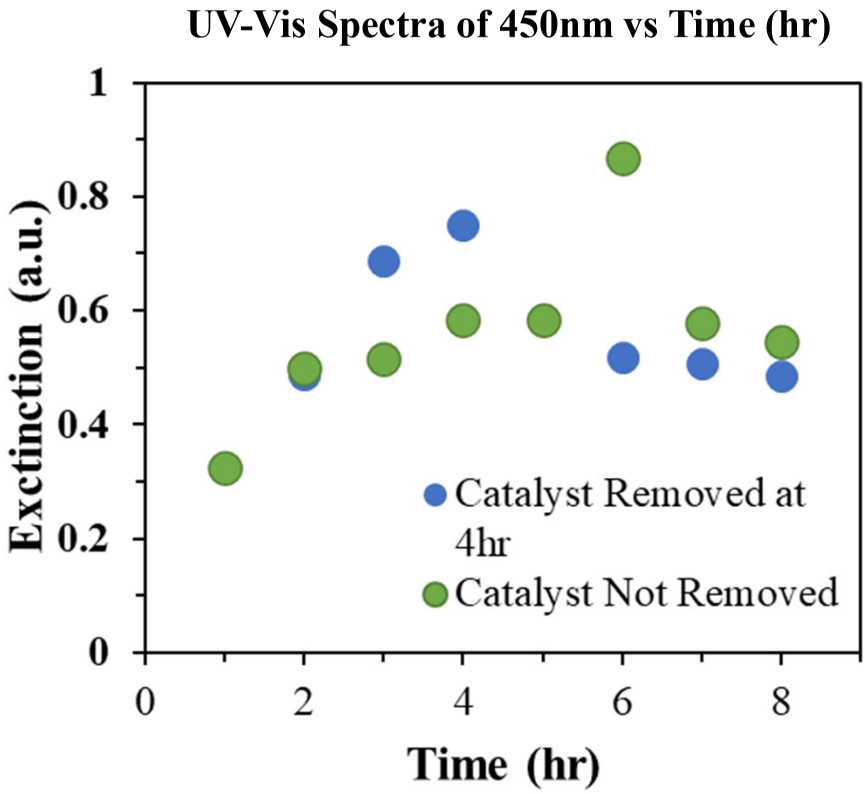

Summary

To bring an efficient alternative to PMN - dielectric nanostructures (e.g., Cu_2O)

- Dielectric materials use light to enhance photocatalytic activity using Mie resonances.

- In-situ separation of the photocatalyst from the reaction reduces the activity in the supernatant mixture

- There is negligible impact of thermal effect on the activity of the reaction

- This idea can be extended to other metal-oxides as well, (e.g., α-Fe_2O_3, CeO_2)

Future Work: Summary

- Visible light-mediated Cu_2O catalyzed C-C couplings can be extended to Suzuki, heck, and Buchwald coupling reactions

- Possible Applications in Continuous Flow Reactor

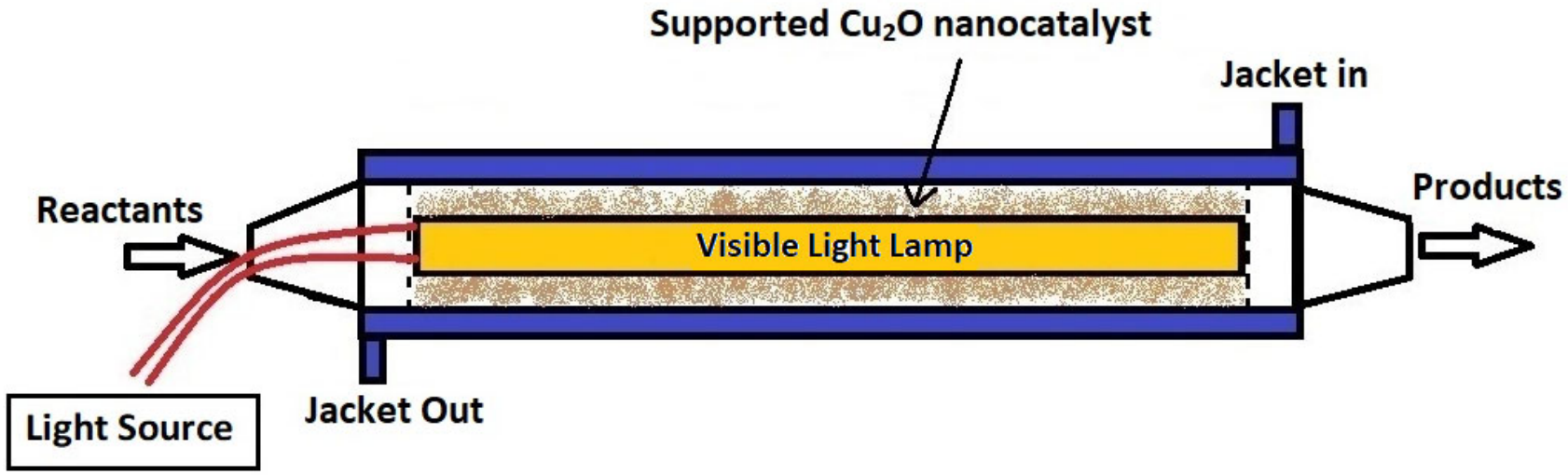

Acknowledgements

Advisor: Dr. Marimuthu Andiappan

Team Members:
- Ravi Teja Addanki Tirumala
- Sundaram Bhardwaj Ramakrishnan

Niblack Research Scholarship Program
- Dr. and Mrs. Niblack

National Science Foundation

CBET-2102238
CBET-2102239

Oklahoma Center for the Advancement of Science and Technology

HR18-093

Questions?

Morphological characterization of wing shapes of tiny insects

Sam Glenn

Mechanical and Aerospace Engineering
Faculty Sponsor: Arvind Santhanakrishnan
Graduate Student Mentor: Mitchell Ford

ABSTRACT

The bristled wings of numerous species of tiny insects such as thrips and fairyflies show remarkable diversity in shape, ranging from short, teardrop-shaped to long, slender profiles. We document the interspecific diversity in forewing shape of thrips and fairyflies based on principal component analysis of wing geometries of 13 species of thrips and 28 species of fairyflies. Wing shapes and geometric characteristics (chord, wingspan, wing area) were measured in ImageJ from published forewing images of thrips and fairyflies. The first three principal axes of variation were found to be linearly correlated ($p << 0.01$) with: Axis 1 = total wing area (A_T, $R^2 = 0.91$); Axis 2 = ratio of the area of the leading edge (LE) portion of the wing to the area of the trailing edge (TE) of the wing, which factors variation in bristle and membrane lengths on the LE and TE portions measured relative to a fictitious straight line on the wing membrane connecting the wing root to the wing tip (LE/TE, $R^2 = 0.46$), and Axis 3 = LE/TE ($R^2 = 0.20$). While wing area is expected to directly impact aerodynamic force generation, the effects of varying LE/TE on the aerodynamics of tiny insect flight are unknown. We measured aerodynamic forces generated by scaled-up bristled elliptical wing models with LE/TE of 0.125, 0.25, 0.375, 0.5, 1 and 2. Each wing was fitted onto a 3D flapping robotic model that was programmed to replicate previously published thrips kinematics under hovering conditions (i.e., time-varying position and pitch angles at zero elevation angle). Strain gauges bonded to custom-built brackets were used to measure time-varying horizontal (drag) and vertical (lift) forces at the wing root, and glycerin was used to operate each wing model at chord-based Reynolds number of 10 that is relevant to tiny insect flight. We found that varying LE/TE had relatively minimal effect on cycle averaged drag and lift coefficients, with a slight trend of increasing peak lift over peak drag coefficients as LE/TE increased. These findings suggest that biological variation in bristle lengths minimally influences hovering aerodynamics, which can be helpful in situations where irregular mechanical damage and/or wearing of bristles is present.

1. Introduction

There are a great number of species of tiny, flight-capable insects with body lengths on the order of 1 mm, including fairyflies and thrips. These tiny insects are of significant

ecological and agricultural importance. Thrips can transmit viruses that are known to cause damage to crops that are economically important, such as tomatoes and onions. Understanding the flight and dispersal of these tiny insects can aid in the development of effective pest management strategies. In spite of the numerous species of tiny insects, there is relatively little known about flight at this scale. The majority of the current literature on insect flight is focused on larger insects, such as dragonflies and fruit flies.

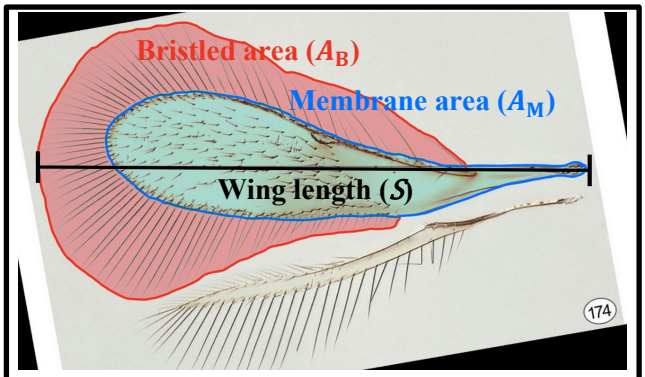

Figure 1: Representative fairyfly forewing[1]. Blue shaded area is the membrane area and red shaded area is the bristled area. The black line drawn from root to tip is the wing length. LE/TE is the ratio of the area above the black line to the area below the black line.

Tiny insects fly at a chord-based Reynolds number (Re) on the orders of 1 to 10 which is significantly lower than larger insects that fly at Re of 100 and above. Re is defined as the ratio of inertial forces (force to move the wing) to viscous forces (resistance offered by air). At such a low Re, tiny insects have to deal with large viscous forces that their larger counterparts do not have to contend with. Tiny insects have evolved to have thin membranous wings with long bristles around the edges. In addition to bristled wings, these insects have also evolved to use a wing motion referred to as "clap-and-fling"[2]. Clap-and-fling is when a pair of wings comes together at the end of the upstroke and fling apart at the beginning of the downstroke, effectively increasing the stroke amplitude.

Past studies have concluded that bristled wings can reduce the force required to fling wings apart[3,4]. Several studies in the past have also looked at the morphological variation in tiny insect wings. Ford et al.[4] examined how varying the ratio of membrane wing area (A_M) to total wing area (A_T) affected aerodynamic forces. One study[5] analyzed forewing images of both thrips and fairyflies, and then looked at how varying forewing bristle morphology affected aerodynamic forces. Another study[6] analyzed morphological wing variation in fairyflies and used numerical simulations to determine whether bristled wings reduced the force required to fling wings apart. However, none of these studies looked at how varying wing shape affects the flight of these insects.

In this study, we documented the morphological variation in wing shape of 28 species of fairyflies and 13 species of thrips. Principal component analysis was performed for the wing

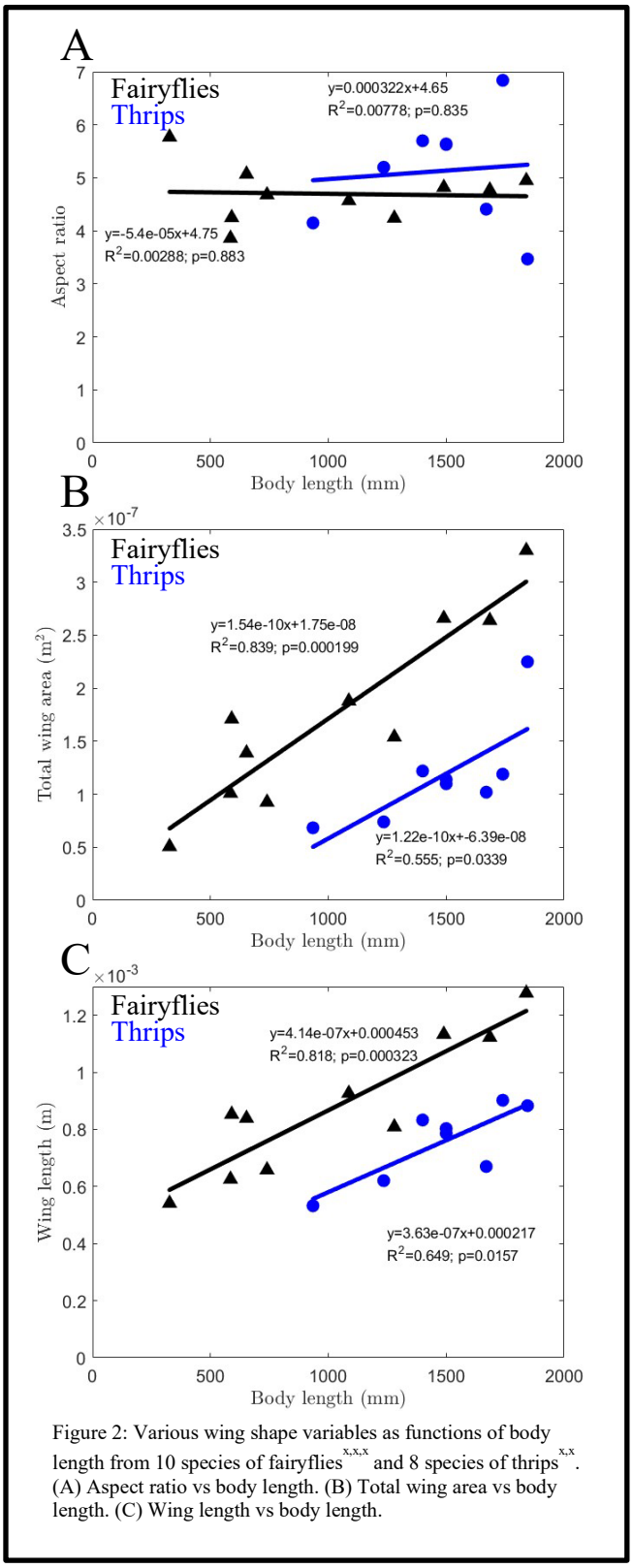

Figure 2: Various wing shape variables as functions of body length from 10 species of fairyflies[x,x,x] and 8 species of thrips[x,x]. (A) Aspect ratio vs body length. (B) Total wing area vs body length. (C) Wing length vs body length.

geometries. We then performed regressions for important wing shape variables against the first three axes from the principal component analysis. This morphological data allowed us to design six scaled-up wing models that covered the biologically relevant range of LE/TE. Time varying lift and drag forces were then comparatively measured between the wings to determine the effects of varying LE/TE on the flight of tiny insects.

2. Experimental Details

Morphological data on wing shapes of tiny insects were collected from published images[1,7,8,9,10] of 13 species of thrips and 28 species of fairyflies to characterize the variation in wing shapes of tiny insects. Images were analyzed in Image J[11]. 20 points were manually placed around the top of the bristled wing area, top of the membrane wing area, bottom of the membrane wing area, and bottom of the bristled wing area. These points were then used to make a spline fit of 20 evenly spaced points. The distances of each of these points to a line going from wing root to wing tip, along with wing length, were the inputs to the principal component analysis. Principal component analysis gives axes which contain the most variation of the data in descending order, for instance, axis 1 contains the most variation in the data. The points used as inputs to the principal component analysis allowed us to directly measure total wing area (A_T), membrane wing area (A_M), leading edge

area, trailing edge area, and wing length (S). The ratio of bristled wing area to membrane wing area (A_M/A_T) was then calculated as well as the ratio of leading-edge area to trailing-edge area (LE/TE). In addition, aspect ratio (AR) was calculated as AR = S^2/A_T. 10 species of fairyflies[1,7,8] and 8 species of thrips[9,10] with available body lengths, had linear regressions run for A_T, AR, and S against body length as shown in Figure 2. Linear regressions were also run for the first three axes of the principal component analysis, against A_M/A_T, LE/TE and A_T.

This morphological data was then used to design six scaled up wing models, encompassing the biologically relevant range of LE/TE. Bristled, elliptical wing models were designed in SolidWorks software (Dassault Systèmes SE, Vélizy-Villacoublay, France). LE/TE values of 2, 1, 0.5, 0.375, 0.25, and 0.125 were chosen for this study. The wing membranes were laser cut from 3 mm thick acrylic. The wing bristles were made from 0.305 mm diameter wire cut to length and attached to the wing membrane using epoxy. A_T, A_M/A_T, gap to bristle diameter ratio (G/D) and number of bristles were kept constant to ensure that any differences found between wing models would be purely a result of changing LE/TE. The value of A_M/A_T chosen for this study was 0.45, as this was in the middle of the biologically relevant range found from the morphological analysis for all species we looked at. The G/D of the models was 5 and the number of bristles used was 80, both of which are in the biologically relevant range of tiny insects[4].

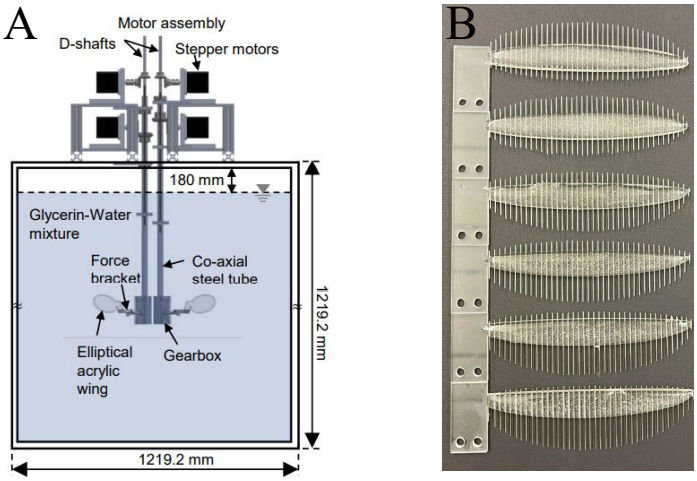

Figure 3: (A) Flapping robot model experimental setup. (B) Scaled up wing models from top to bottom LE/TE = 2, LE/TE = 1, LE/TE = 0.5, LE/TE = 0.375, LE/TE = 0.25, LE/TE = 0.125.

A dynamically scaled robotic model was used to replicate the wing motion of tiny insects for pitch angle and position angle in the horizontal stroke plane. The wing models were submersed in a square acrylic tank filled with glycerin. Wings were attached using custom L-brackets with strain gauges mounted on both sides to measure lift and drag forces. The experimental setup shown in Figure 3(A) was programmed to replicate published thrips wing kinematics[12] shown in Figure 4. All wing models were tested using these kinematics at Re = 10, where Re is defined as,

$$Re = \frac{2\Phi f R c}{\nu}$$

where Φ is the stroke amplitude, f is the stroke frequency, R is the wing tip radius, c is the wing chord, and ν is the kinematic viscosity of the fluid.

As with previous studies[13,4] force data was collected using strain gauges mounted on both sides of custom L-brackets. Voltages were constantly measured from the strain gauges. One bracket was used to measure normal forces (F_N), while another bracket was used to measure tangential forces (F_T), non-simultaneously. 30 cycles of raw voltages were measured with a pause of 30 seconds between each cycle. The first 10 cycles were discarded to ensure the fluid had reached a steady state. The data was then processed using a custom MATLAB (The Mathworks Inc., Natick, MA, USA) script to find the time varying lift and drag forces over the course of one cycle. The lift and drag coefficients were defined as follows,

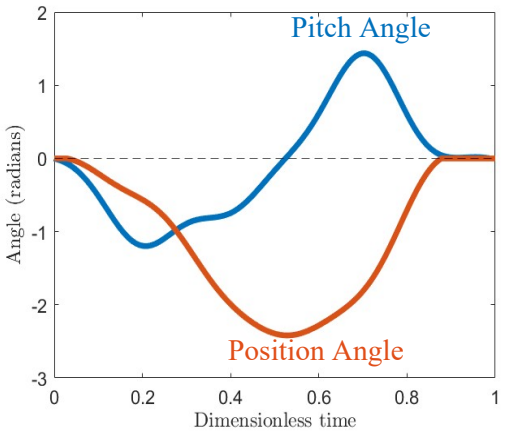

Figure 4: Thrip kinematics. Blue line represents the pitch angle, and the red line represents position angle. Both are plotted against dimensionless time.

$$C_L = \frac{F_T cos(90 - \Psi) + F_N sin(90 - \Psi)}{0.5\rho U^2 A}$$

$$C_D = \frac{F_T sin(90 - \Psi) + F_N cos(90 - \Psi)}{0.5\rho U^2 A}$$

where Ψ is the angular position of the wing relative to vertical, ρ is the fluid density, U is the wing tip velocity, and A is the wing area.

3. Results

There was a high degree of variability in the wing variables measured in the morphological analysis. For thrips LE/TE ranged from 2.61 to 0.24 and for fairyflies LE/TE ranged from 1.98 to 0.56. For thrips A_{T} ranged from 0.22 mm^2 to 0.044 mm^2 and for fairyflies A_{T} ranged from 0.541 mm^2 to 0.051 mm^2. Lastly, for thrips $A_{\mathrm{M}}/A_{\mathrm{T}}$ ranged from 0.44 to 0.162 and for fairyflies $A_{\mathrm{M}}/A_{\mathrm{T}}$ ranged from 0.9 to 0.13.

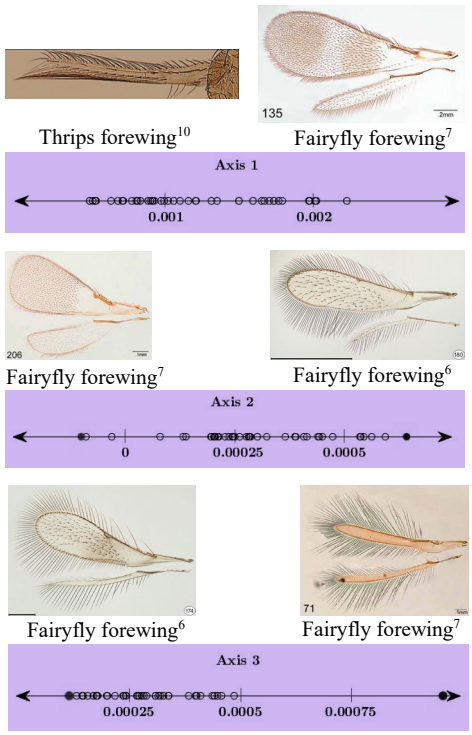

Figure 5: The first three axes of the principal component analysis plotted on a number line. The wing shapes of the left side are the wings with the smallest value for each axis. The images on the right side are the wing shapes that had the highest value for each axis.

Figure 2 shows A_T, AR , and S plotted as functions of body length. As body length increased, both total wing area and wing length increased. There was no correlation, however, between body length and aspect ratio.

After gathering all the morphological data, a principal component analysis was performed and linear regressions were run for the first three axes against LE/TE, A_{T}, and $A_{\mathrm{M}}/A_{\mathrm{T}}$. For axis 1, we found that it strongly correlated to increasing total wing area (R^2=0.91, p << 0.01), and also strongly correlated to increasing $A_{\mathrm{M}}/A_{\mathrm{T}}$ (R^2=0.57, p << 0.01). For axis 2, we found it correlated to decreasing $A_{\mathrm{M}}/A_{\mathrm{T}}$ (R^2=0.24, p << 0.01), and it also correlated to decreasing LE/TE (R^2=0.46, p << 0.01). For axis 3, we found it correlated to increasing LE/TE (R^2=0.20, p=0.0018), and we also found it weakly correlated with decreasing $A_{\mathrm{M}}/A_{\mathrm{T}}$ (R^2=0.12, p=0.019).

Figure 5 shows several representative wings of both thrips and fairflies. Looking at the extremities of axis 2 it is visually evident that as axis 2 increases $A_{\mathrm{M}}/A_{\mathrm{T}}$ decreases. The wing with the lowest axis 2 value has almost no bristled area, whereas the wing that had the highest value for axis 2 has significant bristled area. In axis 3, the correlation between increasing axis 3 and decreasing $A_{\mathrm{M}}/A_{\mathrm{T}}$ is also evident.

Cycle averaged lift and drag coefficients were calculated to show the effect of varying LE/TE on a complete cycle, as shown in Figure 6. Taking the standard deviations into account, altering LE/TE had little to no effect on the cycle averaged force coefficients.

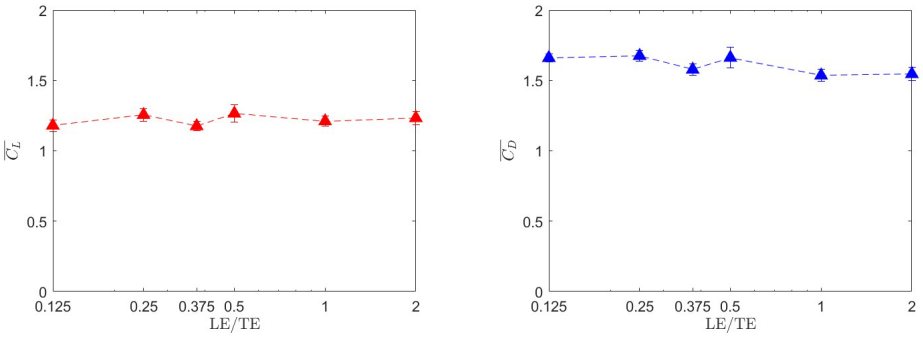

Figure 6: Cycle averaged lift and drag coefficients plotted against LE/TE. Plus or minus one standard deviation is included with each point

4. Discussion and Conclusions

The findings from our morphological analysis indicated that A_T is the most important variable for characterizing wing shapes of tiny insects. There was a strong correlation between axis 1 and A_T indicating that most of the variation in wing shape we found could be explained by the changes in A_T. Axis 2 and axis 3 were both correlated with LE/TE and $A_\mathrm{M}/A_\mathrm{T}$ indicating that they are both also important for characterizing wing shapes of tiny insects. The effects of varying A_T as well as $A_\mathrm{M}/A_\mathrm{T}$ are well understood, which is why we chose to investigate the effects of LE/TE on tiny insect flight.

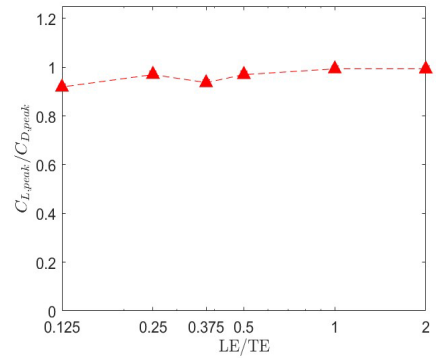

Figure 7: Peak lift coefficient over peak drag coefficient plotted against LE/TE.

Figure 7 shows the peak lift over drag coefficients plotted against LE/TE. Although we found very little variation in the cycle averaged lift and drag coefficients, there did appear to be a trend of increasing peak lift over peak drag coefficients with increasing LE/TE. The data from the morphological analysis showed the median LE/TE value for thrips and fairyflies combined to be 0.87. This may mean that there is some benefit to having a higher LE/TE for tiny insects, as lower LE/TE values show a slight drop off in peak lift coefficient over peak drag coefficient. A promising direction for future work would be to vary the aspect ratio of wings to see how this affects the aerodynamic performance of tiny insects.

5. Summary

The forewings of various species of tiny insects were analyzed based on principal component analysis. This showed that total A_T, $A_\mathrm{M}/A_\mathrm{T}$, and LE/TE were all important

variables for characterizing diversity in forewing shapes of tiny insects. Scaled-up bristled wing models of various LE/TE were fabricated and tested to examine aerodynamic performance. Varying LE/TE had negligible effects on cycle averaged lift and drag coefficients. There was a small increase in peak lift over drag coefficients as LE/TE increased, indicating that perhaps there is some slight benefit to higher LE/TE on aerodynamic performance.

6. Appendices

6a. Acknowledgements

I would like to express my utmost gratitude to Dr. and Mrs. Niblack for providing funding that has allowed me to pursue this independent research project. I would also like to thank Dr. Santhanakrishnan as well as Mitchell Ford for their insight and guidance during this project.

6b. Papers Published

Sam G. Glenn, Mitchell P. Ford & Arvind Santhanakrishnan *Morphological characterization of wing shapes of tiny insects.* (Poster). 2023 Annual Meeting of the Society for Integrative & Comparative Biology, January 3-7, Austin, TX.

6c. Literature Cited

[4]Ford, M. P., Kasoju, V. T., Gaddam, M. G. and Santhanakrishnan, A., 2019. Aerodynamic effects of varying solid surface area of bristled wings performing clap and fling. Bioinspir. Biomim., 14(4).

[1]Huber, J. T., 2017. Eustochomorpha Girault, Neotriadomerus gen. n., and Proarescon gen. n. (Hymenoptera, Mymaridae), early extant lineages in evolution of the family. J. Hymenopt. Res. 57: 1-87.

[7]Huber, J. T., Mendel, Z., Protasov, A. and La Salle, J., 2006. Two new Australian species of Stethynium (Hymenoptera: Mymaridae), larval parasitoids of Ophelimus maskelli (Ashmead) (Hymenoptera: Eulophidae) on eucalyptus. J. Nat. Hist. 40: 1909-1921.

[6]Jones, S., Yun, Y., Hedrick, T., Griffith, B. and Miller, L., 2016. Bristles reduce the force required to 'fling' wings apart in the smallest insects. J. Exp. Biol. 219: 3759–3772.

[5]Kasoju, V. T., Ford, M. P., Ngo, T. T. and Santhanakrishnan, A. 2021. Inter-species variation in number of bristles on forewings of tiny insects does not impact clap-and-fling aerodynamics. J. Exp. Biol., 224(18).

[13]Kasoju, V. T., Terrill, C., Ford, M. and Santhanakrishnan, A., 2018. Leaky flow through simplified physical models of bristled wings of tiny insects during clap and fling. Fluids 3 44.

[8]Lin, N. Q., Huber, J. T. and LaSalle, J., 2007. The Australian genera of Mymaridae (Hymenoptera: Chalcidoidea). Zootaxa, 1596: 1-111.

[12]Lyu, Y. Z., Zhu, H. J. and Sun, M. 2019b. Flapping-mode changes and aerodynamic mechanisms in miniature insects. PHYSICAL REVIEW E 99(012419).

[9]Minaei, K. and Aleosfoor, M., 2013. A new species of Haplothrips from southern Iran (Thysanoptera, Phlaeothripidae). *Zookeys*. 275: 91-99.

[10]Riley, D. R., and others, 2011. Thrips Vectors of Tospoviruses. Journal of Integrated Pest Management. 2(1): 1-10.

[3]Santhanakrishnan, A., Robinson A., Jones S, Low A. A., Gadi S., Hedrick T. and Miller L., 2014. Clap and fling mechanism with interacting porous wings in tiny insect flight. J. Exp. Biol., 217: 3898–3909.

[11]Schneider, C. A., Rasband, W. S., and Eliceiri, K. W., 2012. NIH Image to ImageJ: 25 years of image analysis. Nature methods, 9(7): 671–675.

[2]Weis-Fogh, T., 1973. Quick estimates of flight fitness in hovering animals, including novel mechanisms for lift production. J. Exp. Biol., 59: 169–230.

Morphological characterization of wing shapes of tiny insects

Sam Glenn, Mitchell Ford and Arvind Santhanakrishnan

School of Mechanical & Aerospace Engineering
Oklahoma State University

Supported by NSF CBET 1916061/1706762/1512071

APPLIED FLUID MECHANICS LAB
@ OKLAHOMA STATE UNIVERSITY
APPLIEDFLUIDSLAB.ORG

Flapping Flight of Tiny Insects

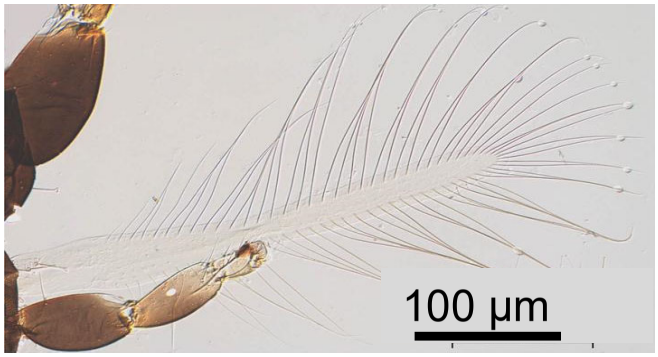

MAF Plant Health & Environment Laboratory (2011)

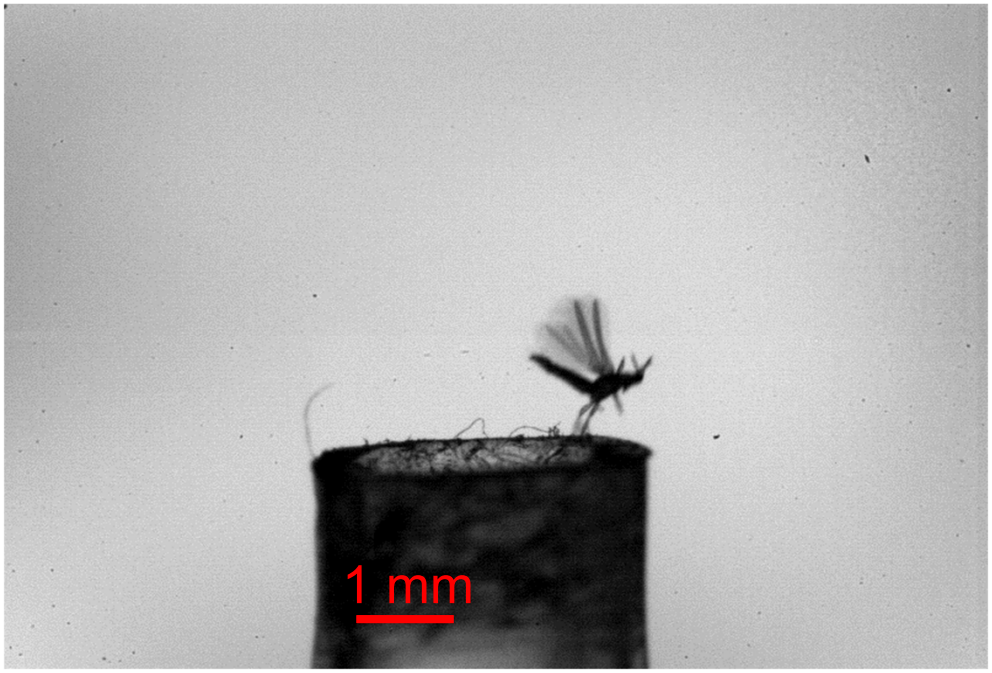

Motivation

- Agricultural
  - Biological vectors of plant viruses (e.g., Tospoviruses)
  - Invasive pests for commercially important crops such as tomatoes and onions

http://hosting.caes.uga.edu/tswvramp/vectors/index.html

- Engineering
  - Design of Micro Air Vehicles

RoboBee ~ 0.5g

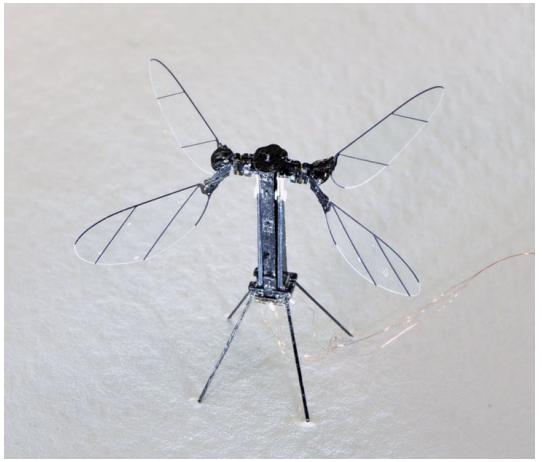

Jafferis, Noah T., et al, *Nature* 570.7762 (2019): 491-495.

Forewing Diversity

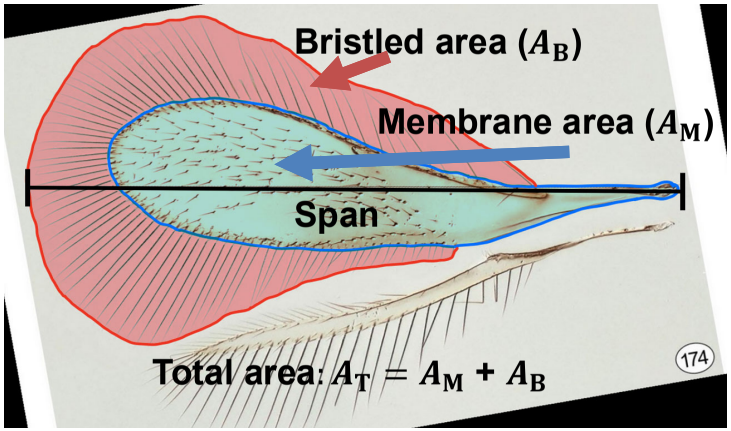

Huber, *J. Hymenopt. Res.* 57, 2017.

Riley et al., *J. Integr. Pest Manag.* 2, 2011

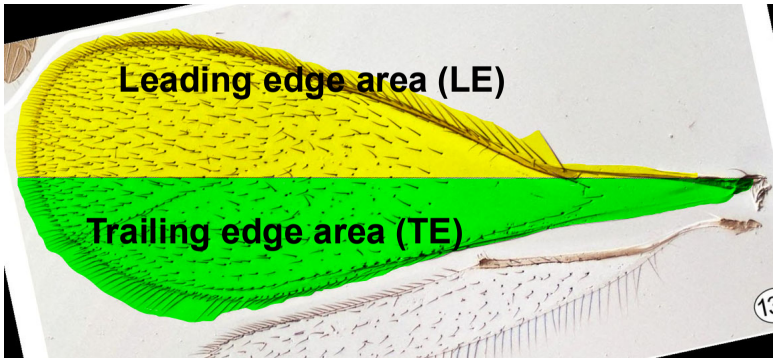

Huber, *J. Hymenopt. Res.* 57, 2017.

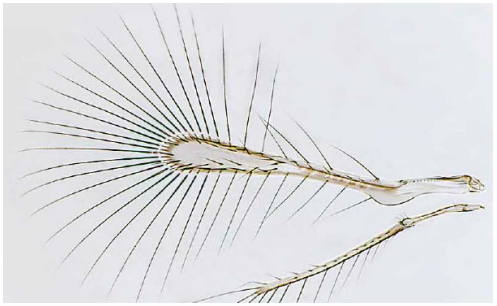

Huber et al., *Zootaxa*, 2007.

Parameters of interest

- A_M / A_T
- Aspect Ratio:
  AR = $(span^2 / A_T)$
- LE/TE

Wing Imaging

- Insect eggs were ordered from online suppliers
- Insects euthanized then placed on cover slip
- Wings were imaged using a compound microscope on 20x magnification

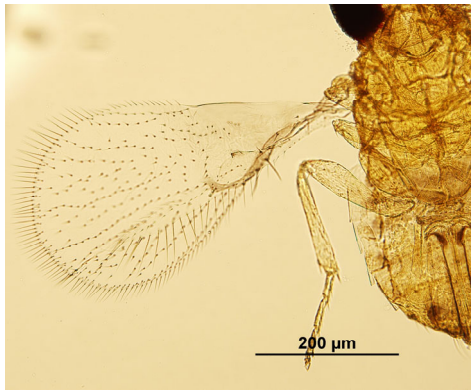

Eretmocerus eremicus

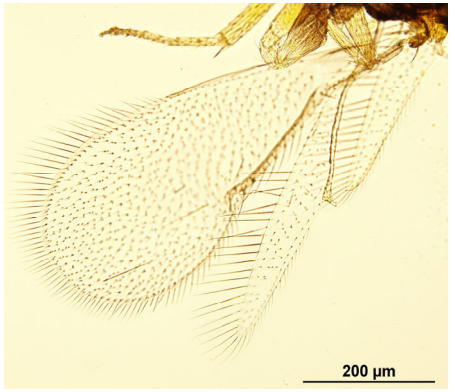

Encarsia formosa

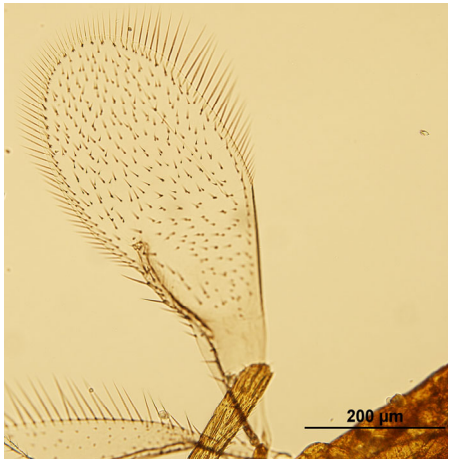

Trichogramma minutum

Morphological Analysis

- Forewing geometries of 13 species of thrips and 28 species of fairyflies extracted from published images
- Workflow
  - *Line drawn from root to tip in Image J*
  - *Points placed around wing*
  - *Lines were spline fit to each of these, and 20 evenly spaced points were extracted using the spline fit in MATLAB*
  - *A_{M}, A_{T}, AR, and LE/TE was calculated in MATLAB for each wing*

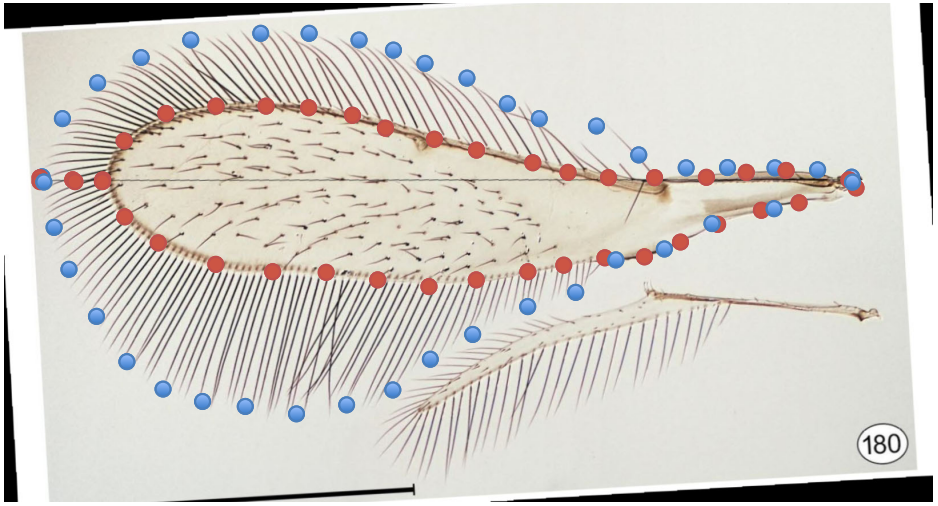

Huber, *J. Hymenopt. Res.* 57, 2017.

Forewing Morphometrics

LE/TE	AR	$A_T(\mathrm{mm}^2)$	A_M / A_T
0.24 - 2.6	3.5 - 8.1	5.4e-7 - 4.4e-8	0.13 – 0.9

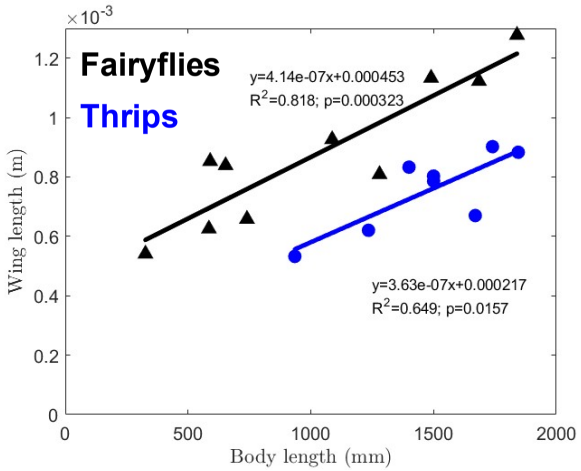

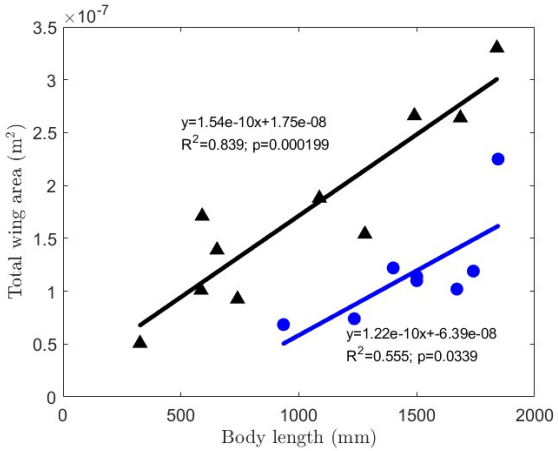

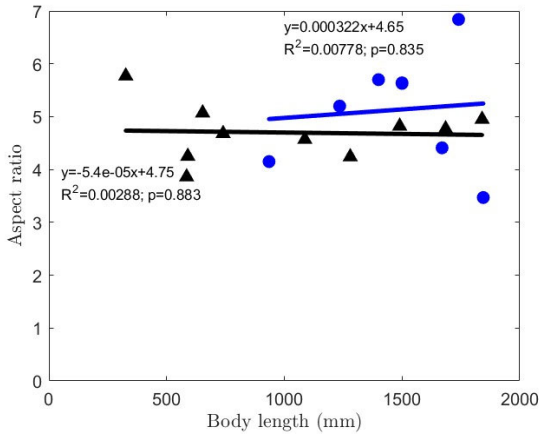

Principal Component Analysis (PCA)

- Vertical distances from span to spline fit points, along with wing span were inputs to PCA
- Axis 1
  - *strongly correlated to increasing total wing area (R^2=0.91, p << 0.01). Axis 1 also correlated to increasing A_M/A_T (R^2=0.57, p << 0.01).*

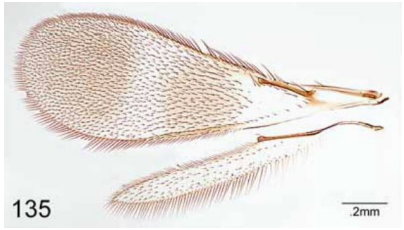

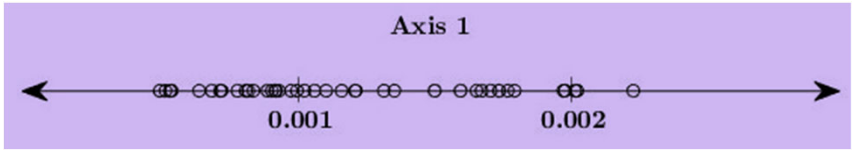

Principal Component Analysis (PCA)

- Vertical distances from span to spline fit points, along with wing span were inputs to PCA
- Axis 2
  - *correlated to decreasing A_M/A_T (R^2=0.24, p << 0.01). Axis 2 also correlated to decreasing LE/TE (R^2=0.46, p << 0.01).*

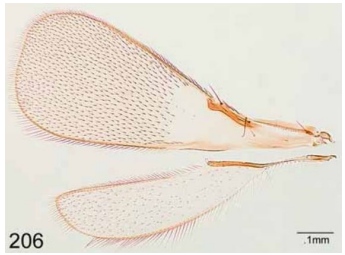

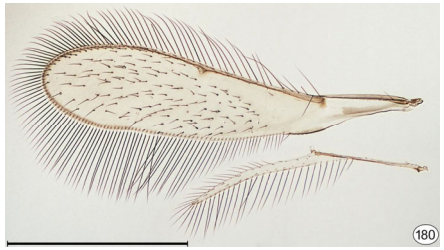

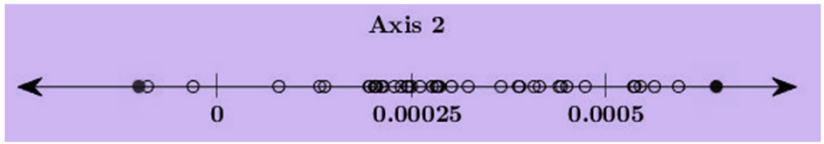

Principal Component Analysis (PCA)

- Vertical distances from span to spline fit points, along with wing span were inputs to PCA

- Axis 3
  - *correlated to increasing LE/TE (R^2=0.20, p=0.0018). Axis 3 also weakly correlated to decreasing A_M/A_T (R^2=0.12, p=0.019).*

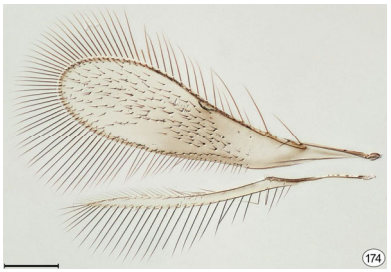

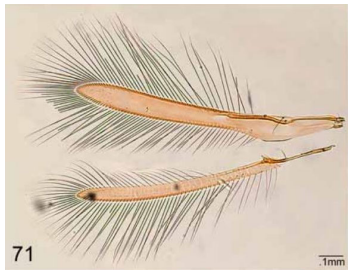

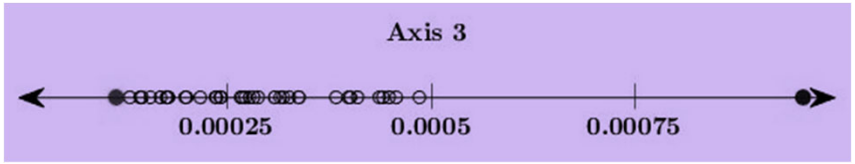

Experimental Design

- Fabricated 4 scaled up wing models encompassing biologically relevant range of LE/TE
- Other dimensionless parameters kept within biologically relevant range
  - Re_c ≈10
  - Re_b ≈ 0.05
  - Number of bristles (n) = 128
  - A_M / A_T = 0.32

$$Re = \frac{\text{Inertial force}}{\text{Viscous force}}$$

$$Re_c = \frac{2\phi Rc}{\nu T}$$

$$Re_b = \frac{2\phi RD}{\nu T}$$

ϕ = stroke amplitude
R = wing tip radius
T = stroke period
c = max chord
D = bristle diameter
ν = kinematic viscosity

LE/TE=2

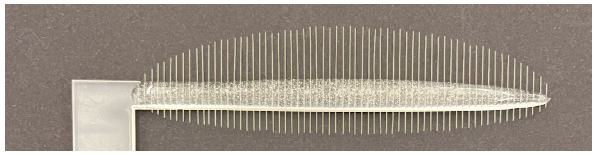

LE/TE=1

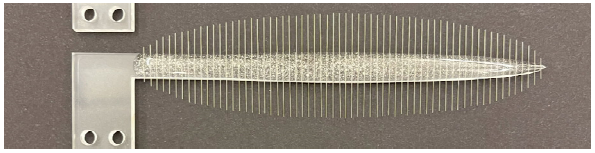

LE/TE=1/2

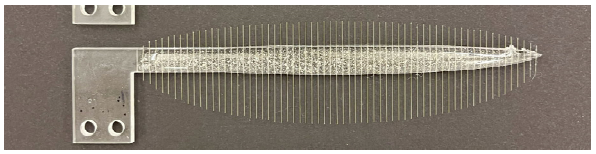

LE/TE=1/4

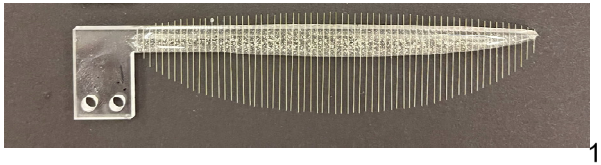

Experimental Design

- 1 thrips, 1 fairyfly idealized replica models were fabricated

Parameter	Thrips	Fairyflies
Re_b	0.074	0.07
Re_c	10	10
n	52	38
A_M / A_T	0.29	0.36

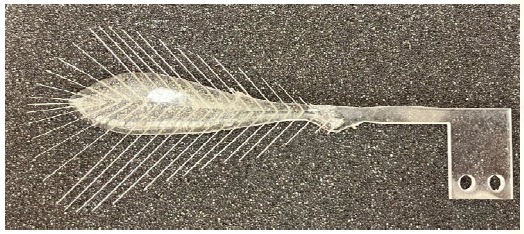

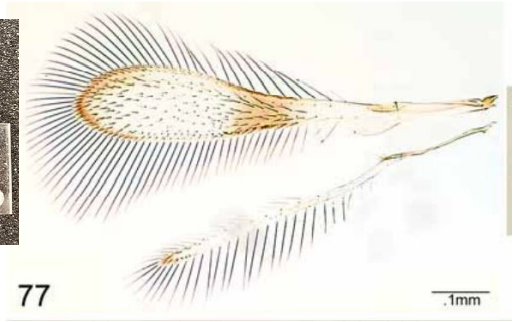

Lin et al., *Zootaxa* 1596, 2007

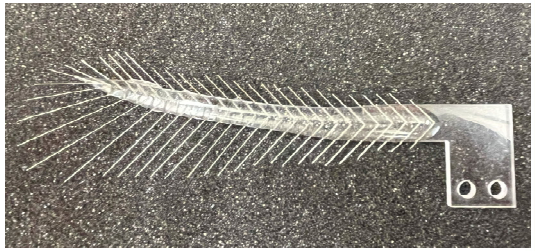

Riley et al., *J. Integr. Pest Manag.* 2, 2011

Experimental Setup

- 4 ft x 4 ft x 4 ft acrylic tank filled with ~99% glycerin solution
- Forces measured using strain gauges bonded to custom made L-brackets
- Robotic model programmed to replicate thrips kinematics in horizontal plane

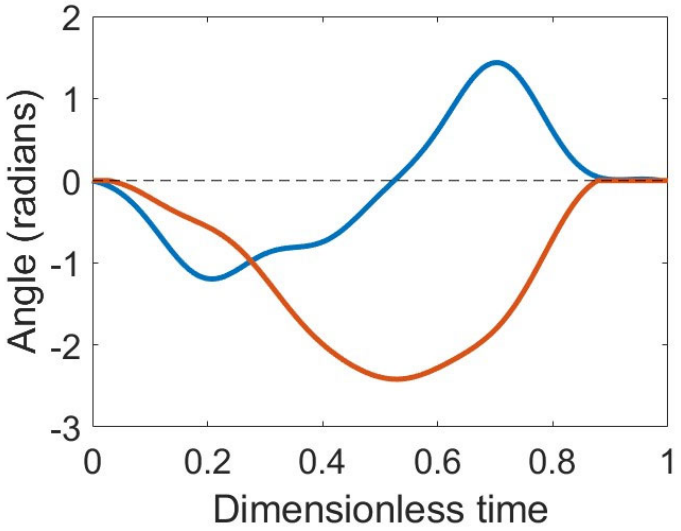

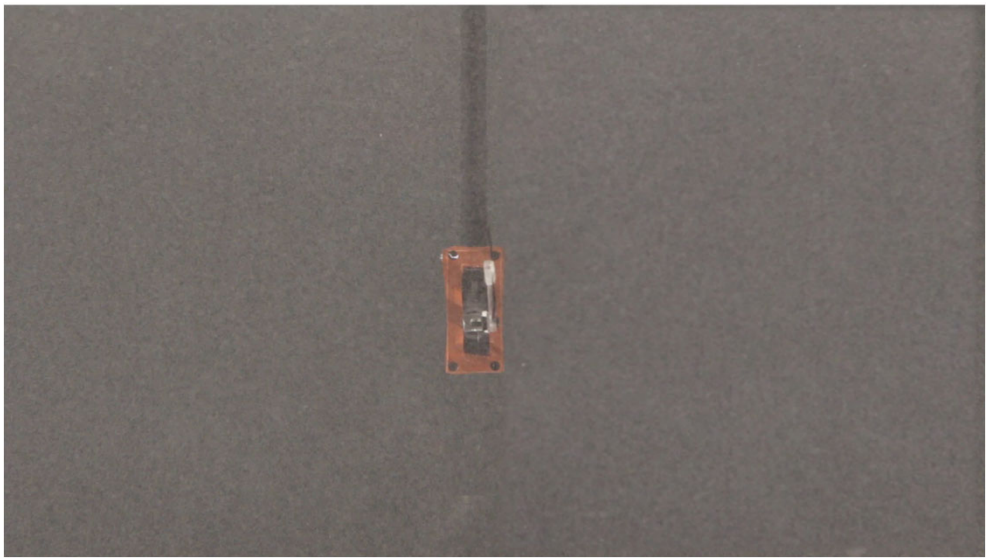

Drawn using data from:
Lyu, Y.Z., Zhu, H.J. and Sun, M., 2019. *Phys. Rev. E*, *99*(1), p.012419.

LE/TE Force Coefficients

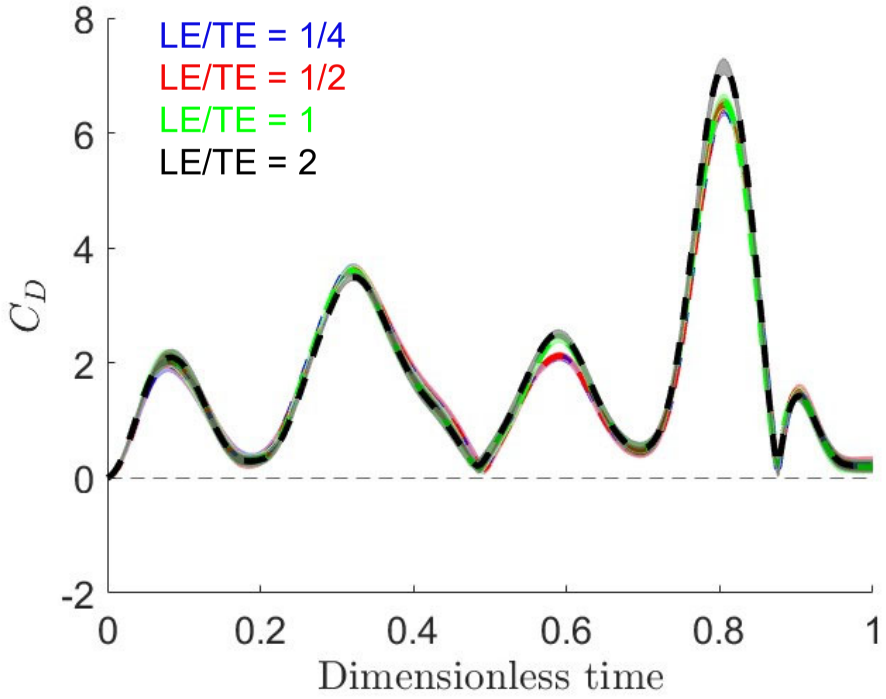

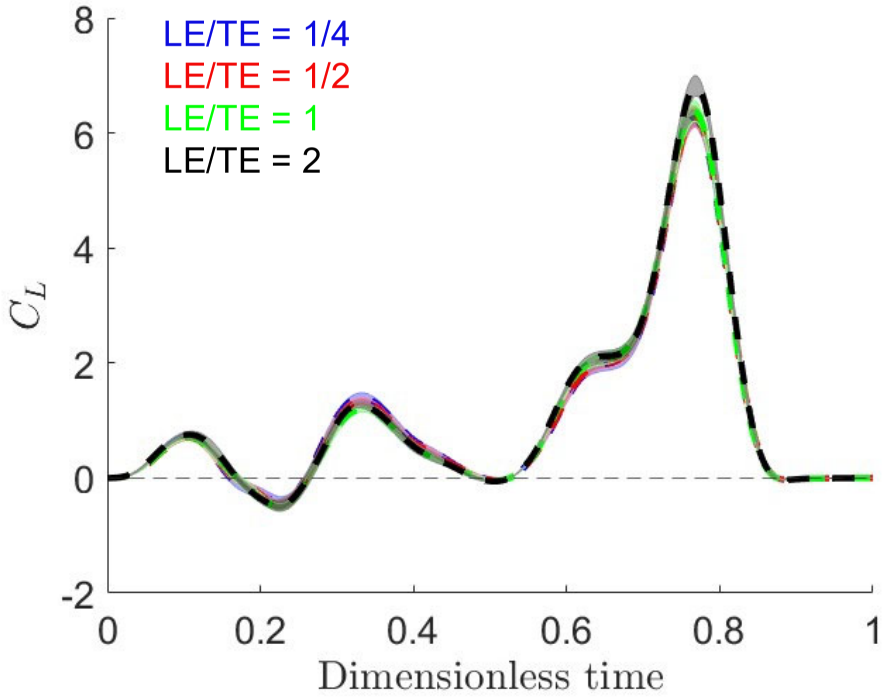

Replica Model Force Coefficients

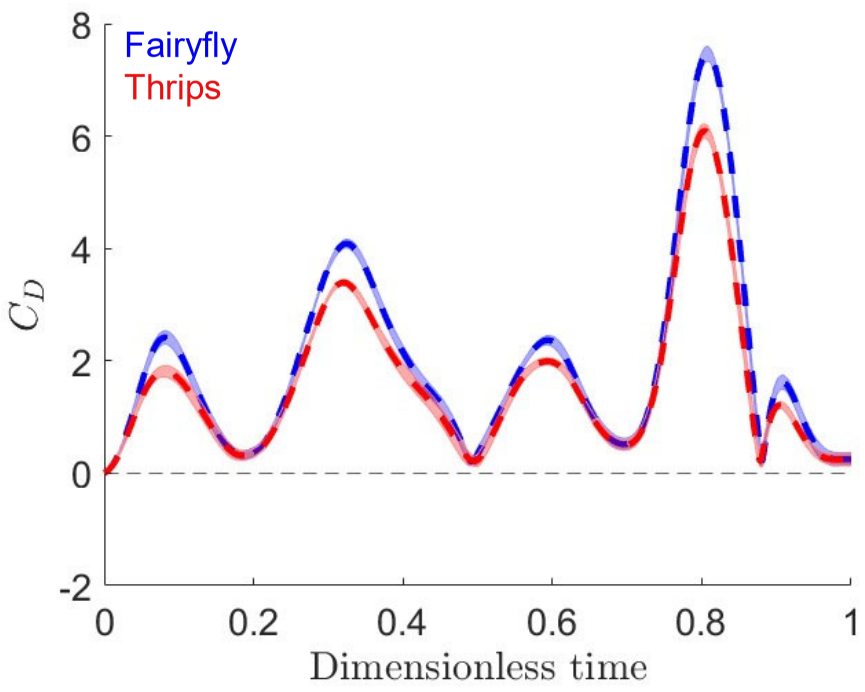

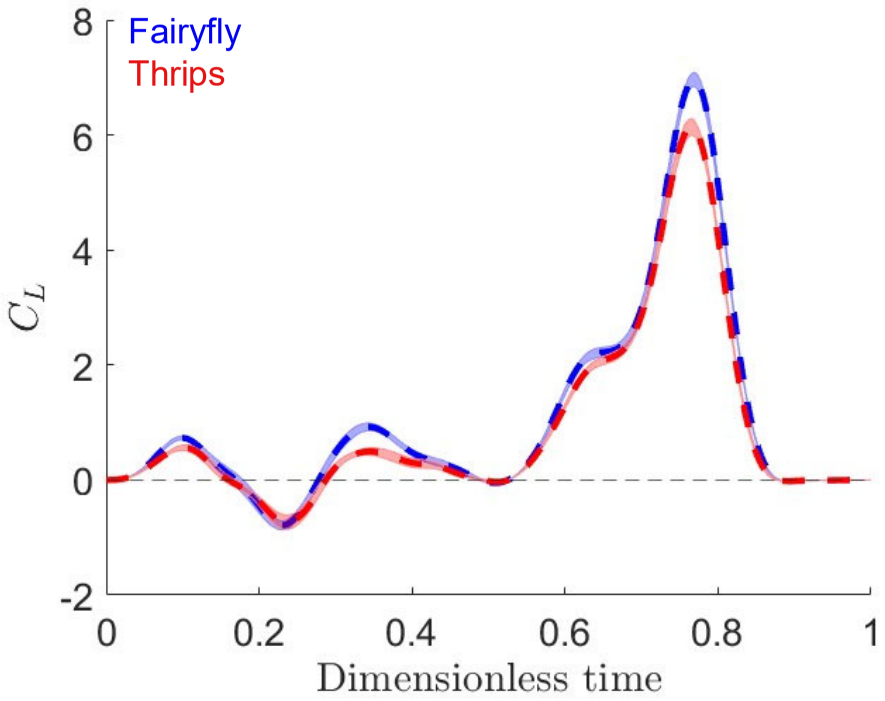

Cycle Averaged Force Coefficients

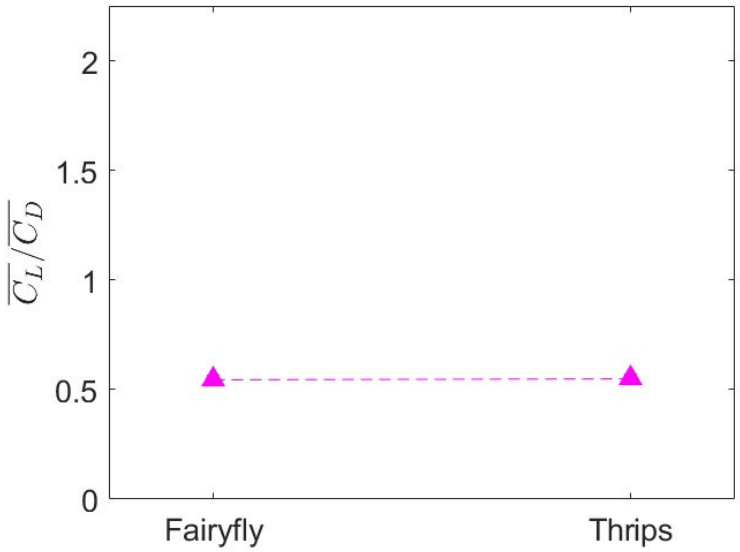

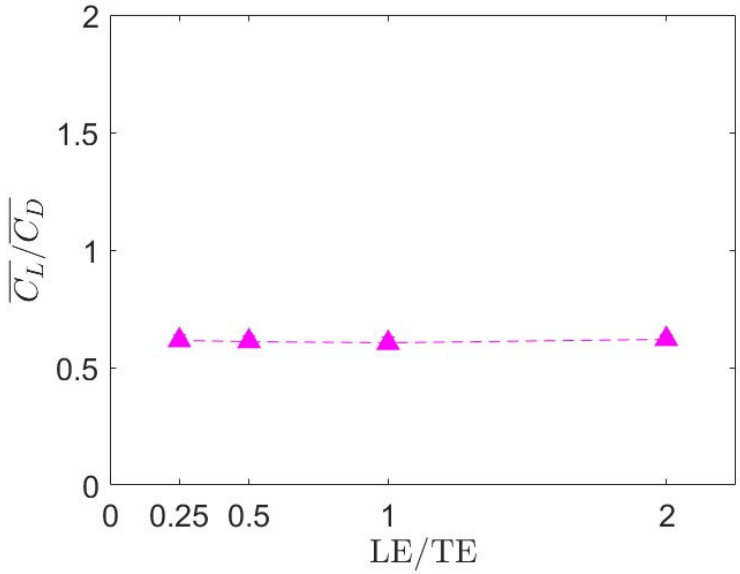

2D Phase Locked Particle Image Velocimetry (PL-PIV)

- Performed for 10 evenly spaced timepoints at 3 planes located at:
  - 50% span, 70% span, and 90% span
- LETE 2, ½, and both replica models were tested

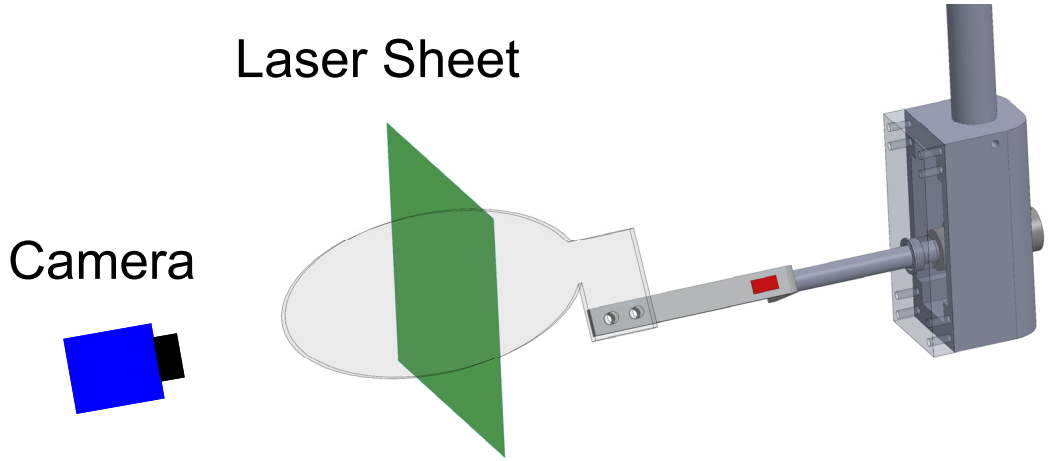

Mid-span Flow Field

LE/TE = ½

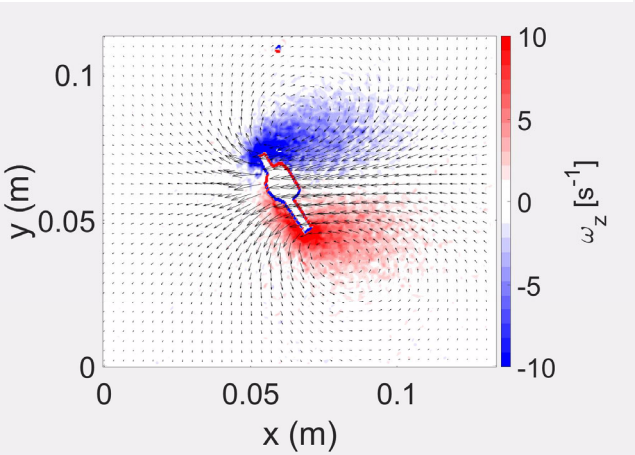

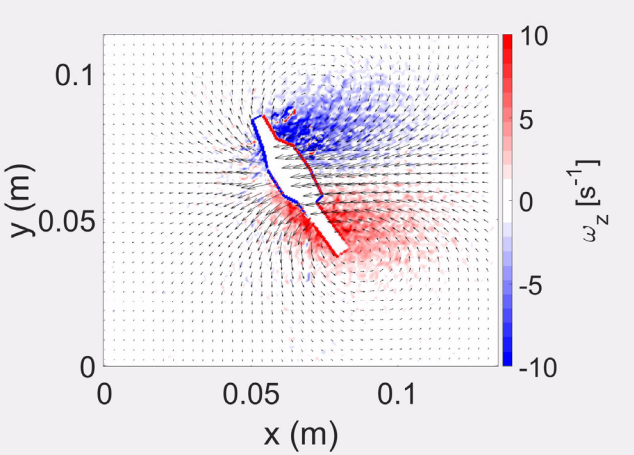

Fairyfly Replica

LE/TE = 2

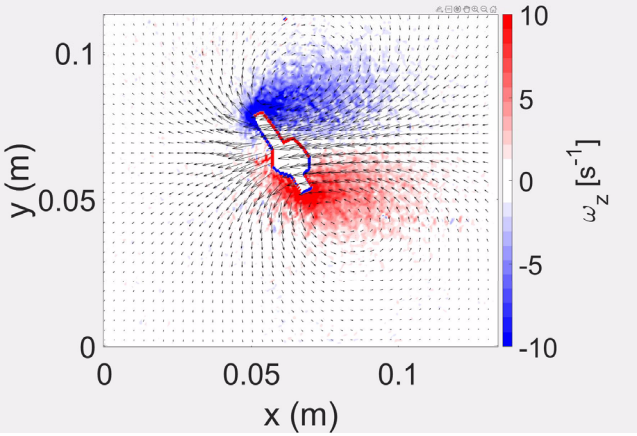

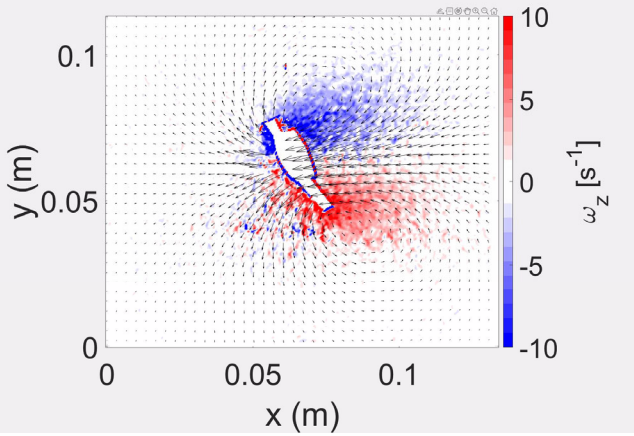

Thrips Replica

Flow Field for LE/TE = 2

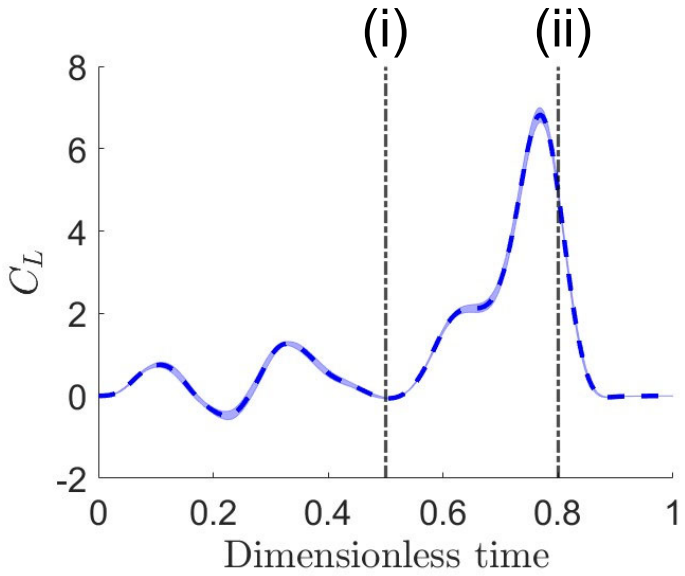

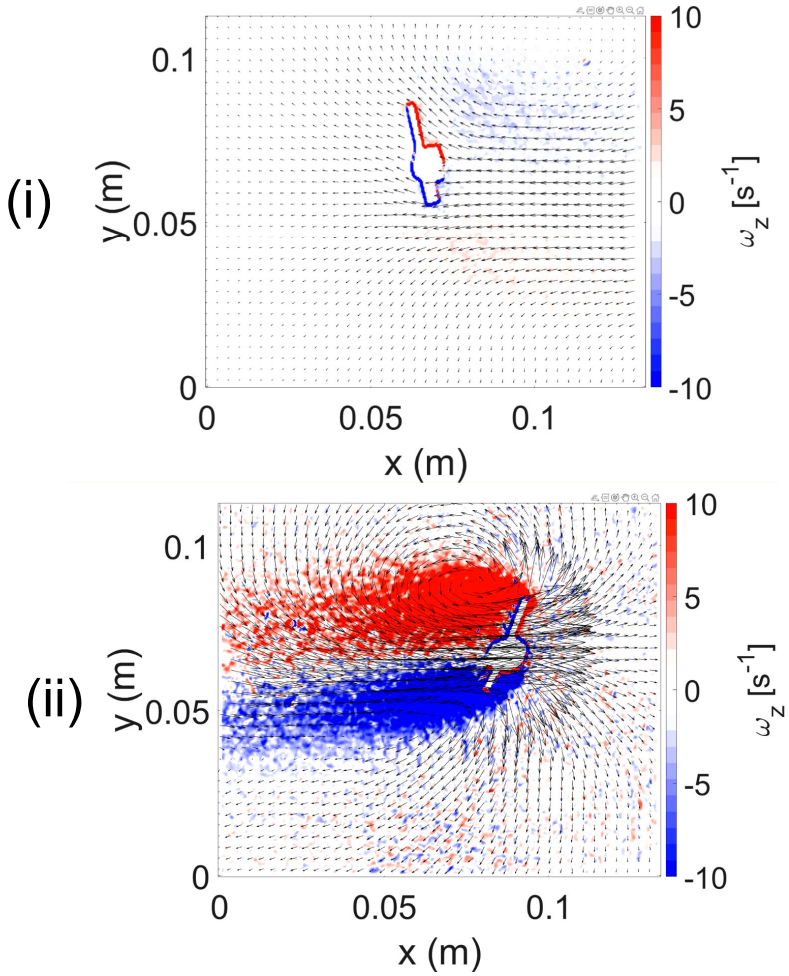

Summary

- Varying LE/TE within the biologically relevant range had minimal effect on time varying lift and drag coefficients
- Varying LE/TE had minimal effect on aerodynamic efficiency
- Helpful in situations where bristles can be damaged without significantly altering flight performance of insects

Future Work

- Construction of vertical wind tunnel
  - *Passive dispersal*
- Free-flight videos of live insects
- Wing kinematics reconstruction

Acknowledgements

- Dr. Arvind Santhanakrishnan
- Dr. Astri Wayadande
- Mitchell Ford
- Dr. and Mrs. Niblack

Backup/Additional Materials

Biologically Relevant Ranges

Fairyflies							
LE/TE			AT			AM/AT	
max	1.98		max	5.41E-07		max	0.90
median	0.89		median	2.29E-07		median	0.65
min	0.56		min	5.07E-08		min	0.13
Thrips							
LE/TE			AT			AM/AT	
max	2.61		max	2.25E-07		max	0.44
median	0.66		median	1.12E-07		median	0.25
min	0.24		min	4.42E-08		min	0.16

70% Span Flow Fields

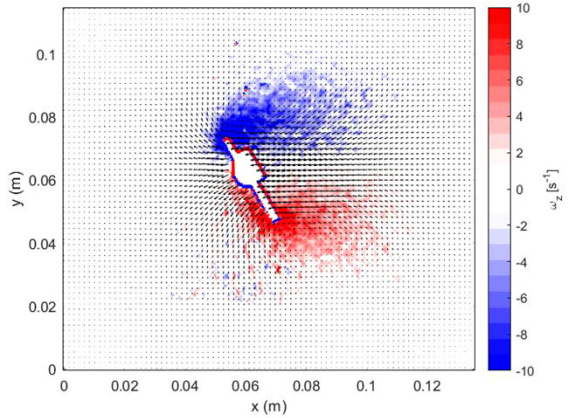

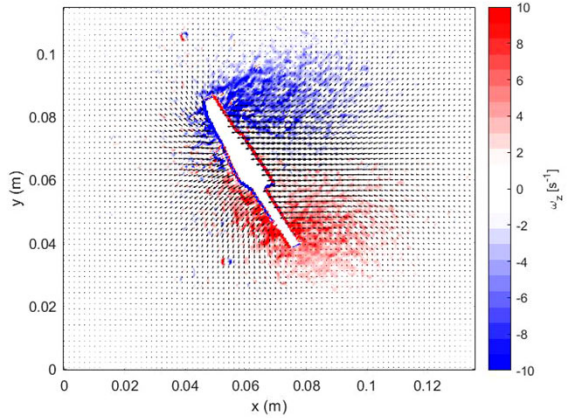

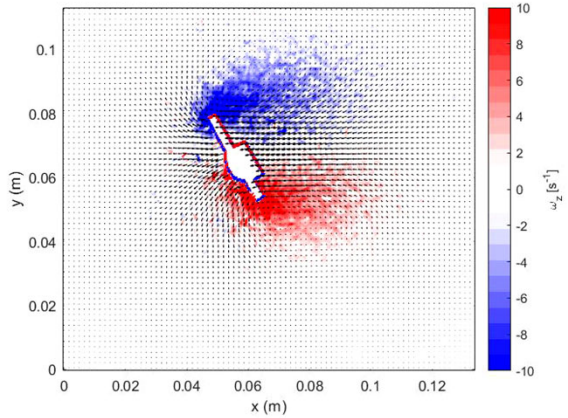

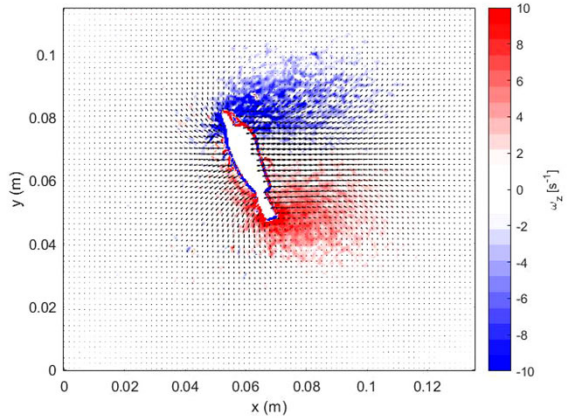

90% Span Flow Fields

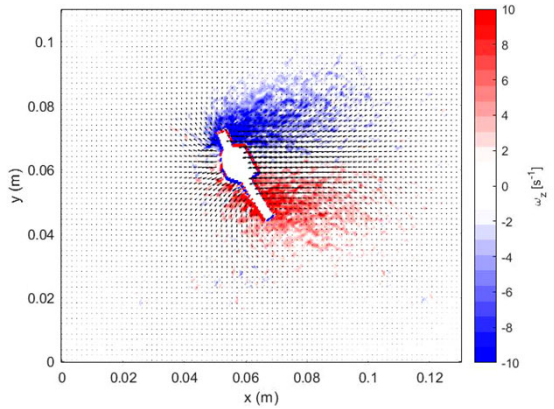

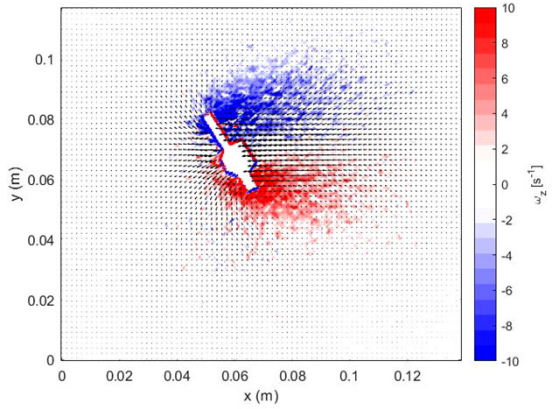

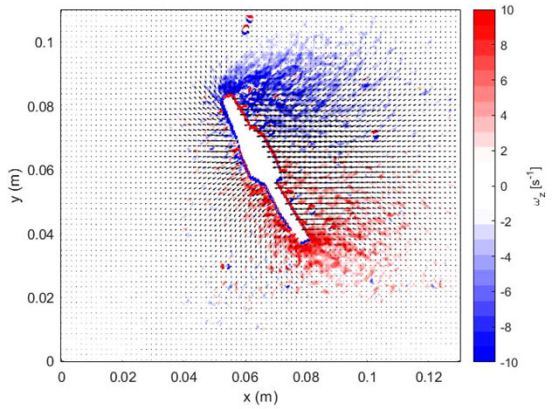

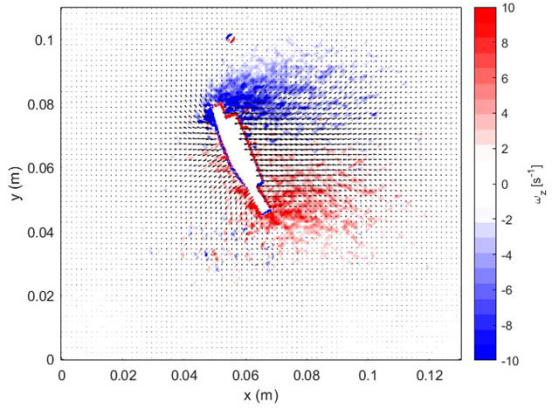

Free Flight of Video of Thrips

Kinematics Validation

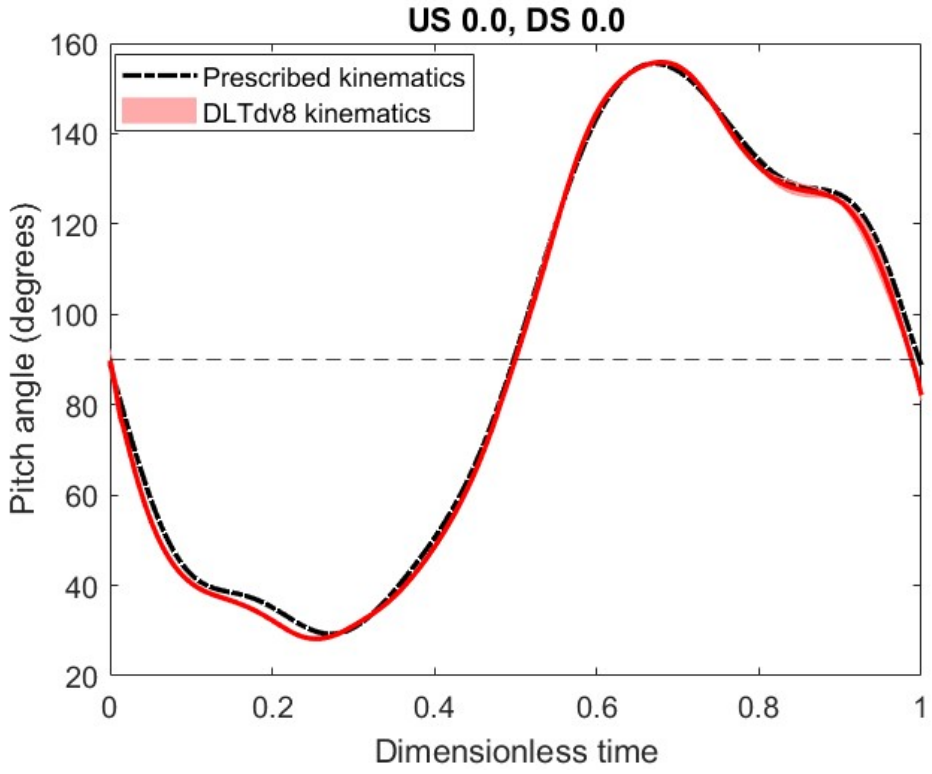

SESSION FOUR:

Sarah Teeman

"Exploring the Evolutionary Process of Losing Unselected Genes as a Potential Avenue to Addressing Bacterial Antibiotic Resistance"

Research Area: Microbiology and Molecular Genetics
Faculty Sponsor: Dr. Wouter Hoff
Graduate Student Mentor: Rosalie Dohmen

Rebecca Wilson

"Investigating Mechanisms of Antibiotic Resistance in Microbes from Cystic Fibrosis Patients"

Research Area: Microbiology and Molecular Genetics
Faculty Sponsor: Dr. Erika Lutter
Graduate Student Mentor: Noopur Dasgupta

Exploring the Evolutionary Process of Losing Unselected Genes as a Potential Avenue to Addressing Bacterial Antibiotic Resistance

Sarah M. Teeman

Microbiology and Molecular Genetics
Faculty Sponsor: Wouter D. Hoff, PhD
Graduate Student Mentor: Rosalie L. Dohmen, MS

ABSTRACT

Antibiotic Resistance (AR) in pathogenic bacteria is widely recognized as a major emerging health problem. We explore the feasibility of addressing AR by using a global rotation cycle of antibiotics. If a bacterium does not encounter an antibiotic to which it has a resistance gene, how long will it keep that gene? Retaining a "useless" gene, like an AR gene in the absence of antibiotic, may impose a fitness cost, making it evolutionarily advantageous to lose the gene. In addition, random mutations damaging this AR gene would not be removed by purifying selection, resulting in a gradual erosion of this gene over evolutionary time. In this project, we explore the expectation that sustained non-use of a particular antibiotic would result in AR gene loss from human pathogens and thus recovery of sensitivity of the pathogen to that antibiotic. While the timescale for the emergence of AR, or the on-rate, in the presence of antibiotics has become clear, less is known about the timescale of AR gene loss, or the off-rate, in the absence of an antibiotic. We ran 200-generation Long-Term Evolution Experiments (LTEE) on multiple *E. coli* strains with varying fitness costs to develop methods to characterize the off-rate with which unused AR genes are spontaneously lost. First, we used *E. coli* strains designed to have a different fitness cost due to useless genes and performed direct competition experiments with these strains. Second, we used chemical mutagenic agents at various concentrations to accelerate the rate of gene loss to a feasible timeframe for laboratory studies. We use a gene encoding green fluorescent protein (GFP) in *E. coli* as an easily monitored "useless gene." In these experiments, loss of the *gfp* gene is detected as a decrease in GFP fluorescence intensity. Through method development in simple conditions, we pave the way for future work on quantifying the rate of loss of unused AR genes by extrapolation to zero mutagen concentration. The conceptual framework developed here can also be applied to further work on the loss of unused AR genes under real-world conditions.

1. Introduction

Antibiotic Resistance (AR) in pathogenic bacteria is a major emerging health problem, directly causing 1.27 million deaths and associated with nearly 5 million deaths annually around the globe (Antimicrobial Resistance Collaborators, 2022). In the year 2050, AR is predicted to cause nearly 2 million more deaths than cancer (Dadgostar, 2019). Reminiscent of the 19th century and a time before antibiotics, infectious disease will cause more deaths than chronic disease. The origin of this emerging health crisis lies at the interface of medicine and evolutionary biology. Traditionally, the field of pharmacology in general does not include considerations from molecular evolution. From the view of classical pharmacology, penicillin binds to and inhibits penicillin binding proteins that are required for cell wall biosynthesis. Thus, in the presence of penicillin, bacteria are not able to produce functional cell walls and therefore die. However, bacteria are not static objects–they evolve. In the example of penicillin, pathogenic bacteria evolved several different mechanisms that allow them to become insensitive to penicillin. Thus, the problem of AR is evolutionary in nature.

The question emerges of how to best address this challenge. One approach could be to develop novel antibiotics. The price tag is $1.5 billion to develop with annual revenue of $50 million, meaning there is little economic incentive for drug development (Plackett, 2020). In addition, there is every reason to expect that over the course of one- or two-decades, bacteria will have evolved to become resistant to this new antibiotic. A different approach to find a more fundamental and definitive solution to the issue of AR is a strategy that is based on evolutionary considerations. To fight fire with fire, so to speak.

Here we study the feasibility of addressing AR using a global rotation cycle of different antibiotics, where specific antibiotics would be selectively and exclusively prescribed for a certain period. The core expectation of this approach is that in the prolonged absence of an antibiotic, the genes encoding resistance to this antibiotic are useless to a human pathogenic bacterium and therefore over time will tend to be lost. Furthermore, loss of such genes from a population of pathogenic bacteria would likely be faster if the unused AR gene imposes a fitness cost compared to a situation where the presence of the gene is evolutionarily neutral (zero fitness cost to having or losing the gene). Thus, after a sufficiently long time, the sensitivity of this antibiotic is restored, allowing it to be effectively clinically useful once more. Bacteria will then evolve to become resistant to this antibiotic again, and in the approach explored here one would switch to another effective antibiotic. By implementing a proper global rotation scheme of antibiotics, one can envision a scheme in which we keep repeating this slow rotation cycle indefinitely. Bacteria would likely be defenseless against this evolutionary strategy. The big question in this proposed strategy is as follows: is the loss of unused AR genes fast enough to make this strategy practical?

To start exploring this question, we studied the evolution of unnecessary genes in *Escherichia coli* (*E. coli*) by evolving this bacterium in the laboratory. In a general sense, this builds on the long-term laboratory evolution experiment of Richard Lenski, who has been growing *E. coli* for over twenty years. The *E. coli* he grew took a food source (citrate) it previously could not use and evolved the mechanisms necessary to utilize it (Blount *et. al,* 2008). Here we focus on the evolutionary process of the loss of unused genes. In general, the rate at which genes that are not under selective pressure are lost is important for understanding evolutionary dynamics. If a bacterium were to never retain a temporarily useless gene, it would lead to a constantly changing genome and the loss of genes that the organism would need in a fluctuating environment. However, a gene that is not under selective pressure (i.e., not used) for a prolonged period would be expected to be damaged by ever-occurring random mutation events. In the case of AR, a resistance trait will become useless (and may even impose a fitness cost) when the antibiotic is no longer used. If the bacterium indeed is observed to lose a resistance gene, this will support the possibility of a global rotation cycle. When reintroducing an antibiotic for clinical use, the bacteria would be sensitive to the antibiotic. In this approach no new antibiotics would need to be developed, providing a cost-effective strategy to combat the emergence of AR. A key practical issue is the rate at which unused AR genes would be lost, which could take a few years to many centuries.

The core of our **experimental strategy** consists of two elements:

- We selected *gfp*, the gene encoding green fluorescent protein (GFP), as an easily monitored useless gene, and we used *E. coli* strains containing a *gfp* gene. Specifically, we introduced the pGLO plasmid into *E. coli*. This plasmid contains a gene that confers resistance to the antibiotic ampicillin (amp), providing a mechanism to force cells to retain the plasmid, and a *gfp* gene that is inducible by the addition of the sugar L-arabinose. Thus, the addition of 0.8% arabinose causes the *E. coli* cells to turn on the *gfp* gene leading to the production of GFP. We expect that the *gpf* gene should carry a small but measurable fitness cost, and that this fitness cost will increase somewhat upon induction of the *gfp* gene with arabinose.

- Based on results published in literature, we anticipate the loss of useless genes to occur on a time scale of ~10 years, which is outside the range of almost all laboratory experiments (the Lenski experiment being the exception). To accelerate this process, we grow *E. coli* cells producing GFP in the presence of mutagenic agents at a range of concentrations. The idea is that mutagenic agents increase mutation frequency, thus "speeding up" evolutionary time: the higher the (non-lethal) mutagen concentration, the faster the expected rate of loss of the *gfp* gene. Extrapolating of such experimental data to

zero mutagen concentration would then yield a first estimate of the rate of loss of useless genes, including – presumably – unused antibiotics resistance genes.

2. Experimental Details

Preparing Competent E. coli MG1655 cells

Wild type (WT) *E. coli* MG1655 (strain provided by Randy Morgenstein, PhD) was chemically transformed with both purified pGLO and pBAD18 plasmid. pGLO was provided by Gary Marley, PhD and pBAD18 was purchased from Novopro Labs. The pGLO plasmid contains an amp resistance gene and a *gfp* gene under the control of an arabinose-inducible promoter (Appendix A). The pBAD18 plasmid does not contain the *gfp* gene and is used here as a control. For transformation, first competent cells of *E. coli* MG1655 were prepared. 5 mL of Luria-Bertani (LB) Broth was inoculated with *E. coli* and shaken at 220 RPM overnight at 37 °C. 0.05 mL of the overnight culture was transferred into 99mL of LB. It was shaken at 220 RPM until OD_{600} of 0.5-0.6 was reached, where the cells are in log phase (actively growing). The culture was split into two 50 mL falcon tubes and were placed in an ice bath for 20 minutes. They were centrifuged for 5 minutes at 4500 RPM at 4°C. The supernatant was discarded. The pellet was resuspended in 20 mL of chilled 100 mM $CaCl_2$ and was incubated on ice for one hour. The centrifugation step was repeated, and the supernatant was discarded. Next, 2mL of chilled 85 mM $CaCl_2$ with 15% glycerol was added to the pellet. Upon resuspension, the cells were aliquoted and frozen at -80°C (Chen, 2021).

Transformation

Next, the plasmid pGLO and pBAD18 was transformed into the competent *E. coli* cells. First, the cells were thawed on ice. Then, 2 µL of chilled plasmid solution was transferred to 50 µL of *E. coli* cells in a microcentrifuge tube. The tube was placed on ice for 30 minutes then heat shocked for 30 seconds at 42°C. 950 µL of Super Optimal Broth with Catabolite Repression (SOC) media was added to the tube. The tube was shaken at 250 RPM for one hour at 37 °C. LB plates with amp were warmed, and then 100 µL of cell solution was spread plated onto the plate to select for amp-resistant transformants. After 12-16 hours, only colonies of *E. coli* that were successfully transformed remained (NEB, n.d.). Sequencing confirmed the transformation of the plasmid into *E. coli*.

Measuring manual Growth Curves

The first method of growth curve measurements was to manually take samples from growing cultures and use these samples to measure cell density at 600 nm. Starting with a lower accuracy method, these curves were intended to detect a potential deficit in fitness cost and subsequent growth deficit that the pGLO plasmid might confer to *E. coli.* First, minimal media was prepared according to the Rathod *et al*., (2012) protocol with modifications to

histidine and tyrosine. A preculture of WT *E. coli, E. coli* transformed with pBAD18 (referred to as pBAD), and *E. coli* with pGLO (referred to as pGLO), were prepared by adding one loopful of frozen stock into 20 mL of minimal media (MM) in a falcon tube. These tubes were prepared 16 hours prior to the initial reading. Amp was added to the tubes containing pBAD and pGLO to achieve a final amp concentration of 100 µg/mL that is selective for a high copy number plasmid (Openwetware, 2008). A tube of MM + amp and MM (no amp) were used as controls to ensure proper media preparation. The tubes were then allowed to shake at 220 RPM for 16 hours. The next morning, the spectrophotometer (Hewlett Packard) was blanked with MM + amp. The OD_{600} of the three pre-culture tubes were then measured. To prepare the main culture, the OD_{600} of the pre-cultures were normalized to one, or 10 µL of bacteria in 250 µL of media. This improves accuracy of the read- especially for dense cultures. The corrected volume of pre-culture was then transferred to 100 mL of fresh MM + amp for pBAD and three pGLO flasks (one for pGLO, and two for pGLO induction), and to fresh MM for *E. coli*. For one of the pGLO flasks, 1 mL of 0.8% L-arabinose (Sigma-Aldrich) was immediately added to achieve a final concentration of 0.8%. This concentration is typical for induction and was supported by testing it against 0.2% L-arabinose. The flasks were then covered with aluminum foil and placed on the shaker under the same conditions as the pre-culture flasks. After thirty minutes of shaking, the OD_{600} was measured for each flask. Once the pGLO + amp (third pGLO flask) reached log phase of growth, 1 mL of 20% L-arabinose was added to achieve a final concentration of 0.8%. OD measurements were repeated every 30 minutes until the culture stopped growing, which occurred after approximately 8-9 hours of growth. In another set of experiments, this was replicated by taking measurements every hour rather than every thirty minutes.

Automated Growth Curves in 96-well plates with combined OD_{600} and GFP fluorescence detection

The second method to measure *E. coli* growth curves was through the usage of a 96-well plate reader (Biotek Synergy H1). The pre-cultures were prepared using the same pre-culture procedure outlined above, but with 125 mL of Minimal Media and amp at a final concentration of 100 µg/mL. The following morning at 8:00 AM, the OD_{600} value was measured with the spectrophotometer (Hewlett Packard) for each flask. The OD_{600} was normalized to a value of one, and the necessary culture volume was added to the corresponding media in the 96-well plate (Fisherbrand Tissue Culture Plate). There were two types of experiments being performed: single well and competition. Single well included WT *E. coli*, pBAD18, and pGLO + 0.8% Arab (with/without amp). Competition included pGLO + pBAD + 0.8% Arab (with/without amp) and pGLO + pBAD + amp. Amp with Arab selected for both plasmids. We predicted the additional *gfp* gene in pGLO hindered its fitness and placed it at an evolutionary disadvantage, making it advantageous to lose the plasmid. Amp (no arab) reduced the fitness cost in that it equally selected for both plasmids, where

pGLO was not induced. We predicted that there is still a slight fitness cost in gene maintenance that would place it at an evolutionary disadvantage. Arab (no amp) eliminated the selection pressure for both plasmids making it possible to lose either plasmid to increase fitness-but induced pGLO would be more costly than pBAD. Each condition was performed using a set of five biological replicates, one per well. Under sterile conditions in the hood, the 96-well plate was prepared according to Appendix B. The plate was read every 12 hours then transferred to a new plate. The plate reader was set to read optical density at a wavelength of 600 nm and fluorescence emission at 550 nm using an excitation wavelength of 395 nm. After 12 hours- or 6.7 generations of growth, 2.5 μL (100x dilution) of each culture was transferred from the old 96-well plate into a new one (Lenski, 2017). This process was repeated for a total of 207 generations for the long-term evolution experiment (LTEE) 1 and 154.1 generations for LTEE 2.

Automated long-term mutagenesis experiments in the presence of Mutagenic Agents

To meet experimental strategy one, we repeated the methods outlined in the section above, but using two different mutagenic agents. We used Methylnitronitrosoguanidine (MNNG)-purchased from Medchemexpress- and Acridine Orange (AO)-purchased from Sigma Aldrich. MNNG is an alkylating agent and AO is an intercalating agent. Samples were grown in a concentration range of 0-114 μg/ml AO and 0-45 μg/ml MNNG. Loosely, the concentration values suggested by short-term AO mutagen experiment literature agreed with experimental data (Arshad, 2006) but was too high of a concentration of MNNG for long term culture growth (Arshad, 2010). 0.2% AO stock was prepared in water and MNNG was prepared at a concentration of 1 mg/mL in 100 mM Citrate buffer, pH 5.5. We selected pGLO + Arab 0.8% + amp and pGLO + Arab 0.8% for this experiment. The presence of amp maintains the selection pressure for the presence of the pGLO plasmid. In the absence of amp, in principle the *E. coli* cells can lose the plasmid in its entirety. MNNG and AO were loaded into their respective plates as described by Appendix 3.

3. Results

Measurement of E. coli growth curves to detect possible GFP-induced fitness costs

We first measured (manual) growth curves of *E. coli* MG1655 grown in the widely used growth medium Luria Broth. Initially we performed these experiments in 100mL cultures. We then decided to switch to measuring growth curves in 96 well-plates to improve accuracy and throughput. We observed a biphasic growth pattern in LB, where cell density rapidly increased to an OD_{600} of approximately 1, and then more slowly increased to an OD value near 1.6 (Fig. 1). To achieve a simpler growth pattern, we switched to a defined growth medium, and indeed observed a pattern with a single growth phase. Using this medium, we tested if the induction of GFP production by the addition of arabinose caused a sufficient

fitness cost to be detectable in the measured growth curves. The data in Figure 1 indicate that the presence of the pGLO plasmid (induced with arabinose or not) did not impose a fitness cost noticeable in the growth curves. This result suggests that the measurement of such growth curves in not sufficient to measure the presumably modest reduction in fitness caused by GFP production. We therefore explored direct competition experiments, in which cultures containing mixtures of cells containing different plasmids as a more sensitive method for detecting modest changes in fitness.

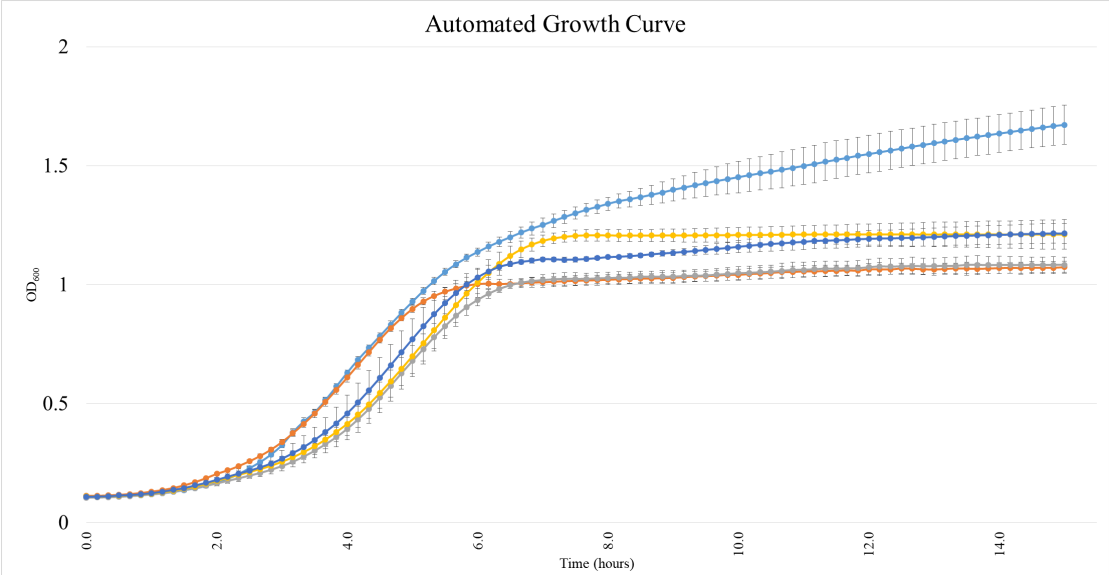

Figure 1: Probing if a classical growth curve can detect fitness cost of inducing *gfp* gene Growth Curve measured in 96-well plate. Growth curves measured for *E. coli* in LB (light blue), pBAD (orange), pGLO (gray), pGLO +0.8% Arab (yellow), and pGLO + 0.2% Arab (dark blue) in MM. Data points are average values of five biological replicates. Error bars indicate one standard deviation.

LTEE direct competition experiments in 96-well plates

We performed competition experiments in 96-well plates to obtain accurate readings of OD_{600} measurements, while also allowing measurements of GFP. To achieve these LTEE competition experiments, we grew *E. coli* in 96- well plates and diluted the resulting cultures in fresh growth media. By repeating this process, we obtained data for 150 to 200 generations of *E. coli* cell division. In total, we performed two consecutive replicates of LTEE competition experiments to test for experimental reproducibility.

We noticed that the cell density at the end of the first growth cycle (first data point in Fig. 2) was slightly lower that the remaining data. We attribute this to inoculation of the plates with a somewhat small number of bacteria. We did not observe (and did not expect) changes in OD caused by the presence or induction of the *gfp* gene. However, unexpectedly,

we observed a quite substantial difference in the OD of cultures grown in the presence of amp versus cultures in the absence of amp (Fig. 2): Cultures grown in the absence of amp were systematically one OD unit higher than in the presence of amp. Figure 2 combines data from LTEE experimental run 1 and 2, indicating the reproducibility of the OD difference between amp and no amp. The data and error bars for the data obtained from the two LTEE experiments separately are very similar to those depicted in Fig. 2. Unexpectedly, the data in Fig. 2 display a degree of semi-sinusoidal fluctuations in culture OD that remain to be explained.

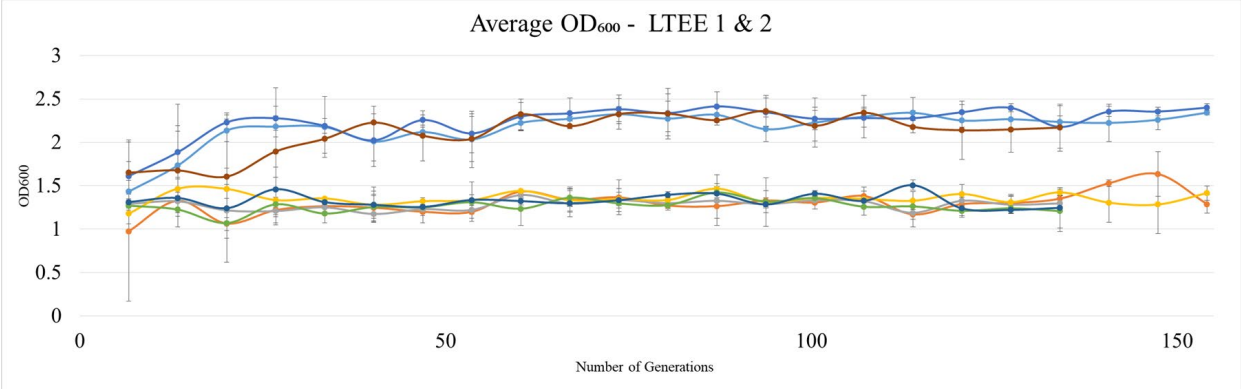

Figure 2: Using OD_{600} readings to establish LTEE experiment over 160 generations in 96-well plates. The top three curves near OD 2.2 display data for *E. coli* (light blue), pGLO + 0.8% Arab (no amp) (dark blue), and pGLO + pBAD + 0.8% Arab (light red). The lower curves near OD 1.5 display data for pBAD + amp (orange), pGLO + amp (gray), pGLO + 0.8% Arab + amp (yellow), pGLO + pBAD + amp (green), and pGLO + pBAD + 0.8% Arab + amp (darkest blue).

To examine how the presence of amp itself reduced the OD values, we performed a simple stain using safranin of *E. coli* (no amp) and pGLO (amp). *E. coli* (left) shows clumping in the dense red splotches. pGLO (right) is much lighter-meaning it is less dense and therefore took up less stain- and is less clumped. These results indicate that ampicillin may cause cellular clumping that scatters light which increases the measured OD_{600}.

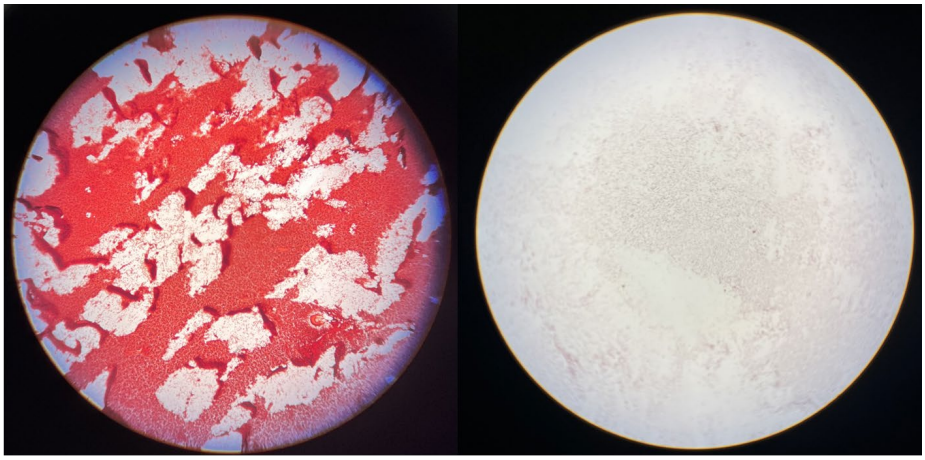

Figure 3: Safranin simple stain of *E. coli* grown in absence of amp (left) and pGLO grown with amp (right) under 10x magnification. Note the cellular clumping in the absence of amp.

In the direct competition experiments, *E. coli* cells containing the empty plasmid vector pBAD were grown in the presence of *E. coli* cells containing the *gfp*-encoding plasmid pGLO. In order to quantify the average GFP content of cells in these mixed cultures, we divided the observed fluorescence intensity by the measured OD_{600}. The rational for this approach is that observed fluorescence intensity indicates the GFP content of cells and OD_{600} indicates the number of cells. Thus, fluorescence / OD_{600} is a measure for how much GFP an average cell contains. In the case that cells containing the pGLO plasmid are out-competed by the cells containing the pBAD plasmid, this would result in a reduction in the value of fluorescence / OD_{600}. The data in Fig. 4 indicates that for early generations in the experiment the highest values are observed for the *gfp*-inducing conditions pGLO + pBAD + amp + arabinose compared to pGLO + pBAD + arabinose or pGLO + pBAD + amp. In addition, we observed that all three trend lines have a negative slope, indicating a gradual loss of GFP over the course of this 150-generation experiment. This is result is consistent with an interpretation that the pBAD *E. coli* strain is out-competing the pGLO *E. coli* strain.

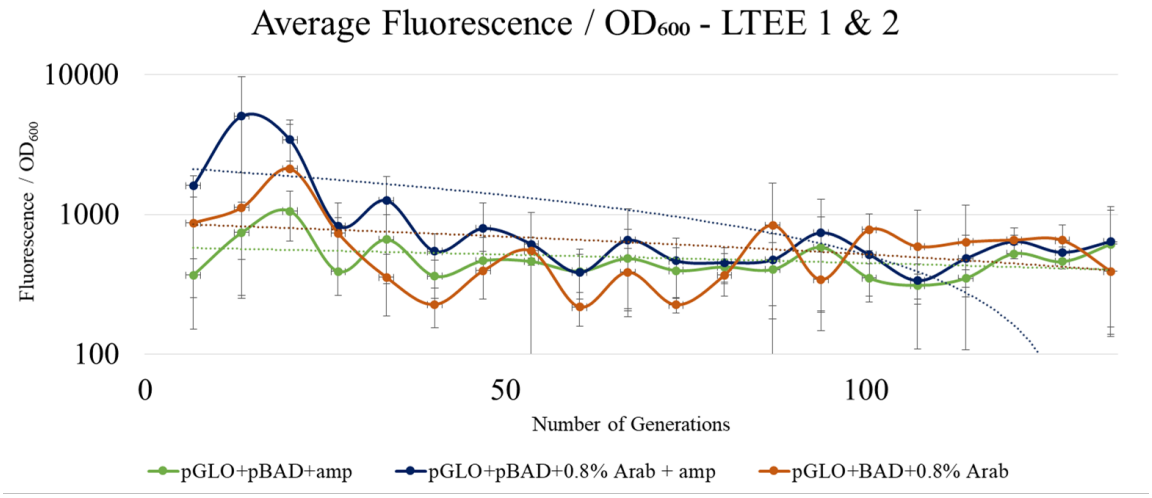

Figure 4: LTEE competition experiments over 130 generations in 96-well plates. The three depicted competition experiments are pGLO + pBAD + amp (green), pGLO + pBAD + 0.8% Arab + amp (dark blue), and pGLO + pBAD + 0.8% Arab (light red). Trend lines are drawn to guide the eye. Note the vertical axis is logarithmic. Error bars were calculated from two independent experiments and five biological replicates per experiment.

It should be noted that the starting point of the pGLO + pBAD + amp + arabinose and pGLO + pBAD + arabinose mixed cultures was predicted to coincide, considering they were inoculated from the same preculture sources. However, the culture containing amp had a somewhat higher GFP value. The discrepancy between the first reading- after 6.7 generations- may be corrected by a time zero measurement of the 96-well plate if competition is already ongoing during the first 6.7 generations. We also noted that, similar to the data in Figure two, all the readings behaved in a semi-sinusoidal manner rather than linear as a function of time. The time dependence of the fluorescence / OD_{600} values generally follows a pattern where the values appear to peak during the same generations. This observation suggests a small systematic error in the experiment from an unknown source.

To establish the dynamic range of the OD and fluorescence values expected in the experiments, we averaged these values over 160 generations for five conditions*: E. coli*, pBAD + amp, pGLO + amp, pGLO + 0.8% Arab + amp, pGLO + 0.8% Arab (no amp), and water. For fluorescence values, we found a background count of water ~ 75 Relative Fluorescence Units (RFU). *E. coli*, pBAD, and uninduced pGLO with amp showed a background fluorescence level ~500 RFU. Induction of pGLO in the presence of amp yielded much higher value of ~4250 RFU. Interestingly, pGLO + 0.8% Arab in the absence of amp had a substantially lower value ~1200 RFU which we tentatively attribute to the fairly rapid loss of the plasmid in the absence of amp. Corresponding values for OD_{600} and fluorescence / OD_{600} are also depicted in figure 5 to help interpret results from the LTEE experiments.

Figure 5 – Panel A:

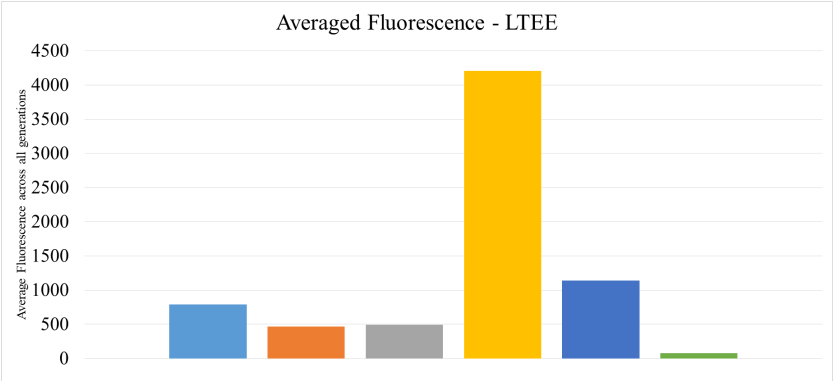

Figure 5 – Panel B:

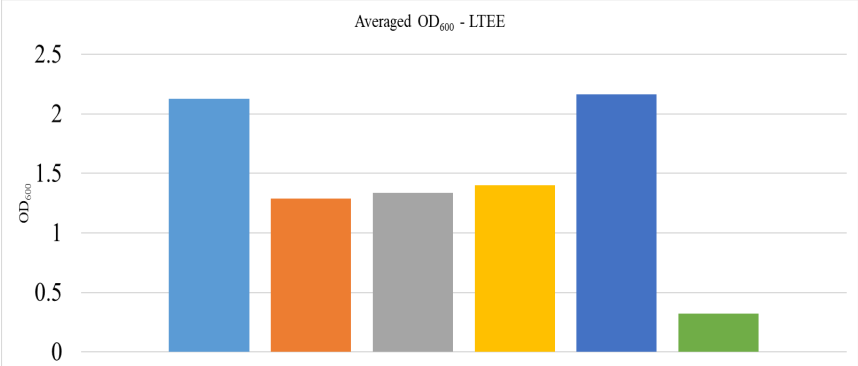

Figure 5 – Panel C:

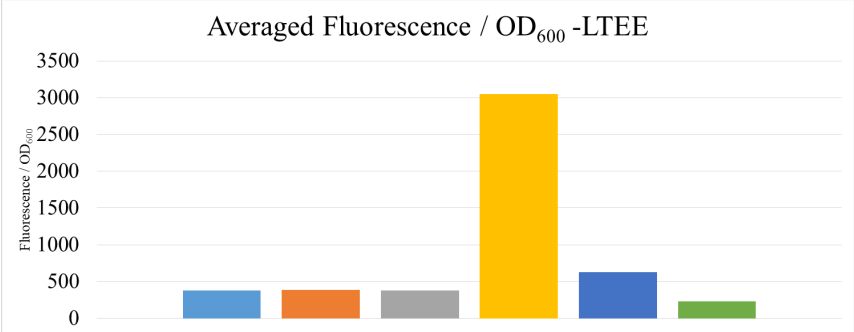

Figure 5: Determining Background levels and range of Fluorescence (Panel A-top left), OD (Panel B-right), and Fluorescence / OD_{600} (Panel C-bottom left) values for the measurement conditions used here. Spectrophotometric backgrounds for fluorescence and OD_{600} values were found to be ~ 75 RFU and 0.3, respectively, based on wells containing water (green bars). Background levels of GFP fluorescence for *E. coli*, pBAD, and uninduced pGLO were ~500 RFU (light blue, dark orange and gray respectively). Upon induction with arabinose,

GFP fluorescence increased to ~4250 (light orange). Induction of pGLO in absence of amp caused only a small increase in average fluorescence to ~ 1200 RFU. All cultures without amp had an OD_{600} near 2, while the presence of amp reduced the OD to ~1.3.

LTEE experiments in the presence of mutagenic agents

The previous section investigated competition between cultures containing a mixture of two *E. coli* strains. As a next step we examined if spontaneous evolutionary loss of GFP fluorescence from a pure culture can be observed in our LTEE experiments. To enhance the rate of gene loss, we also performed experiments in the presence of various concentrations of two different mutagenic agents: Acridine Orange (AO) and Methylnitronitrosoguanidine (MNNG). While AO causes mutations by acting as an agent that intercalates into the DNA double helix, MNNG is a DNA alkylating agent (Armstrong *et al.,* 1970, Kumari *et al.,* 2021).

First, we measured patterns in GFP fluorescence over 160 generations of *E. coli* in the absence of mutagens (Fig. 6). At the beginning of this LTEE experiment, we observed that the *E. coli* cultures containing pGLO in the presence of arabinose displayed fluorescence level at ~ 5000 RFU (Fig. 5). For the other cultures, fluorescence was ~500 RFU, which is near expected levels (Fig. 5). In the presence of amp, we detected a gradual decrease in GFP levels, consistent with gradual loss of a functional *gfp* gene. In contrast, in the absence of amp, there appears to be a rapid drop in GFP levels, which we tentatively attribute to loss of the entire plasmid.

Mutagenesis of bacteria with AO and MNNG by incubation of the cells in these agents for a limited amount of time before growing the mutated cells have been reported (Arshad, 2010, Foster, 1991, Coulondre & Miller, 1977). However, little information has been reported on long-term growth of *E. coli* in the presence of these two agent. We therefore first set out to measure what range of concentrations of AO and MNNG allowed long-term growth of *E. coli* MG1655.

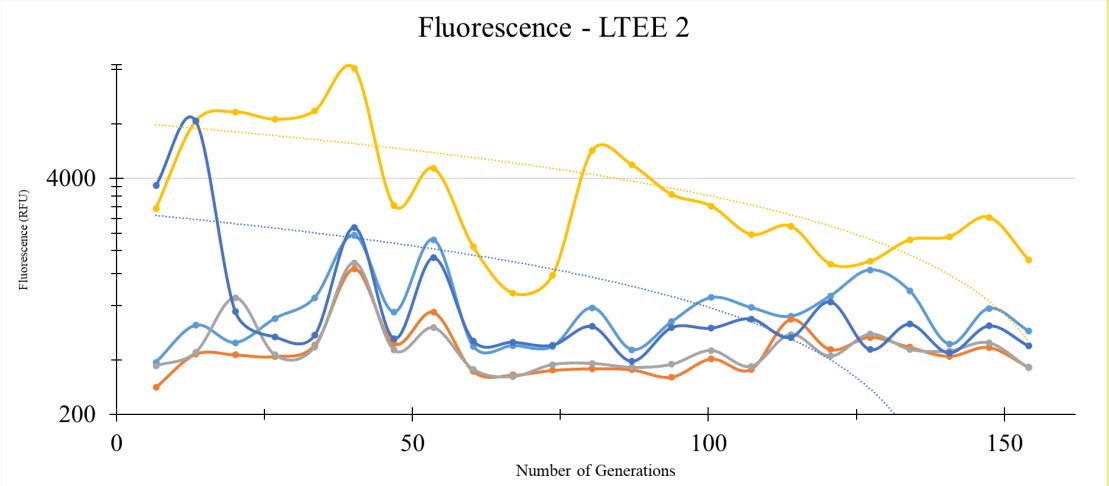

Figure 6: Investigating evolutionary loss of the *gfp* gene in the absence of mutagens. OD_{600} and fluorescence values were measured for 160 generations of *E. coli* cells for the following cultures: *E. coli* (blue), pBAD (orange), pGLO + amp (gray), pGLO + 0.8% Arab + amp (orange), pGLO + 0.8% Arab (no amp) (dark blue). Trend lines were added to help guide the eye.

Figure 7A displays the averaged OD_{600} of *E coli* cultures grown over 150 generations as a function of AO concentration. We predicted that as the concentration of AO increased, the OD would decrease because of the damaging effects of excessive mutations. From 0-20 µg/mL AO, the OD_{600} was essentially unaffected. Over this concentration range, induced pGLO with no ampicillin grew to an OD_{600} ~1 unit higher, consistent with the data depicted above in Fig. 2. However, unexpectedly, from 20-114 µg/mL AO, the difference in OD readings disappeared. The fluorescence data for AO is not depicted here because we found that under our experimental conditions the spectroscopic and fluorescence properties of this agent unexpectedly interfered with the detection of GFP fluorescence. While literature data indicated that the excitation and emission value of 395, 550 nm would be acceptable, we tested the concentration gradient in MM + Amp and found a positive correlation between fluorescence counts and AO concentration (Srivastava *et al*., 2008).

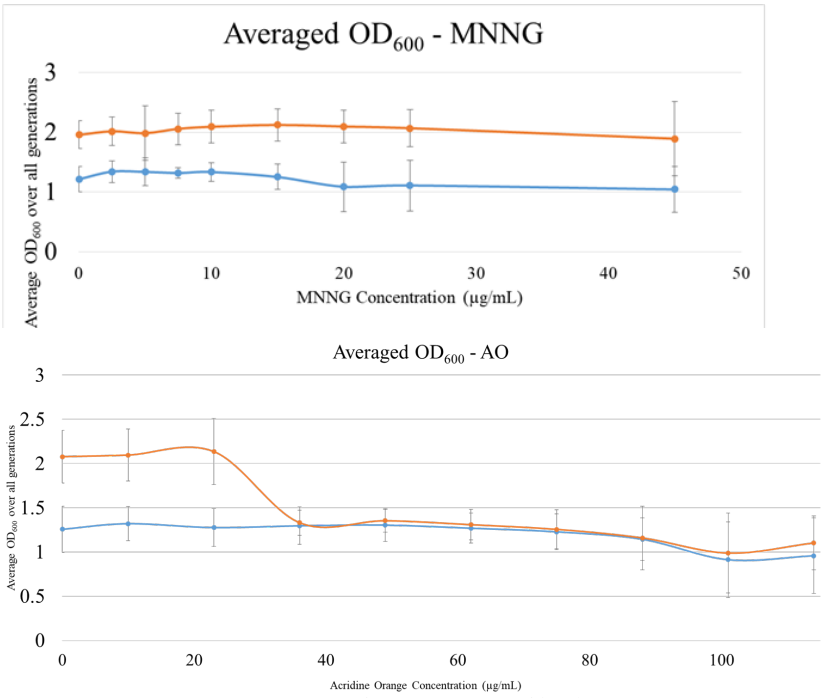

Figure 7: Effect of multiple mutagen concentrations on OD values averaged over 160 generations were determined for AO (Panel A-top left) and MNNG (Panel B-top right).

When we performed a similar analysis for MNNG, averaging the OD_{600} values across all generations for each concentration of mutagenic agent produced similar results (Figure 7B). In this case, up to a concentration of 45 µg/mL MNNG, pGLO grown in media without amp consistently grew ~ 1 OD unit higher than the same pGLO grown in the presence of amp. At high concentrations, pGLO with/without amp grown in MNNG experienced significant multi-generational dips in OD throughout the LTEE-indicating that they struggled to grow.

Next, we examined trends in cellular GFP content during our LTEE experiments, and how these trends were affected by MNNG concentration. Figure 8 displays fluorescence / OD for a 160-generation experiment. The data indicates gradual disruption of the *gfp* gene for all three MNNG concentrations. Future experiments are needed to determine if the gene is disrupted at a faster rate if the concentration of mutagen is increased.

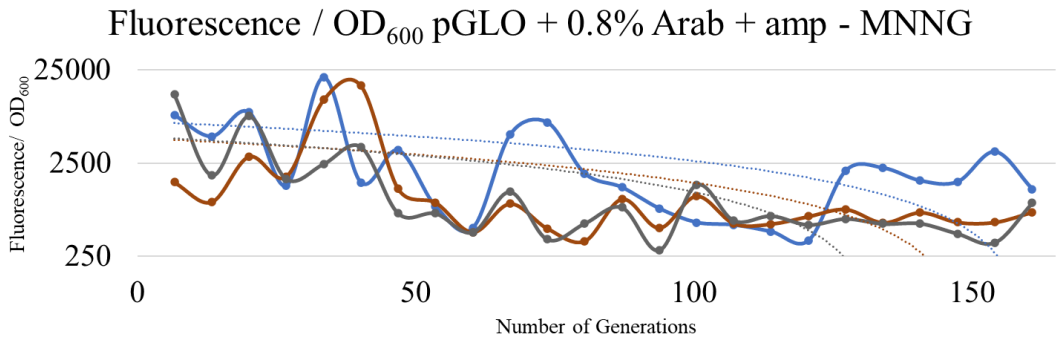

Figure 8: Initial results on the effect of MNNG on evolutionary loss of functional *gfp* gene in the presence of amp. Depicted are pGLO + 0.8% Arab + amp in the presence of 0 (blue), 25 (light red), and 45 (gray) µg/mL MNNG. Note vertical axis is logarithmic. Trendlines added to guide the eye.

4. Discussion and Conclusions

Observations supporting the detection of evolutionary loss of GFP during laboratory based LTEE experiments

We performed two types of LTEE experiments: competition between two strains and loss of GFP fluorescence over evolutionary time in a single strain. Data in Fig. 4 indicates that pBAD is outcompeting pGLO over the course of 150 generations. This observation has potential relevance for the proposed antibiotic rotation strategy. It shows that a bacterial strain containing an unused gene, such as *gfp*, and by extension an AR gene, will tend to be out-competed fairly quickly by a strain lacking that gene.

In our LTEE *gfp* gene loss experiments, our data indicated that even in the absence of mutagens, there was a substantial decrease in GFP production over the course of 150 generations (Fig. 6). In the absence of amp to enforce the retention of the plasmid, the loss of GFP production appeared to be much faster -consistent with rapid loss of the entire plasmid. Future experiments in which cells are plated with and without amp can help confirm this interpretation. At this point, we did not observe a faster loss of GFP production over 150 generations in the presence of MNNG (Fig. 8). Future measurements under improved experimental conditions (see below) may resolve this issue.

Novel and unexpected results

An element of novelty to the mutagen experiment is the process of long-term exposure to mutagen. Most literature that refers to mutagen experimentation exposes the sample to single or short-term mutagenic agent. When combing through literature to determine an estimation of what concentration to use, it was difficult to find data that accurately translated

into the experiment. Arshad (2006) found that 50 µg/mL of AO was the highest concentration permissible for growth, whereas we were able to grow it in 114 µg/mL.

The difference in OD between amp and no amp was seen in all experiments. We attribute this to changes in the degree of clumping together of cells under some conditions, leading to a higher observed OD while the number of cells likely stays the same.

Improving experimental conditions for LTEE experiments

There are several improvements to the current experimental design to be made. After 12 hours in the incubator, the cultures in each well of the 96-well plate appeared to have partially evaporated. We surrounded the samples with water wells, which did not prevent evaporation as much as we expected. In the future, we plan to use breathable film rather than a lid to decrease evaporation and improve oxygen interface. 12 hours of growth translates to 6.7 generations of growth. Meaning, it takes weeks of twice daily measurements to reach the desired number of generations. To increase the number of generations per twelve hours, we plan to dilute the old plate before inoculating the new plate. Through a three-series dilution, we could achieve 200 generations in six days compared to 15. However, there is a risk of founder effect playing a role in evolutionary dynamics as we narrow the amount of genetic diversity through diluting.

AO and MNNG represent only two mechanisms of mutation. In the future, we plan to use 2-Aminopurine (AP) and 4-Nitroquinoline 1-oxide (4QNQ) as mutagens. AP is a base analog mutator and 4QNQ causes the formation of bulky purine adducts. We can then compare all four mutagenic agents to understand if the experimental conditions respond differently to different mechanisms of mutation.

The fluorescence data for AO had to be discarded because there was a large residual fluorescence caused by the mutagen. We attempted to subtract it out from the already obtained fluorescence data, but at higher concentrations it was too large to consider the result accurate, resulting in some instances of negative fluorescence after subtraction. In the future, we plan on adjusting the emission and excitation wavelengths to exclude the fluorescence caused by AO.

Moving from detecting evolutionary loss of GFP to loss of AR genes

The methods tested and development tested here based on automated growth curves are beneficial moving forward into the next phase of experimentation: using AR genes rather than *gfp*. Rather than using fluorescence as the detector, this methodology can be translated by plating onto LB with/without amp to detect gene loss.

Development of the concept of using a global antibiotics rotation scheme

While we can label a gene nonessential, this label is not straightforward and may be used naively. Schulz zur Wiesch *et al*., (2010) found that the fitness cost of a resistance mutation can be compensated for by secondary site mutations, making the net fitness cost zero. From this concept, it may be said that a global rotation scheme is impossible because rather than losing the resistance gene over time, the bacteria would compensate for it and keep its genome intact. However, the concept explored here allows for the idea to proceed even for a net zero fitness cost of having unused AR genes. The on-rate for resistance involves a rare fitness enhancing, strong selection event affected by genetic diversity and natural selection. Humans have also artificially increased the timescale through the heightened use of non-necessary antibiotic prescriptions and use of antibiotics in the natural environment-through the livestock industry and unintentional runoff into surrounding landscape. However, the off-rate is natural over time because of the occurrence of (frequent) random mutations-one or more of which will eventually destroy the resistance mutation. While neutral, these mutations are not maintained through selective pressures. Over time, net zero mutations will eventually become negative. Whole genome sequencing of bacteria generally does not find a large number of pseudogenes, meaning that there is fairly rapid turnover-both in and out- of genes in bacteria. Meaning, neutral mutations that are not positive-and would therefore be maintained by selection pressure-or negative-and would therefore be removed through evolution-will eventually be lost in the rapid turnover of pseudogenes.

5. Summary

AR increasingly threatens to reverse the major medical progress that was made possible by the discovery of antibiotics-unless we quickly find a solution. Drug development to identify novel antibiotics, while important, in the long term is likely to be insufficient because of continuing bacterial evolution of new AR genes and mechanisms. Using our understanding of evolution, here we propose a potential solution: a global rotation scheme of exclusively and selectively prescribed antibiotics. The basic biological question underlying this solution is as follows: how do cells handle non-essential genes-such as AR genes when the antibiotic it is resistant to is stopped. Here we approach this question using the *gfp* gene in pGLO as an unselected gene. To measure evolutionary loss of the *gfp* gene from *E. coli*, we performed both competition experiments and gene loss experiments over ~200 bacterial generations. We competed pGLO and pBAD (same as pGLO but without *gfp*) cells against each other with/without amp, the antibiotics that selects for the presence of the plasmids-and with/without arabinose-the molecule that induces transcription of the *gfp* gene encoded in the pGLO plasmid. The off-rate in which AR is lost is a pressing question that may limit the applicability of a possible global antibiotics rotation scheme. To initiate studies of this rate

under reasonable time constraints, we attempted to speed up the evolutionary "clock" through the introduction of mutagenic agents. From these experiments, we observed that the growth curves of the LTEE experiments were not smoothly linear in time. Measuring OD_{600} and fluorescence, the resulting data was semi-sinusoidal over time. One possible explanation for this phenomenon is different degrees of condensation on the lid of the plate. The plate reader reads with the lid on, meaning that condensation could affect the readings. Therefore, in future experiments, the lid will be wiped dry with a sterile cloth.

Overall, the findings reported here can provide a framework and experimental methods for continued research into the feasibility of a global rotation scale. We plan to continue this research at OSU in 2023 and 2024 with support from a Wentz grant and take it beyond a model of non-essentiality and onto clinical relevance-by using AR as the non-essential gene and using plating rather than fluorescence to measure gene loss.

6. Appendices

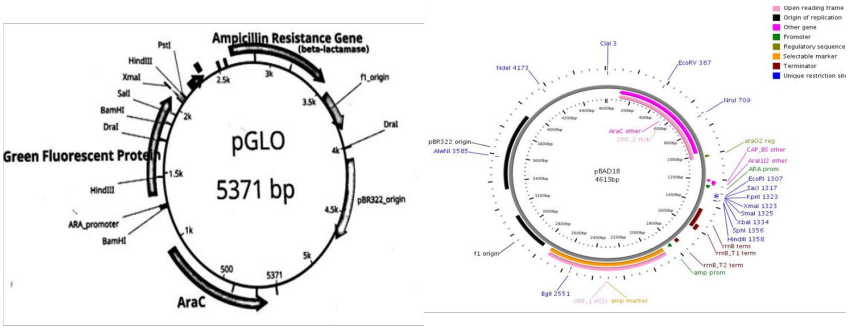

Appendices A: pGLO (left) and pBAD18 (right) plasmid maps.

LTEE Plate Layout

	1	2	3	4	5	6	7	8	9	10	11	12
A												
B		MG1655 *E. coli*	pBAD18	pGLO	*pGLO+ 0.8% Arab*		*Pglo+ Arab*		pGLO + pBAD18	pGLO + pBAD18 + 0.8% Arab	pGLO + pBAD18 + 0.8% Arab	
C		*MG1655 E. coli*	pBAD18	pGLO	*pGLO+ 0.8% Arab*		*Pglo+ Arab*		pGLO + pBAD18	pGLO + pBAD18 + 0.8% Arab	pGLO + pBAD18 + 0.8% Arab	
D		*MG1655 E. coli*	pBAD18	pGLO	*pGLO+ 0.8% Arab*		*Pglo+ Arab*		pGLO + pBAD18	pGLO + pBAD18 + 0.8% Arab	pGLO + pBAD18 + 0.8% Arab	
E		*MG1655 E. coli*	pBAD18	pGLO	*pGLO+ 0.8% Arab*		*Pglo+ Arab*		pGLO + pBAD18	pGLO + pBAD18 + 0.8% Arab	pGLO + pBAD18 + 0.8% Arab	
F		*MG1655 E. coli*	pBAD18	pGLO	*pGLO+ 0.8% Arab*		*Pglo+ Arab*		pGLO + pBAD18	pGLO + pBAD18 + 0.8% Arab	pGLO + pBAD18 + 0.8% Arab	
G												
H												
Arabinose (µL)		*0*	*0*	*0*	*10*		*10*		*10*	*10*	*10*	
Culture (µL)		*2.5*	*2.5*	*2.5*	*2.5*		*2.5*		*2.5*	*2.5*	*2.5*	
Media Volume (µL)		**247.5**	**247.5**	**247.5**	**237.5**		**237.5**		**237.5**	**237.5**	**237.5**	

No amp
amp
H_2O

Appendices B: LTEE Plate layout pipetting scheme for inoculating single-well and competition evolution experiments.

Mutagen: AO & MNNG Plate Layout

		1	2	3	4	5	6	7	8	9	10	11	12
Orange	A												
	B		*pGLO + 0.8%Arab + amp*	*pGLO + 0.8%Arab + amp*	*pGLO + 0.8%Arab + amp*	*pGLO + 0.8%Arab + amp*	*pGLO + 0.8%Arab + amp*	*pGLO + 0.8%Arab + amp*	*pGLO + 0.8%Arab + amp*	*pGLO + 0.8%Arab + amp*	*pGLO + 0.8%Arab + amp*	*pGLO + 0.8%Arab + amp*	
	C												
	D		*pGLO + 0.8%Arab (no amp)*	*pGLO + 0.8%Arab (no amp)*	*pGLO + 0.8%Arab (no amp)*	*pGLO + 0.8%Arab (no amp)*	*pGLO + 0.8%Arab (no amp)*	*pGLO + 0.8%Arab (no amp)*	*pGLO + 0.8%Arab (no amp)*	*pGLO + 0.8%Arab (no amp)*	*pGLO + 0.8%Arab (no amp)*	*pGLO + 0.8%Arab (no amp)*	
	E												
	F		*pGLO + 0.8%Arab + amp*	*pGLO + 0.8%Arab + amp*	*pGLO + 0.8%Arab + amp*	*pGLO + 0.8%Arab + amp*	*pGLO + 0.8%Arab + amp*	*pGLO + 0.8%Arab + amp*	*pGLO + 0.8%Arab + amp*	*pGLO + 0.8%Arab + amp*	*pGLO + 0.8%Arab + amp*		
	G												
	H		*pGLO + 0.8%Arab (no amp)*	*pGLO + 0.8%Arab (no amp)*	*pGLO + 0.8%Arab (no amp)*	*pGLO + 0.8%Arab (no amp)*	*pGLO + 0.8%Arab (no amp)*	*pGLO + 0.8%Arab (no amp)*	*pGLO + 0.8%Arab (no amp)*	*pGLO + 0.8%Arab (no amp)*	*pGLO + 0.8%Arab (no amp)*		
Orange	AO concentration (µg/mL)		*0*	*10*	*23*	*36*	*49*	*62*	*75*	*88*	*101*	*114*	
	Arabinose (µL)		*10*	*10*	*10*	*10*	*10*	*10*	*10*	*10*	*10*	*10*	
	Culture (µL)		*2.5*	*2.5*	*2.5*	*2.5*	*2.5*	*2.5*	*2.5*	*2.5*	*2.5*	*2.5*	
	Mutagen (µL)		*0*	*2.5*	*5.75*	*9*	*12.25*	*15.5*	*18.75*	*22*	*25.25*	*28*	
	Media Volume (µL)		**237.5**	**235**	**231.75**	**228.5**	**225.25**	**222**	**218.75**	**215.5**	**212.25**	**209.5**	
	MNNG concentration (µg/mL)		*0*	*2.5*	*5*	*7.5*	*10*	*15*	*20*	*25*	*45*		
	Arabinose		*10*	*10*	*10*	*10*	*10*	*10*	*10*	*10*	*10*		
	Culture		*2.5*	*2.5*	*2.5*	*2.5*	*2.5*	*2.5*	*2.5*	*2.5*	*2.5*		
	ul mutagen		*0*	*0.625*	*1.25*	*1.875*	*2.5*	*3.75*	*5*	*6.25*	*11.25*		
	Media Volume (µL)		**237.5**	**236.88**	**236.25**	**235.63**	**235**	**233.75**	**232.5**	**231.25**	**226.25**		

Appendices C: LTEE Plate layout with mutagen pipetting scheme for inoculating pGLO + 0.8% Arab with and without amp.

Appendix D:Acknowledgements

I would like to sincerely express my gratitude to Dr. and Mrs. Niblack for their funding and support of the Niblack Scholars program. Because of this program, I have had the opportunity to complete meaningful research over the last three semesters. I have had the opportunity to travel to Houston, Texas and Anaheim, California to present my research, as well as locally at the Undergraduate Research Symposium and Microbiology Departmental Symposium. I would like to thank my faculty mentor, Dr. Wouter Hoff, for his continual support. I have learned the scope of the scientific process-including the hard parts- from his mentorship. I would like my graduate student mentor, Rosalie Dohmen, for her ability to make all the experiments happen-from the ordering supplies, helping with the math of microbiology, time logistics, and filling in for me during plate readings. I would like to thank OK-LSAMP, CAS, the office of Scholar Development and Undergraduate Research, and the Microbiology department for their financial support that has helped me make the project its best. I would like to thank Dr. Garry Marley for his assistance with pGLO, Dr. Matthew Cabeen for being a co-mentor and knowledgeable resource, Dr. Avi Mitra for allowing me to use his plate reader, and Dr. Randy Morgenstein for helping prepare the *E. coli* strain.

Appendix E: Papers Published

Sarah Teeman, Rosalie Dohmen, Matthew Cabeen, Wouter Hoff PhD. Accelerating Bacterial Evolution in the Lab to Study the Loss of Nonessential Genes. American Society of Microbiology: Microbe, Houston, Texas, June 15th-19th, 2023 (poster).

Sarah Teeman, Rosalie Dohmen, Matthew Cabeen, Wouter Hoff PhD. Accelerating Bacterial Evolution in the Lab to Study the Loss of Nonessential Genes. Undergraduate Research Symposium (URS) Oklahoma State University, Stillwater Oklahoma, April 18th, 2023 (poster).

Sarah Teeman, Rosalie Dohmen, Matthew Cabeen, Wouter Hoff PhD. Accelerating Bacterial Evolution in the Lab to Study the Loss of Nonessential Genes. Microbiology Departmental Symposium Oklahoma State University, Stillwater, Oklahoma February 10th, 2023 (poster).

Sarah Teeman, Rosalie Dohmen, Matthew Cabeen, Wouter Hoff PhD. Accelerating Bacterial Evolution in the Lab to Study the Loss of Nonessential Genes. Annual Biomedical Research Conference for Minoritized Scientists (ABRCMS), Anaheim, California, November 9th-12th, 2022 (poster).

Appendix F: Literature Cited

Ampicillin (2008) *OpenWetWare*. Available at: https://openwetware.org/wiki/Ampicillin#:~:text=Typical%20concentrations%20of%20ampicillin%20are,and%20are%20easy%20to%20pipet. (Accessed: 11 August 2023).

Armstrong, W., Kurucsev, T. and Strauss, U. (1970) *Interaction between acridine dyes and deoxyribonucleic acid*, *ACS Publications*. Available at: https://pubmed.ncbi.nlm.nih.gov/5446957/ (Accessed: 11 August 2023).

Arshad, R. *et al.* (2006) *Mutagenic effect of acridine orange on the expression of penicillin G acylase and beta-lactamase in escherichia coli*, *Letters in applied microbiology*. Available at: https://pubmed.ncbi.nlm.nih.gov/16441371/#:~:text=Significance%20and%20impact%20of%20the,for%20industrial%20production%20of%20PGA. (Accessed: 08 August 2023).

Arshad, R., Farooq, S. and Ali, S.S. (2010) *Effect of mutations induced by N-methyl-n'-nitro-N-nitrosoguanidine on expression of penicillin G acylase and β-lactamase in wild-type escherichia coli strains - annals of microbiology*, *BioMed Central*. Available at: https://annalsmicrobiology.biomedcentral.com/articles/10.1007/s13213-010-0104-6 (Accessed: 08 August 2023).

Blount, Z.D., Borland, C. and Lenski, R. (2008) *Historical contingency and the evolution of a key innovation in an experimental population of Escherichia coli*, *Biological Sciences*. Available at: https://www.pnas.org/doi/10.1073/pnas.0803151105 (Accessed: 24 July 2023).

Chen, A. (2021) *DIY chemically competent cells: Easy 10-step protocol*, *Bitesize Bio*. Available at: https://bitesizebio.com/30145/chemically-competent-cells/#:~:text=Innoculate%2010%20mL%20of%20sterile,mid%20log%20phase)%20is%20reached (Accessed: 04 August 2023).

Coulondre, C. and Miller, J. (2004) *Genetic studies of the lac repressor: III. additional correlation of mutational sites with specific amino acid residues*, *Journal of Molecular Biology*. Available at: https://www.sciencedirect.com/science/article/pii/0022283677900560?via%3Dihub (Accessed: 11 August 2023).

Dadgostar, P. (2019) *Antimicrobial resistance: Implications and costs*, *Infection and drug resistance*. Available at: https://www.ncbi.nlm.nih.gov/pmc/articles/PMC6929930/ (Accessed: 24 July 2023).

Foster, P. (1991) *In vivo mutagenesis*, *Methods in Enzymology*. Available at: https://www.sciencedirect.com/science/article/abs/pii/007668799104007B?via%3Dihub (Accessed: 11 August 2023).

Global burden of bacterial antimicrobial resistance in 2019: a systematic analysis (2022) *The Lancet*. Available at: https://www.thelancet.com/journals/lancet/article/PIIS0140-6736(21)02724-0/fulltext (Accessed: 24 July 2023).

Kumari, S. *et al.* (2021) *Unboxing the molecular modalities of mutagens in cancer - environmental science and Pollution Research*, *SpringerLink*. Available at: https://link.springer.com/article/10.1007/s11356-021-16726-w (Accessed: 11 August 2023).

Lenski, R.E. (2017) *Experimental evolution and the dynamics of adaptation and Genome Evolution in microbial populations*, *Nature News*. Available at: https://www.nature.com/articles/ismej201769 (Accessed: 10 August 2023).

Plackett, B. (2020) *Why big pharma has abandoned antibiotics*, *Nature News*. Available at: https://www.nature.com/articles/d41586-020-02884-3 (Accessed: 02 August 2023).

Rathod, R., Kang, Z., Hartson, SD., Kumauchi, M., Xie, A., Hoff, WD., 2012, Side-chain specific isotopic labeling of proteins for infrared structural biology: the case of ring-D4-tyrosine isotope labeling of photoactive yellow protein. Prot. Purif. Expr. 85, 125-132.

Schulz zur Wiesch, P., Engelstädter, J. and Bonhoeffer, S. (2010) *Compensation of fitness costs and reversibility of antibiotic resistance mutations*, *Antimicrobial agents and chemotherapy*. Available at: https://www.ncbi.nlm.nih.gov/pmc/articles/PMC2863634/ (Accessed: 10 August 2023).

Srivastava, S. *et al.* (2008) *Computer-aided identification of ovarian cancer in confocal microendoscope images*, *SPIE Digital Library*. Available at: https://www.spiedigitallibrary.org/journals/journal-of-biomedical-optics/volume-13/issue-02/024021/Computer-aided-identification-of-ovarian-cancer-in-confocal-microendoscope-images/10.1117/1.2907167.full?SSO=1 (Accessed: 09 August 2023).

Transformation protocol (no date) *New England Biolabs*. Available at: https://www.neb.com/protocols/2012/05/21/transformation-protocol (Accessed: 07 August 2023).

Exploring the Evolutionary Process of Losing Unselected Genes as a Potential Avenue to Addressing Bacterial Antibiotic Resistance (AR)

Niblack Research Scholars Symposium
September 15th, 2023

Sarah M. Teeman
3rd year Undergraduate Student
Sarah.Teeman@okstate.edu | Graduate mentor: Rosalie Dohmen | Dr. Wouter Hoff Laboratory

Antibiotic Resistance: the risk of losing a cornerstone of modern medicine

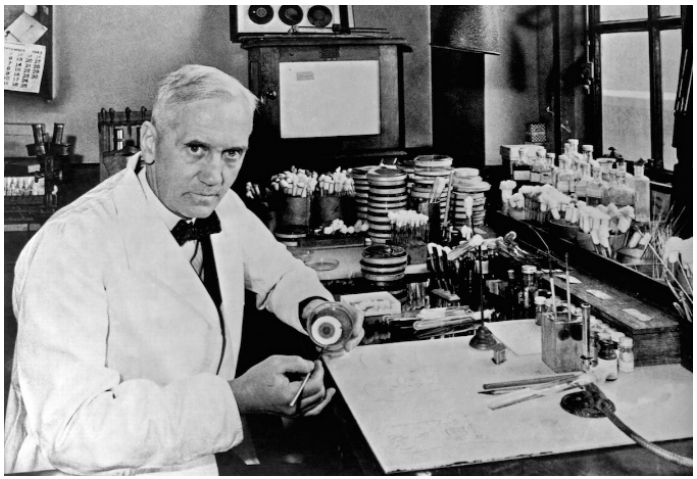

1928: Dr. Alexander Fleming discovered penicillin

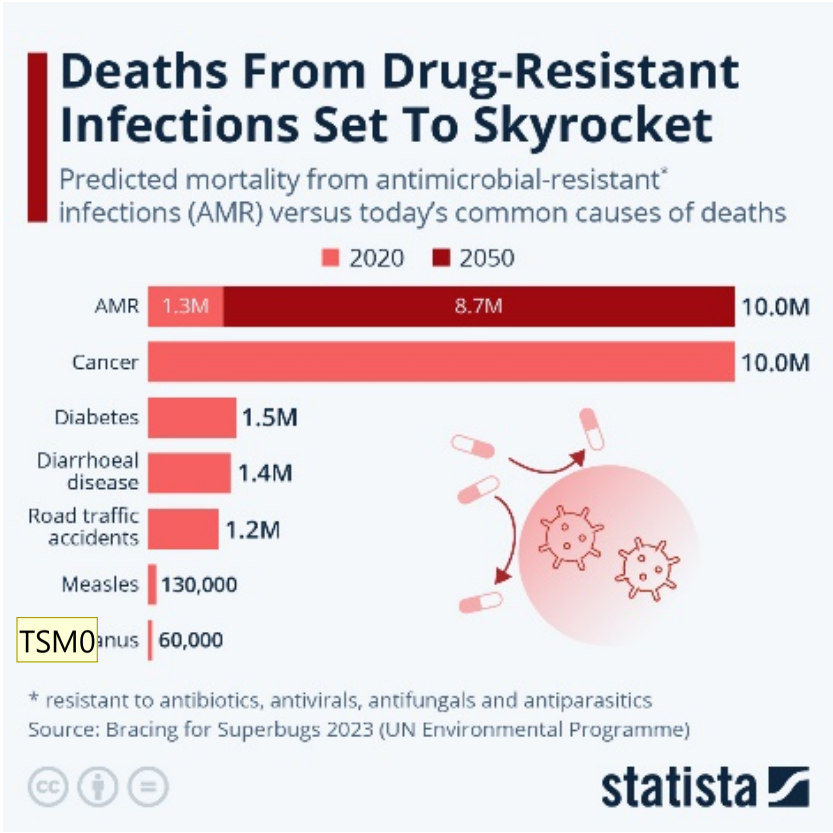

Analysis of infectious disease mortality data from the U.S. government reveals that antibacterial agents may save over 200,000 American lives annually, and add 5-10 years to U.S. life expectancy at birth. (Joseph Gottfried, https://dash.harvard.edu/)

TSM0

Stages in the efficacy of an antibiotic

Stage 1: the antibiotic is effective

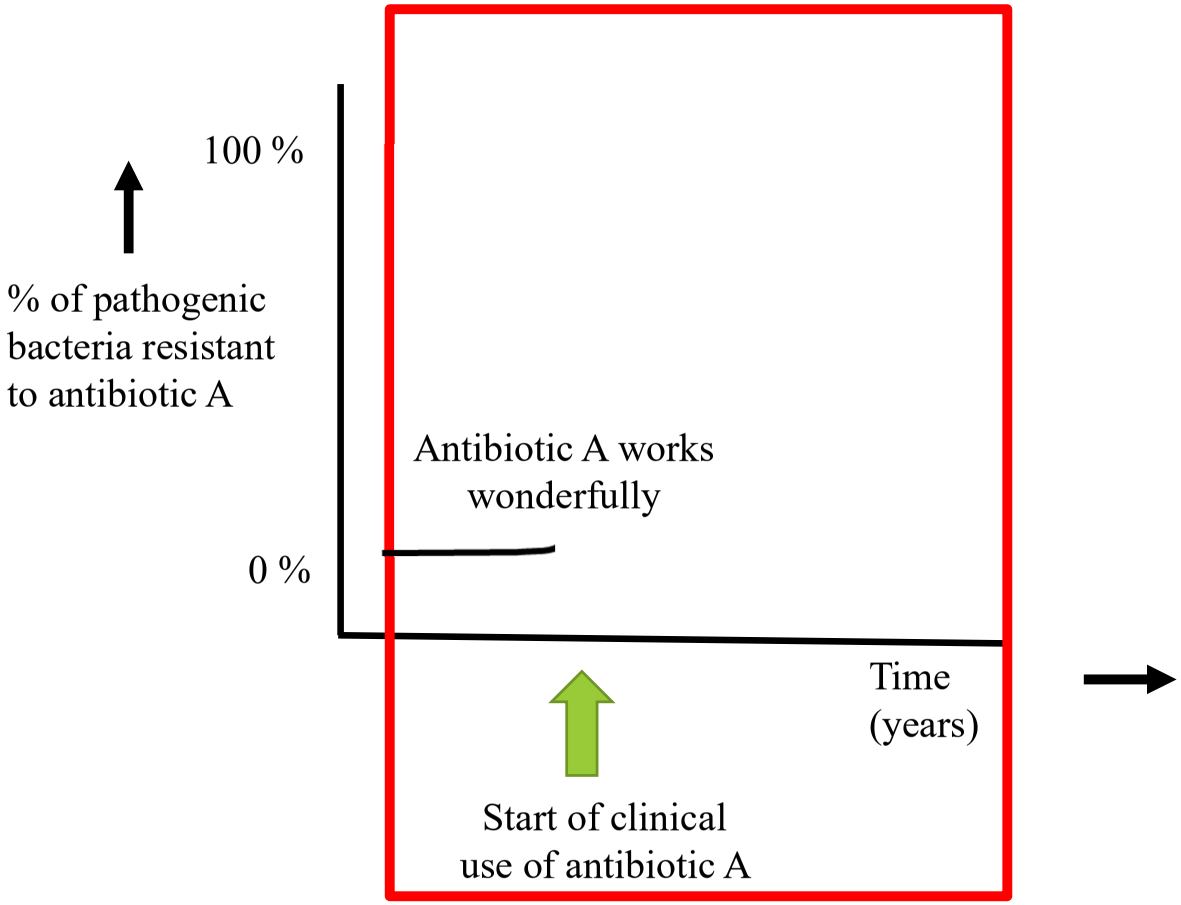

TSM0

Stages in the efficacy of an antibiotic

Stage 2: bacterial pathogens evolve resistance to the antibiotic

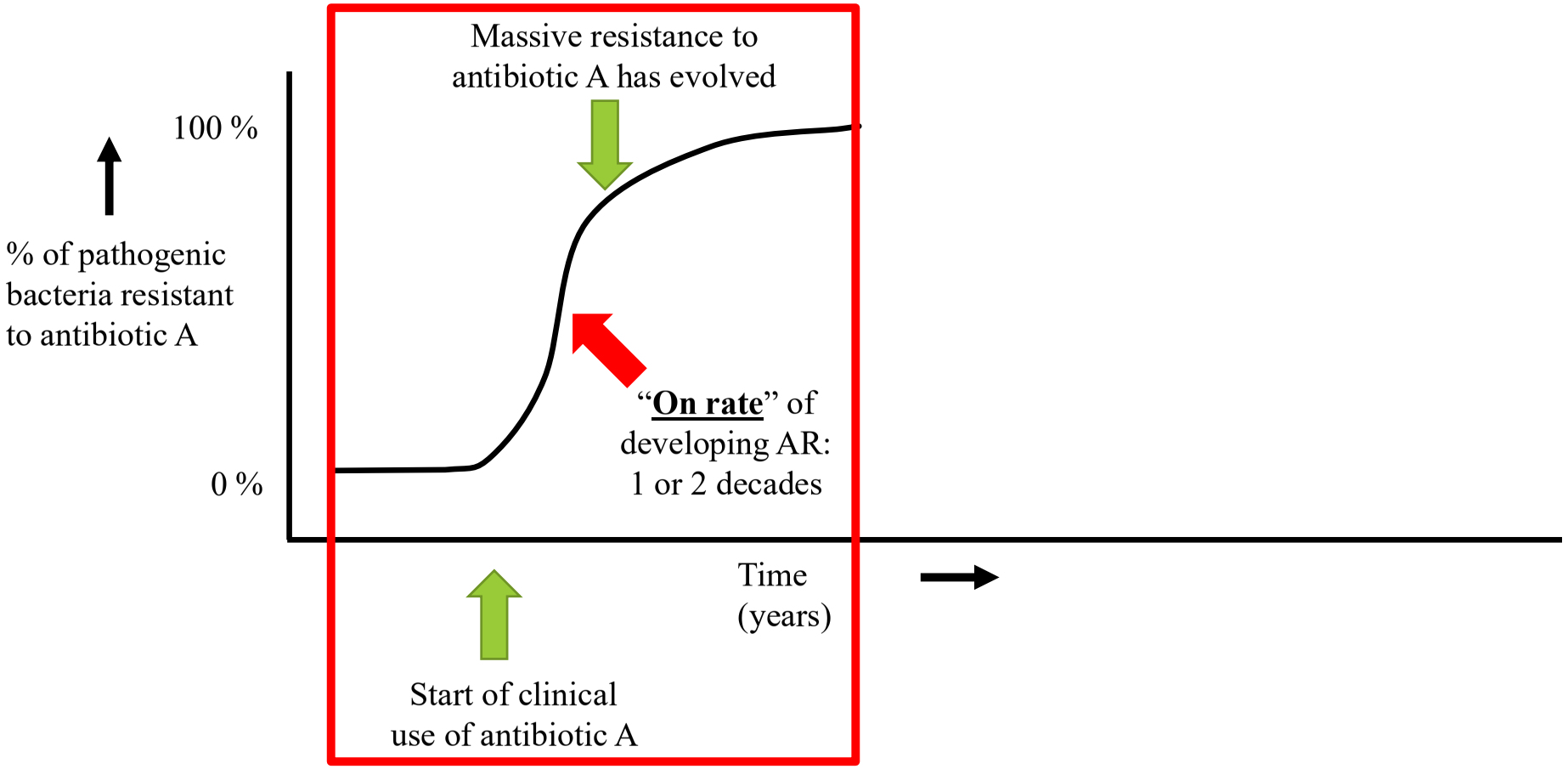

TSM0

Stages in the efficacy of an antibiotic

Stage 2: bacterial pathogens evolve resistance to the antibiotic

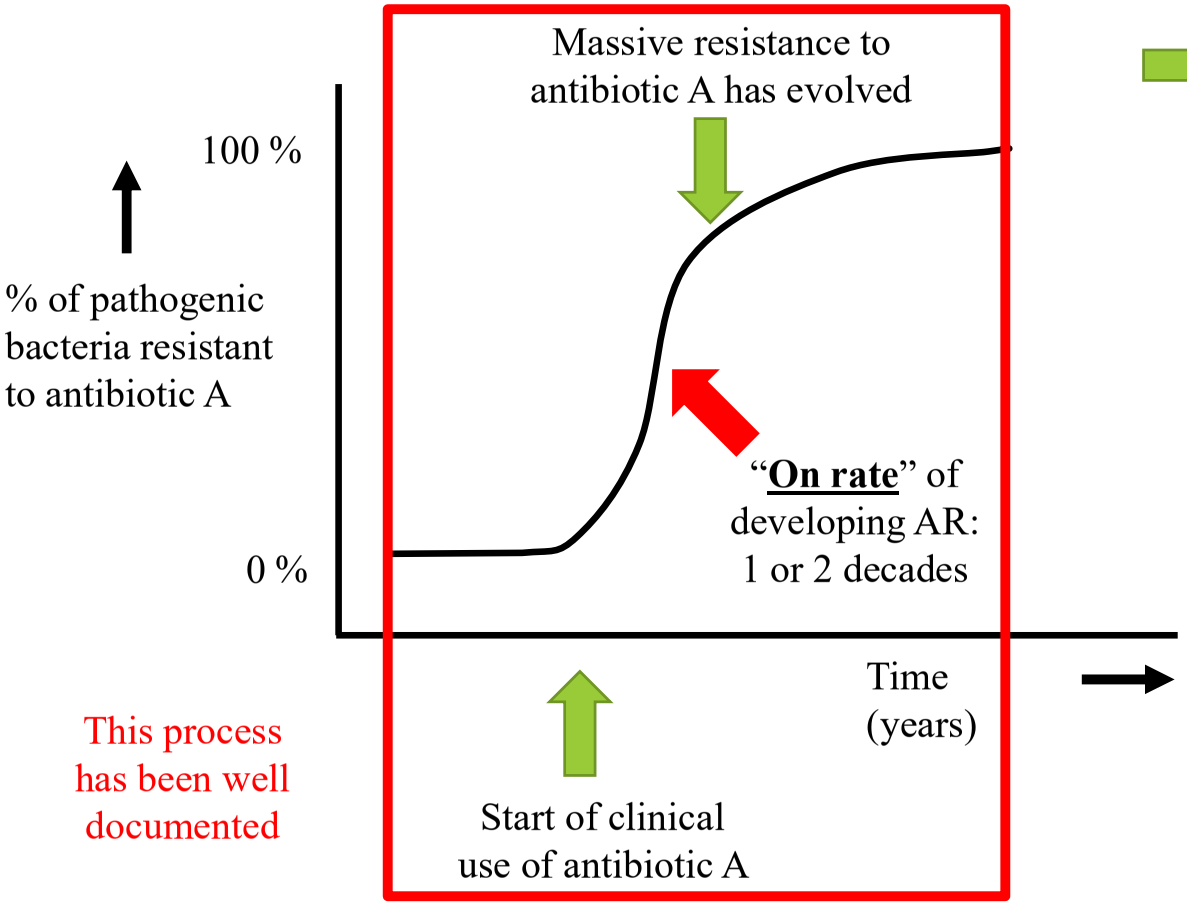

This process has been well documented

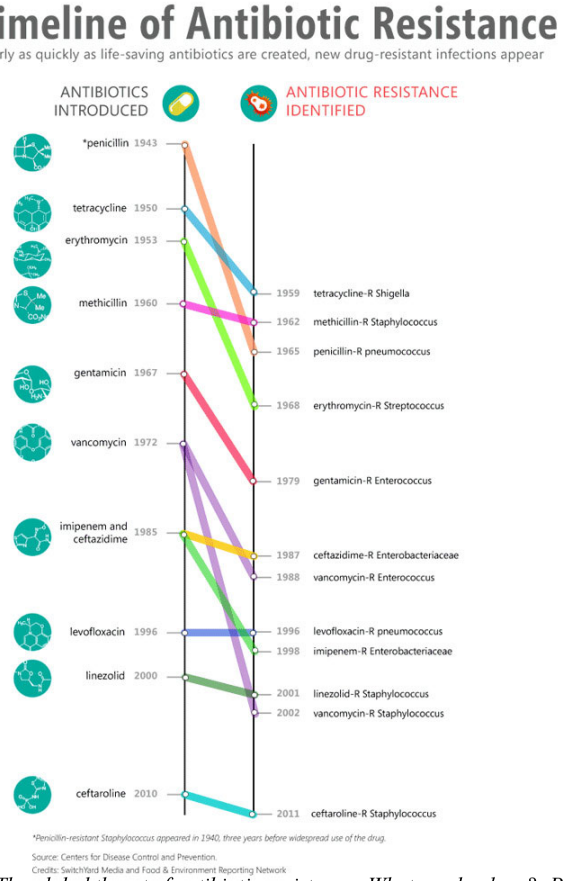

(Graham, *The global threat of antibiotic resistance: What can be done?: Published in Journal of Global Health Reports* 2017)

TSM0

The overall question we aim to investigate:
Predicted stage 3: sensitivity to the antibiotic can be restored

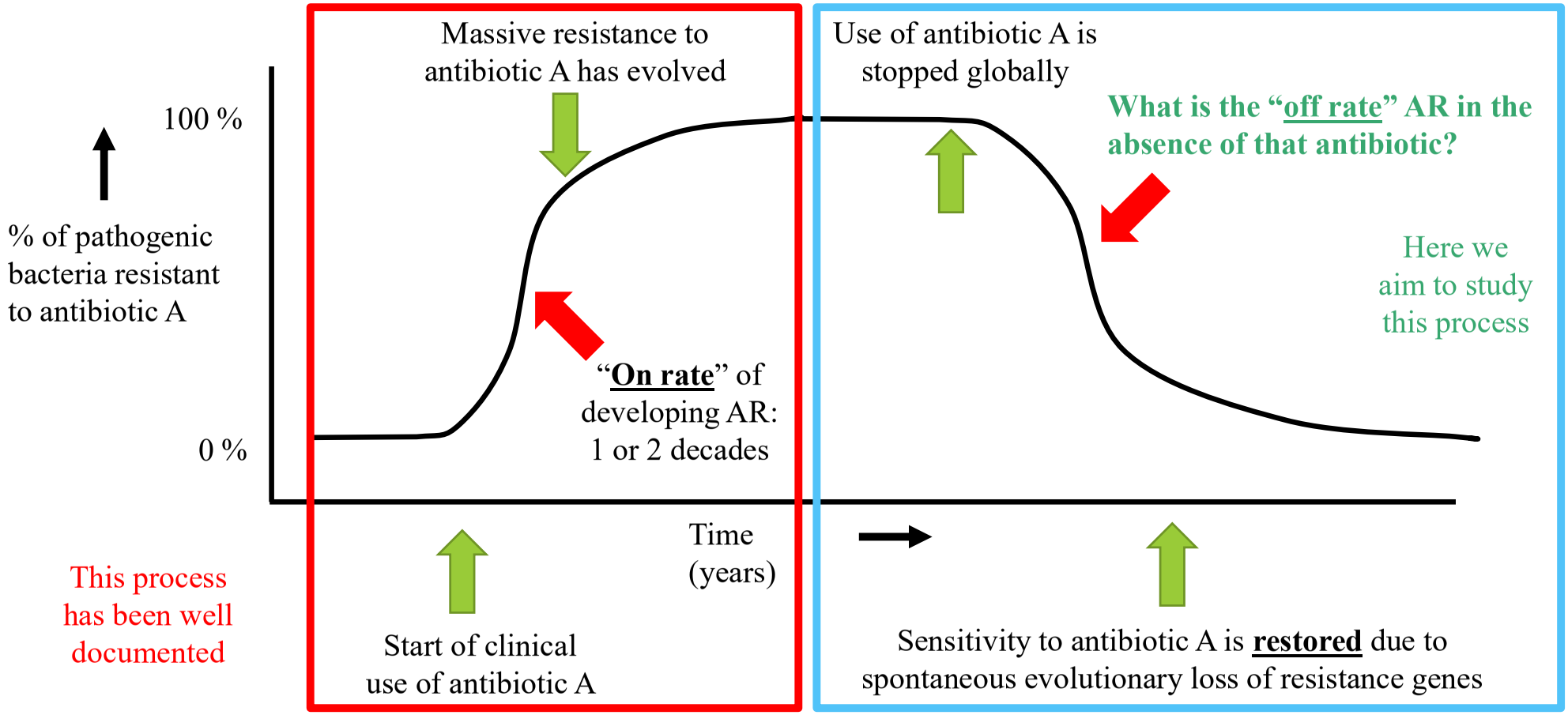

Research Question

Do bacteria lose useless genes over the course of many generations?

And how fast?

TSM0

Research strategy: study the loss of *gfp* as an easily detectable unselected gene

Green Fluorescent Protein (GFP)

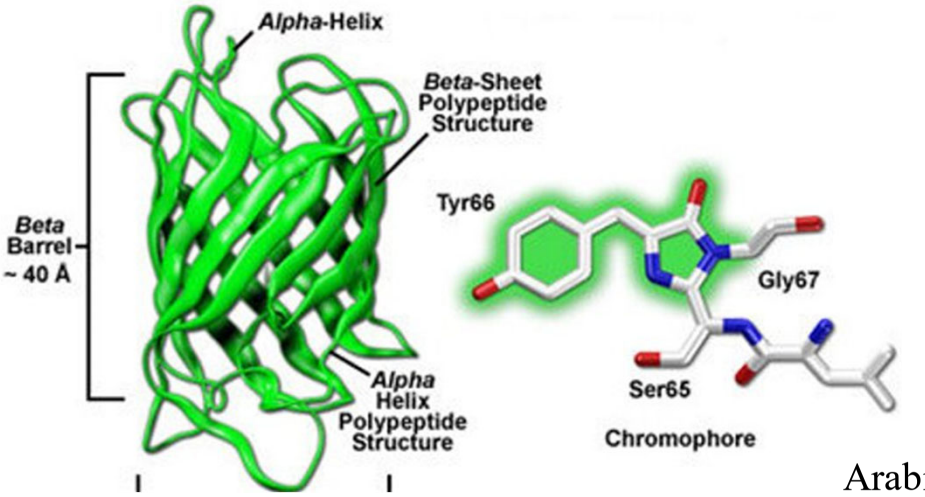

(Zeiss, *Education in microscopy and digital imaging*)

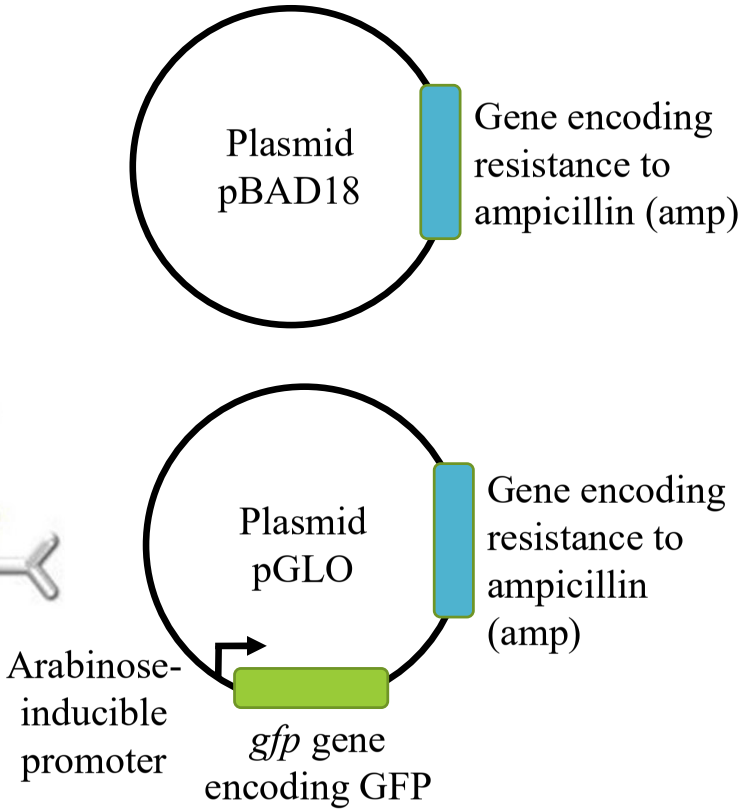

This is the empty vector (control experiment). Amp in growth medium "forces" *E. coli* to retain the plasmid.

This plasmid causes *E. coli* to produce GFP in the presence of arabinose.

TSM1

Experimental design of long-term evolution experiments (LTEE)

1) Let *E. coli* cultures grow for 12 hours
2) Measure OD_{600} to quantify cell growth
3) Measure fluorescence to quantify GFP production
4) Dilute 100-fold into fresh 96-well plate
5) Repeat ~30 times (15 days) to achieve ~200 *E. coli* generations

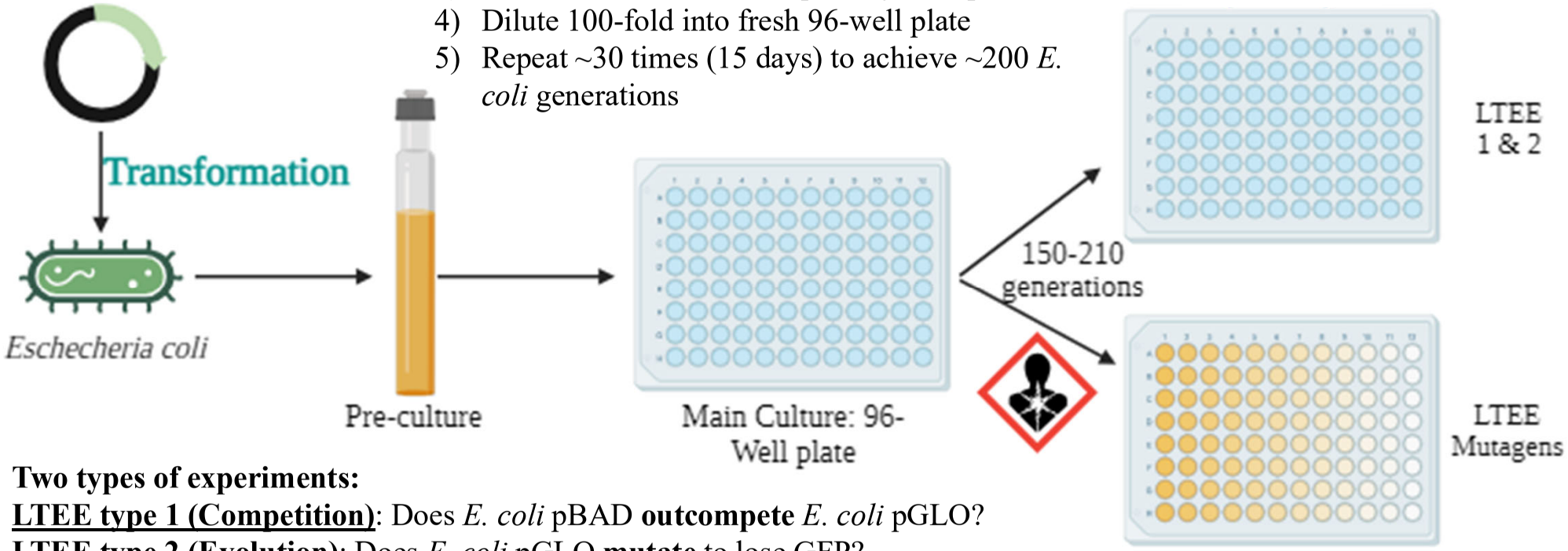

Two types of experiments:

LTEE type 1 (Competition): Does *E. coli* pBAD **outcompete** *E. coli* pGLO?

LTEE type 2 (Evolution): Does *E. coli* pGLO **mutate** to lose GFP?

Figure made with Biorender

TSM2

Competition: Does *E. coli* without *gfp* (pBAD) outcompete *E. coli* making a useless protein (pGLO)?

This is a measure of cellular GFP content

Note: the data are on a log scale

Experiment: Grow these two strains together in a 50/50 mixed culture

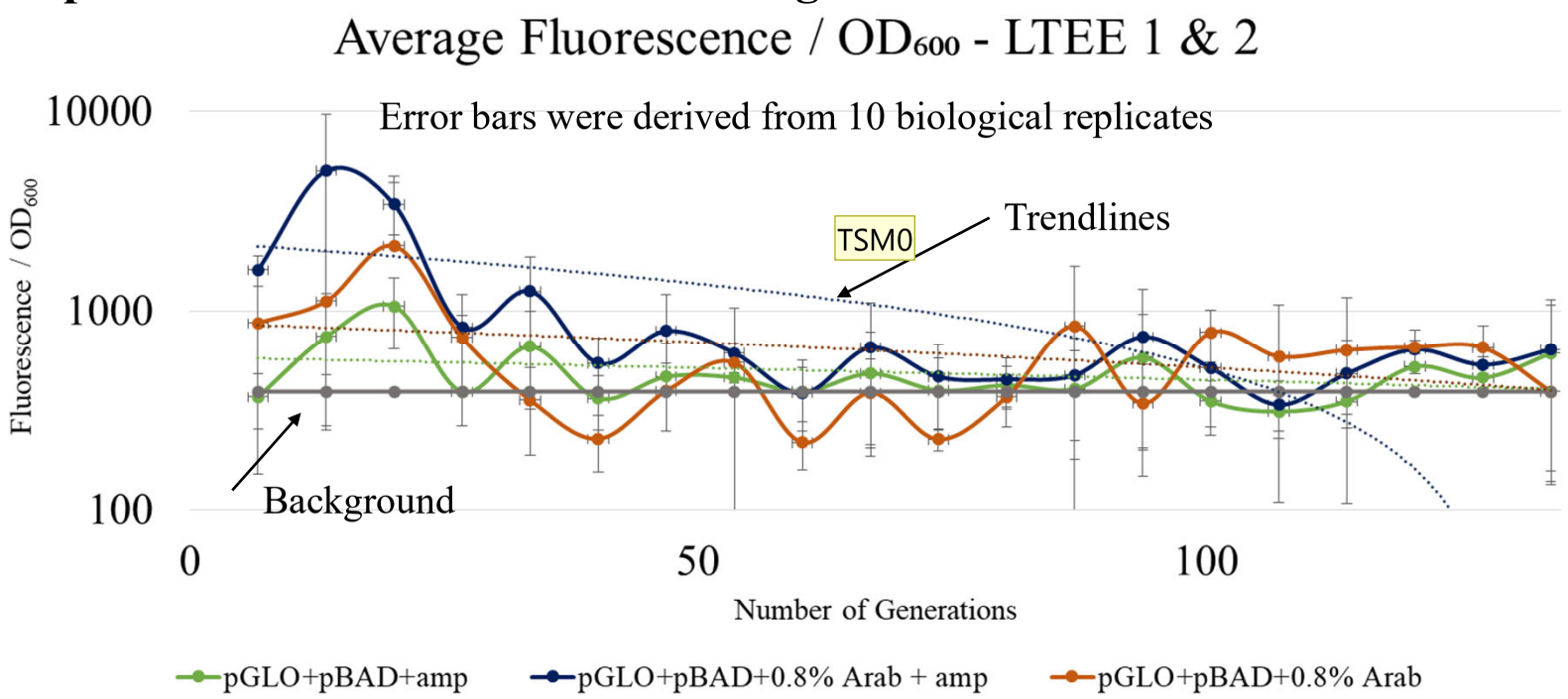

Observation: GFP signal trends downward in all three cases, indicating that *E. coli* pBAD indeed outcompetes *E. coli* pGLO.
Tentative translation to AR: pathogens with an unselected resistance gene will be outcompeted by those without resistance.
Technical limitation: Unexpected "oscillations" in the data, suspected to be due to condensation on lid of 96-well plate.

TSM4

Sanity Check of Pure Culture OD_{600} measurements

Data averaged over 155 generations per growth condition

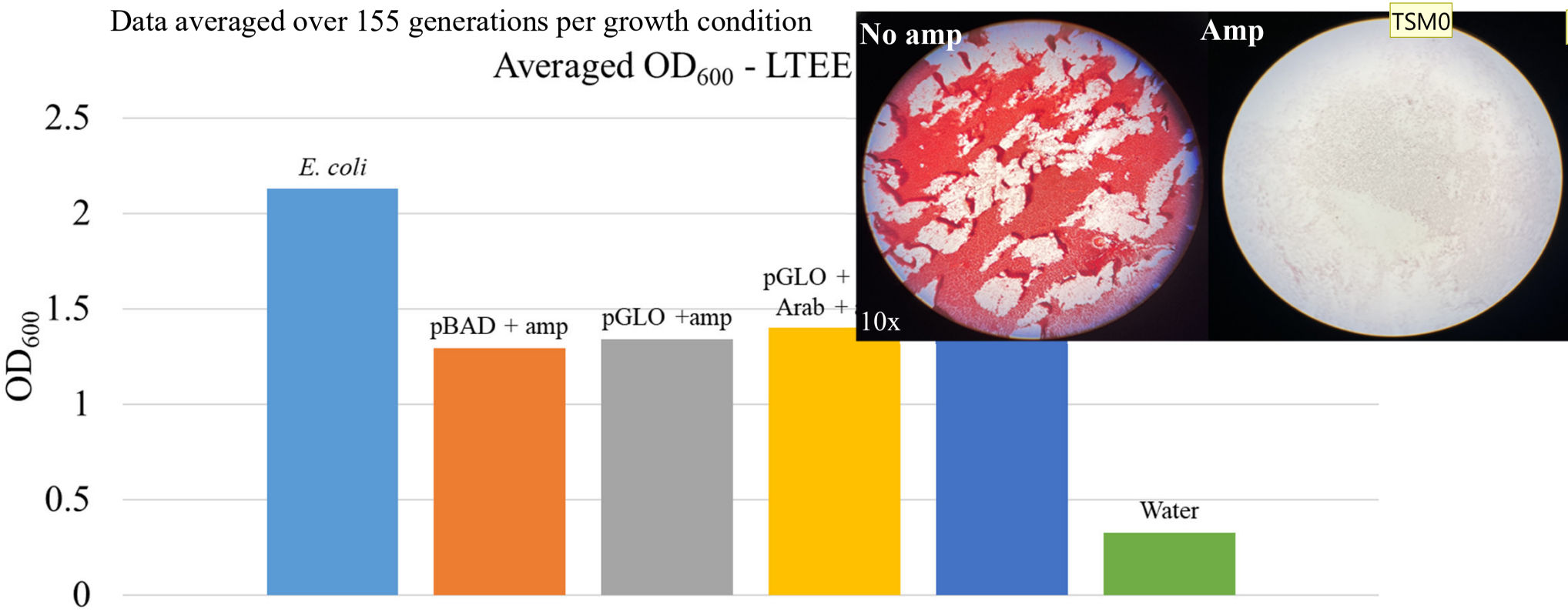

Expected result: All 5 culture conditions yield the same final OD_{600} after 12 hours of growth.
Observation: *E. coli* cultures without ampicillin reached a higher final OD_{600} than th HW5 with amp.
Possible explanation: Cultures without amp showed more cell clumping, which can increase light scattering.

Evolution: Does an *E. coli* strain lose *gfp* over time?

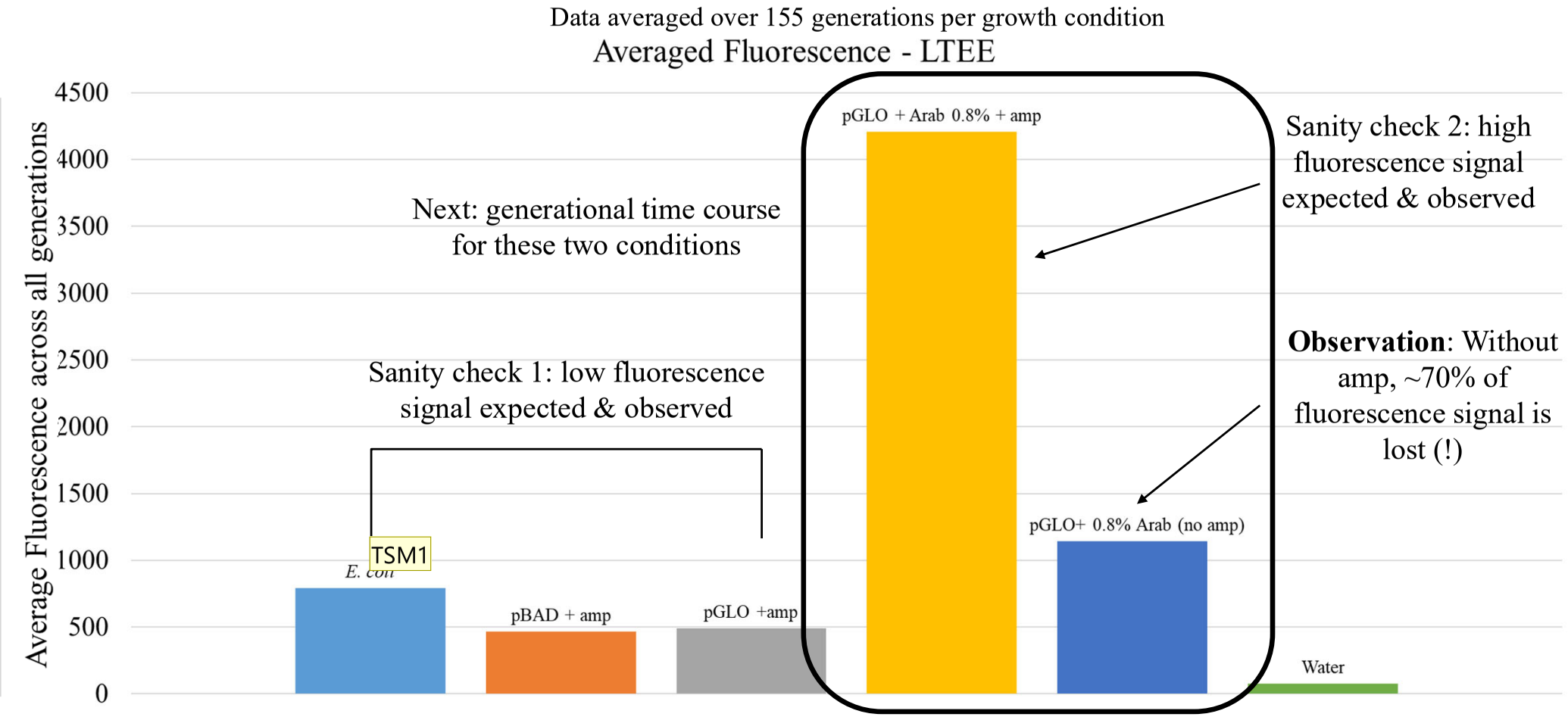

Tentative translation to AR: Plasmid-encoded AR may be lost quickly in the absence of antibiotic.

Evolution: Following the loss of *gfp* from *E. coli* over 160 generations

Note: the data are on a log scale

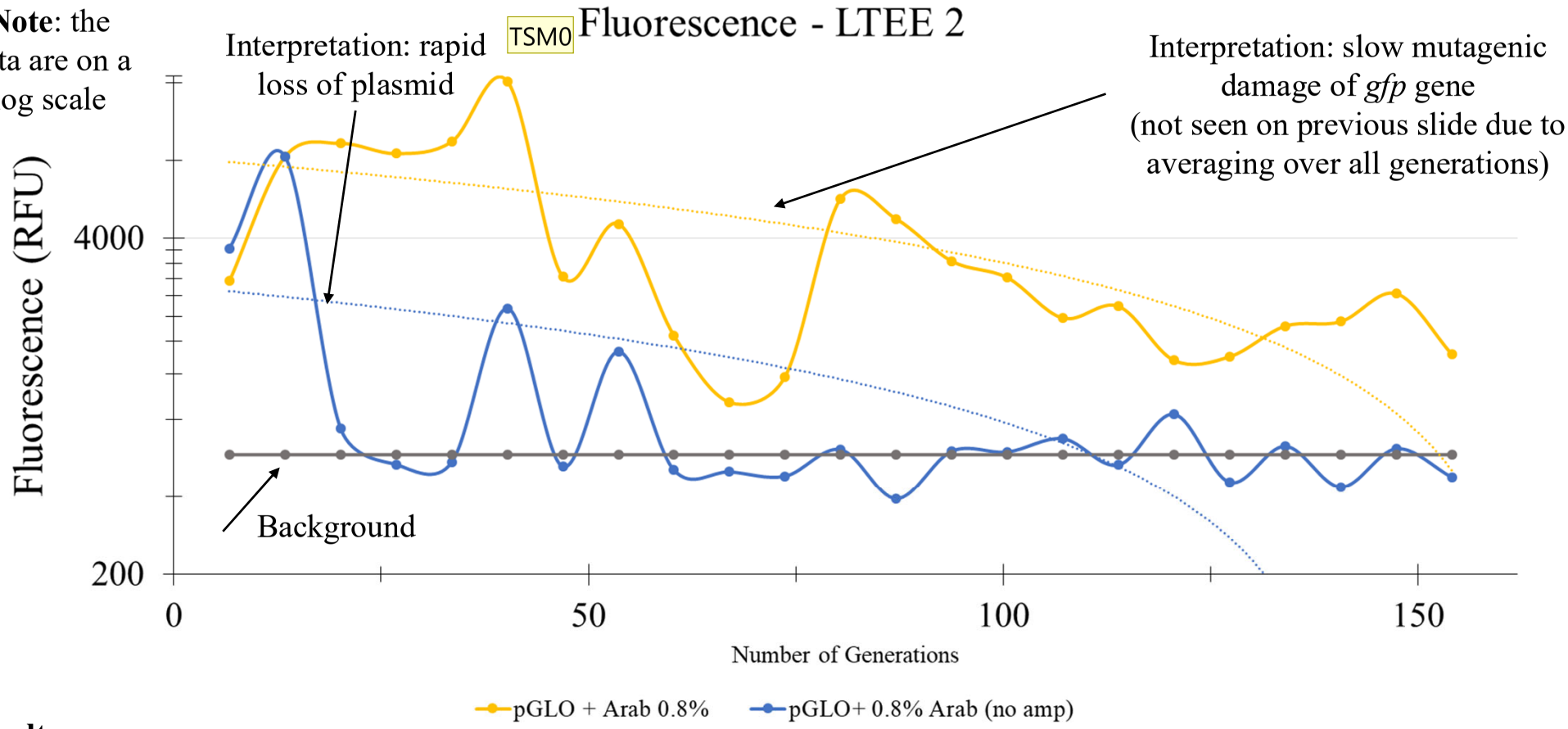

Results:

- Induced pGLO with amp appears to slowly lose the *gfp* gene, presumably due to damaging mutations. Same expected for AR.

Conclusions and Future Directions

We developed LTEE methods that allowed the detection of:

Competition:

- Strains without *gfp* outcompete strains with *gfp*.

Evolution

- In the absence of amp, *gfp* is lost rapidly (loss of plasmid?)
- In the presence of amp, we detect slow loss of *gfp* (damaging mutations?)

These results provide tentative initial support for a possible antibiotics rotation scheme to address AR resistance.

Future Directions

- Optimize methods to reduce noise and finalize the tentative conclusions presented here.
- Confirm loss of plasmids (plating on agar plates with amp) and damaging mutations in *gfp* gene (DNA sequencing).
- Apply this approach to AR and measure using plates with/without antibiotics rather than fluorescence.
- "Real life" test of approach: we predict that resistance against **discontinued** antibiotics is lost in human pathogens.

Acknowledgements

NIBLACK RESEARCH SCHOLARS

Many thanks to Dr. John Niblack and Mrs. Heidi Niblack

RESEARCH
COLLEGE OF ARTS AND SCIENCES

DEPARTMENT OF
MICROBIOLOGY AND
MOLECULAR GENETICS
College of Arts and Sciences

Sarah in full PPE gear to prepare mutagen solutions

Sarah and Rosalie

Sarah and Dr. Hoff

Many thanks to:

- Dr. Garry Marley
- Prof. Matthew Cabeen
- Prof. Avi Mitra
- Prof. Randy Morgenstein

Questions?

Investigating Mechanisms of Antibiotic Resistance in Microbes from Cystic Fibrosis Patients

Rebecca Wilson

Microbiology and Molecular Genetics
Faculty Sponsor: Dr. Erika Lutter
Graduate Student Mentor: Noopur Dasgupta

ABSTRACT

Cystic fibrosis (CF) is a lethal genetic disease, characterized by polymicrobial lung infections that are near impossible to treat due to the high level of antibiotic resistance of the pathogens. Though the multi-drug resistance of pathogens has been previously documented, the mechanisms for antibiotic resistance acquisition are still largely unknown. A prior screen of CF sputa identified the most resistant and multidrug-resistant bacterial candidates. This project aimed to identify the MICs and MBCs against antibiotics used in CF treatment at the time of sample collection for several bacterial isolates with subsequent genome sequencing to determine the genetic basis for their resistance mechanisms. Each isolate was tested in an MIC broth dilution assay with various concentrations of each antibiotic to determine the minimum amount needed to inhibit the growth of each isolate, then plated to determine the minimum concentration to kill the isolate. Genomic DNA was isolated and sequenced with the genomes assembled by external company, SeqCenter. With collaboration from a bioinformatics specialist, the assembled genomes were searched for genes known to confer resistance mechanisms to the antibiotics screened for. Results indicate that resistant microbes including *Staphylococcus aureus* and fungi are able to persist in CF lung despite aggressive antibiotic treatment.

1. Introduction

The lethal genetic disease, cystic fibrosis (CF), is caused by a failure of a chloride channel found in epithelial cells, the CF transmembrane conductance regulator (CFTR) (Gadsby, Vergani and Csanády, 2006). The eventual buildup of a thick mucus layer due to the dysfunctional CFTR becomes a favorable environment for bacterial, fungal, and viral colonization, which has negative impacts on the quality of life for patients (Kiedrowski and Bomberger, 2018). Even with intense antibiotic treatment, it is nearly impossible to clear the infection in CF lungs, which limits the treatment strategies for healthcare teams. One of the major reasons why infections are so difficult to treat is the high level of antibiotic resistance, and many times multi-drug resistance, of the pathogens. *Pseudomonas aeruginosa*, a common and deadly bacillus that colonizes the lungs of CF patients, is well-known for both its intrinsic and acquired antibiotic resistance (Banerjee and Stableforth, 2000). However, there are other bacteria and fungi within the CF lung that can also function as pathogens and

contribute to antibiotic resistance. The presence of bacteria like *Staphylococcus aureus* and *Burkholderia,* and fungi such as *Candida albicans* and *Aspergillus fumigatus* often colonize CF lungs (Magee et al., 2021).

Many of the bacteria found in the CF lung have both intrinsic and acquired resistance mechanisms, rendering the standard therapeutic regimens inadequate to fight repeated infection. There are several classes of antibiotics available for CF patients, each with a different mode of action and target in the bacterial cell. The most used antibiotics are extended-spectrum penicillins, fluoroquinolones, polymyxins, monobactams, aminoglycosides, and cephalosporins. The standard first line treatment is a combination of an aminoglycoside and a β-lactam (Banerjee and Stableforth, 2000).

There is growing evidence that available treatment strategies are unable to completely eradicate pathogens in the CF lungs, and that standard dosing schemes could increase the presence of antimicrobial resistance (AMR). For patients with chronic infection, treatment methods are suppressive rather than curative, relying on long-term use of antibiotics, which further increases the risk of AMR (Flume et al, 2018). This risk makes it vital that the correct concentration of antibiotics is administered.

The goal of this study was to characterize the level of antibiotic resistance of previously identified resistant microbes isolated from CF patients' sputa, then explore the genetic basis for their resistance via genome sequencing. Our hope is that by determining the MICs against clinically relevant antibiotics *in vitro,* treatment strategies for CF patients can be improved *in vivo.* Four antibiotics were selected based on the treatment regimens at the time of sample collection, 2013 and 2014.

Two extended-spectrum penicillins were chosen, Ticarcillin and Oxacillin, as penicillins are usually the initial antibiotic used to treat moderate-to-severe infections. These antibiotics are β-lactams, which prevent cross-linking of peptidoglycan in bacteria cell wall synthesis (Kapoor, Saigal and Elongavan, 2017). The third drug selected was Ciprofloxacin, part of the fluroquinolone class of antibiotics, which is believed to act by targeting DNA gyrase (topoisomerase II) and topoisomerase IV, which inhibits the DNA repair mechanisms in bacteria (Hurley and Smyth, 2012). The final drug selected was Polymyxin B Sulfate. Though there is high clinical efficacy, polymyxins are considered a last-line drug due to their neurotoxic and nephrotoxic effects. Polymyxins interact with the phospholipids of the bacterial cell membrane, damaging its integrity (Banerjee and Stableforth, 2000).

2. Experimental Details

CF patient sputa was previously collected in 2013 and 2014 from CF clinic at OU Children's Hospital in Oklahoma City and screened to identify microbes that had high levels of antibiotic resistance to any of the chosen antibiotics, resulting in twelve clinical isolates. Pathogens commonly found in CF lungs are known to be multi-drug resistant (MDR)

(George, Jones, and Middleton, 2009*),* hence for each isolate, we wanted to characterize the level of antibiotic resistance against clinically relevant antibiotics. The antibiotics used were Ciprofloxacin, Polymyxin B Sulfate, Oxacillin and Ticarcillin.

Identities of the isolates were kept hidden until later stages of the study to ensure minimal bias. The twelve isolates were removed from -80°C cryostorage and streaked onto a Luria Broth (LB) agar plate, using Fisher BioReagents™ Microbiology Media: LB Broth, Miller, as well as IBI™ Scientific Agar. Plates were incubated at 37°C for 24 h. Then a colony was scraped off each plate and transferred to LB broth, and cultures were grown overnight at 37°C in an incubator shaker.

Resistance of each strain to the chosen antibiotics was characterized by the Minimum Inhibitory Concentration (MIC) assay. MICs were determined using a microdilution method in 96-well microtiter plates. With LB broth as a reference, samples were normalized to an optical density of 0.06 when read at 600 nm with an Eppendorf BioSpectrometer® basic (Eppendorf North America, Enfield, CT, USA). Decreasing concentrations of each antibiotic were added to wells with Mueller Hinton broth (MHB) and the suspension with the bacterial isolates; the methodology is shown in Figure 1. All experiments were set up in triplicate and repeated three times. The positive control was wells with bacteria and MHB, while the negative control contained the antibiotic used and MHB. Following 24 h growth at 37°C, MICs, which represented the lowest concentration of each antibiotic that was required to inhibit visible growth, were obtained (Rodríguez-Melcón et al., 2021).

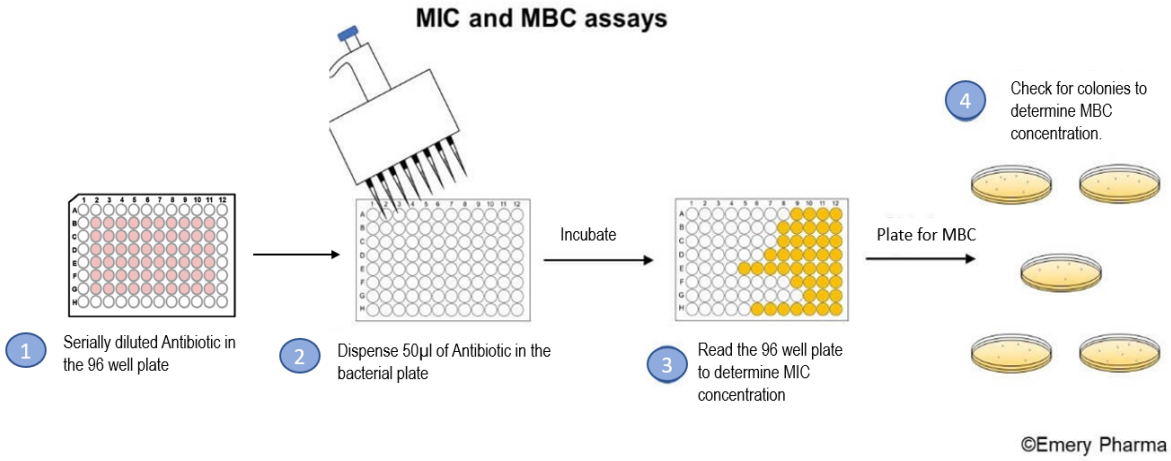

Figure 1: MIC and MBC Assay Methodology. Decreased concentrations of each antibiotic were added to wells with MHB and bacteria, then allowed to incubate overnight at 37°C. MICs were recorded as the lowest concentration that yielded visible growth, then MBCs were determined after stamping onto an MHB plate. Adapted from ©Emery Pharma.

Once MICs were recorded, the contents of the microtiter plate were used to determine the minimum bactericidal concentration (MBC). This value represents the minimum

concentration of antibiotic necessary to visibly inactivate more than 99.99% of the bacteria present on a MHB plate (Rodríguez-Melcón et al., 2021). Each well from the 96-well plate was stamped onto MHB plate using a 48-pin replica plating stamper, shown in Figure 1. After 24 h of incubation at 37°C, the MBC was recorded. The lowest concentration that displayed no growth, an example given in Figure 2, was recorded as the MBC value (Hasanin et al., 2021).

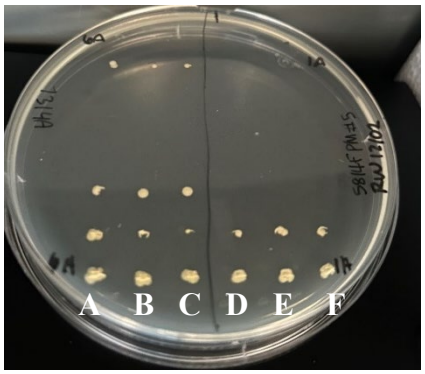

Figure 2: Visual MBC Plate. A-C=7314A, D-F=5814F PM#5.

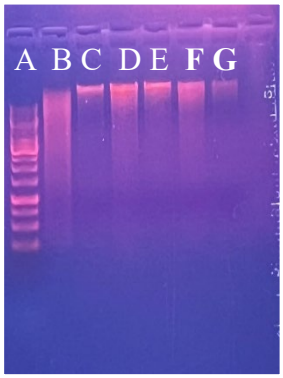

Figure 3: Agarose gel electrophoresis confirming the presence and integrity of isolated genomic DNA. A=1 kb DNA ladder, B=6514A, C=7314A, D=3614A, E=3614C#21, F=5814F PM#5, G=3614C#17

Total genomic DNA from all strains were obtained using a ZR Fungal/Bacterial DNA Miniprep™ Kit (Zymo Research Corporation, Irvine, CA, USA). To ensure sufficient concentration and purity, the DNA was checked on a NanoDrop™ One^{C} Microvolume UV-Vis Spectrophotometer. (Thermo Fisher Scientific, Waltham, MA, USA). Using a 0.8% gel with 1X TEA, we performed gel electrophoresis with a 1kb ladder for comparison to further confirm the integrity and amount of DNA, shown in Figure 3. The extracted DNA of the twelve strains was sent to the external company, SeqCenter (Pittsburg, PA, USA), for sequencing. Upon receiving the genetic information, we collaborated with a bioinformatics specialist to confirm the presence of key genes that have been shown to confer antibiotic resistance in the bacterial isolates.

Isolating the plasmids from each sample was attempted using a ZR Plasmid Miniprep™-Classic Kit (Zymo Research Corporation, Irvine, CA, USA), but plasmids were not detected when checked on a 0.8% agarose gel. We then used a combination of 2X Cracking Buffer (1 M Tris-HCl, 20% SDS, 0.5M EDTA, sucrose) and lysozyme to breakdown the bacterial cell wall to allow for extraction of plasmids. However, bacterial plasmids were still not detected.

3. Results

MICs and MBCs were determined to establish the multi-drug nature of the pathogens found in the lungs of the CF patients. As seen in Table 1, the twelve isolates were found to have different resistance profiles. According to the 2021 Performance Standards for Antimicrobial Susceptibility Testing, the MIC breakpoint for *S. aureus* resistance against Ciprofloxacin is ≥4µg/mL. Isolates 5814F PM#1, 5814F PM#5, 61214B#2, 61214B, 6514A, 7314A, 8714C had MIC values above the breakpoint, and so are classified as resistant (Weinstein and Clinical and Laboratory Standards Institute, 2021). For Oxacillin, the *S. aureus* MIC breakpoint is ≥4µg/mL, and isolates 5814F PM#1, 5814F PM#5, 61214B#2, 61214B, 6514A, 7314A, 8714C have MICs above this value, meaning they are resistant to Oxacillin. *S. aureus* MIC breakpoint for Ticarcillin is ≥128µg/mL. Based upon our findings, isolates 5814F PM#1, 5814F PM#5, 61214B#2, 61214B, 6514A, 7314A, 8714C are classified as resistant.

Isolates 3614A, 3614C#17, 3614C#21, 5813E and 5814B were found to be mixed or fungal cultures (Table 2), so their antibiotic resistance cannot be attributed to one organism. Therefore, the discussion will focus on only the pure isolates.

Table 1: MIC and MBC values for clinical isolates.

Strain ID #	Antibiotics							
	CIPR		OXA		PM B		TIC	
	MIC	MBC	MIC	MBC	MIC	MBC	MIC	MBC
61214B	0.56	1.125	1	0.5-1	0.03125-0.0625	0.0625	2	2
5813E	9	9	>8	>8	>2	0.25	>32	>32
8714C	4.5-9	1.125-2.25	0.5-1	0.25-0.5	0.125	0.0625-0.125	2	2
6514A	2.25-4.5	1.125-2.25	1	0.5-1	0.0625-0.125	0.125	2	2
3614A	4.5-9	0.28-0.56	8	>8	0.125-0.25	0.125-0.25	>32	>32
5814B	9-18	9-18	>8	>8	>2	0.0625	>32	>32
3614C#17	2.25-4.5	4.5	>8	>8	0.03125	0.03125	>32	>32
3614C#21	4.5-9	4.5-9	>8	>8	<0.015625	<0.015625	>32	>32
5814F PM#1	0.28	0.28-0.56	1	1	0.0625-0.125	0.0625-0.125	2	2
5814F PM#5	0.14-0.28	0.56-1.125	1	1	0.0625-0.125	0.0625-0.125	2	2
7314A	0.14-0.28	0.56-1.125	0.25	0.25	0.0625-0.125	0.03125-0.0625	2	1-2
61214B#2	0.56-1.125	0.56-2.25	1	0.5	0.0625	0.0625-0.125	2	2

CIP=Ciprofloxacin, OXA=Oxacillin, PM B= Polymyxin B, TIC=Ticarcillin. Values reported in mg/mL.

As seen in Table 2, collaboration with the bioinformatics specialist yielded a full genome analysis, identifying the species present in the samples. Seven of the twelve samples were identified as pure *S. aureus* species, and two were mixed cultures. Three of the isolates contained fungal species: *Trichosporon asahii* and *Candida albicans*.

Table 2: Identity of the clinical isolates.

Sample ID	**Identity**
3614A	MIXED: *P. aeruginosa* & *Enterococcus faecium*
3614C#17	Minor contamination: *Trichosporon asahii*
3614C#21	*Trichosporon asahii*
5813E	Minor contamination: *Candida albicans*
5814B	MIXED: *Mesobacillus* sp. nov., *Candida albicans*, *+more?*
5814F PM#1	*Staphylococcus aureus*
5814F PM#5	*Staphylococcus aureus*
61214B#2	*Staphylococcus aureus*
61214B	*Staphylococcus aureus*
6514A	*Staphylococcus aureus*
7314A	*Staphylococcus aureus*
8714C	*Staphylococcus aureus*

After discovering the identities of the isolates, the genome sequences of the *S. aureus* isolates were run against The Comprehensive Antibiotic Resistance Database (CARD) Resistance Gene Identifier to extract AMR genes. Genes that were found to be common between the seven isolates are shown in Table 3 and the unique genes for each isolate are shown in Table 4. Genes classified as perfect were an identical match to a gene in the CARD database, and those labeled as strict matched a gene in the database so strongly that it was considered functional. Eight perfect matches were found to be common between the seven *S. aureus* isolates, and nine strict matches were identified.

Table 3: Common AMR genes between all *S. aureus* genomes.

AMR Genes	
Perfect	*ANT(9)-la, arlR, arlS, ErmA, mecI, mepR, sdrM, Staphylococcus aureus FosB*
Strict	*ANT(4')-la, kdpD, mecA, norC, sepA, Staphylococcus aureus gyrA* conferring resistance to fluoroquinolones*, Staphylococcus aureus LmrS, Staphylococcus aureus parC* conferring resistance to fluoroquinolones*, vanT gene* in *vanG* cluster

Table 4: Unique AMR genes for *S. aureus* isolates.

Genes		Isolates
Perfect	*APH(3')-IIIa*	5814F PM#1, 5814F PM#5
	mecR1	5814F PM#1, 5814F PM#5, 61214B, 61214B#2, 7314A, 8714C
	mgrA	5814F PM#1, 5814F PM#5, 61214B, 61214B#2 6514A, 7314A
	Staphylococcus aureus norA	5814FPM#1, 5814FPM#5, 61214B, 61214B#2, 6514A, 7314A
	tet(K)	5814F PM#1, 5814F PM#5
Strict	*SAT-4*	5814F PM#1, 5814F PM#5
	Staphylococcus aureus mupA conferring resistance to mupirocin	5814F PM#1, 5814F PM#5
	mecR1	6514A
	PC1 beta-lactamase (blaZ)	7314A
	mgrA	8714C
	Staphylococcus aureus parC conferring resistance to fluoroquinolones	8714C

4. Discussion and Conclusions

The MIC and MBC values described in Figure 1 confirm AMR in the microbes isolated from CF patient lungs, consistent with previous findings (Flume et al., 2018). The antibiotics chosen were selected based on the treatment regimens used on patients at the time of collection. The resistance levels for Polymyxin B Sulfate are not clinically relevant, as Polymyxin B Sulfate is effective against gram-negative bacteria and the *S. aureus* isolates are gram-positive.

Genome analysis revealed that at the time of our sample collection in 2013 and 2014, antibiotic resistant *S. aureus* was present in the patients' lungs. Studies have found that *P. aeruginosa* is one of the most prevalent bacteria found in CF lungs, but after screening for the bacteria most resistant to our selected antibiotics, this pathogen did not appear (Perikleous et al., 2023). The antibiotics selected for use in this study were the common treatments at the time of sample collection, 2013 and 2014, and the absence of *P. aeruginosa* indicates that if *P. aeruginosa* was present in the patients' lungs, it was not resistant to the antibiotics in question. Other species of bacteria and fungi are able to develop AMR to these treatments, persist in the lungs, and be identified in our samples.

S. aureus has often been resistant to common antimicrobials, including fluroquinolones, and are considered to be resistant to all β-lactams, such as Ticarcillin and Oxacillin (Lee, 2003). This is confirmed by the results of this study, which found that the *S. aureus* isolates were resistant against Oxacillin, Ticarcillin and Ciprofloxacin. The *S. aureus* isolates, particularly 5814F PM#5 and 5814F PM#1, possessed high numbers of AMR genes, but we do not yet know if these genes are functional or expressed. Future directions are to explore if these genes are active or inactive within these organisms.

Consistently, the mixed and fungal strains had higher MIC and MBC values compared to the S. *aureus* isolates. Antibiotics do not affect fungal species, which could account for the increased resistance seen in isolates 3614C#21, 3614C#17 and 5813E. The presence of *Trichosporon asahii* is of particular significance, as it is a newly recognized pathogen that has a propensity for CF patients (Hickey et al., 2009). To better characterize and explore treatment strategies for these fungal species, it is recommended that these isolates be tested with antifungals such as amphotericin B or fluconazole.

5. Summary

This study aimed to characterize the resistance of microbes isolated from CF patient lungs. We determined the MIC and MBC values for Ciprofloxacin, Oxacillin, Ticarcillin and Polymyxin B Sulfate and found that the *S. aureus* isolates were resistant to all antibiotic tests. Genomic analysis identified seven of the twelve isolates as *S. aureus,* one as *T. asahii,* and the other four were mixed cultures. Genome analysis using the CARD database to extract AMR genes identified many AMR genes in *S. aureus*. Information gathered from further genome analysis will aim to correlate the AMR genes to phenotypes, with the final goal of publishing resource announcements for the *S. aureus* isolates and the *T*. *asahii* isolate.

6. Appendices

6a. Acknowledgements

Thank you to Dr. and Mrs. Niblack for their support in funding this research project. I would also like to thank Dr. Chelsea Murphy for her assistance with the bioinformatics analysis. Finally, I would like to thank Dr. Erika Lutter and Noopur Dasgupta for their guidance, teaching, and encouragement as I learned new skills.

6b. Paper Published

Poster presentations:

Rebecca Wilson, Noopur Dasgupta, Erika Lutter, Understanding Antibiotic Resistance in Cystic Fibrosis Patients. OSU Spring Undergraduate Research Symposium. **Poster**. April 2023.

Rebecca Wilson, Noopur Dasgupta, Erika Lutter, Understanding Antibiotic Resistance in Cystic Fibrosis Patients. 2023 Undergraduate Summer Research Expo. **Poster**. August 2023.

6c. Literature Cited

Banerjee, D. and Stableforth, D. (2000). The treatment of respiratory pseudomonas infection in cystic fibrosis: what drug and which way? *Drugs*, [online] 60(5), pp.1053–1064. doi:https://doi.org/10.2165/00003495-200060050-00006.

Flume, P.A., Waters, V.J., Bell, S.C., Van Devanter, D.R. and Stuart Elborn, J. (2018). Antimicrobial resistance in cystic fibrosis: Does it matter? *Journal of Cystic Fibrosis*, 17(6), pp.687–689. doi:https://doi.org/10.1016/j.jcf.2018.08.015.

Gadsby, D. C., Vergani, P., & Csanády, L. (2006). The ABC protein turned chloride channel whose failure causes cystic fibrosis. *Nature,* [online] 440(7083), pp. 477–483. doi:https://doi.org/10.1038/nature04712.

George, A.M., Jones, P.M. and Middleton, P.G. (2009). Cystic fibrosis infections: treatment strategies and prospects. *FEMS Microbiology Letters*, [online] 300(2), pp.153–164. doi:https://doi.org/10.1111/j.1574-6968.2009.01704.x.

Hasanin, M.S., Abdelraof, M., Fikry, M., Shaker, Y.M., Sweed, A.M.K. and Senge, M.O. (2021). Development of Antimicrobial Laser-Induced Photodynamic Therapy Based on Ethylcellulose/Chitosan Nanocomposite with 5,10,15,20-Tetrakis(m-Hydroxyphenyl)porphyrin. *Molecules*, 26(12), p.3551. doi:https://doi.org/10.3390/molecules26123551.

Hickey, P.W., Sutton, D.A., Fothergill, A.W., Rinaldi, M.G., Wickes, B.L., Schmidt, H.J. and Walsh, T.J. (2009). Trichosporon mycotoxinivorans, a Novel Respiratory Pathogen in Patients with Cystic Fibrosis. *Journal of Clinical Microbiology*, [online] 47(10), pp.3091–3097. doi:https://doi.org/10.1128/JCM.00460-09.

Hurley, M. and Smyth, A. (2012). Fluoroquinolones in the treatment of bronchopulmonary disease in cystic fibrosis. *Therapeutic Advances in Respiratory Disease*, 6(6), pp.363–373. doi:https://doi.org/10.1177/1753465812459899.

Kapoor, G., Saigal, S. and Elongavan, A. (2017). Action and Resistance Mechanisms of antibiotics: a Guide for Clinicians. *Journal of Anaesthesiology Clinical Pharmacology*, [online] 33(3), p.300. doi:https://doi.org/10.4103/joacp.joacp_349_15.

Kiedrowski, M.R. and Bomberger, J.M. (2018). Viral-Bacterial Co-infections in the Cystic Fibrosis Respiratory Tract. *Frontiers in Immunology*, [online] 9. doi:https://doi.org/10.3389/fimmu.2018.03067.

Lee, J.H. (2003). Methicillin (Oxacillin)-Resistant Staphylococcus aureus Strains Isolated from Major Food Animals and Their Potential Transmission to Humans. *Applied and Environmental Microbiology*, 69(11), pp.6489–6494. doi:https://doi.org/10.1128/aem.69.11.6489-6494.2003.

Magee, L.C., Louis, M., Khan, V., Micalo, L. and Chaudary, N. (2021). Managing Fungal Infections in Cystic Fibrosis Patients: Challenges in Clinical Practice. *Infection and Drug Resistance,* [online] 14, pp.1141–1153. doi:https://doi.org/10.2147/IDR.S267219.

Perikleous, E.P., Gkentzi, D., Bertzouanis, A., Paraskakis, E., Sovtic, A. and Fouzas, S. (2023). Antibiotic Resistance in Patients with Cystic Fibrosis: Past, Present, and Future. *Antibiotics*, 12(2), p.217. doi:https://doi.org/10.3390/antibiotics12020217.

Rodríguez-Melcón, C., Alonso-Calleja, C., García-Fernández, C., Carballo, J. and Capita, R. (2021). Minimum Inhibitory Concentration (MIC) and Minimum Bactericidal Concentration (MBC) for Twelve Antimicrobials (Biocides and Antibiotics) in Eight Strains of Listeria monocytogenes. *Biology*, 11(1), p.46. doi:https://doi.org/10.3390/biology11010046.

Weinstein, M.P. and Clinical And Laboratory Standards Institute (2021). *Performance standards for antimicrobial susceptibility testing*. Clinical And Laboratory Standards Institute.

Understanding Antibiotic Resistance In Cystic Fibrosis Patients

Rebecca Wilson

Microbiology and Molecular Genetics

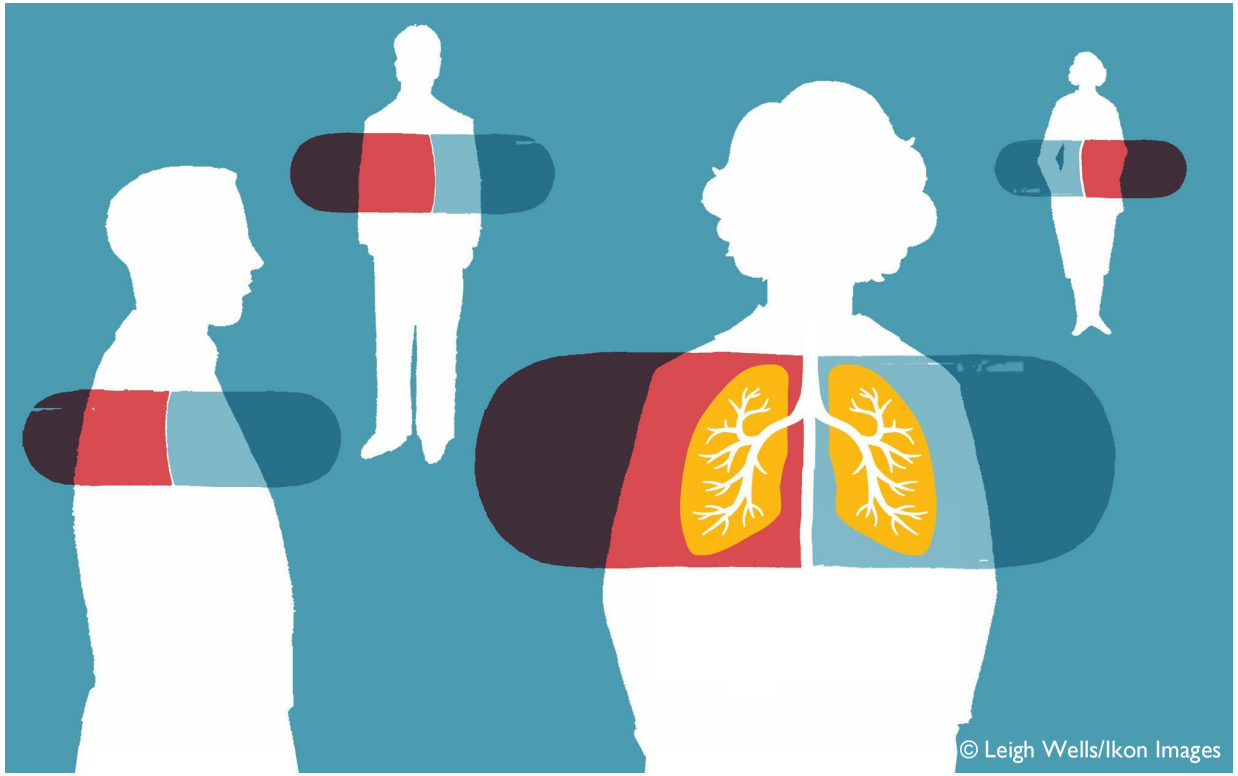

THE PROBLEM:

CYSTIC FIBROSIS

- The most common lethal inherited disorder affecting Caucasians (1/2500)
- Mutations in the CF transmembrane conductance regulator gene (*cftr)*
  - Decreased chloride secretion into airways, increased sodium absorption from airways
- Dehydration of airway mucous- reduced clearance, mucous retention, chronic infection (George, Jones and Middleton, 2009).

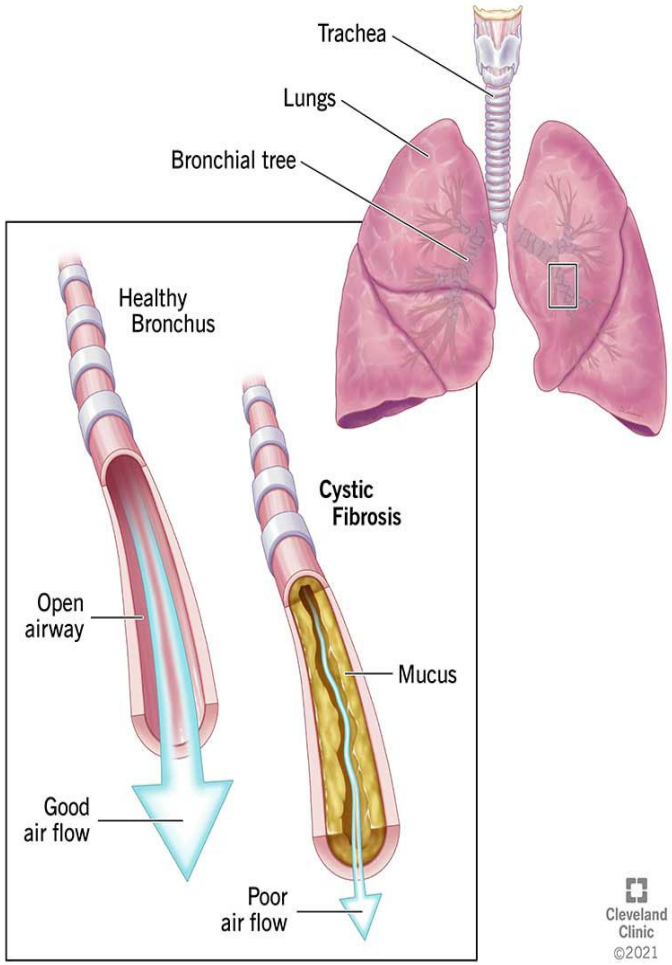

BACTERIAL INFECTIONS

- Repeated infection, lower airway inflammation, tissue damage
- *Pseudomonas aeruginosa* and *Staphylococcus aureus*
- Progressively more diverse, uncommon, and difficult to treat (Perikleous et al., 2023).

CURRENT SOLUTION: ANTIBIOTICS

- Systemically (oral or parenteral), inhalation
- Many classes and mechanisms of action
- Evidence suggests available therapies not adequate – standard dosing strategies suppressive rather than curative (Flume et al, 2018).
- Long term use of antibiotics increases risk of antibiotic resistance

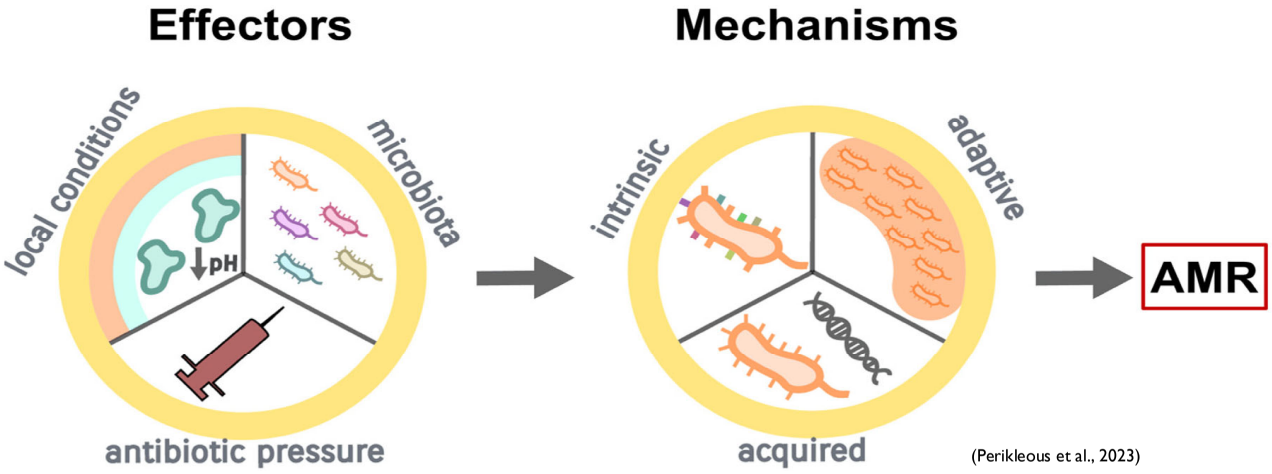

(Perikleous et al., 2023)

OUR GOAL

Characterize the antibiotic resistant nature of bacteria isolated from the lungs of CF patients

- MIC and MBC

Key antimicrobial (AMR) genes

- Isolate genomic DNA
- Genetic basis for resistance

More informed and effective antibiotic use

THE SAMPLES

- Sputa from CF patients from CF clinic (OU Children's Hospital in OKC)
  - 2013-2014
- Screened for most resistant microbes
  - Twelve isolates chosen

THE ANTIBIOTICS

Ticarcillin and Oxacillin
Extended-spectrum penicillins
β-lactams
Ciprofloxacin
Fluroquinolone
Polymyxin B Sulfate
Polymyxin

METHODS

Determining Resistance

Isolating DNA

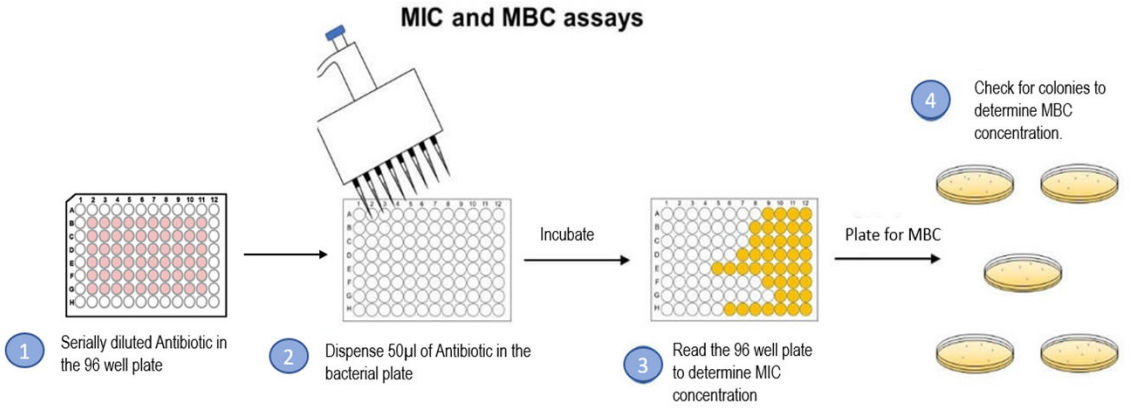

MIC and MBC Assay Methodology.

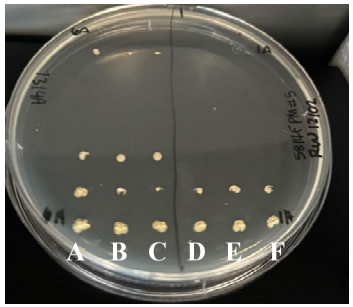

MBC Plate. A-C=7314A, D-F=5814F PM#5.

ZR Fungal/Bacterial DNA Miniprep™ Kit

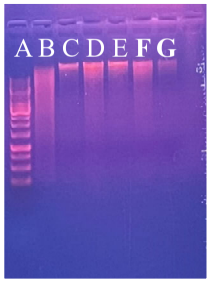

Agarose gel electrophoresis of genomic DNA

A=1 kb DNA ladder, B=6514A, C=7314A, D=3614A, E=3614C#21, F=5814F PM#5, G=3614C#17

Results

Strain ID #	Antibiotics							
	CIPR		OXA		PM B		TIC	
	MIC	MBC	MIC	MBC	MIC	MBC	MIC	MBC
61214B	0.56	1.125	1	0.5-1	0.03125-0.0625	0.0625	2	2
5813E	9	9	>8	>8	>2	0.25	>32	>32
8714C	4.5-9	1.125-2.25	0.5-1	0.25-0.5	0.125	0.0625-0.125	2	2
6514A	2.25-4.5	1.125-2.25	1	0.5-1	0.0625-0.125	0.125	2	2
3614A	4.5-9	0.28-0.56	8	>8	0.125-0.25	0.125-0.25	>32	>32
5814B	9-18	9-18	>8	>8	>2	0.0625	>32	>32
3614C#17	2.25-4.5	4.5	>8	>8	0.03125	0.03125	>32	>32
3614C#21	4.5-9	4.5-9	>8	>8	<0.015625	<0.015625	>32	>32
5814F PM#1	0.28	0.28-0.56	1	1	0.0625-0.125	0.0625-0.125	2	2
5814F PM#5	0.14-0.28	0.56-1.125	1	1	0.0625-0.125	0.0625-0.125	2	2
7314A	0.14-0.28	0.56-1.125	0.25	0.25	0.0625-0.125	0.03125-0.0625	2	1-2
61214B#2	0.56-1.125	0.56-2.25	1	0.5	0.0625	0.0625-0.125	2	2

Clinical MIC Breakpoints:

- **Ciprofloxacin:** ≥4µg/mL

(5814F PM#1, 5814F PM#5, 61214B#2, 61214B, 6514A, 7314A, 8714C)

- **Oxacillin**: ≥4µg/mL

(5814F PM#1, 5814F PM#5, 61214B#2, 61214B, 6514A, 7314A, 8714C)

- **Ticarcillin:** ≥128µg/mL

(5814F PM#1, 5814F PM#5, 61214B#2, 61214B, 6514A, 7314A, 8714C)

- **Polymyxin B Sulfate:** not clinically relevant

(2021 Performance Standards for Antimicrobial Susceptibility Testing)

Genomic Analysis - Identification

Sample ID	Identity
3614A	MIXED: *P. aeruginosa* & *Enterococcus faecium*
3614C#17	Minor contamination: *Trichosporon asahii*
3614C#21	*Trichosporon asahii*
5813E	Minor contamination: *Candida albicans*
5814B	MIXED: *Mesobacillus* sp. nov., *Candida albicans*, +more?
5814F PM#1	*Staphylococcus aureus*
5814F PM#5	*Staphylococcus aureus*
61214B#2	*Staphylococcus aureus*
61214B	*Staphylococcus aureus*
6514A	*Staphylococcus aureus*
7314A	*Staphylococcus aureus*
8714C	*Staphylococcus aureus*

- Fungi
- Mixed samples
- *Staphylococcus aureus*

Polymyxin B Sulfate?

effective against gram-negative bacteria

Genomic Analysis – Common AMR Genes

	AMR Gene	Resistance Mechanism
Perfect	*ANT(9)-Ia*	antibiotic efflux
	arlR	antibiotic target alteration
	arlS	antibiotic target replacement
	ErmA	antibiotic target alteration
	mecI	antibiotic target replacement
	mepR	antibiotic efflux
	sdrM	antibiotic efflux
	Staphylococcus aureus FosB	antibiotic inactivation
Strict	*ANT(4')-Ia*	antibiotic efflux
	kdpD	antibiotic inactivation
	mecA	antibiotic target alteration
	norC	antibiotic target alteration
	sepA	antibiotic efflux
	Staphylococcus aureus gyrA conferring resistance to fluoroquinolones	antibiotic target alteration
	Staphylococcus aureus LmrS	antibiotic efflux
	Staphylococcus aureus parC conferring resistance to fluoroquinolones	antibiotic target alteration
	vanT gene in *vanG* cluster	antibiotic target alteration

- **Perfect**=an identical match to a gene in the CARD database
- **Strict**=matched a gene in the database so strongly that it was considered functional.

Genomic Analysis – Unique AMR Genes

	AMR Genes	Resistance Mechanisms	Isolates
Perfect	*APH(3')-IIIa*	antibiotic inactivation	5814F PM#1, 5814F PM#5
	mecR1	antibiotic target replacement	5814F PM#1, 5814F PM#5, 61214B, 61214B#2, 7314A, 8714C
	mgrA	antibiotic efflux	5814F PM#1, 5814F PM#5, 61214B, 61214B#2 6514A, 7314A
	Staphylococcus aureus norA	antibiotic efflux	5814FPM#1, 5814FPM#5, 61214B, 61214B#2, 6514A, 7314A
	tet(K)	antibiotic efflux	5814F PM#1, 5814F PM#5
Strict	*SAT-4*	antibiotic inactivation	5814F PM#1, 5814F PM#5
	Staphylococcus aureus mupA conferring resistance to mupirocin	antibiotic target alteration	5814F PM#1, 5814F PM#5
	mecR1	antibiotic target replacement	6514A
	PC1 beta-lactamase (*blaZ*)	antibiotic inactivation	7314A
	mgrA	antibiotic efflux	8714C
	Staphylococcus aureus parC conferring resistance to fluoroquinolones	antibiotic target alteration	8714C

CONCLUSIONS

- **Ciprofloxacin** MIC values for isolates 5814F PM#1, 5814F PM#5, 61214B#2, 61214B, 6514A 7314A, 8714C were above the breakpoint – resistant
- **Oxacillin** MIC values for isolates 5814F PM#1, 5814F PM#5, 61214B#2, 61214B, 6514A, 7314A, 8714C were above breakpoint – resistant
- **Ticarcillin** MIC values for isolates 5814F PM#1, 5814F PM#5, 61214B#2, 61214B, 6514A, 7314A, 8714C were above breakpoint – resistant
- **Polymyxin B Sulfate** MIC values not clinically relevant
- After whole genome sequencing, six isolates were identified as *S. aureus*

WHY IS THIS IMPORTANT?

- 2013-2014, antibiotic resistance *S. aureus* present in patients' lungs
  - What about *P. aeruginosa?*
- *S. aureus* isolates possessed high number of AMR genes
  - Especially 5814F PM#1 and 5814F PM#5
- Are these genes functional or expressed?
  - Genomics does not necessarily give the full story

FUTURE DIRECTIONS

Genome Announcements (2)

- *S. aureus* AMR genes and phenotypes *T. asahii* isolated form cystic CF patient
- *T. asahii* isolated form cystic CF patient

CONCLUSIONS

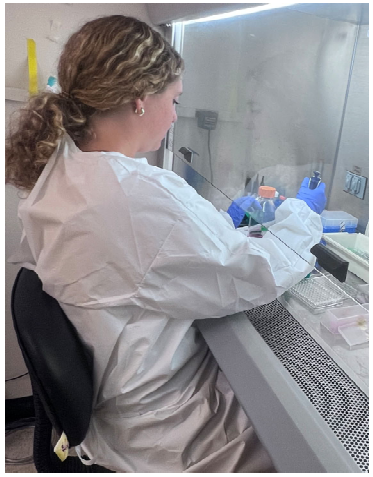

- Lots of trial and error
  - Troubleshooting
- Perseverance
- Attitude of curiosity

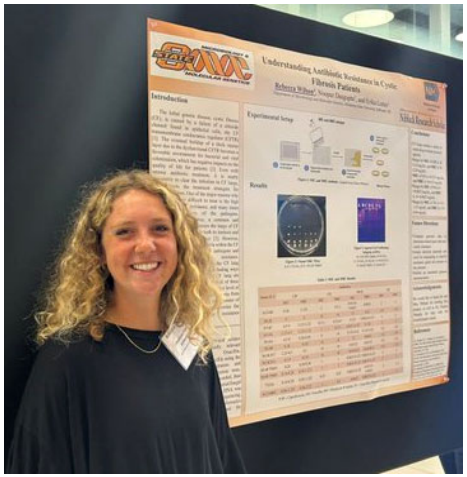

- Technical skills
- Communication
- Professionalism

- Appreciation for medicines
- Future career as physician
- Network and team of individuals

THANK YOU

- **Dr. and Mrs. Niblack**
- VPR Office
- Dr. Erika Lutter
- Dr. Chelsea Murphy
- Noopur Dasgupta

SOURCES

Perikleous, E.P., Gkentzi, D., Bertzouanis, A., Paraskakis, E., Sovtic, A. and Fouzas, S. (2023). Antibiotic Resistance in Patients with Cystic Fibrosis: Past, Present, and Future. *Antibiotics*, 12(2), p.217. doi:https://doi.org/10.3390/antibiotics12020217.

Flume, P.A., Waters, V.J., Bell, S.C., Van Devanter, D.R. and Stuart Elborn, J. (2018). Antimicrobial resistance in cystic fibrosis: Does it matter? *Journal of Cystic Fibrosis*, 17(6), pp.687–689. doi:https://doi.org/10.1016/j.jcf.2018.08.015.

George, A.M., Jones, P.M. and Middleton, P.G. (2009). Cystic fibrosis infections: treatment strategies and prospects. *FEMS Microbiology Letters*, [online] 300(2), pp.153–164. doi:https://doi.org/10.1111/j.1574-6968.2009.01704.x.

Hickey, P.W., Sutton, D.A., Fothergill, A.W., Rinaldi, M.G., Wickes, B.L., Schmidt, H.J. and Walsh, T.J. (2009). Trichosporon mycotoxinivorans, a Novel Respiratory Pathogen in Patients with Cystic Fibrosis. *Journal of Clinical Microbiology*, [online] 47(10), pp.3091–3097. doi:https://doi.org/10.1128/JCM.00460-09.

Questions?